

Multi-sensory integration in the olfactory bulb

The effect of metabolic state on the representation of odours

Cédric Stefens

Submitted in accordance with the requirements for the degree of
Doctor of Philosophy

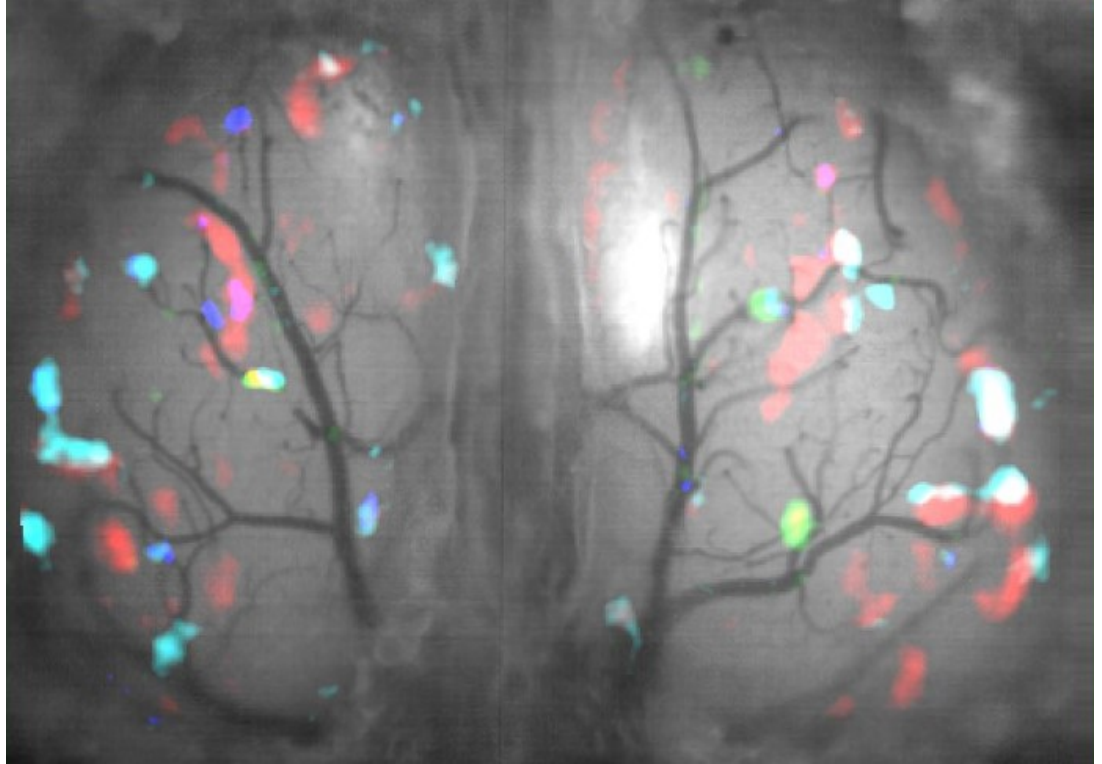
The University of Leeds
School of Biomedical Sciences

November, 2021

The candidate confirms that the work submitted is his own and that appropriate credit has been given where reference has been made to the work of others.

This copy has been supplied on the understanding that it is copyright material and that no quotation from the thesis may be published without proper acknowledgement.

The right of Cédric Stefens to be identified as Author of this work has been asserted by him in accordance with the Copyright, Designs and Patents Act 1988.



Conference abstracts

Cédric Stefens and Jamie Johnston (2017). Multi-sensory integration in the olfactory bulb: The effect of metabolic state on the representation of odours.

The Physiological Society, Future physiology 2017 – Leeds, UK

Selected as a finalist contestee for poster communication

Cédric Stefens and Jamie Johnston (2018). Multi-sensory integration in the olfactory bulb: The effect of metabolic state on the representation of odours.

FBS/FMH Postgraduate Symposium 2018 – Leeds, UK

Cédric Stefens and Jamie Johnston (2019). Multi-sensory integration in the olfactory bulb: The effect of metabolic state on the representation of odours.

FBS Postgraduate Symposium 2019 – Leeds, UK

Cédric Stefens and Jamie Johnston (2019). Multi-sensory integration in the olfactory bulb: The effect of metabolic state on the encoding of odours.

CAJAL course on Biosensors and actuators for cellular and systems neuroscience 2019 – Bordeaux School of Neuroscience, Bordeaux, France

Acknowledgements

This research has been carried out by a team which has included Dr Jamie Johnston. My own contributions, fully and explicitly indicated in the thesis, have been surgery; in vivo imaging; developing software: pipeline for calcium imaging data, intrinsic signal optical imaging data and OMMI data, olfactometer control, intrinsic signal optical imaging and OMMI setup control; developing hardware: custom-build preliminary olfactometer, modification of a pre-built olfactometer, respiration monitoring device and the OMMI system; data analysis, and conducting behavioural tests. The other members of the group and their contributions have been as follows: Dr Jamie Johnston and Louis Vande Perre on the development of the OMMI system; Gemma Gothard and Charlotte Hall for immunohistochemistry; Dr Paul Armstrong for the help setting up behavioural tests,

Transitioning from engineering to neurobiology was an exciting ride and would not have been as enjoyable without the following people. I thank Dr Jamie Johnston, for his supervision and the opportunity to pursue research in neuroscience in his nascent lab. I learned from his expertise and guidance through this academic journey. I am thankful for the moral support and camaraderie of Dr Emily Johnston, Mark Conway, Louis Vande Perre, Maxime Verstraeten, Andreea Pantiru, Dr Scott Dunkley, Dr Lynda Djerbal, and Dr Vincenzo Prato.

Thanks to the University of Leeds, Boehringer Ingelheim Fonds, and the physiological society for the funding to attend international school and conferences.

I am grateful for the encouragement from my parents and grandparents and their unconditional support.

Abstract

This thesis aims to investigate how the metabolic state can influence perception, specifically how the circuitry of the olfactory bulb is modulated by signals of satiety. The multi-sensory integration of satiety and olfaction has been studied using behavioural paradigms (Aimé et al. 2007; Berg et al. 1963; Soria-Gómez et al. 2014a; Yeomans 2006) which show that fasting increases olfactory sensitivity as satiation decreases it. This integration seems to happen in the olfactory bulb (Julliard et al. 2017a; Tucker et al. 2013a).

The hypothesis defended here is that glycemia-olfaction integration occurs at the first synapses in the brain, in the glomerular layer of the olfactory bulb where olfactory sensory neurons project their axons. The inhibitory interneurons, periglomerular cells, provide feedback inhibition onto the olfactory sensory neurons. Furthermore, the glucose-sensing molecular machinery, Kv1.3, and GLUT4 are known to be present in glomeruli neuropile (Al Koborssy et al. 2014; Kovach et al. 2016). Therefore the periglomerular cells are ideally placed to dampen olfactory sensitivity by sensing glucose and subsequently reduce the glutamatergic afferent transmission from the olfactory sensory neurons onto the principal neurons, the mitral cells.

I used calcium imaging in anaesthetised GCaMP6fxVGAT mice to record odour-evoked activity of periglomerular cells, with a two-photon microscope. Using a widefield one-photon microscope combined with intrinsic signal optical imaging, I simultaneously imaged the afference and the periglomerular activity. In adjunct, I conducted odour detection tests. Mice were observed fasted and sated following intraperitoneal glucose injection.

I found that increased blood glucose increased the excitability of periglomerular cells for odours at low concentration and a co-occurring reduced activity of the afference. These results suggest that this aspect of satiety amplifies the feedback inhibition at the first synapse in the olfactory bulb and participates in an increased odour detection threshold in perception.

Table of Contents

Conference abstracts	iv
Acknowledgements	vi
Abstract	vii
Table of Contents	viii
List of Tables	xii
List of Figures	xiii
List of Abbreviations	xvi
Chapter 1 Introduction	1
1.1 The olfactory system	1
1.1.1 General overview	2
1.1.2 Nasal Cavity	3
1.1.3 The nasal epithelium	4
1.1.3.1 Organisation.....	4
1.1.3.2 Olfactory transduction	7
1.1.4 The olfactory bulb.....	9
1.1.4.1 Organisation.....	9
1.1.4.2 Neural populations	11
1.1.4.3 Olfactory Sensory Neurons	11
1.1.4.3 Cell types of the glomerular layer.....	14
1.1.4.4 Periglomerular Cells	14
Heterogeneity.....	14
Neurochemistry	17
1.1.4.5 Connectivity of PGCs	18
Periglomerular Cell inputs	18
Periglomerular Cell outputs	19
Periglomerular Cells -> Olfactory Sensory Neurons.....	19
Periglomerular Cells -> Mitral cells.....	20
Periglomerular Cells -> External Tufted cells	20
Periglomerular Cells -> Periglomerular Cells	20
Superficial Short Axon cells -> PGC/ETC/MTC.....	21
1.1.4.6 Morphology of PGCs.....	21
1.1.4.7 Electrophysiological properties of PGCs	22
1.1.4.8 In vivo responses of PGCs.....	24
1.1.4.9 External Tufted cells.....	25

1.1.4.10 Granule Cells	26
1.1.4.11 Mitral / tufted cells	26
1.1.4.12 Neural circuits	28
Intraglomerular circuit.....	28
Interglomerular circuit.....	30
1.1.5 Roles in olfaction	33
1.1.5.1 Encoding	33
1.1.5.2 Processing	36
1.1.5.3 Transmission.....	37
1.1.6 Centrifugal inputs	37
1.1.6.1 Noradrenergic inputs.....	38
1.1.6.2 Serotonergic inputs	39
1.1.6.3 Cholinergic input	40
1.1.6.4 Global aspects of neuromodulatory inputs	41
1.2 Metabolic sensing.....	42
1.2.1 Metabolism signalling in the OB	43
1.2.1.1 The neural circuits of nutrients sensing.....	43
1.2.1.2 Ghrelin.....	45
1.2.1.3 Leptin	46
1.2.1.4 CCK.....	46
1.2.1.5 Orexin.....	47
1.2.1.6 neuropeptide Y	48
1.2.1.7 Endocannabinoids.....	48
1.2.2 Insulin.....	49
1.2.2.1 Insulin in metabolism homeostasis.....	49
1.2.2.2 Insulin signaling to the CNS	50
1.2.2.3 Insulin in the olfactory bulb MTC	52
1.2.2.4 Insulin-mediated behaviour	53
1.2.3 Glucose	53
1.2.4 Summary.....	54
1.3 Aims and objectives	55
1.3.1 Characterise odour-evoked PGC activity and infer PGC subtypes.....	55
1.3.2 Manipulate feedback inhibition at the first synapses	55
1.3.3 Demonstrate the effect of blood glucose on OSNs and PGCs	56

Chapter 2 Methods	57
2.1 Animals	57
2.1.1 VGATxGCaMP6f mice	57
2.1.2 Fasted and sated states	57
2.2 Surgery for acute cranial windows	58
2.3 Pharmacology	59
2.4 Immunostaining	59
2.5 Monitoring	62
2.6 Olfactometer.....	63
2.7 Two-photon imaging.....	68
2.8 Calcium imaging data processing.....	72
2.9 Glucose tolerance test.....	74
2.10 Odour detection test.....	74
2.11 Statistical tests	75
Chapter 3 Odour-evoked periglomerular cells properties	77
3.1 Introduction	77
3.2 Results	78
3.2.1 General overview of odourant-evoked calcium responses in PGC	80
3.2.2 Characterisation of response dynamics	84
3.2.3 Estimating connectivity between PGCs and glomeruli	93
3.2.4 Sensitivity of PGCs connected to a same glomerulus	101
3.2.5 Oscillatory activity and phase coding	112
3.2.6 PGC subtypes inference from function and connectivity	123
3.3 Conclusion	128
Chapter 4 OMMI: Optical multi-modal imaging	130
4.1 Introduction	130
4.2 Multi-population imaging	131
4.3 OMMI: Optical Multi-Modal Imaging	134
4.3.1 Description of necessary Hardware	137
4.3.2 Control of equipment.....	139
4.3.3 Experimental design: A walkthrough of an experiment	143
4.3.4 Analysis of Experiment.....	146

4.4 Circuit manipulation: blocking afferent glutamatergic inputs	149
4.5 Conclusion	152
Chapter 5 The effect of blood glucose on olfactory sensitivity	154
5.1 Introduction	154
5.2 Sensory-metabolic integration	155
5.2.1 Expression of metabolically sensitive proteins	155
5.2.2 Modulating blood glucose levels	157
5.3 The effect of increased blood glucose on olfactory sensory neurons and periglomerular cells at the first synapses of the olfactory bulb.....	165
5.4 Glycemia-driven transformation of PGC dose-response curve in somata and glomeruli	178
5.5 Displacement of the PGC activation thresholds in regards to blood glucose time course	185
5.6 Conclusion	206
Chapter 6 Summary discussion, future perspectives and Conclusion.....	207
6.1 Characterisation of odour-evoked PGC properties	207
6.1.1 odour-evoked periglomerular cells properties	207
6.1.2 PGC inheritance of mechano-sensitive signals from OSN	208
6.1.3 determining PGC subtypes based on odour-evoked activity.....	209
6.2 Optical Multi-Modal Imaging for simultaneous recording of OSN and PGC.....	210
6.3 Effect of blood glucose on OSN and PGC in glomeruli	212
6.4 Future suggestions.....	213
6.5 Overall conclusion	217
Bibliography	219
Appendix A python scripts.....	235
Appendix B PGC characteristics details	254
Appendix C cosinus and Hill functions fitting	261
Appendix D PGC activation thresholds for isoamyl acetate	264

List of Tables

Table 1.1 Ligands and functions of receptors in olfactory sensory organs	6
Table 1.2 Periglomerular cell subtypes	13
Table 2.1 Primary antibody details	61
Table 2.2 Secondary antibody details	62
Table 2.3 PID measurements for isoamyl acetate step stimuli.	67
Table 4.1 OMMI materials.	8

List of Figures

Figure 1.1 Overview of the olfactory system	4
Figure 1.2 Transduction and receptor field of olfactory receptors	8
Figure 1.3 Basic structure of the olfactory bulb	10
Figure 1.4 Identity and anatomy of PGC subtypes	16
Figure 1.5 Connectivity per periglomerular cell subtypes in the glomerular layer	22
Figure 1.6 Intraglomerular circuits	30
Figure 1.7 Interglomerular circuits	32
Figure 1.8 Nutrients signaling in fasted and satiated states	45
Figure 1.9 Kv1.3 as an insulin-glucose cellular sensor	52
Figure 2.1 Olfactory bulb craniotomy	59
Figure 2.2 Immunohistochemistry control images	61
Figure 2.3 Custom-built respiratory monitoring device	63
Figure 2.4 Odour pulse delays to final valve opening and closing	66
Figure 2.5 Olfactometer diagram	67
Figure 2.6 Comparison between 1-photon and 2-photon excitation	70
Figure 2.7 Two-photon microscope diagram	71
Figure 2.8 Calcium imaging data pipeline	71
Figure 3.1 In vivo calcium imaging of PGCs under odour stimulations	80
Figure 3.2 Parsing of odour-evoked responses	82
Figure 3.3 Respiration-evoked oscillations	84
Figure 3.4 Clustering of odour-evoked PGC responses	85
Figure 3.5 Repartition of shape clusters across odours.	87
Figure 3.6 Repartition of shape clusters across relative activations	89
Figure 3.7 Repartition of shape clusters across odour in the same cell or glomerulus	92
Figure 3.8 Glomeruli-PGC connectivity	95
Figure 3.9 Comparison of response sequences within glomerulus-PGCs groups	98
Figure 3.10 Glomeruli are the input sources to PGCs	100
Figure 3.11 Sensitivity variation within glomerulus-PGC groups	104
Figure 3.12 Hill function parameters variations within glomerulus- PGC groups	109

Figure 3.13 PGCs reflect OSN breathing mechano-sensitivity. The PGCs inherit the respiration-evoked activity from the OSNs.....	113
Figure 3.14 Respiration-triggered averaging and phase coding.....	116
Figure 3.15 Phase shift variability within glomerulus-PGCs groups.....	119
Figure 3.16 Phase shift variability across glomerulus-PGCs groups.....	121
Figure 3.17 Relation of PGCs and PGC-odour pairs metrics to connectivity and odour tuning.....	125
Figure 3.18 Principal Component Analysis of PGC and PGC-odour metrics.....	127
Figure 4.1 two-photon multi-population imaging.....	132
Figure 4.2 OMMI setup and control of equipment.....	136
Figure 4.3 OMMI Graphical User Interface.....	140
Figure 4.4 File splitting and odour map creation in the GUI.....	142
Figure 4.5 OMMI results.....	146
Figure 4.6 preprocessing and segmentation of glomeruli.....	148
Figure 4.7 Changes of activity in olfactory sensory neurons and periglomerular cells following iGluR blockers.....	150
Figure 4.8 PGC-OSN feedback inhibition reduces following iGluR blockers.....	152
Figure 5.1 Expression of GLUT4 and Kv1.3 in the olfactory bulb glomerular layer.....	156
Figure 5.2 Modulating blood glucose levels and hunger.....	158
Figure 5.3 Olfactory sensitivity test.....	159
Figure 5.4 Locomotion tracking.....	162
Figure 5.5 Olfactory sensitivity test with tracking.....	163
Figure 5.6 Naïve olfactory preference test.....	164
Figure 5.7 Changes of activity in olfactory sensory neurons and periglomerular cells following heightened blood glucose.....	168
Figure 5.8 Distribution of changes in OSN-PGC glomeruli activity following heightened blood glucose.....	169
Figure 5.9 Changes of activity in olfactory sensory neurons and periglomerular cells following heightened blood glucose with reduced glutamatergic inputs.....	173
Figure 5.10 Distribution of changes in OSN-PGC glomeruli activity following heightened blood glucose with reduced glutamatergic inputs.....	174
Figure 5.11 Summary of change of activity in OSN-PGC-odour pairs following glucose administration.....	177

Figure 5.12 Profile of activation of periglomerular cells in fasted and sated states	180
Figure 5.13 Changes in earliest and maximum responses of PGCs somata and glomeruli	182
Figure 5.14 Transformations of Hill functions of PGCs somata and glomeruli.....	184
Figure 5.15 PID calibration and ramp stimulus	187
Figure 5.16 Ramp stimuli as a tool to estimate dose-response curves.....	188
Figure 5.17 Ramp stimuli as a tool to estimate sensitivity threshold.....	191
Figure 5.18 ramps experiment.	192
Figure 5.19 Average ramp responses and activation detection in PGCs following glucose administration.....	196
Figure 5.20 Average ramp responses and activation detection in glomeruli following glucose administration	197
Figure 5.21 Change in sensitivity and maximum responses following glucose administration across 3 time periods.....	200
Figure 5.22 Difference in sensitivity threshold and maximum responses between the fasted state and the 60 minutes following glucose administration	204
Figure 6.1 Graphical summary of glucose experiments	215
Figure 6.2 Hypothesis of glucose-mediated inhibition of the olfactory afference	216

List of Abbreviations

PGC	Periglomerular cell
OSN	Olfactory sensory neuron
SSA	Superficial Short Axon cell
MGC	Monoglomerular cell
UGC	Uniglomerular cell
POGC	Polyglomerular cell
OGC	Oligoglomerular cell
ET	External tufted cell
MT	Mitral cell
ISOI	Intrinsic signal optical imaging
MRR	Molecular receptive range
AP	Action potential
IP	intraperitoneal
GUI	Graphical user interface
iGluR	Ionotropic glutamate receptor
API	Application program interface
CCK	Cholecystokinin
NPY	Neuropeptide Y
OB	Olfactory bulb
GL	Glomerular layer

Chapter 1

Introduction

This thesis aims to explore how our internal state can influence our perception and behaviour, specifically how the circuitry of the olfactory bulb is modulated by signals of satiety. The multi-sensory integration of satiety and olfaction has been studied using behavioural paradigms (Aimé et al. 2007; Berg et al. 1963; Soria-Gómez et al. 2014b; Yeomans 2006) which show that fasting increases olfactory sensitivity as satiation decreases it. In neurobiology, the integration seems to happen in a multitude of areas of the olfactory system (Julliard et al. 2017b), in the olfactory epithelium principal neurons (Kaniganti et al. 2019; Negroni et al. 2012), in the olfactory bulb principal neurons (Tucker et al. 2013b) and later brain structures (Critchley and Rolls 1996; O'Doherty et al. 2000).

The hypothesis defended here is that glycemia-olfaction integration occurs at the earliest synapses in the brain, in the glomerular layer of the olfactory bulb which receives olfactory receptor neuron input. I speculate the periglomerular cells are responsible for this integration. This introduction will lay out the pre-requisite knowledge needed to interpret our results: how the olfactory bulb process and transmit sensory information, how metabolic sensing is integrated into olfaction, and how these mechanisms relate to the animal food-odour behaviours.

1.1 The olfactory system

To persist in its environment, any biological system must retrieve data about its surroundings and act upon them accordingly. Airborne volatile molecules can carry information about food, predators, and the sexual cycle of conspecifics, which is processed by the olfactory system. Olfaction is one of the oldest senses, as the first bacteria had only a simple set of sensory mechanisms limited by their membrane possibility to host chemical receptors. These membrane channels are the precursors to chemosensing, which ended up as taste and olfaction in current animals that evolved to dispose of complex chemosensing organs. Olfaction evolved from being receptor-based to organ-based through evolution. This evolution to a more complex processing unit has led to an increase in the repertoire of detectable olfactory stimuli.

The olfactory system detects odourants and transmits their identity and attributes as electro-chemical signals to the brain. Odourants are small volatile molecules; a particular mix of molecules can give rise to a specific odour as it is the case with the olfactory percept of coffee. On the other hand, some odours such as banana can be meaningfully designated by a single odourant such as isoamyl acetate. One might argue that chemosensing ability co-evolved with the increasing richness of the molecular environment, which required a more nuanced sensing. The high dimensionality of odourants representation compared to other senses like vision or audition has remained a challenge in sensory system neuroscience until nowadays. For a matter of perspective, a perceived image can be essentially represented as a 2-dimensional array of colour values and a perceived sound as a temporal trace that is sampling air pressure variations. Mice express around 1500 olfactory receptor genes, and elephants even 2000. This broad spectrum of receptors increases the ability for a complex representation. However, keep notice that in humans, the olfactory receptor gene family, while being the largest in the human genome with 400 genes, remains restrained compared to other mammals. This translates well into the differential necessity of olfaction for survival for each species as it is well-known rodents are more reliant on olfaction than humans (Olender, Lancet, and Nebert 2008). However, human olfaction can still outscore rodents and other animals for particular odourants (Kass et al. 2017) suggesting a species-dependent olfactory specialisation.

Finally, rodents possess an exacerbated chemosensing system amongst mammals, ideal for the study of that sense, by which I will introduce the components of the olfactory system.

1.1.1 General overview

Odourants are transduced into neural signals at the olfactory epithelium which, therefore, serves as an interface between molecular-based and action potential-based information about odourants. Each olfactory sensory neuron (OSN) in the epithelium expresses one type of olfactory receptor, and depending on that type, will synapse into principal neurons apical dendrites within a glomerulus in the olfactory bulb. The glomeruli, neuropile structures representing each type of receptor, with the juxtaposed interneurons form the first layer of inhibition. A second layer of neurons inhibits the principal neurons

at their base. The olfactory information is thus modified by two layers in the OB before its broadcast by the principal neurons down the cortex. I will now review each stage of the olfactory pathway in more scrutiny.

1.1.2 Nasal Cavity

Odourants can enter the nasal cavity either through “sniffing”, the orthonasal route, or via the oral cavity, the retronasal route. There are number of sensory areas within the nasal cavity (Fig. 1.1). The Grueneberg ganglion located in the anterior region of the nose projects to the olfactory bulb (Fuss, Omura, and Mombaerts 2005) and is both thermal (Joerg Fleischer and Breer 2010) and chemo sensitive (C. Y. Liu, Fraser, and Koos 2009; Storan and Key 2006), responding to danger pheromones (Brechtbühl et al. 2013; Jörg Fleischer et al. 2006; Moine et al. 2018). The septal organ, in the ventral base of the nasal septum, is chemo-sensitive (Ma et al. 2003) and mechanosensitive (Grosmaître et al. 2007), and projects to the olfactory bulb (Tian and Ma 2004). The Vomeronasal organ projects to the accessory olfactory bulb (Rodriguez, Feinstein, and Mombaerts 1999) and provides conspecific and environmental recognition (Su, Menuz, and Carlson 2009). With the accessory olfactory bulb, it forms the accessory olfactory system. In humans, it remains non-functional and vestigial (Kouros-Mehr 2001). Finally, the trigeminal nerve, which innerves the face, also provides chemosensation and thermosensation within the nasal mucosa (Gerhold and Bautista 2009).

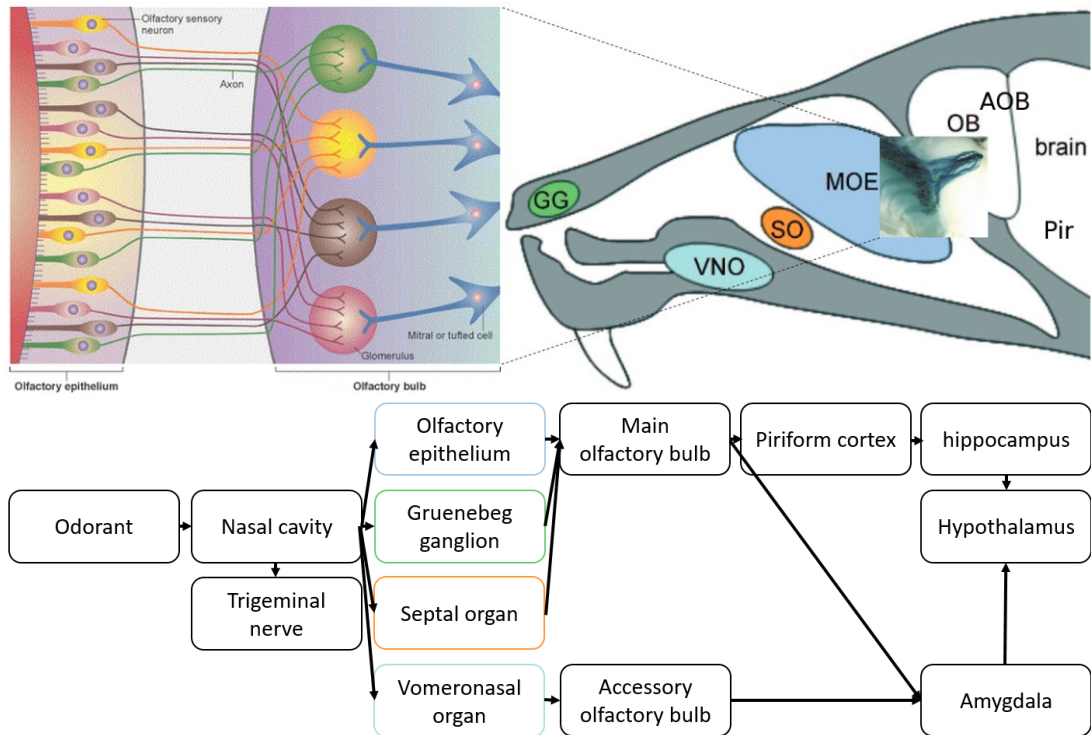


Figure 1.1 Overview of the olfactory system. Sensory organs (Grueneberg ganglion (GG), Vomerolnasal organ (VNO), Septal organ (SO), Main olfactory epithelium (MOE)) possess sensory neurons that transduce the presence of odourant molecules in the nasal cavity. Olfactory information is subsequently transferred and processed by primary olfactory brain areas (olfactory bulb (OB), accessory olfactory bulb (AOB), piriform cortex (Pir)). Top: Axonal wiring at the interface of the MOE and OB. Adapted with permission from Mombaerts (2006). Olfactory sensory neurons expressing a same receptor send their axon to a same glomerulus. Example staining of M71-LacZ gene-targeted axons merging into a glomerulus. Adapted with permission from Feinstein and Mombaerts (2004). Bottom: tracks of odourant information processing in the olfactory system.

1.1.3 The nasal epithelium

1.1.3.1 Organisation

The nasal epithelium is the main interface between the molecular features of odourants flowing through the nasal cavity and the first olfactory-evoked signals in the brain. The molecular information is transduced into action potentials by the olfactory sensory neurons. There are 1141 olfactory receptor genes in the mouse genome, giving a high dimensionality to represent odours. Each OSN expresses one type of olfactory receptor (Chess et al. 1994; Malnic et al. 1999) and OSNs having the same receptor project their axons into 2 glomeruli per bulb (Mombaerts et al. 1996; Ressler, Sullivan, and Buck 1994;

Vassar et al. 1994) (Fig. 1.1). Each of the ~2000 glomeruli receives more than 5000 OSN axons, making it a high convergence of inputs (Mombaerts 2006) (Fig. 1.1).

The spatial organisation of OSN by type of receptor remains complex. Although regions have been determined, the immense amount of olfactory receptors to stain for makes it difficult. While distinct organs of the nasal cavities express a wide diversity of receptors, the scope of this thesis is restricted to the classical olfactory receptors of the main epithelium (Table 1.1). It was previously thought the main olfactory epithelium is divided into 4 non-overlapping zones (Strotmann et al. 1994). However, Zapiec and Mombaerts (2020) showed, using 3D-reconstructed multi-colour fluorescence in situ hybridization the presence of at least 9 highly overlapping zones, only classifying the expression areas of 68 olfactory receptors.

Organ	Receptors	Ligands	Origin	Proposed Functions
MOE	ORs	general odours	food, environment	odour recognition, discrimination, attraction/repulsion
		MHC class I peptides	urine, bodily secretions	social recognition of other strains
	TAARs	volatile amines	urine	stress response, gender recognition, acceleration of female puberty onset
	GC-D	CO ₂ (bicarbonate)	atmosphere	avoidance behaviour
		peptide hormones (uroguanylin and guanylin)	urine	salt/water homeostasis, detection of cues related to hunger, satiety, or thirst
VNO	V1Rs	volatile pheromones, sulfated steroids	urine	conspecific recognition, male sexual behaviour, maternal aggression, regulation of female estrous cycles, stress level indicator
	V2Rs	MHC class I peptides	urine, bodily secretions	mate recognition in the context of pregnancy block (Bruce effect)
		exocrine gland-secreting peptides (ESPs)	tears from specific genders or strains	information about gender and individual identity, conspecific recognition
		major urinary protein (MUP) complex	male urine	male aggression
		sulfated steroids	female urine	indication of stress levels
	Formyl Peptide Receptors	formyl peptides	gram-negative bacteria	indication of pathogenicity or health status
		CRAMP, lipoxin, uPAR peptides	immune system	indication of pathogenicity or health status
GG	TAARs, V2r83	alarm pheromones	Stressed conspecifics	avoidance of dangerous situations
SO	GRs	General odours	Food, environment	Alerting role or “mini-nose”

Table 1.1 Ligands and functions of receptors in olfactory sensory organs. Abbreviations: MOE, main olfactory epithelium; OR, olfactory receptor; GG, Grueneberg ganglion; SO, septal organ of Masera; TAARs, trace amine-associated receptors; TRPM5, transient receptor potential channel M5; GC-D, receptor guanylyl cyclase; VNO, vomeronasal organ; MHC, major histocompatibility complex. Adapted with permission from Su et al. (2009).

1.1.3.2 Olfactory transduction

For the brain to process an odour, first its molecular form must be transduced into neuronal activity in the form of action potentials. The olfactory sensory neurons (OSN) take care of that transduction and their axons project directly to the OB. OSNs are present in the nasal epithelium and possess cilia that bind odourants dissolved in the nasal lumen. The binding is done with olfactory receptors (OR), a type of G protein-coupled receptor (GPCR) whose family is expressed in OSN (Buck and Axel 1991) (Fig. 1.2). A molecule can activate multiple receptors and a receptor can be activated by multiple molecules. The range of OR-activating molecules defines the receptive field of an OSN type.

The transduction mechanism is operated through a second messenger cascade (Restrepo, Teeter, and Schild 1996) (Fig. 1.2) which results in the triggering of an action potential. The binding of an odourant molecule on the GPCR starts a cascade of enzymatic activity involving a G protein that activates adenylyl cyclase 3 (AC3) which converts ATP into the second messenger cyclic AMP (cAMP). cAMP then opens cyclic nucleotide-gated (CNG) ion channel (Firestein, Zufall, and Shepherd 1991) permeable to Na^+ and Ca^{2+} , which contribute to depolarizing the membrane potential. The Ca^{2+} entry reinforces the depolarisation by activating Ca^{2+} dependent Cl^- channels. OSNs maintain a high intracellular Cl^- concentration, therefore opening of Cl^- channels results in depolarisation by efflux of Cl^- (Firestein 2001). OSNs can not only be excited by odourants but also inhibited (Duchamp-Viret, Duchamp, and Chaput 2003; Kurahashi, Lowe, and Gold 1994; Oka et al. 2004; Pfister et al. 2020; Sanhueza, Schmachtenberg, and Bacigalupo 2000; Takeuchi et al. 2009). Odourant receptor inhibition increases encoding capacity by creating a sparser receptor code (Pfister et al. 2020). The mechanism of inhibition involves in part phosphoinositide signaling (Ache, 2010). Odourants can suppress basal activity of receptors via inverse agonism (Reisert 2010). The resulting action potentials generated by olfactory transduction are sent along the olfactory nerve, passing through the cribriform plate, to the olfactory bulb.

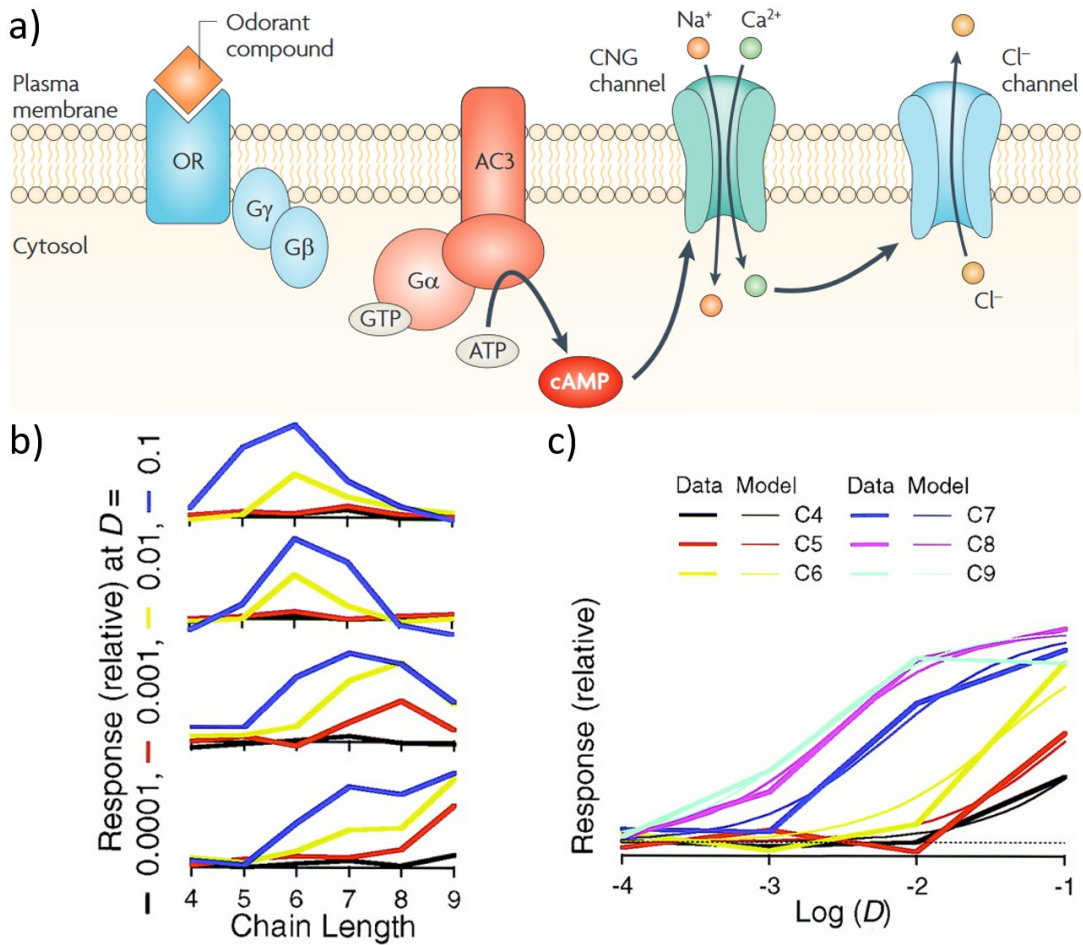


Figure 1.2 Transduction and receptor field of olfactory receptors. a) The odourant transduction pathway. Adapted with permission from Zou, Chesler, and Firestein (2009). The binding of an odourant compound leads to the depolarisation of the cell membrane. Through a second messenger cascade, a G protein activates AC3 that turns ATP into cAMP which opens CNG channel, letting enter Na⁺ and Ca²⁺ cations. This depolarization is reinforced by the Ca²⁺ provoking a Cl⁻ efflux. An odourant can bind to multiple olfactory receptors and vice versa. **b)** Molecular receptive range. Receptive field of 4 different OSNs with relation to aliphatic aldehyde of chain length from 4 to 9, at different concentrations D. The top two plots show narrower tuning while the bottom two are broadly tuned (Meister and Bonhoeffer 2001). **c)** Concentration dependence of OSN responses. Response of a single type of OSN depending on odourant concentration D for different size aliphatic aldehyde (Meister and Bonhoeffer, 2001). Model plots fit the Hill equation, a sigmoidal curve that describes the binding of ligands. Adapted with permission from Meister and Bonhoeffer (2001).

1.1.4 The olfactory bulb

The first stage of odour processing occurs in the olfactory bulb, its localization at the rostral-dorsal end of the brain in mice makes experimental access easy and its basic structure is known (Shepherd 1972) (Fig. 1.1), even if some debate remains concerning the precise organisation of the circuit (Gire and Schoppa 2009; Ressler, Sullivan, and Buck 1994; Soucy et al. 2009). In the context of developing knowledge in the functioning of the brain, especially how sensory information is encoded and processed through neural circuits, the olfactory bulb (OB) is a well-suited brain area to investigate.

1.1.4.1 Organisation

From the nose to the OB, the molecular features of odourants are transformed into a spatial map of neural activity. The main afferent input to the OB comes from the olfactory sensory neurons (OSN) in the nasal epithelium. Odourant binding to an olfactory receptor causes depolarisation and action potential firing, which propagates along the axon to synapse in a glomerulus. Glomeruli are ellipsoidal neuropil structures where OSN axons, juxtglomerular cells processes and output neurons dendrites meet and synapse in complex micro-circuits. The output of the OB is carried by mitral and tufted cells (Fig.1.3), whose axons form the lateral olfactory tract, which sends signals to several target regions including the olfactory cortex, entorhinal cortex, and amygdala (Fig. 1.1). Within the OB there are two layers of inhibition: in the outer layer, there are periglomerular (PG) cells and superficial short axon (SA) cells (Fig. 1.3), which interact with OSN synapses and Mitral/tufted cell apical dendrites. In the inner layers, granule cells interact with Mitral/tufted cell lateral dendrites (Fig. 1.3).

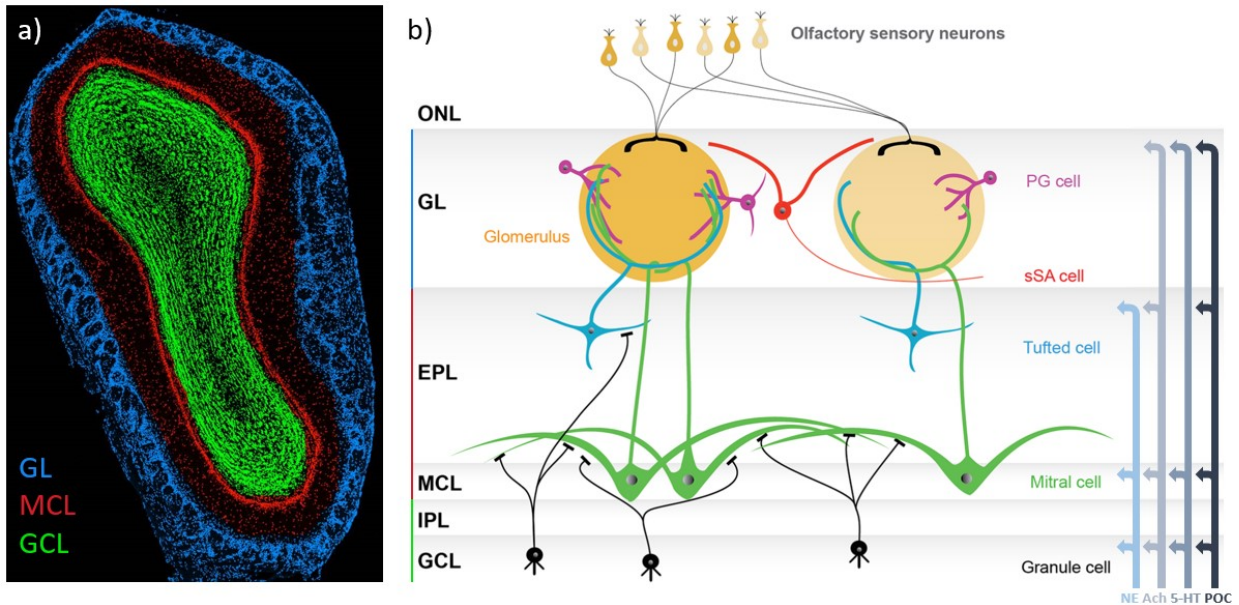


Figure 1.3 Basic structure of the olfactory bulb. a) Coronal image of mouse main olfactory bulb cell nuclei, adapted with permission from Zou et al. (2009). Axons of olfactory receptor neurons, forming the olfactory nerve, project into the outermost layer of the bulb. These axons converge into glomeruli where they synapse with interneurons and second-order projection neurons in the glomerular layer (GL; in blue). Mitral cell bodies which outputs signal from the bulb, makes up the mitral cell layer (MCL; in red). Migrating immature interneurons, lying at the centre of the bulb, form The granule cell layer (GCL; in green). **b)** Schematic diagram of the olfactory bulb layers. Adapted with permission from Nagayama, Homma, and Imamura (2014). The external plexiform layer (EPL) hosts outputs neurons bodies in green and blue. The main interneurons are found the GL and GCL in black, red and purple. The OB receives centrifugal inputs from the primary olfactory cortex, locus coeruleus (norepinephrine), diagonal band (acetylcholine) and raphe (serotonin). ONL: Olfactory Nerve Layer, GL: Glomerular Layer, EPL: External Plexiform Layer, MCL: Mitral Cells Layer, IPL: Internal Plexiform Layer, GCL: Granule Cells Layer, NE: norepinephrine, Ach: acetylcholine, 5-HT: serotonin, POC: primary olfactory cortex.

1.1.4.2 Neural populations

1.1.4.3 Olfactory Sensory Neurons

Olfactory sensory neurons project within the glomerulus, forming axo-dendritic glutamatergic synapses with output neurons, the mitral/tufted cells, and with periglomerular and short-axon interneurons (Fig. 1.3). Odour-evoked and sniffing-evoked OSN action potential induces the release of glutamate into mitral/tufted and periglomerular cells via activation of AMPA and N-methyl-D-aspartate (NMDA) ionotropic glutamate receptors (V. Aroniadou-Anderjaska, Ennis, and Shipley 1997; Keller et al. 1998; Murphy et al. 2004).

There is a very high level of convergence with each glomerulus receiving input from ~5000 ORNs all of which express the same olfactory receptor. Such high convergence might be useful to amplify OSN signals by pooling inputs, reducing overall noise and giving a more accurate precision on the intensity of activation of a group of OSNs. This suggests that such large convergence increases sensitivity to concentration (Cleland et al. 2012), where the steepness of the receptors hill function is smoothed out by sequential recruitment of axons with increasing concentration. The OSN input to the glomeruli is therefore defined by a sigmoid-like graded signal depending on the number of activated OSNs and the binding of ligands in each OSN (Fig 1.2). The selectivity of an OSN ligand can be seen as a receptive field. It determines for which range of odours the OSN is tuned for, which is also the same tuning of the glomerulus the OSN projects to.

The receptive field of an OSN is described in terms of the molecular receptive range (MRR) (Mori and Shepherd 1994). Unlike in the visual system where receptive fields correspond to a single point in space, the MRR of OSNs lack such selectivity, a single OSN will bind to multiple different odourants. Although the MRR is broad for most OSNs, some OSNs have a narrow MRR (Fig. 1.2) responding to very few odourants, which may be due to the

importance of a particular odour for the organisms ecology (Wilson and Mainen 2006). The amplitude of OSNs response is increasing in a concentration-dependent manner and therefore can convey the intensity of an odourant in terms of its density (Fig. 1.2) (Meister and Bonhoeffer, 2001).

OSNs are also mechanosensitive. A rise in airflow alone can drive OSN activity (Iwata and Kiyonari 2017). Thus a periodically varying airflow due to the breathing rhythm generates sniff-coupled oscillations in OSN. Those mechanosensory-based oscillations are reflected in the glomerular input and output activity and are propagated through the olfactory brain pathway in the piriform cortex and further brain areas (Wachowiak 2011). The sniff coupling is impaired during naris occlusion and follows the inhalation frequency, as shown with an airflow-modulating tracheotomy. While the dogma instructs that mechanotransduction is conveyed by force-gated ion channels, it appears that G protein-coupled receptors underlie mechanosensitivity, as its genetic ablation eliminates the transduction (Connelly et al. 2015). Inhalation-driven neural dynamic plays a central role in phase coding of odours as it sets a temporal structure for sensory inputs (Iwata and Kiyonari 2017; Jordan et al. 2018; Wachowiak 2011).

The output from the OSN is modulated at its terminals by the presence of GABA_B and D2 receptors, which activated, reduces Ca²⁺ influx to terminals resulting in a lower probability of glutamate release. This inhibition could serve to preserve synaptic resources or extend the dynamic range when strong stimuli occur (McGann, 2013). This allows more degrees of graded excitation as this inhibition delays the point where the OSN activity saturates. GABA_B-mediated and D2-mediated presynaptic inhibition modulates the strength of the input signal transmitted from OSN to MTC/TC (Ennis et al. 2001a; Pérez and Wachowiak 2008; Zak, Whitesell, and Schoppa 2015). The GABAergic mediation exerts a tonic and a phasic components, and is organized intraglomerularly. On the other hand, dopaminergic mediation is based across multiple glomeruli (McGann, 2013).

subtypes	Microglomerular	Uniglomerular	Oligoglomerular	Polyglomerular
Corresponding previous nomenclature	Periglomerular	Periglomerular (Pinching and Powell, 1971), Uniglomerular (Kiyokage et al., 2010)	Periglomerular, Oligoglomerular (Kiyokage et al., 2010)	Superficial short axon (Pinching and Powell, 1971; Aungst et al., 2003), Polyglomerular (Kiyokage et al., 2010)
Extension	Tuft within parts of 1 glomerulus	1–3 glomeruli	2–6 glomeruli	≥7 glomeruli
Dendritic length (μm)	469 ± 168	966 ± 377	1821 ± 6	3977 ± 1679
Median soma area (μm ²)	42.2	55.9	87.5	79.0
Median soma diameter (μm)	6.4	7.4	9.3	8.8
Input	ETC	ETC, TC, MC	ETC, OSN	ETC, OSN
Time constant (ms)	37.1 ± 8.7	19.7 ± 10.5	15.3 ± 12.2	13.4 ± 6.7
Input resistance (GΩ)	2.34 ± 1.02	0.71 ± 0.45	0.42 ± 0.20	0.37 ± 0.20
AP amplitude (mV)	40.0 ± 20.4	46.3 ± 14.7	48.1 ± 14.9	54.4 ± 14.5
Function	Unclear	Feedback and feedforward inhibition (Murphy et al., 2005; Shao et al., 2009; Gire et al., 2012; Najac et al., 2015)	Lateral inhibition between local glomeruli (Kiyokage et al., 2010; Whitesell et al., 2013)	Lateral inhibition between distant glomeruli (Aungst et al., 2003; Whitesell et al., 2013)
Expected molecular subtypes	CR, GAD65 (Kosaka et al., 2007; Parrish-Aungst et al., 2007; Whitman and Greer, 2007; Kiyokage et al., 2010)	CB, GAD65 (Kosaka et al., 2007; Parrish-Aungst et al., 2007; Whitman and Greer, 2007)	TH, GAD67 (Kosaka et al., 2007; Parrish-Aungst et al., 2007; Whitman and Greer, 2007; Kiyokage et al., 2010)	TH, GAD67 (Kosaka et al., 2007; Parrish-Aungst et al., 2007; Whitman and Greer, 2007; Kiyokage et al., 2010)

Table 1.2 Periglomerular cell subtypes. Connectivity, morphology, and electrophysiology metrics differentiating PGC subtypes. Adapted with permission from Tavakoli et al. (2018).

1.1.4.3 Cell types of the glomerular layer

PGC is the main type of interneuron in the glomerular layer. The interneurons surrounding glomeruli are more generally called juxtaglomerular cells. That definition can be limited to PGC or extended to all glomerular interneurons. The juxtaglomerular cells are morphologically heterogeneous and a simplified approach would categorise them as threefold: periglomerular cells (PGC), superficial short-axon (SSA) cells, and external tufted cells (ETC). They are the principal actors of the intra-glomerular and lateral circuitry in the glomerular layer. PG cells are thought to be principally involved in local glomerular processing, while SSA may qualify for communication across glomeruli, and ETC to be involved in indirect connections inter and intra-glomeruli.

1.1.4.4 Periglomerular Cells

Periglomerular cells are the most abundant type in the GL. They are small neurons of 5-10 μ m in diameter and usually their dendrites ramify into one or sometimes multiple glomeruli (Nagayama et al., 2014). They are mostly GABAergic with a subset additionally transmitting dopamine. Besides input from the OSN, PGC can receive input from External Tufted, Mitral, Superficial Short Axon and other Periglomerular cells as well as autapses. PG cells are mainly inhibitory releasing GABA onto mitral, PG and the presynaptic terminals of the OSN.

Heterogeneity

PGCs display heterogeneity in morphology, neurochemistry, connectivity and functionality (Crespo et al. 2013; T. Kosaka and Kosaka 2011, 2016; Wachowiak and Shipley 2006). Classification of this heterogeneity in subtypes is a problem that has been tackled multiple times using different approaches including, electrophysiological, morphological and connectivity data (Bywalez et al. 2017; Kiyokage et al. 2010; T. Kosaka, Pignatelli, and Kosaka 2019;

Tavakoli et al. 2018). The classical view simply dividing PGCs according to ETC (PGe) or OSN driving (Pgo) (Kiyokage et al. 2010; K. Kosaka et al. 1998; Z. Shao et al. 2009) has evolved in a distribution of up to 4 subtypes (Tavakoli et al., 2018; Kosaka et al., 2019; Kiyokage et al, 2010; Bywalez 2017). Recently, Tavakoli et al. (2018) addressed the heterogeneity of JGC by an extensive measurement of morphological and electrophysiological features of nearly 100 cells. Subsequent hierarchical clustering of those features corroborates previous classification (Kyokage 2010) of uniglomerular cells (UGC), oligoglomerular cells (OGC) and polyglomerular cells (POGC) while adding a 4th class that is microglomerular cells (MGC). By order of dendritic extent, MGC, UGC, OGC, POGC respectively connect to 1 glomerulus, 1-3 glomeruli, 2-6 glomeruli, and more than 7 glomeruli. POGC branches into glomeruli at the highest distance amongst PGCs, and may actually fall into the SSA category as it possesses an axon, express TH, and inhibit distant glomeruli (Fig. 1.4).

Unfortunately, these categories tend to overlay and make categorisation based on a subset of measurements challenging. Isolated metrics often cannot clearly predict a cell type due to cells features being spread from a continuous differentiation. Somata diameter of PGCs spread roughly from 5 to 15 μm on a continuous spectrum. The diameter distribution of small and large PGCs is however overlapping, which makes that metric not sufficient for a clear demarcation. Connectivity and the number of associated glomeruli are other metrics that contribute to establishing homogeneous but overlapping classes of PGCs. Finally, neurochemistry seems to be the best delimitator of classes as its measurement is not subject to hit-and-miss observations like it occurs with connectivity measurements such as in electrophysiology pair recordings in slices.

To summarise, PGCs main morphological axis of clustering are somata size plus the proximity and number of linked glomeruli. Their heterogeneity translates into different functions in shaping the afferent sensory signals and mediating transmission to output neurons. Each subtype exerts inhibitory effects from a single local glomerulus to many distantiated glomeruli. Notably, UGC implements feedback and feedforward inhibition (Gire et al. 2012; Murphy, Darcy, and Isaacson 2005; Najac et al. 2015; Z. Shao et al. 2009),

OGC, lateral inhibition between local glomeruli (Kiyokage et al. 2010; Whitesell et al. 2013), and POGC, lateral inhibition between distant glomeruli (Aungst et al. 2003; Whitesell et al. 2013).

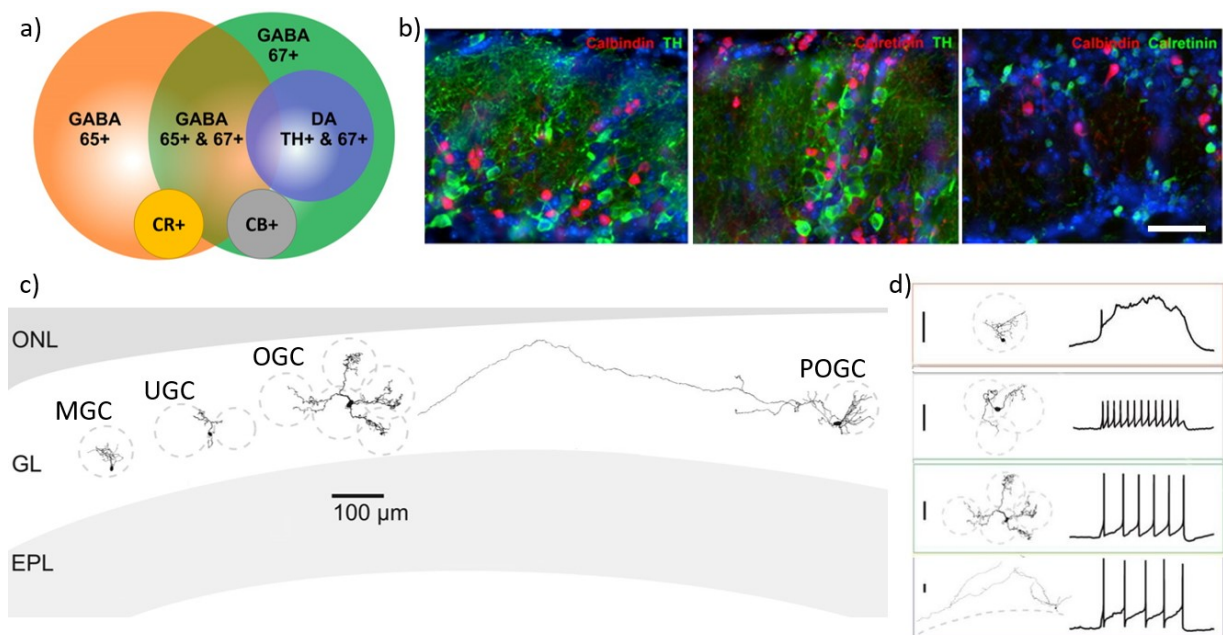


Figure 1.4 Identity and anatomy of PGC subtypes. a) Venn diagram showing the heterogeneity in expression of CR, CB, GAD65, GAD67, and TH. Adapted with permission from Kiyokage (2010). b) Immunostaining showing the non-colocalization of TH+/calbindin+/calretinin+ periglomerular cells. Adapted with permission from Kohwi et al. (2007). Scale bar, 50 µm. c) Morphological examples for each periglomerular cell subtypes: microglomerular (MGC), uniglomerular (UGC), oligoglomerular (OGC) and polyglomerular (POGC). d) Corresponding physiotypes for MGC, UGC, OGC, and POGC (response to a square current pulse). Scale bars, 50 µm. Adapted with permission from Tavakoli et al. (2018)

Neurochemistry

PGCs can be discerned by their proteins expression: glutamic acid decarboxylase GAD65 and GAD67, tyrosine hydroxylase (TH), calbindin (CB), calretinin (CR), and the marker of axon initial segment Ankyrin-G (Fig. 1.4).

The proteomic signature of a PGC resides in a mixed expression of GAD65 and GAD67 (Panzanelli et al. 2007; Parrish-Aungst et al. 2007) as they all express one or the other, given their GABAergic nature. Parrish-Aungst et al. (2007) showed that most juxtglomerular cells are GABAergic by using GAD65-GFP mice and antibodies against GAD67. GAD65+ cells co-express in minor amounts with TH+, CB+, CR+ and PV+ while they colocalize around 50% with GAD67. GAD67+ PGCs subdivide into non-overlapping TH+, CB+, CR+ groups (Panzanelli et al., 2007). CR+, CB+ and TH+ subtypes are mutually exclusive (K. Kosaka and Kosaka 2007; Sawada et al. 2011) and therefore enable cell categorisation. All of TH+ PGC expresses GAD67 and accordingly are dopaminergic-GABAergic PGC (Kiyokage et al. 2010). The OGC and POGC fall in that category.

Calbindin- and calretinin-positive PGCs (CB-PGC, CR-PGC) are PGe and respectively express mostly GAD67 and GAD65, and are expected molecular markers of UGC and MGC (K. Kosaka and Kosaka 2007; Najac et al. 2015; Panzanelli et al. 2007; Parrish-Aungst et al. 2007; Whitman and Greer 2007). CR+ PGCs are the most abundant subtype with three times more presence than CB+ PG (Panzanelli et al., 2007; Parrish-Aungst et al., 2007; Whitman and Greer, 2007). Additionally, some PGC subtypes that barely

express CR, CB or TH form connexin-36 gap junctions with MTC (K. Kosaka and Kosaka 2005).

Axon initial segment (AIS) markers are only expressed in large TH+ PGC (Chand et al. 2015; T. Kosaka and Kosaka 2011, 2016). This chemical marker is required and sufficient to identify more accurately a PGC as an SSA or POGC. This concludes that all PGCs are GABAergic and a TH+ subset is also dopaminergic. CB and CR expressions will prove to be useful as a determinant of connectivity and morphology. Expressing GAD implies PGCs receive inputs from glutamatergic neurons which are, around glomeruli, either OSN or ETCs.

1.1.4.5 Connectivity of PGCs

A simplified approach of the glomerular layer microcircuits, in the point of view of PGCs, could be summed up as direct feedforward excitation (OSN/ETC->PGC), lateral inhibition (SSA->PGC) and feedback excitation (MTC->PGC). JGCs dynamic actually relies on complex indirect and transglomeruli connectivity. Those interactions will be laid out in the next section, taking PGC as a point of reference.

Periglomerular Cell inputs

Glutamatergic inputs from OSN, ETC and MTC excite PGCs. 30% of GAD65+ PG cells are OSN driven (PGo), receiving direct monosynaptic input from the OSN, whereas the rest is likely driven polysynaptically through ET cells (PGe) (Kiyokage et al. 2010; K. Kosaka et al. 1998; Z. Shao et al. 2009). By these definitions, a glomerulus organisation can be demarked by OSN-driven and non-OSN-driven zones. Remarkably PGo sends its processes in both these zones as PGe dendritic trees remain contained to the non-OSN-driven zone (K. Kosaka and Kosaka 2005). CR+ MGC and CB+ UGC are PGe (Shao et al., 2009). Uniglomerular cells (UGC) also receive input from TC and MTC (Najac et al., 2015). Furthermore, a single MTC firing can drive recurrent inhibition in a glomerulus by activating UGCs (Najac et al, 2015)

Dopaminergic inputs from distant SSA, a subtype of TH+/GAD67+ cells, can inhibit PGCs via D1 dopamine receptor (Zuoyi Shao et al. 2019). As for TH+/GAD67+ PGCs, they are OSN and ETC-driven in similar proportions as GAD65+ cells while the most glomeruli-connected TH+/GAD67+ cells,

POGC, are only ETC-driven (Kiyokage et al. 2010; Maher and Westbrook 2008).

Periglomerular Cell outputs

Periglomerular Cells -> Olfactory Sensory Neurons

PGCs release GABA onto OSN via GABA(B) receptors (Vassiliki Aroniadou-Anderjaska et al. 2000; Bonino, Cantino, and Sassoè-Pognetto 1999; Margeta-Mitrovic et al. 1999; Murphy, Darcy, and Isaacson 2005). PGC-mediated presynaptic inhibition was shown by stimulating OSN in pair recording and that mechanism was blocked with GABA(B) antagonist CGP 55845 (Murphy, Darcy, and Isaacson 2005). It is further confirmed by using baclofen as an agonist (Maher and Westbrook, 2008).

PGo and PGe appear to mediate OSN glutamate release in two inhibitory components (McGann 2013). A phasic component is likely provided by PGo whereas PGe primarily procures a tonic “feedback” participation (Shao et al., 2009). Generally given, in an OSN/PGC/MTC synaptic triad, PGC->OSN feedback inhibition reduces the ON->MTC excitatory drive.

In a glomerulus, PGC co-release of dopamine and GABA can activate different routes. Co-occurring with the GABA(B)-mediated feedback inhibition, TH+ PGCs inhibits OSN terminal via D2 receptor and decrease OSN transmitter release (Coronas et al. 2002; Ennis et al. 2001b; Hsia, Vincent, and Lledo 1999; Koster et al. 1999; Maher and Westbrook 2008). This was demonstrated by applying a D2 agonist, quinpirole, and a D2 antagonist, sulpiride, in an OB preparation (Berkowicz and Trombley 2000). In slice, this evidence was supplemented by the application of cocaine, blocking dopamine uptake, reducing ON->PGC EPSC (Maher and Westbrook, 2008). However, the ability of SSA to provide presynaptic inhibition to OSN afference remains uncertain (McGann 2013). The difficulty to observe it might arise from the requirement of a combined activation of several cells to elicit a measurable inhibitory dopaminergic effect corresponding to normal physiological conditions (Maher and Westbrook, 2008). Similar to the GABAergic mediation, D2 receptor activation of OSN modulates the synaptic transmission between OSN and OB neurons (Berkowicz and Trombley, 2000).

Periglomerular Cells -> Mitral cells

PGo main feature is its participation in a OSN-MTC-PGC synaptic triad where PGCs inhibit MTC/TC via GABA(A) receptors (Isaacson and Strowbridge 1998; Schoppa 1998). As for PGe, UGC is monosynaptically excited by MTC and monosynaptically inhibits MTC (Najac et al, 2015). Another source of MTC inhibition is the spillover of glutamate produced by ETC and that is triggering GABA release by PGCs in glomeruli (Gire et al. 2019). Both microcircuits OSN->PGo->MTC and ETC->PGe->MTC implement feedforward inhibition and mediates OSN->MTC glutamatergic transmission, shaping the olfactory bulb output signal.

Periglomerular Cells -> External Tufted cells

PGCs provide mixed excitation/inhibition to ETC (Murphy, Darcy, and Isaacson 2005; Najac et al. 2015; Parsa, D'Souza, and Vijayaraghavan 2015; Zak, Whitesell, and Schoppa 2015). ETC inhibition is mediated by D1 and GABA(A) receptors (S. Liu et al. 2013). UGC expresses reciprocal connections with all glutamatergic neurons of the glomerular layer: ETC, MTC and TC (Najac et al., 2015).

Periglomerular Cells -> Periglomerular Cells

GABA release from PGC can self-signal and signal neighbour PGCs (Murphy, Darcy, and Isaacson 2005; Smith and Jahr 2002; Zak, Whitesell, and Schoppa 2015). PGC self-inhibition is induced by GABA(A) spillover (Smith and Jahr 2002) and is calcium-dependent (Maher and Westbrook, 2008). In fact, GABA release from one PGC exerts a bimodal control on other PGCs excitability. Some PGCs induce quiescent PGCs to fire and amplify the extracellular GABA via GABA-induced GABA release (Parsa et al, 2015). While this observation appears to transgress the neurotransmitters dogma, GABAergic excitation is not unknown in the cortex (Bracci and Panzeri 2006; Tanaka et al. 2009). Finally, it results that a single PGC activation can trigger a whole glomerulus suppression of MTC/TCs by recruiting additional PGCs. Gap junction coupling between PGCs supports furthermore this coordination of PGC activity (Schoppa 2006).

Superficial Short Axon cells -> PGC/ETC/MTC

Superficial Short Axon cells connectivity hallmark is its 1-3 axons projecting to sparse remote glomeruli where, via a co-release of GABA and dopamine, it inhibits in reciprocity PGCs, directly inhibits and indirectly excite distant MTCs (Zuoyi Shao et al. 2019).

SSA plays a role in interglomerular excitation via the SSA→ET→MTC circuit, synapsing with ET adjoined to a remote glomerulus. This ET then directly excites MTC/TC (S. Liu et al. 2013). It was demonstrated by optogenetic means that SA→ET synapse elicits a postsynaptic biphasic response. The biphasic response is composed of an initiatory GABA(A)-mediated inhibition succeeded by a D1-mediated excitation (S. Liu et al. 2013; Whitesell et al. 2013).

In comparison to MTC excitation at distance by SSA (S. Liu et al. 2013), Banerjee et al. (2015) preconises an SSA-mediated suppression of MTC/TC on distant glomeruli, corroborating another modeled bulb-broad SSA(glomerulus A)→ET(glomerulus B)→SSA→MTC circuit increase sharpness in odour representation by annihilating weakly activated glomeruli at a distance (Banerjee et al. 2015; Chaudhury et al. 2010).

SSA prospected overall role is the excitation and inhibition of distant glomeruli MTC, respectively in the SSA→ET→PGC→MTC (Gire et al. 2012; Hayar et al. 2004; De Jan et al. 2009; S. Liu, Puche, and Shipley 2016; Z. Shao et al. 2009) and SSA→ET→MTC (Liu et al., 2016; Whitesell et al., 2013; Banerjee et al., 2015) circuits. The former is disrupting the PGC→MTC drive and causes MTC disinhibition while the latter decreases the excitatory ET→MTC drive.

1.1.4.6 Morphology of PGCs

The GAD65+ PGCs, MGC and UGC, are the smallest GABAergic PGCs. MGC dendritic arborisation is limited to a portion of a single glomerulus in which lies the cell somata. While its total dendritic volume is the most compact amongst PGCs, its dendritic density is the highest. On the other hand, UGC projects its processes in 1-3 glomeruli (Tavakoli et al., 2018). MGC and UGC somata diameters are around 7µm. OGC and POGC are very close with a median somata diameter of 9µm (Tavakoli et al., 2018). However, other

studies report sizes up to 20um (T. Kosaka, Pignatelli, and Kosaka 2019). Despite an overlapping somata size distribution across PGCs, TH+ marker coincides with a higher probability of larger cells. Nonetheless, larger TH+ cells are more likely to be SSA or POGC. POGC can also be related to inhibitory juxtglomerular association (IJGA), proposed by T. Kosaka, Pignatelli, and Kosaka (2019) as the largest TH+ cells with a somata diameter ranging from 10 to 20um and 1-3 axons reaching glomeruli up to 500um (T. Kosaka, Pignatelli, and Kosaka 2019).

Additionally, the dopaminergic PGCs are also secluded in small TH+ PGCs, which constitute 85% of TH+ PGCs (Pignatelli et al. 2005), POGC, and OGC (Tavakoli et al., 2018). Small TH+ PGCs link to a single or a few close glomeruli (Pignatelli and Belluzzi 2017). Only the POGC possesses an axon. All other PGCs are therefore considered anaxonic. In contrast to POGC which synapses up to 15 remote glomeruli, OGC has a higher dendritic density that is more localized around up to 5 close glomeruli.

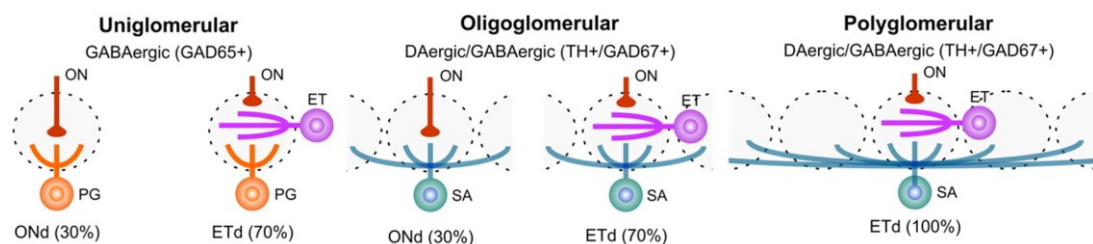


Figure 1.5 Connectivity per periglomerular cell subtypes in the glomerular layer. Periglomerular cell subtype participates in ON→PG and ON→ET→PG circuits. Uniglomerular periglomerular cells (GAD65+) are driven by the olfactory nerve (30%) or by external tufted cells (70%). Oligoglomerular DAergic/GABAergic cells (GAD67+) are connected to 2-6 glomeruli and receive input from ON (30%) and ET (70%). Polyglomerular cells (GAD67+) are connected to more than 7 glomeruli and are only driven by external tufted cells. Polyglomerular and oligoglomerular cells are assimilated as short axon cells. SA: short axon cell, PG: periglomerular cell, ON: olfactory nerve, ETd: external tufted cell driven, ONd: olfactory nerve driven. Adapted with permission from Kiyokage et al. (2010).

1.1.4.7 Electrophysiological properties of PGCs

AMPA and NMDA receptors mediate excitatory synaptic input to PGC (Grubb et al. 2008; Markopoulos et al. 2012; Murphy et al. 2004; De Saint Jan and Westbrook 2007) that leads to a back propagating dendritic action potential. As for GABA(A) and D1 receptors, they mediate inhibitory inputs

(Fig. 1.5). PGCs have generally a high input resistance of 1-2G Ω which allows them to be depolarized by small input currents. Input resistance is inversely proportional to cell size, making MGC value around 2G Ω and up to 4G Ω while other PGCs input resistance is restrained to 1 G Ω or less (Tavakoli et al., 2018) (Table 1.2). Depolarisation of MGC elicit a plateau response. On the contrary, UGC, POGC and OGC are bursting spike trains upon activation. UGC action potentials are smaller in amplitudes and express a shorter inter-spike time in comparison to POGC and OGC that display a relatively similar spiking (Fig. 1.4).

UGCs are strongly connected to the glomerulus and respond to OSN-evoked input. MGCs on the other hand are weakly connected but still generate plateau potentials, due to their smaller size, which contribute to GABAergic signalling (Benito et al. 2018; Najac et al. 2015). The plateau potential relates to what differentiates electrophysiologically MGC from the rest of PGC subtypes: an earlier afterhyperpolarization, a higher action potential halfwidth, and higher time constant but principally a higher input resistance (Tavakoli 2018).

Some PGCs fire repetitively to OSN glomerular activation but many express a limited firing capacity because of a L-type CaV-mediated plateau potential (Fogli Iseppe, Pignatelli, and Belluzzi 2016; Hayar et al. 2004; Masurkar and Chen 2011; Murphy, Darcy, and Isaacson 2005; Z. Shao et al. 2009). These plateau potentials lead to asynchronous and action potential-independent GABA release (Murphy et al., 2005; Smith and Jahr 2002). Dendrodendritic release of GABA does not require L-type Ca²⁺ spiking but requires Ca²⁺ influx through activation of P/Q type channels, whereas single APs do not seem effective (Murphy et al., 2005). The dendritic Ca²⁺ conductance participates in potentiating EPSP then shunting and reducing the amplitude of the next EPSPs. This acts as a low-pass filter that converts inputs to a lower frequency close to the respiration rate – e.g. the frequency cut of 2.6±0.8 Hz in rats that respire at 1-3Hz - (Zhou et al., 2011) as higher frequencies are shunted.

1.1.4.8 In vivo responses of PGCs

The PGCs odour-evoked response patterns are quite diverse with odour-onset excitatory and inhibitory responses, odour-offset excitatory and inhibitory responses, and a mix of both in biphasic responses. Biphasic responses may relate to the biphasic activation of ET by SSA. These ET could in turn have a biphasic effect on PGCs (See Connectivity).

Therefore, odour identity, concentration, onset and offset can be encoded in PGC odour-evoked activity. Homma et al. (2013) and others have demonstrated employing two-photon imaging and cell-attached recordings *in vivo* that odour-evoked activity can either be excitatory or inhibitory and triggered at the afference stimulation onset or offset. The amplitudes of odour-evoked responses and the fraction of recruited cells increase with concentration. Interestingly, some cells are excited at low concentrations and inhibited at higher concentrations. This latter attenuation is likely due to other PGCs. Tested concentrations were restrained from 0.1 to 9% of saturated vapour, enough to record baseline and saturated activity levels, which allowed complete characterisation of odour-response profiles. More than odour evoked activity, PGCs demonstrate a baseline activity that is sniffing-phase coupled (Adam et al. 2014; Najac et al. 2015; Tan et al. 2010). Furthermore approving the encoding capabilities of PGCs, the sniffing-locked oscillation phase does shift in an odour-dependent manner (Iwata et al., 2017).

This myriad of response types foretells that PGC is involved in a multitude of glomerular mechanisms that modulate information transmission from afference to efference. PGo plays a role in the synaptic triad, in a single synaptic cleft, receiving glutamate from OSN and emitting GABA onto OSN and MTC (Fig. 1.6). PGe may play a phasic inhibition role driven by the autonomous bursting of ET cells (Shao et al., 2009) and therefore participate in the synchronized rate of odourant phase coding. A subset of PG cells practice self-inhibition (Smith and Jahr, 2002) caused by GABA spillover during glomerular activation and allows the recruitment of near quiescent PGCs via GABA-induced GABA release (Parsa, D'Souza, and Vijayaraghavan 2015).

1.1.4.9 External Tufted cells

External tufted cells are excitatory neurons and the largest cells in the outer layer of the OB, with a soma of 10-15µm diameter (Pinching and Powell 1971) and compared to PG cells, ET dendrites take more space in the glomerulus (Nagayama, Homma, and Imamura 2014). These cells are intrinsically bursting (S. Liu and Shipley 2008) and provide the major excitatory component coordinating glomerular activity (Hayar et al., 2004). ET cells provide glutamatergic monosynaptic inputs to PG and SSA cells (Hayar et al., 2004) and receive inputs from OSNs (Fig. 1.5), other ET from the same glomerulus and SSA from neighbouring glomeruli. Spontaneous spike bursts of ET cells appear to be synchronized to the sniffing rate or in the theta frequency range (6-10 Hz) (Hayar et al., 2004). The function of synchronous ET cell bursting might be to amplify OSN input and harmonize glomerular output (Hayar et al., 2004). ET cells may also be a locus of state-dependent modulation of OB function through neuromodulation by cholinergic (D'Souza and Vijayaraghavan 2014), serotonergic (S. Liu et al. 2012) and endocannabinoid receptor-mediated (Wang, Sun, and Heinbockel 2012) systems.

Recently, through whole-cell patch-clamp recordings, (Tavakoli et al., 2018) established 3 types of ETC: the classical ETC, the vertical superior tufted cells (vSTC) and the horizontal superior tufted cells (hSTC). The ETCs are confined to a unique glomerulus. The STC differs from ETCs by the absence of basal dendrites (Hayar et al. 2004; De Jan et al. 2009; Macrides and Schneider 1982; Pinching and Powell 1971; Tatti et al. 2014). The vertical and horizontal STCs have respectively prominently lateral dendrites and dendrites going in deeper (Antal et al. 2006). ETCs excite hSTCs, MTCs, TCs, UGCs and other ETCs. hSTCs in their turn excite UGCs and MGCs, playing a role in lateral JGC recruitment (Tavakoli et al., 2018).

Generally, ETCs provide feedforward excitation to MTCs and the other interneurons within the glomerular layer (Hayar et al., 2004a,b, 2005; Murphy et al., 2005; De Saint Jan et al., 2009; Najac et al., 2011; Gire et al., 2012). Furthermore, a subset of VGLUT3+ ETC are exciting TCs, but not MTCs (Tatti et al., 2014).

1.1.4.10 Granule Cells

Granule cells are the most numerous inhibitory neurons in the OB, providing reciprocal synapses with the basal dendrites of mitral/tufted cells in the external plexiform layer (Fig. 1.3). They serve as an inhibitory isolation system between mitral cells branching to different glomeruli and therefore increase the decorrelation of mitral cells representation of an odour. The granule cells do not have axons. They form reciprocal dendodendritic connections with mitral cell basal dendrites. GC release GABA into neighbouring MTC GABA(A) receptors following an MTC releasing glutamate in GC mGluR receptors. GC is the main population subject to neurogenesis in the OB migrating from the subgranular zone and may thus play an important part in learning.

GCs are excited through multiple modes. Locally in distal dendodendritic synapses that elicit slower APs and convey MTC-GC-MTC lateral inhibition, and globally in proximal synapses from Piriform cortex and cortical feedback, eliciting a somatic AP (Balu, Pressler, and Strowbridge 2007). Weak activation of MTCs elicits dendrite spine Ca²⁺ spikes in GCs. Strong activation produces a low-threshold Ca²⁺ spike in the GC apical dendrite (Egger, Svoboda, and Mainen 2005). Local and global spikes play roles in complex dendritic computations. Notably, a dendritic spike can stop a somatic back-propagating AP (Zelles et al. 2006). Somatic and dendritic spikings interplay at a specific temporality to regulate feedback and feedforward inhibition between mitral cells synapsing on different dendrites of the same GC.

1.1.4.11 Mitral / tufted cells

Mitral and tufted cells, the principal neurons of the OB, send olfactory information through the lateral olfactory tract to the olfactory cortex, following the brain's hierarchical pathway. Tufted cells rhythmic neural activity plays a role in structuring neural information and mitral cells form the second representation space of odours after the glomerular layer. Two distinct and parallel output channels (Adam et al. 2014; Fukunaga et al. 2012) are generated due to the difference between tufted and mitral cells. MTC and TC oscillatory rhythms are in the opposing phase of the sniff cycle. While TC

phase remains unperturbed by odourant stimulation, MTC phase is advanced in a stimulus-dependent manner (Fukunaga et al. 2012). Therefore MTC phase-shift is a part of the odour encoding. TC has a shorter onset latency and responds to a wide range of stimulus intensity whereas MTC is only activated by stronger concentration (Igarashi et al. 2012). Mitral cells responses are narrower in terms of molecular receptive range (MMR) than tufted cells (Fig. 1.6) (Kikuta et al. 2013), possibly because mitral cells are subject to stronger periglomerular inhibition. This causes a delay in their relative firing, which places their firing in the opposite phase relative to the sniff cycle (Fukunaga et al., 2012). The difference between the synchronous rhythm of tufted cells and the spike-timing of mitral cells may participate in temporal information processing. By comparing mitral activity to the rhythm imposed by tufted cells, the glomerular microcircuit may separate signals in time.

Mitral cells are glutamatergic principal neurons with somas situated in a deeper mono-layer called the mitral cell layer. Their principal dendrites ramify into a single glomerulus in the glomerular layer. 20-40 sister mitral cells receive input from a single glomerulus (Dhawale et al. 2010) (Fig. 1.3) and multiple mechanisms exist that synchronise sister mitral cells (Schoppa and Westbrook 2001). The response of Mitral cells can differ markedly from that of the OSNs providing their afferent input. As a result, the mitral cell layer forms a second-order representation map with a sparser spatial coding and narrower tuning curves (Kikuta et al., 2013) than in the glomerular layer. Their spiking pattern differs the most from the OSN spiking pattern (Friedrich and Laurent 2001) and can also differ between sister mitral cells (Kikuta et al., 2013). These transformations are thought to arise through interaction with the granule cells deeper in the OB. MTC and TC, after integrating synaptic inputs from its apical to basal processes, project the shaped information to different downstream targets to transfer distinct but complementary phase-based encoded odour information (Cavarretta et al. 2018; Igarashi et al. 2012; Iwata and Kiyonari 2017). MTC target all olfactory cortex area whereas TC project to focal targets restricted to the anterior area (Igarashi et al., 2012).

1.1.4.12 Neural circuits

The particular wiring of the neural circuitry in the glomerulus can perform processing functions on the input. Two computation examples will be discussed respectively implemented by intraglomerular circuits and interglomerular circuits: contrast enhancement where the tuning of the output is narrowed, thus becoming more stimulus selective and normalisation where the activity of glomeruli are "normalised" by the global activity of glomeruli, thus providing a means for concentration independence. Such pre-processing is a fundamental part of stimuli encoding.

Intraglomerular circuit

The chemotopic organisation of glomeruli is quite poor with weak consistency in the spatial relationship between glomeruli chemical tuning at a fine and coarsescale (Soucy et al. 2009). This topology property calls for sharpening of representation otherwise odour representations overlapping would be detrimental to perception, in an analogy to two blurred images in vision.

The excitatory molecular receptive range (eMRR, or tuning curve) of mitral cells is much narrower than the OSN input, as shown by Kikuta et al. (2013) data (Fig. 1.6), indicating that some form of contrast enhancement is occurring. Contrast enhancing is a subtractive effect on weakly responding sides of MTC tuning curves made by inhibitory neurons. Periglomerular cells show a lower activation threshold (Gire and Schoppa 2009) and broader odour tuning (Tan et al, 2010) than MTC/TC. Therefore, they can attenuate the OSN-induced excitation of MTC via feed-forward inhibition for odourant eliciting weak activity. This removes perturbation in MTC of weak odourants while henceforth reinforcing the contrast of a stronger odourant which the MTC is tuned for.

The sharpening of the odour tuning curves observed in mitral cells was initially explained by a model involving centre-surround inhibition and a chemotopic organisation of glomeruli (Yokoi, Mori, and Nakanishi 1995) as discussed above. However, this has been brought into question as chemotopy does not appear to be a feature of the glomerular layer (Fantana, Soucy, and

Meister 2008; Soucy et al. 2009). An alternative explanation has been proposed, a non-topographical contrast enhancement (Cleland and Sethupathy 2006) and demonstrated (Gire and Schoppa, 2009) whereby weak stimuli are filtered out of the mitral cell response, creating binarisation of OSN odour-responses, as an all or nothing effect.

The binarisation is implemented by 3 cell types ON-PG-M (Gire and Schoppa, 2009) (Fig. 1.6) and is one of the elucidated functions of the glomerulus: to filter out weak signal inputs from OSN, that fires less due to low affinity or selectivity of the odorants. This mechanism is implemented by a synaptic triad in the ON zone of the glomeruli where PGo cells form dendrodendritic reciprocal connections with Mitral cells and receive axo-dendritic input from OSNs. PG cells, with a very high input resistance (typically 1-2 G Ω), according to Ohm's law, are excited strongly when mitral cells are still below threshold. PG cells, therefore, shunt away the depolarising glutamatergic current in mitral cells, inhibiting mitral cells activity. However this inhibition saturates for high OSN activity (and even becomes less due to self-inhibition), PG cells thus stop counterbalancing OSN excitation and Mitral cells override the synaptic triad. This results in a form of contrast enhancement that does not rely on chemotopic organisation (Cleland 2010) (Fig. 1.6).

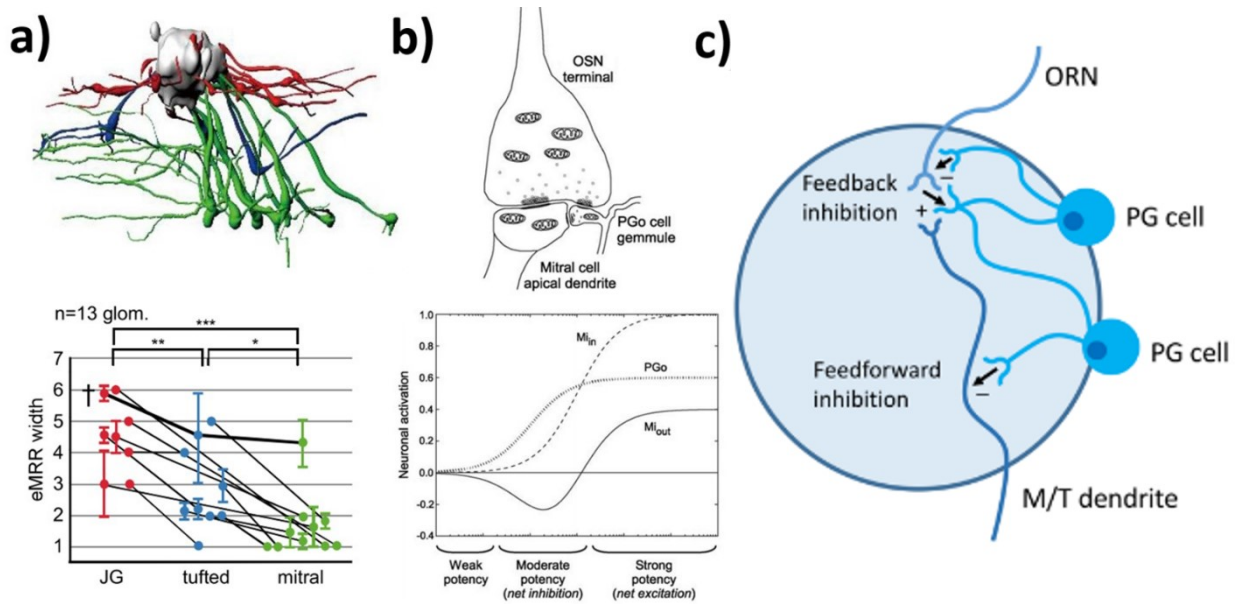


Figure 1.6 Intraglomerular circuits. **a)** Amelioration of selectivity observed along the hierarchical pathway. Top: Dendrites merging into a glomerulus (Kikuta et al., 2013). Green: mitral cell, red: interneurons, blue: tufted cell. Bottom: Direct comparisons of eMRR widths within the same glomerular module. Cells associated with the same glomerular module are connected with lines (Kikuta et al., 2013). Output cells are more selective than the input cells. Adapted with permission from Kikuta et al. (2013). **b)** Illustration of the nontopographical model for olfactory receptive field decorrelation (Cleland and Linstner, 2005). Top: Synaptic triad. PGo effectuates feedforward inhibition on mitral cells according to OSN level of activation. Weak signals from low-affinity odourants will be shunted by PG, while stronger signals will be overdriven by M. Bottom: Level of activation of selected Mitral cells as a function of potency in its presynaptic OSN population. This curve can be seen as an ON-OFF transfer function. The M_{in} sigmoid curve, showing a graded response, is convolved by the feedforward inhibition characterized by the curve PGo. The output M_{out} response contrast is thus enhanced via this Mexican-hat filter. Adapted with permission from Cleland and Linstner (2005). **c)** Periglomerular cells driven by olfactory receptor neurons provide feedback inhibition to the olfactory receptor neuron and feedforward inhibition to the mitral/tufted cells.

Interglomerular circuit

The activity map of the glomeruli can change for the same odour presented at different concentrations. That leads to the problem of having different representations for the same odour. For example, we recognise the smell of hot bread whether we are in front of the oven or in another room. This is

termed as concentration invariance and one way to achieve this is to normalise the input for the total activity across all inputs.

The corresponding implementation has not been clearly established yet and to what extent it occurs in the glomerular layer or later. Cleland et al. (2007) proposes a model of normalisation implemented by a subset of cells, PG, ET and SSA in the glomerular layer (Fig. 1.7) that works on the principle of feedforward global inhibition mediated by SSA cells in the inter-glomerular space. SSA cells, are located in 50% of the cases over 5-7 glomerular diameters away from its glomerulus (Cleland 2010), and 10% of them extend even to 20-30 glomerular diameters. SSA cells are therefore well placed to sense the average activity from multiple glomeruli and thus the global increased activity coming along with stimulus concentration. It is thought that the activity of the mitral output from a single glomerulus is therefore affected by a subtraction of the average activity in the local neighbourhood, computed by SSA cells.

To summarize how this normalisation is thought to occur: the excitatory loop of SSA cells would compute the global average of glomerular activity and transmit that value by dopaminergic excitation of ET cells which in turn makes glutamatergic synapse into PGe that then inhibit mitral cells (Fig. 1.7). SSA was demonstrated furthermore to be implicated in an interglomerular network via other synaptic pathways (S. Liu, Puche, and Shipley 2016), by gap junction-mediated electrical coupling between SSA and mitral cells, and direct release of GABA into mitral by SSA cells.

Other cell types have also been implicated in normalisation. For example, later in the OB hierarchy, in the external plexiform layer, Parvalbumin-expressing (PV) interneuron relies on the same idea of global averaging, shaping the OB output. PV cells have a broad receptive field and synapse reciprocally with widely distributed mitral cells (Kato et al. 2013; Miyamichi et al. 2013). They modulate mitral gain proportionally to global activity. Uchida, Eshel, and Watabe-Uchida (2013) show PV cells normalise Mitral responses by the sum of population activity, potentially to adjust sensitivity and facilitate intensity-invariant information processing. This finding might need refinement

as the panel of odourant was too restricted to clearly display changes in sensitivity.

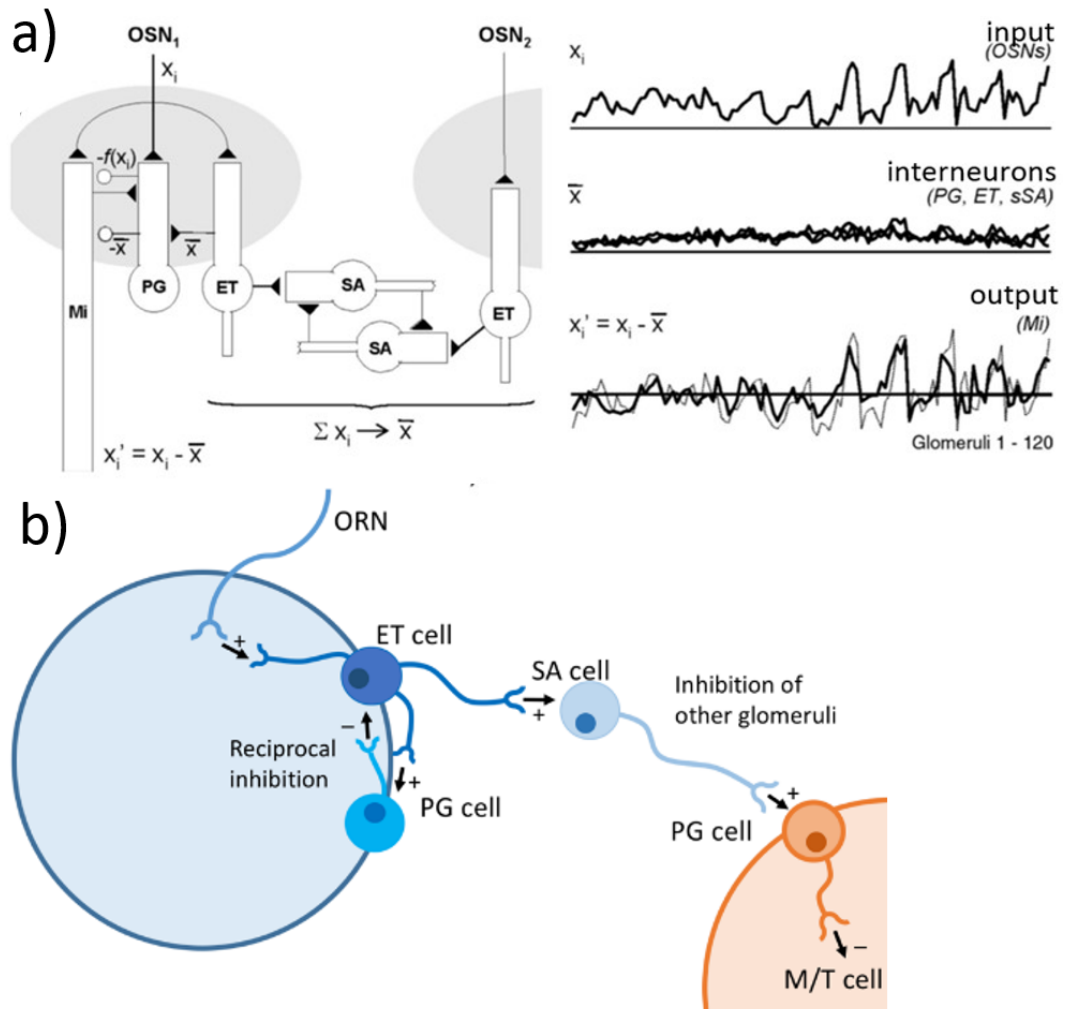


Figure 1.7 Interglomerular circuits. a) Model of normalisation of OSN inputs by glomerular layer microcircuits (Linster and Cleland, 2009). Left: Schematic of microcircuitry. Each OSN participates in the pooling done by the SSA loops which the average result is communicated to ET cells in each glomerulus which apply a subtraction of that value to the mitral output via the excitation of an inhibitory PGC cell. Right: Simulation results. At the top, responses of projecting OSNs for 120 glomeruli. At the middle, computation of average activity by SSA-ET-PG. At the bottom, subtraction of that average activity from the mitral output via PGC inhibition. The output trace is similar to a normalising Z-score (dotted line). OSN: olfactory sensory neuron, PG: periglomerular cell, ET: external tufted cell, SSA: superficial short axon cell, Mi: Mitral cell. Adapted with permission from Linster and Cleland (2009) **b)** ET-driven superficial short axon (SSA) cells inhibit lateral glomeruli by exciting neighbour PGCs. ET cells are excited by OSN inputs and received reciprocal inhibition by local PGCs.

1.1.5 Roles in olfaction

The olfactory bulb is made of columnar structures linked to a glomerulus where join sensory axons and output neuron apical dendrites. The glomerular modules of the olfactory bulb are important functional units in the transmission of odourant signals and the processing of olfactory information. Its neural operation can be summarized as feedforward excitation tuned by local and global inhibition. This connectivity contributes to the shaping of the olfactory bulb output.

By converging (5000:1 OSN to glomerulus) then diverging (20~40 MTC per glomerulus), the glomerular layer acts as an information bottleneck where activity depending on OSN properties comes in graded and concentration-dependent and comes out binarised and normalised. Comparison between glomeruli is thought to be operated by mitral and granule cells in the mitral cell layer. In terms of machine learning, the glomerular module does typical pre-processing of information with a view to make it easier to extract relevant features in the next layers, such as the combination of activated glomeruli or the shaping of the odourant signal dynamic range.

1.1.5.1 Encoding

Encoding of odourants in the olfactory bulb is spatio-temporal and successively represented in two maps formed in the glomerular layer (GL) and the Mitral cell layers (MTCL). The odour spatial fingerprint is revealed by a unique set of activated glomeruli or MTCs. These spatial elements are not activated all at once but each of them has their spiking differently delayed in relation to the sniffing phase. Phase-based coding was shown to be more robust than rate coding alone. The delay of phase to the sniffing cycle remains stable against concentrations which thus serves as a concentration-invariant signature of the odourant (Iwata et al., 2017). Therefore an odourant signature in the OB is determined by the mapped activated cells and the lag of these activations. Nonetheless, the amplitude of activity is also encoding the intensity of the stimulus. More than representing an odour identity, the cell ensembles also encode the stimulus concentration, sniffing rate and nasal airflow. In the second representation by MTC, the message has been cleared and enhanced to be broadcasted and understood in diverse brain regions.

The output signal is shaped by limiting activity range, denoising, and enhancing the contrast of the sensory afference.

The activation of OSNs due to odour stimulation is reflected in the respectively linked glomeruli forming a map. The pattern and strength of activated glomeruli can be measured for different odours. Due to the broad tuning of the MRR the same glomerulus can contribute to multiple odours, causing overlapping activities in respective maps. Practically, these glomerular activity maps inform us of which olfactory receptors are activated in the periphery. It might be seen as an odour signature. However, other inputs might modulate the activity of OSN terminals. Amongst them, Serotonergic, cholinergic, and noradrenergic centrifugal inputs are possible candidates (Brill et al. 2016; Linster, Nai, and Ennis 2011; Matsutani and Yamamoto 2008).

Whether an ensemble of glomeruli will be activated, depends on the airflow rate and odor concentration in the nasal cavity (Oka, Takai, and Touhara 2009). For each glomerulus, a ligand-binding sigmoid-like curve describes the response as a function of the logarithm of odour concentration. The glomerular pattern will differ according to the odourant. Increasing odour concentrations would result in increased response amplitude and the recruitment of additional glomerular units while the sequence of activated glomeruli would be maintained (Spors and Grinvald 2002).

Topographic maps exist for other senses, whereby the stimulus is mapped onto the brain structure in a logical pattern, e.g. somatotopic maps exist in the somatosensory cortex, tonotopic maps exist in the auditory pathway and retinotopy is a key feature of the visual system. A chemotopic map has been proposed for the organisation of the glomeruli in the OB. Chemotopy implies that glomeruli are spatially distributed under an organisational principle relating to their odourant stimuli. For example, glomeruli responding to particular molecular functional groups would be located in clustered zones and their position within this zone would vary systematically with the structure of the odourant (Meister and Bonhoeffer 2001; Mori et al. 2006; Uchida, Eshel, and Watabe-Uchida 2013). Here, the two-dimensional arrangement of glomeruli responding for each odour can be seen as a map of which olfactory receptors were activated (Wachowiak, Denk, and Friedrich 2004). Thus each

glomerulus must correspond to the molecular features the related receptor reacts to. An odourant has multiple molecular features that will leave a spatial signature of glomeruli (Mori et al, 2006). However, Chae et al. (2019) determined, using 1,666 physical–chemical descriptors of odour, that molecular features space is an ineffective predictor of odour perception as similar odours were quite dissimilarly represented in that space.

There appear to be clusters of cells across the different layers whose activity is relevant to specific behavioural functions like fear, feeding or learning. Those clusters may be individually modulated according to internal state and context. Few examples were investigated in olfactory circuits. In the glomerular layer, Kobayakawa et al. (2007) indicates that, for aversive information, separate sets of glomeruli are devoted to innate and learned responses; multiple glomeruli eliciting a fear response are activated by the fox odour TMT (Saito et al. 2017). Some hardwired glomeruli relate to innate avoidance behaviours such as predator fear or spoiled food avoidance (Kobayakawa et al., 2007). They suppressed innate aversive odour avoidance using a mutant mouse with dorsal olfactory bulb lacking glomeruli. While avoidance behaviour itself was not disrupted, the mice were able to condition new odours avoidance with the remaining glomeruli. This implies some dorsal glomeruli were necessary for innate avoidance. Indeed the predator odour TMT is hardwired to dorsal glomeruli in which one particular glomerulus was shown to directly elicit freezing behaviour, whether it was naturally or artificially optogenetically activated (Saito et al., 2017).

Reward or punishment-paired odour learning modulates bulbar representation. Shakhawat et al. (2014) observed that learning stabilised MTC representation after training with rewarded odours but not with non-rewarded odours. Behavioural demand task increases odour discrimination (Koldaeva, Schaefer, and Fukunaga 2019). Threat or reward-predictive odours are better discriminated (Wang et al. 2019). During appetitive learning, adult-born granule cells boost odour–reward association (Grelat et al. 2018). This concept of the modification of odour encoding remains the same as well in the context of punishment as electroshock-paired odour representations were enhanced to elicit earlier avoidance (Fletcher 2012; Kass et al. 2013).

1.1.5.2 Processing

Odourant information processing can be divided vertically, by particular mechanisms in the GL and MTCL, and horizontally, whether the implementing microcircuits are localized or spread, e.g. intraglomerular and interglomerular processing in the GL. Intraglomerular shaping of afference by a mix of ET and PGC procures some binarisation to the input signal. It removes signature ambiguity, between two close odours codes for example, by annihilating weak elements. The pulling of thousands of OSN axons in a single glomerulus participate in decreasing input noise. Interglomerular processing plays a role in normalising the range relatively to the whole representation and therefore implies long connecting neurons SSA. This shaping results in a more compact code than the one evoked in the sensory periphery. In the MTC representation, PV cells participate again in the normalisation by synapsing multiple MTCs between their soma and their apical dendrites. Finally, the salience of activated MTCs is increased thanks to GC-mediated lateral inhibition to non-representative MTCs.

How the map is ordered has an impact on the possible action of inhibition, for example, lateral inhibition in other sensory systems generates a center-surround effect that privileges on-centre stimuli while attenuating surrounding weaker stimuli. This contrast enhancement mechanism necessitates an organised chemotopy. Lateral inhibition can then implement this computation; the activation of an element of the map would lead to inhibition of its neighbours response, equivalent to the sharpening of edges in vision. Basically, the excitation of one principal neuron would inhibit its direct lateral neighbours through the excitation of inhibitory interneurons by the principal neuron. It was thought that the same implementation is used for discerning odours, due to the similarities between vision and olfactory canonical circuits as they both possess feedforward excitation and lateral inhibition. Lateral inhibition is useful because it implements a Mexican hat filter that decorrelates signals between overlapping representations (Fig 1.7). Given the broad and overlapping MRR of OSN, decorrelation is an important step to discern odours. On the other hand, with a non-ordered topography, nonspecific local decorrelation is still possible (Fig. 1.6).

1.1.5.3 Transmission

The lateral olfactory tract (LOT) formed by MTC/TC axons transmits odourant information down to ipsilateral cortical regions. The LOT targets include the anterior olfactory nucleus, the olfactory tubercle, the piriform cortex, the amygdala, and the entorhinal cortex (Imai 2014). The piriform (aka olfactory) cortex classifies inputs and enables learning by conveying feedback to the olfactory bulb (Boyd et al. 2015). The sense of smell can directly activate recall and aversive behaviour through its connectivity to fear and memory areas, the amygdala, and entorhinal cortex. For example, the predator odour 2,4,5-trimethyl thiazoline (TMT) innately activates the amygdalopiriform transition area (AmPir) which induces a stress response (Kobayakawa et al. 2007; Kondoh et al. 2016; Saito et al. 2017).

1.1.6 Centrifugal inputs

The olfactory bulb receives extensive centrifugal input from neuromodulatory fibres and higher cortical areas. In particular, the anterior olfactory nucleus (AON) and the piriform cortex (PCX) modulate odour representation in the OB via odour-evoked feedback signals. These target all cell types with granule cells being the predominant target (Boyd et al. 2015; In'T Zandt et al. 2019; Rothermel and Wachowiak 2014). This feedback from the piriform cortex and AON enables learning and classification of odours and is particularly enhanced during wakefulness (Boyd et al., 2015; Rothermel and Wachowiak, 2014). The odour-evoked activity of MTCs is modulated by glutamate release onto granule cell dendritic spines (Isaacson, 2010). This excitatory feedback facilitates inhibition of MTC/TC by GC and decorrelates MTC representations, increasing odour saliency (Otazu et al. 2015). Interestingly, this odour separation is only applied to MTC but not TC, reinforcing the idea that MTC signs for the odour as the TC only serves as phase reference for synchronization (Iwata et al., 2017; Boyd et al., 2015).

All these top-down projections to the OB suggest that early odour representation is integrated with state information such as attention, past

odour experience, memory, and emotions. Odour-behaviour associations rely on these integrations.

All the major neuromodulatory systems have extensive projections in the olfactory bulb suggesting that function of the olfactory bulb is heavily influenced by behavioural state. A behavioural state relates to the internal brain state that could be roughly defined by a weighted mixture of present neurotransmitters. For example, dopamine signals expectation of reward while noradrenaline is associated with arousal and acetylcholine with attention.

1.1.6.1 Noradrenergic inputs

Noradrenaline (NA) centrifugal inputs from the locus coeruleus (LC) provide 40 % of its efference to the OB. NA plays a role in sensory vigilance, synaptic plasticity, arousal, and attention (Brennan and Keverne, 1997; Veyrac et al., 2005; Mandairon et al., 2008, Aston-Jones and Bloom 1981). Its role in rewarded and spontaneous odour discrimination makes it required for perceptual learning (Brennan and Keverne, 1997; Veyrac et al., 2005; Mandairon et al., 2008; Vineria et al 2015). The role in learning is even more evident given the importance of NA for signal-to-noise modulation of sensory inputs in rewarded tasks. Therefore, voluntary olfaction enhances odourant concentration threshold via attention-mediated NA release in the OB (Escanilla et al 2012).

The NA fibres reach all OB layers. They express at the highest density in the granule cell layer with the lowest density in the glomerular layer. Interestingly, each fibre only approaches one MTCs-glomerulus column (Michael T. Shipley et al 1985), suggesting that NA-dependent modulation may be able to operate on discreet glomerular columns, rather than on a global level.

Juxtglomerular interneurons undergo adrenergic-modulation through $\alpha 1$ and $\beta 1$ receptors (Tani et al, 1992; Yuan et al., 2003) and NA modulates the olfactory bulb at the first synapses as LC activation can suppress odour-evoked OSN activity (Eckmeier and Shea 2014). As for granule cells, they are modulated by $\alpha 2$ and β receptors (Young and Kuhar, 1980). Finally, the OB output is also modulated by NA which both enhances and suppresses MTC

activity directly and indirectly by inhibition of dendrodendritic GC-MTC feedback inhibition (Jahr and Nicoll, 1982; Trombley, 1992 ; Hayar et al., 2001; Nai et al., 2009; Nai et al., 2010; Zimnik et al., 2013). Overall noradrenergic input to the OB facilitates detection of weak odours and heightens saliency in neural representation in view to increase perceptual attention and learning.

1.1.6.2 Serotonergic inputs

The raphe nuclei project serotonergic fibres to the olfactory bulb (McLean Shipley, 1987a) and principally to the glomerular layer (Won et al ., 1998). The dorsal raphe nucleus targets the GCL as the medial raphe nucleus reaches the GL (Steinfeld et al., 2015). 5-HT(2A/2C) receptors in the OB are required for olfactory learning (McLean et al ., 1996) and conditioned olfactory learned behaviours (McLean et al., 1993; Petzold et al., 2009; Liu et al., 2012; Schmidt and Strowbridge, 2014). This might be due to serotonin boosting ETC frequency into an active sniffing rate (Liu et al,2012). Remarkably, activity in the raphe nuclei is closely related to the satiety state (Yang and sternson, 2017; Voigt and Fink, 2015). One could assume satiety state-related computations might reflect in the OB serotonergic input and modulates sensory processing.

The fibres target OSN, ETC, PGC (Dugue and Mainen, 2009; Hardy et al., 2005 ; Liu et al., 2012; Steinfeld et al., 2015), GC (Hardy et al., 2004;Hardy et al., 2005 ; Schmidt and Strowbridge, 2014) and MTC (Whitaker-Azmitia et al., 1993;Hamada et al., 1998). Glomeruli contain both 5-HT(1A) and 5-HT(2A) receptors (Shipley and Ennis, 1996) which are also present in the MCL and the GCL (Whitaker-Azmitia et al., 1993; Hamada et al., 1998) with a decreasing gradient of 5-HT2 concentration from the MCL to the GL. Juxtglomerular cells are excited via 5-HT(2C), and MTC and ETC via 5-HT(2A) receptors (Tani et al, 1992; Hardy et al ., 2005; Brill et al., 2015; Liu et al,2012).

Raphe nucleus activation elicits an increased basal activity of PGC and SSA via glutamate intake which might be due to increased excitatory inputs (Brunert et al., 2016). MTCs are distinctly bi-modulated which might indicate a behavioural state serotonin-dependent shaping of the OB output (Brunert et al., 2016; Brill et al., 2015). Serotonin-mediated GABA release from both SSA

excited by serotonin-excited ETs (Brill 2016; Gracia-Llanes et al., 2010a; Brill et al., 2015) and GCs (Liu et al,2012; Schmidt and Strowbridge, 2014) are amongst the mechanisms participating in the attenuation of MTCs. In the glomerular layer, Petzold, Hagiwara, and Murthy (2009) demonstrated in anesthetised mice that half of the PGCs were modulated via 5-HT_{2C} receptors which were activated by serotonin release from dorsal raphe nuclei fibres, following electrical stimulation of that nuclei. They showed OSN presynaptic activity and PGC postsynaptic activity were inversely oppositely modulated and subsequently determined that serotonin modulates GABA(B)-mediated feedback inhibition of PGC onto OSN. A raphe nucleus activation leads to increased inhibition of olfactory input to the olfactory bulb. 5HT global role might be to enhance MTCs sensitivity while keeping their activity range restrained.

1.1.6.3 Cholinergic input

Acetylcholine (ACh) from the horizontal limb of the diagonal band of Broca (HDB) in the basal forebrain (BF) sends fibres to the OB (Gracia-Llanes et al., 2010b; NunezParra et al., 2013; Rothermel et al., 2014, Zaborszky et al ., 1986; Senut et al ., 1989). The fibres reach all OB layers but mainly the glomeruli layer (Ichikawa Hirata, 1986 ; Ojima et al ., 1988) with a higher abundance into some atypical glomeruli described by a lack of OSN axons (Zheng et al., 1987). Acetylcholine is related to behaviour by its role in motivation, attention and wakefulness (Zaborszky et al., 2012; Hasselmo and Sarter, 2011). Acetylcholine in the OB appears critical for olfactory perceptual learning by enhancing MTC representation of familiar odourants (Chaudhury et al, 2009; Wilson et al., 2004) but is also implicated in dishabituation of odour investigation (Ogg et al, 2018).

Muscarinic and nicotinic receptors are present in the GL and EPL (Shipley and Ennis, 1996). Granule cells are presumably activated by muscarinic receptors (Castillo et al ., 1999; Pressler et al ., 2007; Kasa et al ., 1995) whereas nicotinic receptors activate MTCs and PGCs (Castillo et al ., 1999; Kasa et al ., 1995; Smith et al., 2015). Interestingly dopaminergic PGCs are down-modulated by muscarinic receptor activation (Pignatelli and Belluzzi, 2008). Acetylcholine-mediation of PGCs plays a role in balancing inhibition in glomerular circuits (D'Souza and Vijayaraghavan, 2012 ; Liu et al.,

2015). At the glomerular level, acetylcholine bi-directionally modulates the sensitivity of glomeruli (Bendahmane et al, 2016). Strong inputs are decreased via m2 muscarinic receptors activations whereas weak inputs are increased via nicotinic receptor activation. This reduces the dynamic range of glomeruli activity, making the representation more similar across odourant concentrations. In MTC representation, as well as in behaviour, ACh ameliorates odour discrimination (Escanilla et al 2012; Linster and Cleland, 2002). This is supplemented by an acetylcholine-induced narrower tuning curve of MTC activation (Rothermel et al., 2014, Mandairon et al., 2006; Ma and Luo, 2012).

1.1.6.4 Global aspects of neuromodulatory inputs

Globally, all noradrenaline, serotonin, and acetylcholine fibres modulate directly or indirectly JGCs, GCs, and MTCs. The innervations are distributed heterogeneously in the OB. PGCs are mainly mediated by cholinergic and serotonergic inputs, although noradrenaline has also shown effects at the first synapses. These systemic neurotransmitters are crucial in state-dependent modulation of olfaction. They participate in learning because they reinforce OB-cortex synchronization during acquisition and multi-modal integration. Finally, they shape the OB output and keep the dynamic range of the output compact.

In reality, neurotransmitters interact with each other and give birth to complex profiles of neurotransmitter distribution that assure a balance in mood and cognition which influences behaviour (Liu et al, 2018). For instance, both noradrenergic and serotonergic inputs to the OB are required for odour learning (Yuan et al., 2003). They form a fingerprint of brain state and influences perception by modulating neuron ensembles in sensory representations (Jacob and Hendrikje, 2018). They are implicated in learning, memory acquisition, discrimination of odours, and regulation of cell survival (Vinera et al., 2015). Their effects cannot be simply taken out independently but tend to overlap (Linster and Cleland, 2016).

It should be noted that anesthesia disrupts neuromodulation (Muller et al, 2011) and neurotransmitters centrifugal inputs are usually disregarded when studying peripheral neural circuits in anesthetised animals.

1.2 Metabolic sensing

Olfaction is the primordial modality of perception. Early life forms developed, through evolution, mechanisms linking their environmental perception to their behaviour with the aim of survival. The basic example is bacteria metabolism-dependent chemotaxis. This dependence relates to energy taxis receptors perceiving variations in intracellular energy status (Alexandre, 2010). Bacterial movement, with the activation of the flagella, is stimulated while there is the presence of chemoattractant molecules in its surrounding. For instance, Fan and Endres (2014) suggest that, in *R. sphaeroides*, a metabolism-dependent selective stopping strategy is used to navigate toward favourable environments. Those mechanisms between perception and behaviour, happening at the earliest stage of evolution implies the existence of counterpart equivalent functions in mammals and likely in other modalities of perception.

Our internal state affects our perception of the world. Our senses can be modulated to be over- or under-sensitive. This shift in sensitivity can affect behaviour. Impairment in the involved mechanisms can lead to pathologies. In the case of gastro-olfactive interactions, a feedback loop regulates olfactory sensitivity by the level of satiety (Aimé et al., 2007, Cameron et al., 2012, Tong et al., 2011). An increased olfactory sensitivity leads to a larger food intake (Soria-Gomez et al., 2014). The amount of food intake also depends on the attraction of its odour (Palouzier-Paulignan et al., 2012) which is lowered in response to satiety (Albrecht et al., 2009, Cameron et al., 2012). Alteration of olfactory function is correlated with several pathologies including type 2 diabetes (Hubert et al., 1980); Obesity (Obrebowski et al., 2000), and anorexia (Fedoroff et al., 1995) patients with respective heightened and reduced olfactory sensitivity. Furthermore proving the impact of olfaction ability on metabolism regulation, loss of olfactory neurons induces resistance against fast mass accumulation and heightens energy expenditure (Riera, 2017). Bulbectomy is also known to modulate feeding behaviour but it co-occurs with

depressive symptoms (Meguid,1993; Primeaux, 2007; Kalshetty, 2012). Olfaction plays an underappreciated role in metabolic health, usually left to the hypothalamus circuits.

1.2.1 Metabolism signalling in the OB

How does satiety alter olfactory function? At least two mechanisms signal satiety; an increase in nutrients entering the blood and an expansion of the stomach. Increased insulin and glucose can increase the sensitivity of mitral cells, the output neurons of the olfactory bulb (Marks et al., 2009, Tucker et al., 2013) but it is not yet known if satiety alters the representation of odours earlier in the circuitry of the olfactory bulb.

Although this mechanism involves modulation of the potassium channel Kv1.3 (Marks et al., 2009, Tucker et al., 2013), it is not yet clear how such modulation alters olfactory function as Kv1.3 as well as glucose transporters are expressed in numerous cell types including periglomerular (PG) interneurons and MTCs. This provides a potential mechanism for glucose to modulate the signal arriving from the olfactory afferents. Gastric distension is signalled through the vagal nerve and has been shown to modulate PG cell activity (Garcia-Diaz et al., 1985, Garcia-Diaz et al., 1984) as well as that of the mitral output neurons (Chaput and Holley, 1976). PG cells are therefore good candidates to state-modulate olfactory information transmission as they can modulate glutamate release from the afferent olfactory nerve (Aroniadou-Anderjaska et al. 2000; Petzold et al. 2009) and appear sensitive to both gastric distension and glucose concentration. This thesis focuses on the possibility of satiety to alter how odours are represented in the brain at the first synapse in the olfactory bulb.

1.2.1.1 The neural circuits of nutrients sensing

Why the OB is considered metabolism-sensitive compared to the rest of the cortex? There is a high density of satiety signals receptors, higher variability of extracellular glucose, and a particularly permeable blood-brain barrier with a high density of capillary microcirculation. This dense complexity

might be due to co-evolution of chemical and metabolism sensing, as the former is dictated by the latter. The dogmatic main hub linking food intake behaviours and satiety state is the hypothalamus which is also communicating with the olfactory bulb (Hardy, 2005) (Fig 1.8).

The OE, OB, and PC contain a high level of satiety-mediating hormone receptors. Glucose, insulin, CCK and leptin are anorexigenic signals as opposed to the orexinergic agents ghrelin, NPY and orexine (Palouzier-Paulignan, 2012). These signals are mainly produced in the periphery (Fig 1.8). They work in synergy and activate a cascade of events through the body, reaching the brain to finally influence behaviour. For example, the serotonergic satiety signal works in concert with the anorexigenic agents leptin and cholecystinin (Voigt and Fink,2015). This systemic aspect however affects the CNS and the periphery differently. This poses a problem for drug targeting. Solutions like selectively opening the blood-brain barrier exist. Another approach is nasal injections which enable the propagation of molecules straight to the CNS.

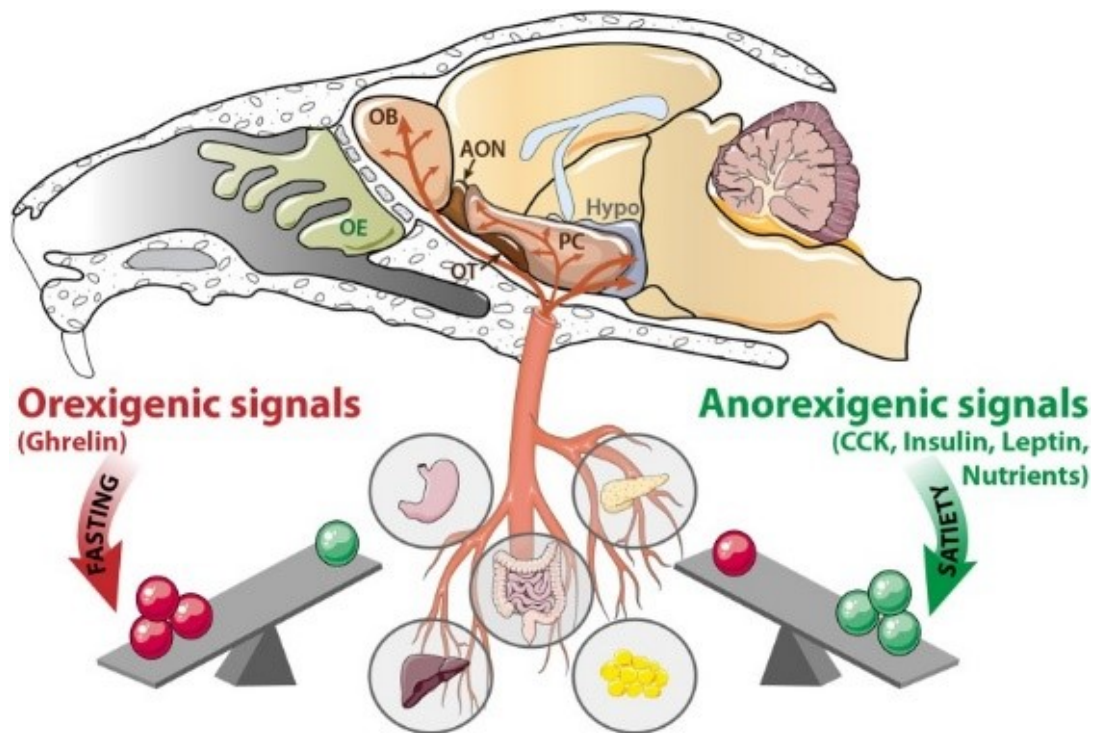


Figure 1.8 Nutrients signaling in fasted and satiated states. Satiety states are conveyed by nutrients delivered in the blood flow to the central nervous system from the stomach, pancreas, intestine, liver, and adipose tissues. The satiety signals are received from the olfactory bulb to the hypothalamus. The fasted state is signaled by Ghrelin and a lack of nutrients, while the satiated state is signaled by CCK, insulin, leptin, and an abundance of nutrients. Hypo, hypothalamus; OE, olfactory epithelium; OB, olfactory bulb; AON, anterior olfactory nucleus, OT, olfactory tubercle; PC: piriform cortex; CCK, cholecystokinin. Adapted with permission from Julliard et al. (2017).

1.2.1.2 Ghrelin

Ghrelin is produced in the gastroenteric tract in anticipation of food intake, to increase gastric motility and acid secretion (Kojima, 1999; Müller, 2015). It is also produced by the hypothalamus where it interacts competitively with leptin to guide satiety state (Nakazato et al. 2001). Ghrelin receptors GHSR are expressed in diverse brain regions including the OB where ghrelin levels are the highest (Rhea, 2018). Ghrelin increases olfactory sensitivity and food-seeking sniffing frequency (Tong, 2011). GHSR1a is expressed in OSNs and its activation enhances olfactory responsiveness (Loch, 2015). Ghre-expressing MTCs project to the amygdala and hypothalamus, connecting odour responses to the feeding behaviour hub (Russo, 2018).

Ghrelin acts in synergy with other nutritive molecules. Activation of NPY and AGRP neurons in the hypothalamus is required to establish ghrelin-induced feeding (Nakazato, 2001, Müller, 2015; Dickson, 1997). The ghrelin system procures a glucose-regulation action. Notably, it suppresses glucose-stimulated insulin secretion in the pancreas (Heppner, 2014). By its action on the dopaminergic system, ghrelin facilitates food odour conditioning (Han, 2018). Ghrelin might be involved in learning as it promotes hippocampal plasticity and neurogenesis, and caloric restriction facilitates new adult-born OB neurons via a Ghrelin-dependent pathway (Ratcliff, 2019).

1.2.1.3 Leptin

Leptin is produced in adipose cells and enterocytes. It downregulates fat storage in adipocytes, and through cell receptors in the hypothalamus, suppresses appetite. However, receptors are also expressed in the OB GCs/MTCs/TCs and in the Piriform cortex. Leptin could also be synthesised in the olfactory mucosa (Baly, 2006). Leptin mediates olfactory behaviours by a decrease in odour sensitivity and discrimination ability (Getchell, 2005; Karlsson, 2002; Julliard, 2007; Sun, 2019). Ob/ob mice, mutants lacking the leptin-producing Ob(Lep) gene, are better at odour discrimination (Chelminski, 2017). While it affects bidirectionally odour-evoked firing of MTC/TC, it only inhibits their spontaneous firing (Sun, 2019). On the contrary, odour-evoked calcium responses in GC and MTC/TC were attenuated (Sun, 2019). The reduction in excitability of MTC involves modulation of potassium channels by leptin (Sun, 2019). In OSNs, it increases spontaneous but reduces odour-evoked firing frequencies. This would lead to a lower SNR fitting with the lower smelling ability of the satiety state (Savigner, 2009). Leptin injection can induce a fasting state by attenuating food-seeking locomotion and sniffing behaviours (Prud'homme, 2009).

1.2.1.4 CCK

Cholecystokinin is secreted in the gastric system to facilitate the release of digestive enzymes and bile and therefore stimulate the digestion of protein and fat (Bowen 2001, Johnson 2013). In the central nervous system, it mediates satiety, nociception, anxiety, and memory via CCK receptors. CCK is not blood-brain barrier permeable but some parts of the hypothalamus and

brainstem allow it to pass. The main CCK receptor in the CNS is CCK(B), as opposed to the CCK(A) in the gastrointestinal tract. In the OB, CCK immunoreactivity was found in the GL and EPL, in PGC, deep short axon cells, MTC/TC but not in GC (Seroogy, 1985; Ma, 2013; Gutiérrez-Mecinas, 2005). MTC/TC are directly excited via both CCK(A) and CCK(B) receptors and inhibited indirectly via CCK-potentiated GABA release (Ma, 2013). CCK inhibitory effect on MTC and ETC is caused by CCK(B)-potentiated SSA (Liu and Liu, 2018). It also potentiates presynaptic inhibition of OSN and postsynaptic inhibition of glomerular neurons. The inhibitory effect of CCK on OB representation seems a priori to go against the hunger-induced odour sensitivity enhancement paradigm but Liu and Liu (2018) still suggest it might increase SNR for weak stimuli detection. CCK exerts a bulb-wide excitatory effect as well. Intrabulbar CCKergic TCs that reach the opposite side IPL of the OB inhibit GCs which thus disinhibits MTCs (Liu and Shipley, 1994). Additionally, in behaviour CCK(B) receptor antagonists elicit a memory-enhancing effect in olfactory recognition (Lemaire, 1994).

1.2.1.5 Orexin

Orexin produced in the perifornical area and the hypothalamus is broadcasted throughout the CNS to regulate wakefulness and food intake. There are two types of orexin (A and B) and corresponding receptors (type 1 and 2) (Marcus, 2006). Orexinergic neurons are inhibited by leptin and excited by ghrelin. They are also sensitive to a plethora of neurotransmitters: glutamate, endocannabinoids, 5-HT, NPY, CCK, and more. Hyperglycemia reduces orexin signaling via the orexin receptor-2 (Tsuneki, 2010). In turn, orexinergic neurons regulate acetylcholine, serotonin, and noradrenaline release (Frederick-Duus, 2007; Soffin, 2004).

Orexinergic centrifugal fibres reach the OB in the GL, MTCL, and GCL (Date, 1999). Orexin receptors 1 and 2 are primarily expressed in MTCs/TCs but also present in PGCs and GCs (Caillol, 2003; Hardy, 2005; Gascuel, 2012; Shibata, 2008). Orexin A directly depolarises a subset of MTCs and indirectly hyperpolarises a third of MTCs via GABA(A) receptors. The latter implies orexin is signalling through GCs and/or PGCs. Both of these effects are mediated via the orexin receptor-1 (Hardy, 2005; Apfelbaum, 2005). This leads

to changes in odour responsiveness (Apelbaum, 2005). Orexin A administration mimics fasting as food odour increases OB Fos expression (Prud'homme, 2009). Conversely, it increases olfactory sensitivity similarly to the physiological fasted state (Julliard, 2007)

1.2.1.6 neuropeptide Y

The neuropeptide Y is principally produced by neurons from the sympathetic nervous system. In the periphery, it conducts a vasoconstrictor effect and induces the growth of fat tissues (Kuo, 2007). In the CNS, it is secreted in the hypothalamus to reduce pain perception, stress, and anxiety while increasing food intake and energy storage (Tatemoto, 2004). NPY is synthesised by GABAergic interneurons (Kask, 2002), mainly in the hippocampus and hypothalamus (Acuna-Goycolea, 2005; Kautz, 2017). However, there is a comparatively high concentration of NPY in the OB. Neuropeptide Y-like immunoreactivity was localized in SSAs and dSAs (Gall, 1986; Scott, 1987; Seroogy, 1989). A quarter of NA neurons projecting to OB from the locus ceruleus contains NPY as well (Bouna, 1994). NPY suppresses spontaneous activity in OB interneurons and excitatory synaptic transmission between OB neurons by a presynaptic effect on glutamate release (Blakemore, 2005). NPY increases OSN neuroproliferation via NPY Y1 receptor (Hansel, 2001, Tsung-Wei, 2019). Hunger-induced NPY enhances olfactory responsiveness in the OE (Negroni, 2012; Kaniganti, 2019).

1.2.1.7 Endocannabinoids

Anandamide and 2-arachidonoyl-glycerol are endogenous cannabinoids and bind respectively to CB1 and CB2 receptors. The endocannabinoid system can also be activated by exogenous THC. CB1 activation hyperpolarises neurons via G-protein-coupled mechanism. CB1 receptors through the body and CNS coordinate synergies to increase food intake and energy storage (Piazza, 2017). CB2 rather relates to the immune system. CB1 receptors are localized in the OE, OB, and OC. They have behavioural consequences on odour sensitivity and food intake (Terral, 2020). CB1 is present in glutamatergic AON and Piriform cortex afference synapsing into GCs. Presynaptic-inhibition of these centrifugal fibres disinhibits GCs which

then disinhibit MTCs, resulting in enhanced olfaction conversely to promote food intake. CB1 in the OB is sufficient and necessary to induce hyperphagia after fasting and couples olfaction to feeding. This works with endo- and exo-cannabinoids (Soria-Gomez, 2014). Additionally, CB1 was present in PGCs dendrites, which provide another manner of MTC regulation via CB1-mediated GABA(A) release (Wang, 2019).

While this olfacto-hyperphagia mechanism is known in mice, CB1 has not been found in the human olfactory system (Lötsch, 2015). Furthermore, THC seems to decrease olfactory ability in humans (Walter, 2014). However, keep notice that the olfactory-induced hyperphagia enhancement in mice has a biphasic effect as 0.25mg/kg and 1.75mg/kg did not alter odour detection and food intake while 1mg/kg was effective.

1.2.2 Insulin

1.2.2.1 Insulin in metabolism homeostasis

Insulin plays a central role in metabolic homeostasis, notably lowering glycemia. It is produced by beta cells of the pancreas, as a response to heightened glycemia, and acts as an anorexinergetic signal circulating in the blood. When glycemia is low, the release of insulin is inhibited. Insulin serves as an anabolic hormone that promotes glucose uptake and metabolisms in cells, resulting in lowering glycemia. In opposition, alpha cells release glucagon when blood glucose is low. That enhances neoglucogenesis by the liver to readjust glycemia (Ruud, 2017).

Insulin binding to a receptor induces phosphorylation of proteins inside the cell, the insulin receptor substrates (IRS). Other kinases are activated in cascade. This cascade leads to the translocation of a GLUT glucose transporter to the membrane which then facilitates the cell glucose intake.

Thus, glucose and insulin signaling are linked. An elevated level of blood glucose will be followed by an increase of insulin and an injection of insulin will lower glycemia. These signals co-fluctuates during acute variations of concentration in the blood such as injection, food intake, and circadian rhythm. The biological clock orchestrated by the CNS and the circadian rhythm plays an important role in glucose/insulin phases (Kalsbeek, 2010).

The daily variations have brain and hepatic dependencies (Lamia 2008, Kalsbeek, 2010). Circadian rhythm and glucose metabolism are intrinsically related (Jha, 2015).

The distribution of insulin in the CNS is particularly marked in the OB and that relates to the higher glucose and insulin variation in the OB versus cortex after glucose or insulin injection (Al Koborssy et al., 2014; Fadool, 2000; Hill, 1986).

1.2.2.2 Insulin signaling to the CNS

Insulin receptor signaling in the CNS participates in energy metabolism and is a growth factor during development. Insulin can cross the blood-brain barrier (BBB). In the CSF, insulin reaches 5-10% of its plasma concentration. Probable pathways for insulin to the brain interstitial fluid are the choroid plexus through the blood-cerebrospinal fluid barrier and the brain microvascular endothelial cells through the BBB (Gray, 2014; Fernandez, 2012). However, Insulin gene expression was found at low levels in the OB and hippocampus (Devaskar, 1994) but there is not enough evidence for CNS-produced insulin.

Insulin exerts an action in the hypothalamus and dorsal vagal complex (DVC) to regulate liver glucose production and food ingestion (Abraham, 2014; Dodd, 2018; Diggs-Andrews, 2010). Contrary to the periphery, glucagon and insulin both are food intake suppressants in the CNS (Filippi, 2013). Insulin in the DVC promotes food intake and hepatic glucose inhibition via Erk1/2 signaling and K ATP activation (Filippi, 2014; Filippi, 2012). ATP-sensitive K⁺ channels are required to sense hypoglycemia and activate a counterregulatory glucagon response (Evans, 2004). K ATP couples glucose levels to insulin release. GLUT2 transports glucose inside the cell which leads via a mitochondrial mechanism to an increase in ATP that closes K ATP channels and therefore depolarises the cell. The depolarisation opens voltage-gated Ca²⁺ channel and Ca²⁺ influx generates exocytosis of insulin granules (Ashcroft, 2005).

In the olfactory bulb, where there is a high concentration of IR, the voltage-gated potassium channel Kv1.3 serves as an insulin sensor in MTCs (Fig 1.9). Insulin-induced phosphorylation of Kv1.3 makes cells more excitable

by suppression of outward potassium currents (Fadool, 2009; Fadool, 2000). A large proportion of currents are due to Kv1.3 in MTCs (Tucker, 2010).

Synaptic activity induces insertion of GLUT4 to the axonal plasma membrane. GLUT4 is necessary for sustained AP firing by its action on synaptic vesicle recycling (Ashrafi, 2016). This mobilisation is distinct from insulin signaling. Insulin-induced Kv1.3 phosphorylation promotes translocation of GLUT4 (Xu, 2004, Julliard, 2017, Li, 2006). This translocation happens faster in neurons than in muscles. Insulin inhibits Kv1.3 making the neuron more excitable with a higher calcium activity. Therefore neurons translocate GLUT4 quicker because the calcium-induced AP firing is energy-intensive and requires glucose transport to fulfill its energy need (Ashrafi, 2016). However, GLUT4 knockout mice showed decreased insulin sensitivity and failure to counter-regulate hypoglycemia (Reno, 2017).

In the olfactory cortex, glucose-dependent insulin modulates sporadic firing (Koborssy, 2018). Insulin reduces odour-evoked local field potentials (Zhou, 2017). In contradiction, they also find insulin increases LOT-evoked EPSC in principal neurons.

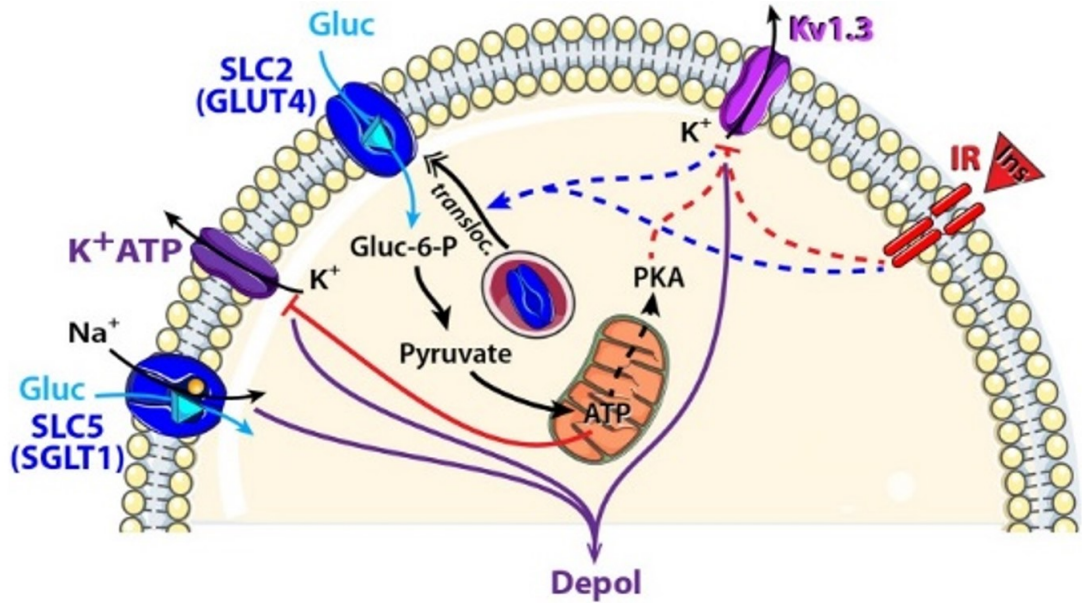


Figure 1.9 Kv1.3 as an insulin-glucose cellular sensor. Insulin receptor (IR) activation induces the inhibition of Kv1.3 channels and GLUT4 translocation to the membrane. Glucose intake increases the cytosolic protein kinase A (PKA) and mitochondria production of ATP. The cell becomes easier to depolarise. Activation: blue arrow, inhibition: red line. Direct action: dotted line. Indirect action: full line. Adapted with permission from (Julliard et al., 2017).

1.2.2.3 Insulin in the olfactory bulb MTC

Historically, Pager (1972) suggested insulin mimics fasting by increasing positive responses and decreasing negative responses in MTCs. Insulin in fact can elicit a bidirectional effect on MTCs, both spontaneous and OSN-evoked (Kuczewki, 2014). This would allow the nutritional status to take control of the OB representation and enhance it based on discerning odour valance. Intranasal insulin elicits an increased MTC basal firing. Chronic insulin, obesity inducing, makes acute insulin inhibits MTC (Fadool, 2011). However, insulin modulation fails in *kv1.3*^{-/-}, As more than 80% of outward current are due to Kv1.3, and depends on the duration of exposure and metabolic state. Part of insulin-induced modulation of MTC firing is intrinsic as it is not changed by the application of synaptic blockers (Fadool et al. 2011; Mast & Fadool, 2012). With an increase of insulin, most MTCs increase sporadic firing (Kuczewki, 2014; Papadaki, 2014) due to K⁺ current inhibited, as this effect was shown to disappear when K⁺ channel blockers were applied. However, K⁺ channels blockers didn't cancel downregulation of MTCs, which

suggests insulin-induced GABAergic interneuron inhibitory input to MTCs is not disrupted. GC and PGC are the inhibitory neurons that would come to mind for reducing odour-guided food intake following insulin signaling.

1.2.2.4 Insulin-mediated behaviour

A lack or an excess of insulin perturbs odour-guided food-seeking behaviours. Insulin deteriorates both aversive learned odour detection and food-odour seeking behaviour in fasted rats (Aimé, 2012). Notably, intracerebroventricular administration of insulin was within physiological concentrations (14 mU). Conversely in humans, heighten insulin levels reduced olfactory capacity (1 mU) (Ketterer, 2011). On the contrary, intranasal insulin delivery, while evoking robust phosphorylation of Kv1.3 as expected, increased odour discrimination and barely changed odour threshold (Marks, 2009). In humans, Thanarajah (2019) suggests peripheral insulin administration leads to poor olfactory performance as intranasal administration increases odour perception in a dose-dependent manner.

1.2.3 Glucose

Glucose is transported across the blood-brain barrier by GLUT1 (Dobrogowska and Vorbodt, 1999). The glucose transport capacity is modulated by the brain metabolic exigency and glucose availability. Fluctuation of glycemia could be dealt with by varying expression of GLUT1 accordingly (Simpson et al., 1999). Fasted rats showed a two-fold increase in BBB permeability compared to fed animals.

Insulin and glucose signaling are tightly linked. Glucose increase signal usually precedes insulin increase in the blood which promotes glucose cell intake. Extracellular glucose alters the sensitivity of the olfactory bulb's output neurons (Tucker et al., 2013). This effect is bimodal with a majority being decreasing.

Although it is not yet known if glucose affects periglomerular neurons or glutamate release from the olfactory nerve, the required receptors and transducers are present in some PG cells (Al Koborssy et al., 2014). Again the effect may be either a global change in the response of all glomeruli or the

effect may be restricted to a subset of glomeruli. The glucose transporter, GLUT4, shows dramatically different expression levels in different glomeruli (Al Koborssy et al., 2014). This could mean only a part of the odour representation would be involved in the gastro-olfactory feedback loop such as a selective effect for food odours.

SGLT1 and GLUT4 are Na⁺-dependent and –independent glucose transporters. SGLT1 uses Na⁺ gradient to transport glucose against its gradient. SGLT1 expressing neurites in the EPL could provide glucose-mediated inhibition to a subclass of MTCs (Tucker et al., 2013). IR and GLUT4 are usually colocalised (Kang et al., 2004). GLUT4 is the limiting factor for insulin-stimulated glucose uptake in the brain (Alquier, 2006). GLUT4 expression in glomeruli seems dependent on the satiety state as not for SGLT1 (Al Koborssy, 2014). However, SGLT1 is shown to be regulated in obese vs lean rats (Aime et al, 2014). Interestingly, both GLUT4 and SGLT1 are present only in a subset of glomeruli at different intensities (Al Koborssy, 2014).

1.2.4 Summary

Olfactory-induced hyperphagia is conveyed by orexinergic systemic signals. A heightened olfaction for food odour and food cues naturally promotes food intake. As anorexigenic signals would suppress the food-odour attention removing the pleasantness of eating. Disruption of the hedonic value of eating is well-known symptom of anorexia. Obesity, on the contrary, would suggest resistance to anorexigenic signals. Nutritional status dictates a behavioural state that prioritises olfactory perception with an objective of energy homeostasis.

The role of PGCs in metabolism sensing is poorly known and has not been studied but their place at the first synapse gives them an unresolved gating role for sensory transmission. MTCs and GCs have been largely privileged to sense metabolism and consequently modulate olfaction. (Al Koborssy et al., 2014) and others stained SGLT1, GLUT4, IR at different levels in glomeruli. This may underlie a relation between certain odourant molecules perception and the satiety state.

1.3 Aims and objectives

1.3.1 Characterise odour-evoked PGC activity and infer PGC subtypes

The first aim is characterise odour-evoked PGC activity and to figure out subtypes based only on odour-evoked properties. In fasted anesthetised mice, I planned to measure the activity of PGC across a range of odourant concentrations. This set up dosage-response curves which are required to determine metrics such as sensitivity and gain. These were a control for the case with heightened blood glucose. Furthermore, I aimed to detect and quantify the respiration coupling in the oscillatory activity of PGCs. I expected to collect enough data to make up functional groups of PGCs and relate them to afferent and lateral inputs.

I used two-photon imaging to observe odour-evoked activity in fasted anesthetised mice that express the calcium indicator GCaMP6f in periglomerular cells. The experiment was conducted through the application of a large panel of odours and concentrations delivered by an olfactometer. For the purpose of respiration-locked oscillation analysis, the breathing rhythm was acquired via a piezometric device apposed to the animal thorax. I acquired odour-evoked measurements of the dendritic and soma compartments of periglomerular cells, and extracted their functional features. I wished to observe heterogeneous functional groups and infer periglomerular subtypes with the help of all the collected metrics.

1.3.2 Manipulate feedback inhibition at the first synapses

To study the impact of the inhibition of the olfactory afference by the PGCs, I wanted to set up a method that would able the recording of both OSNs and PGCs populations simultaneously. This would show modulation of OSNs by PGCs and if this modulation holds in different states of the system, would it be drug application or metabolic changes. I expected to observe the feedback inhibition circuit by detecting increased PGC activity inducing decreased OSN activity, and vice versa.

The objective was to image OSN and PGC populations simultaneously *in vivo*. The first option was to add a red functional fluorophore on the OSNs to complete green PGCs in the VGATxGCaMP6f mice, and image them under

two-photon microscopy. An alternative was imaging of the OSNs through intrinsic optical imaging. Observation of the whole feedback inhibition circuit at the first synapses of the olfactory bulb was useful to demonstrate the putative roles of PGC in sensing metabolism, and if they were responsible for OSN activity modulation.

1.3.3 Demonstrate the effect of blood glucose on OSNs and PGCs

The main aim of this thesis is to investigate sensory-metabolic integration in the olfactory bulb, and if the modulation of the olfactory bulb activity by the satiety state occurs at the first synapses. Each experiment was conducted in fasted animal and followed by an injection of glucose to simulate satiation. The blood glucose variation was measured in that effect. Periglomerular cells were imaged similarly as stated in the first aim and the sated metrics were compared with the fasted control. Additionally, immunostaining was used to detect the expression of metabolically sensitive proteins in periglomerular cells. From the second aim, a technique was developed to observe simultaneously the effect of satiety on the olfactory afference.

In addition, I wanted to link sniffing behaviour, and more precisely the olfactory detection threshold, to what was observed in the circuits in the anaesthetised animals. The fasted and sated states were induced similarly for the behaviour tests and the neural circuits imaging. It was interesting to relate any changes in odour sensitivity in behaving mice to changes appearing in the neurons of the olfactory bulb circuits at the first synapses.

Chapter 2 Methods

2.1 Animals

2.1.1 VGATxGCaMP6f mice

The mice used throughout this thesis expressed a genetically encoded calcium indicator selectively in GABAergic interneurons, especially periglomerular cells in the olfactory bulb glomerular layer. The GCaMP6f indicator was chosen for its short rise and decay time, allowing observation of respiration-locked oscillations of the calcium signal baseline and a precise phase delay in odour-evoked responses which are key components of olfactory neural coding. Vesicular GABA transporter-IRES-Cre mice (VGAT.Cre, stock 028862, B6J.129S6(FVB)-Slc32a1^{tm2}(cre)) were crossed with floxed GCaMP6f mice (GCaMP6f.flox, stock 028865, B6J.CgGt(ROSA)26Sor^{tm95.1} (CAGGCaMP6f)), to generate VGATxGCaMP6f mice. Both mouse lines were originally from Jackson Laboratory (Maine, USA) and maintained in-house. Both sexes were used. Mice were kept on a 12h day/night cycle and had access to water and food ad libitum. Animals were experimented on at ages ranging 7-14 weeks old. All experiments were performed under the United Kingdom Home Office Animals (Scientific Procedures) Act (1986).

2.1.2 Fasted and sated states

Emulation of satiety states was approached by fasting the mice for 16 hours overnight and injecting glucose intraperitoneally mid-experiment. Glycemia explains a part of the variance of states between hunger and satiety. Fasting effectively lowers blood glucose to around 10 mmol/L and 1-2% of weight IP injection of 20% glucose (Sigma-Aldrich) in distilled water, increases it around 30 mmol/L. Animals weighted 20-30g and lost 10-20% of mass over a fasted night.

2.2 Surgery for acute cranial windows

In vivo imaging of neurons at the surface of the brain required the placement of a window above the dura. The procedure involved anaesthetising the animal, attaching its head to a stereotactic frame, performing surgery, setting and sealing the window. The choice of urethane as the anaesthetic was motivated by its modest effect on neurotransmitters and its one-shot long-term efficacy ideal for non-recovery procedures.

Before surgery, drugs were administered to assure a painless and stable non-recovery anaesthesia. Anaesthesia was induced with an intraperitoneal injection of urethane 0.012ml/g (Sigma-Aldrich) and successive top-up every 15 minutes if necessary. The initial urethane injection was supplemented by a subcutaneous injection of atropine 0.004ml/g (Sigma-Aldrich) that inhibits salivary and mucus secretions which can accumulate under urethane and cause respiratory issues. In case of respiratory insufficiency, additional atropine was administered. Meloxicam 0.004ml/g (Boehringer Ingelheim) was also injected subcutaneously as an adjunct.

After verifying the mouse was well anaesthetised by checking for any rear paw pinching-reaction, an incision was made along the rostro-caudal axis and skin is removed to access the whole cranium. The skin delimitation was glued and the apparent cranium was cleaned and scored to maximize bar adhesion. A headbar could then be attached with dental cement at the back of the skull to stabilise the brain for craniotomy and imaging (Fig. 2.1). The craniotomy of the dorsal olfactory bulb was executed by drilling window borders upon each bulb, avoiding large blood vessels separating each hemisphere and between the cortex and the OB. Adding artificial cerebrospinal fluid (ACSF) was then softening the thinned parts of the skull and the window could be carefully detached not to damage the brain. After the OB was exposed, it was crucial to keep it wet with ACSF. The space above the dura was then filled with 1.5-2% agarose in ACSF (VWR life science) and covered by a 0.5cm coverglass cautiously placed and fixed by applying acrylic glue and dental cement as an interface between the edge of the glass and the skull. If the experiment required a topical application of drugs, a quick-drying yet flexible rubber is used instead of the glue and cement so the window could be easily unpeeled, without pulling any tissue, to wash in drugs. In the case

of two-photon microscopy with a wet-contact lens, a well was built around the bulb with silicone rubber.

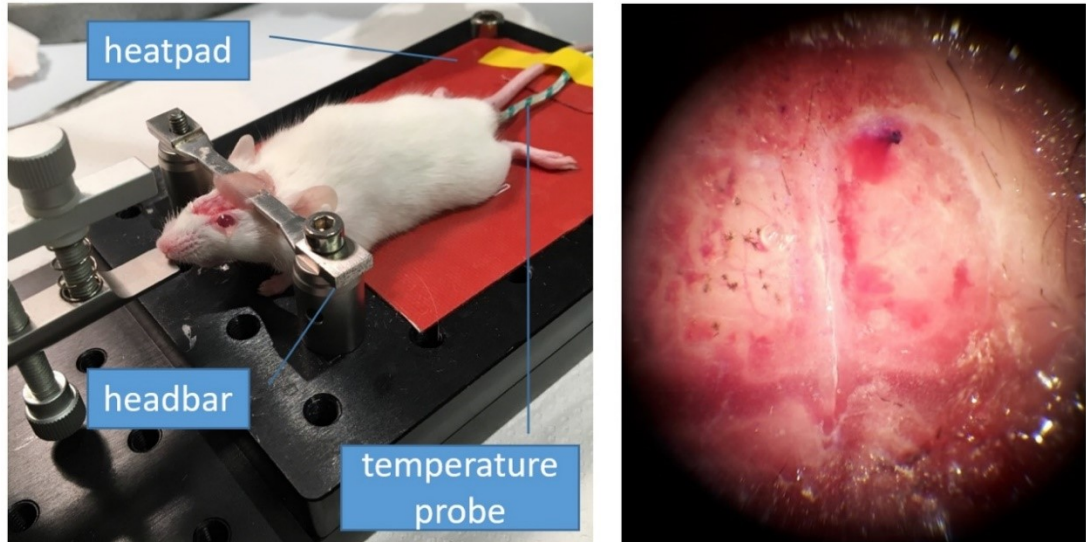


Figure 2.1 Olfactory bulb craniotomy. After anaesthesia, the mouse cranium is attached to a headbar with dental cement in order to perform a craniotomy. A window is drilled around the two bulbs. After applying ACSF to soften the bones, the cranial window can be detached.

2.3 Pharmacology

Neural circuit activity measurements were put under constraints by infusing the ACSF gel above the olfactory bulb with various drugs. These constraints consisted in blocking or attenuating neurotransmitter signaling between cell populations or disrupting specific ion channels within cell subpopulations. Agonist and antagonist molecules were chosen for their molecular weight permeable to the dura.

The glutamatergic transmission was reduced at the NMDA and AMPA receptors by the antagonists D-AP5 and NBQX respectively, allowing isolation of the OB activity from the periphery.

2.4 Immunostaining

Immunohistochemistry for Kv1.3 and GLUT4 was effectuated on olfactory bulb slices from GAD67-GFP using confocal microscopy by bachelor students in our lab, Gemma Gothard and Charlotte Hall. 3 mice expressing

EGFP in cells expressing glutamate decarboxylase 67 (GAD67) were used. Using homologous recombination, they were generated by Tamamaki et al. (2003) and subsequently bred in-house. Mice were anaesthetised at 9 weeks with urethane (1.5-2 g/kg) before getting cardiac perfusions with PBS. The brains were then fixed and olfactory bulbs sliced. Olfactory bulbs were removed and fixed in 4% paraformaldehyde at 4 degrees overnight and then refrigerated until slicing. Olfactory bulbs were fixed in gelatine before slicing. Olfactory bulbs were sliced on a Leica VT 1000s Vibratome at 40 μ M and collected in 24-well plates in PBS. Slices were blocked to minimise non-specific staining with a PBS solution containing 4% donkey or goat serum (dependent upon secondary host used) and either 0.1% triton or tween. Samples were incubated on a plate shaker in this solution for 1 hour at room temperature. Slices were then washed 3 times in PBS for 5 minutes each and mounted onto SuperFrost Plus adhesion slides (Thermo Scientific, USA, cat# J1800AMNZ). Primary antibodies (table 2.1) dilution concentrations were 1:100 except for the GLUT4 mouse antibody which was 1:200. Secondary antibodies (Table 2.2) were prepared at 1:200 (goat anti-mouse 555 and donkey anti-rabbit 555) or 1 drop/mL (donkey anti-mouse 594). 100 μ L of primary and secondary antibody solutions were applied to the slices. Cell nuclei were quantified with DAPI (Sigma, USA, cat# F6057).

Slices were imaged on a Zeiss LSM700 confocal microscope. Images were taken using Zen (2011) software on an objective Plan-Apochromat 40x/1.3W Oil DIC M27 (FWD = 0.21mm) lens at 1024x1024 dimensions. The DAPI and RFP channels were collected together and the GFP channel was collected separately. Pictures were taken at 0.5x zoom, averaging was set to 8. For each condition (GLUT4 and Kv1.3), the glomerular layer was tiled over 7-10 Z-stack images (x7 or x5 stacked images, 2 μ M each). Cells counting and the colocalisation of their staining were assessed by the two students and separately by an algorithm, a script in python that I made based on a published method (Toyoshima et al, 2016). Pre-processing was done by median filtering to remove noise in the images. Background pixels were then subtracted before enhancing the contrast and thresholding the image to only keep relevant pixels. Segmentation was done with the watershed method using

local maxima as markers. Finally, for post-processing, cells too small or identified in multiple slices were removed.

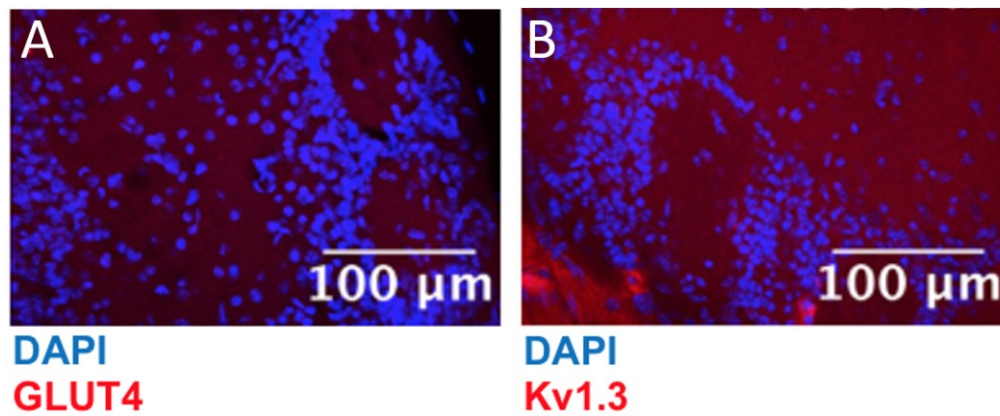


Figure 2.2 Immunohistochemistry control images. a) Control image showing no GLUT4 staining in the olfactory bulb glomerular layer in a slice incubated without the primary antibody. b) Control image showing no Kv1.3 staining in the olfactory bulb glomerular layer in a slice incubated without the primary antibody.

Protein	Species	Detergent used	Dilution	Antibody type	Cat. no	Produced by	Epitope	Specificity confirmation
Kv1.3	Mouse	PBS with 0.1% Tween	1:100	Monoclonal	73-009	NeuroMab, USA	AA residues 485-506 of rat Kv1.3	Western blot (Doczi et al, 2008)
Kv1.3	Rabbit	PBS with 0.1% Tween	1:100	Polyclonal	APC-101	Alomone, Israel	AA residues 263-276 of human Kv1.3	Knockout IHC and antigen preadsorption (Gazula et al, 2010)
GLUT4	Mouse	PBS with 0.1% Triton	1:100	Monoclonal	Ab35826	Abcam, UK	Cytoplasmic portion of rat GLUT4 protein	Western blot (Yin et al, 2009)
GLUT4	Rabbit	PBS with 0.1% Tween	1:100	Polyclonal	AGT-024	Alomone, Israel	AA residues 495-507 of human GLUT4 (intracellular, C-terminus)	Western blot Antigen preadsorption IHC in olfactory bulb

Table 2.1 Primary antibody details. From Gemma Gothard.

Species reactivity	Secondary host	Cat. no	Produced by	Excitation/emission (nm)	Dilution
Anti-rabbit IgG 555	Donkey	A- 31572	Invitrogen, USA	555/565	1:200
Anti-rabbit IgG 488	Donkey	A- 21206	Invitrogen, USA	488/525	1:200
Anti-mouse IgG 594	Donkey	R37115	Invitrogen, USA	590/617	1:200
Anti-mouse IgG 555	Goat	A- 21127	Invitrogen, USA	555/565	5 drops/mL

Table 2.2 Secondary antibody details. From Gemma Gothard

2.5 Monitoring

To assure the stability of vital signs, custom-built temperature and respiratory monitoring devices were used. The respiration rate was recorded using a strain gauge, placed against the mouse thorax, which changes its resistance depending on how much it flexes. The resistance was measured with a bridge circuit (Fig. 2.3). The voltage corresponding to the strip bending was then amplified and acquired with an Arduino microcontroller. The breathing rate was displayed in the Arduino serial plotter during the experiment to monitor anaesthesia depth. The transduced signal was recorded with timestamps from the same clock used for imaging frames. The Arduino output was either saved to text files via a python-controlled labjack interface (cfr. chapter 4) or incorporated in each tiff files via I2C protocol controlled by the Matlab-based two-photon imaging program ScanImage (Vidrio Technologies)

Being under anaesthesia, the animal's temperature needs to be regulated externally. The animal was placed on a heat pad that keeps it at 35°C via a feedback temperature probe. A precision programmable temperature PID Controller (McMaster-Carr, item: 38615K71) received a signal from a temperature probe (McMaster-Carr, item: 9251T91) and used built-in feedback algorithms to actualise the power it provides to the heating pad (McMaster-Carr, item: 35475K722).

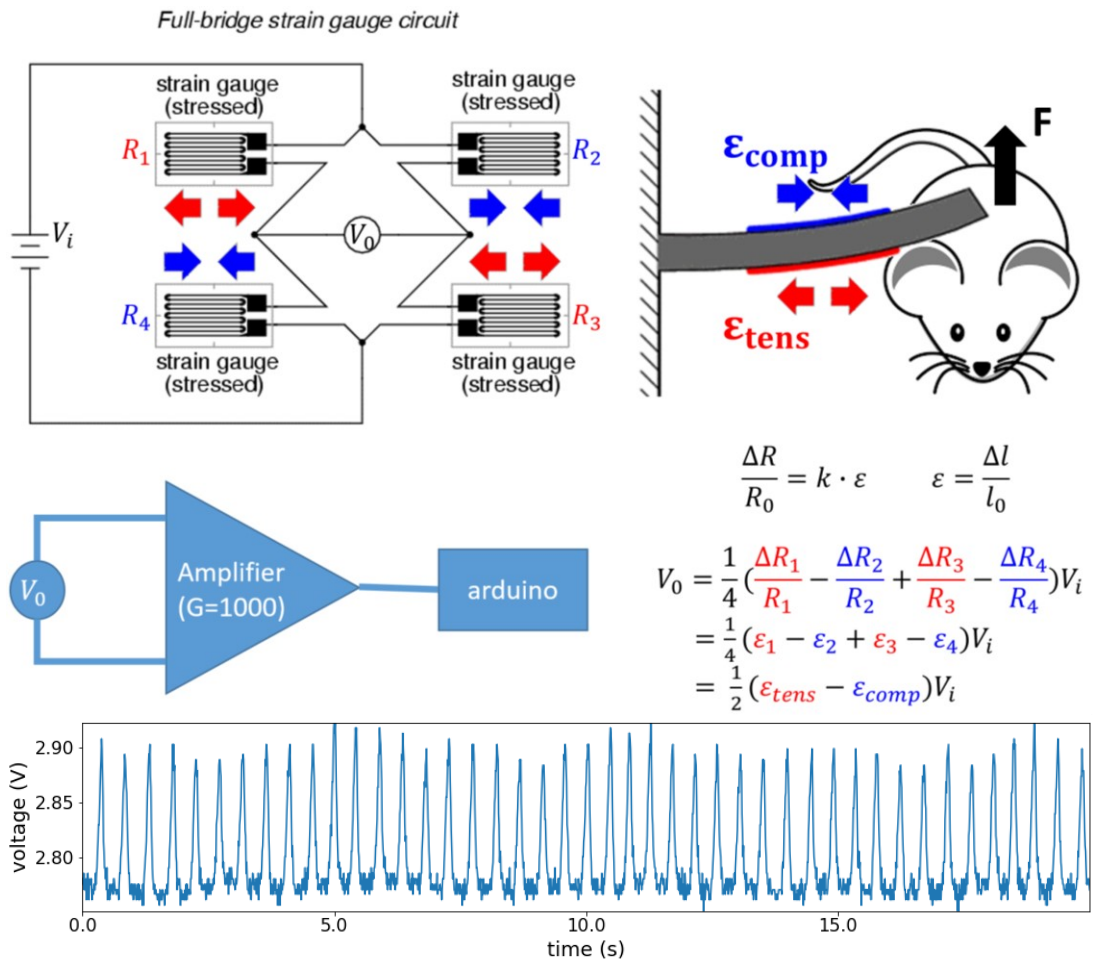


Figure 2.3 Custom-built respiratory monitoring device. To assert anaesthesia and vital signs stability through the experiment, breathing rate is monitored by the bending of resistance strip put against the mouse thorax. The flexion of the resistance is transduced into a voltage with a full-bridge strain gauge circuit. This difference of potential is then amplified and acquired to the computer with an Arduino microcontroller. The resistance relative changes are proportional to the constraints appearing on the strip during flexion.

2.6 Olfactometer

An olfactometer (206A, Aurora Scientific) delivered a range of odours to the animal at the desired concentration. The olfactometer hosted from 4 to 8 odour vials. The delivered concentration was modulated by mass flow controllers (MFC) allowing mixing of fresh air and odourant from the vials (Fig. 2.5). The final concentration can be set between 0.1 and 10% of air dilution. The air diluted the odour vapour present in the headspace of the vials. A square pulse dictated the valve opening and the consequently detected odour concentration follows a similar pattern (Fig. 2.4). While odour release is

repeatedly precise, there is an opening delay of 19ms and closing delay of 50ms (Fig. 2.4). These delays were measured during calibration using a photo-ionisation detector (200B, Aurora Scientific).

The airflow circuit goes as follows (Fig. 2.5). Medical air is regulated at a pressure of 20 psi and supplied to the dilution (MFC1), odour (MFC2) and fresh air (MFC3) MFCs. By default, fresh air is flowing to the animal entirely through MFC3 and the final valve. During odour stimulation, the appropriate vial inlet and outlet valves open, as well as the mixing valve that combines the flows of fresh and odourant air. The rate of dilution of the air-odour vapour mix in air is determined by the flow rates of MFC1 and MFC2. The final odour concentration is given by $c * \frac{rate_{MFC2}}{rate_{MFC1} + rate_{MFC2}}$ where c is the concentration in the vial headspace. In resting time, this flow is redirected to the exhaust and filtered by carbon.

Odour stimulation was controlled by a python script that allows randomisation and repeat of single or combined odours with control on dilution % in air. The script communicated with the olfactometer via instruction sent through USB serial and triggers image acquisition via a labjack output to the NIDAQ board on the 2P setup or to another labjack on the OMMI setup. The opening of the final valve was recorded and its timestamps synced with the microscope images.

Using the API for the olfactometer control I coded in python (appendix A), I was able to generate temporal patterns like sinus or ramps, and modulate total flow rate or odour dilutions. The stimulus intensity was updated at 20Hz and calibrated using the mini PID (Fig. 2.4). I used ramps from 0.5% air dilution to 10% (cfr. chapter 5).

The odour stimulation protocol was set up to test neuron reactivity to a large panel of odours across a wide range of concentrations—using air dilution of 0.1 to 10% of odourant vapours emanating from vials containing from 0.3% diluted in oil to vials containing pure odourant. The wide concentration range ensures access to baseline and saturated neural responses. Under two photon imaging, stimulations lasted 3 seconds with 5 repetitions of each concentration cited above. Each same-odour stimulation was presented at a 1-minute interval to reduce habituation. As for OMMI, stimulations lasted 10

seconds. This longer duration is justified by a lower spatial resolution and SNR of the OMMI. The concentrations were 0.1, 1, 10 % of air dilution of air-odourant vapour, repeated 15 times spaced by 1 minute.

Estimation of dosage-dependent response required a precise measurement of the quantity of odourant entering the nasal cavity as this quantity varies with the odourant vapour pressure. Saturation concentrations of isoamyl acetate in ppm were measured in the outflow of the final valve with a dilution of 0.1 to 10% in air with help of a miniPID photo-ionisation detector (200B, Aurora Scientific) (Table 2.3).

The automated olfactory behavioural test box consisted essentially of an Arduino, recording a nose poke sensor and the olfactometer final valve, and is based on (Qiu, 2014). The PC acquired the beam break and final valve signal, with an option to record from a camera. The camera frames and Arduino signals were synchronised by timestamps using the PC clock. The behavioural test was run with 3 python scripts launched in parallel on the pc, one to set the olfactometer sequence protocol (the same as for the imaging experiments), one to record the Arduino from the behaviour box, and one to display and save camera frames (appendix A).

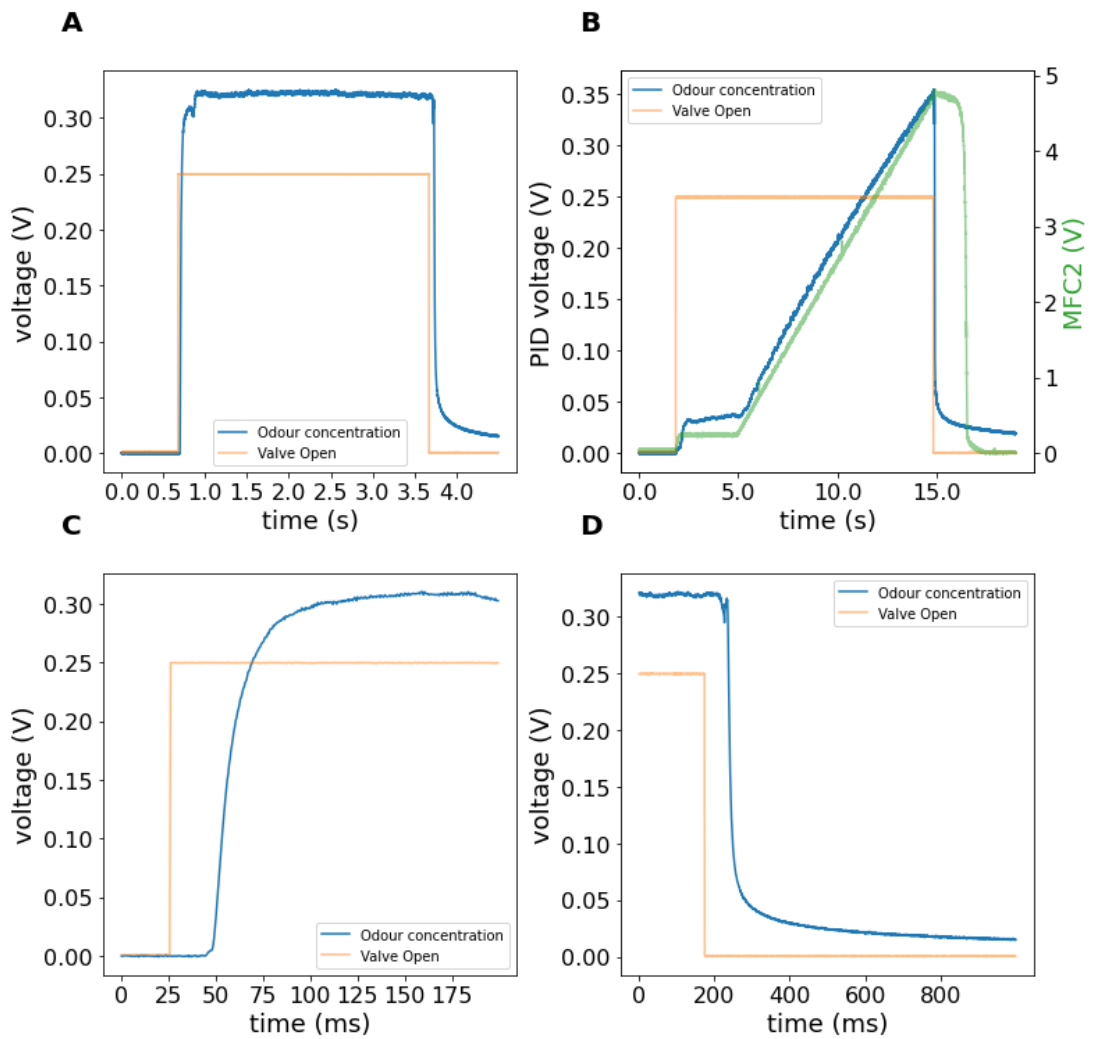


Figure 2.4 Odour pulse delays to final valve opening and closing. PID measurements of isoamyl acetate 2.5% in oil, diluted at 10% in air (A,C,D). **a)** 3-second odour step stimulus PID measurement. **b)** 13-second ramp stimulus composed of 3 seconds at 0.5% air dilution, then rise for 10 second to 10% air dilution. Odour vial shown is 0.3% isoamyl acetate in oil. The mass flow controller 2 (MFC2) controls the dilution ratio. **c)** 19 ms onset delay. Zoom of a). **d)** Closing delay of 50 ms. Zoom of a).

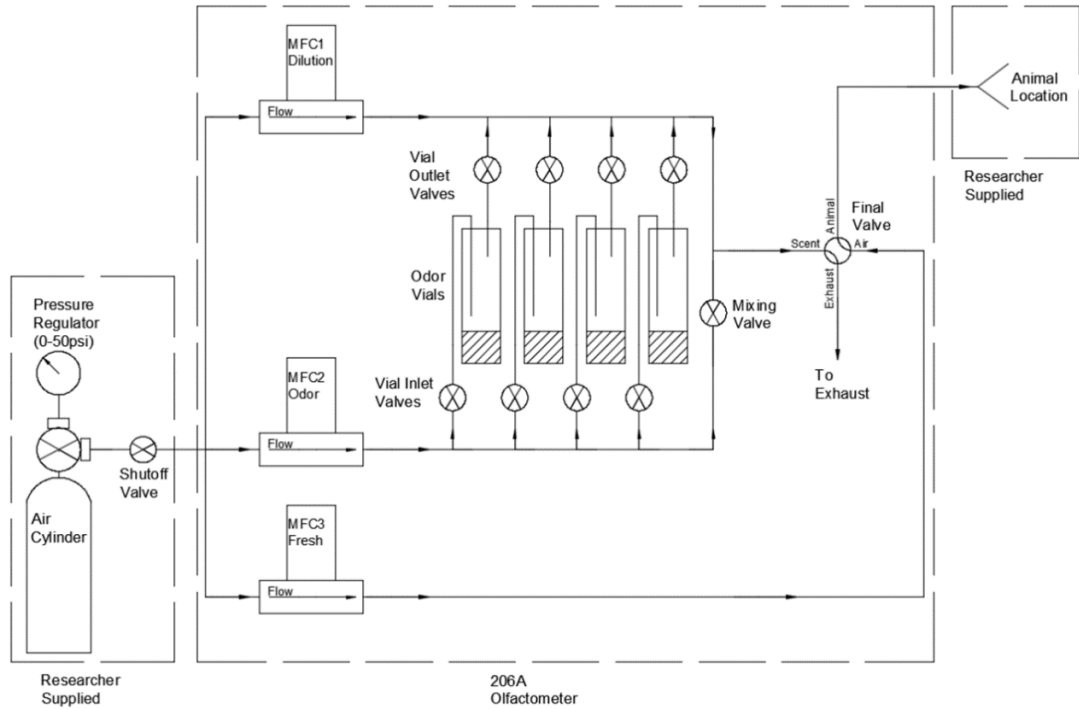


Figure 2.5 Olfactometer diagram. The olfactometer manages 3 MFCs to mix odour vapour and air. Inlet and outlet valves control the odour vials to use. A final valve controls the presentation to the animal or the deviation to the exhaust. MFC: mass flow controller. From the olfactometer manual (206A, Aurora Scientific).

Dilution in oil (%)	Vapour dilution in air (%)	Mix concentration (ppm)
0.03	0.5	0.15
0.03	3	0.58
0.03	10	1.27
0.3	0.5	0.51
0.3	3	1.94
0.3	10	4.55
2.5	0.5	0.66
2.5	3	5.56
2.5	10	14.33
100	0.5	17.22
100	3	67.17
100	10	198.83

Table 2.3 PID measurements for isoamyl acetate step stimuli.

2.7 Two-photon imaging

Two-photon microscopy allows imaging of cellular signals at a subcellular resolution. Calcium signals defined by intracellular Ca^{2+} serve as a proxy for neural activity. Compared to electrophysiological methods, 2-photon imaging provides the possibility to acquire activity from hundreds to thousands of cells, genetically targeted, and simultaneously have access to morphological information.

2-photon microscopy brings a strong advantage against one-photon microscopy. Using multiple photons to excite a fluorophore allows not only to use photons with less energy but also excite only a thin plane where the multiple photons hit the indicator simultaneously in an attosecond window. The fluorophore therefore receives the same energy as a single higher-energy photon would provide (Fig. 2.6). GCaMP is excited by 460nm wavelength photons in one-photon microscopy and 920nm in 2-photon microscopy. The emitted photons remain unchanged, around 520nm, except 2-photon microscopy will only emit light from the volume where lower-energy photons excite the target at the same time, reaching the required energy for excitation. In one-photon microscopy, the excited volume follows a quadratic law starting from the focal plane. This ends up with out-of-focus emitted light which contaminates the signals. Finally, lower-energy infrared photons are less prone to scattering in the tissue and detrimental heating is reduced.

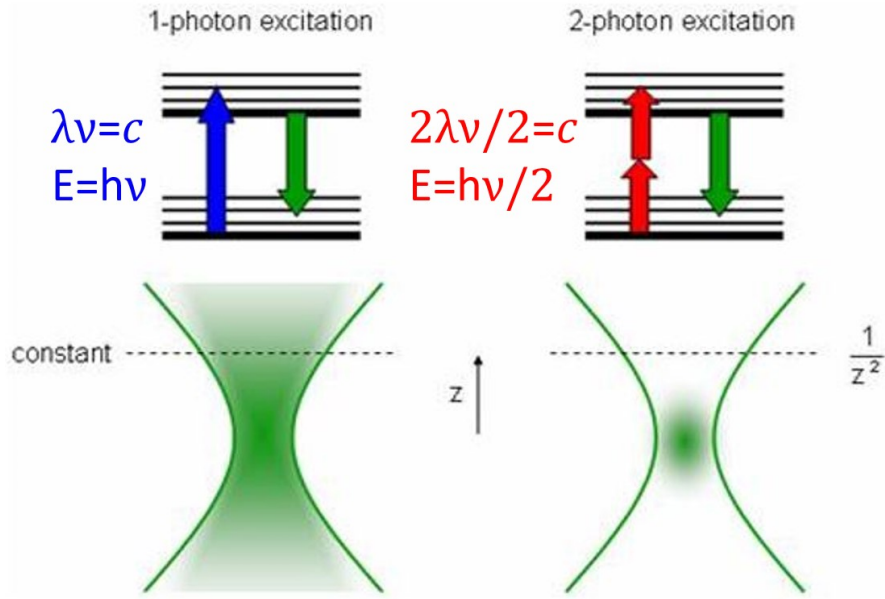
Periglomerular cells were imaged in VGATxGCaMP6f mice. The genetically encoded calcium indicator (GECI) GCaMP6f was chosen for its shortest decay and rise time amongst GCaMP6s, GCaMP6m, and GCaMP6f. The fast reactivity allows observation of rapid calcium fluctuation which is especially useful for quantifying sub-threshold activity such as oscillations in baseline and evoked activity of PGCs. Knowing the phase of oscillations in respect to the respiration cycle is proved to be highly relevant for timing-dependent coding in olfaction.

2-photon microscopy relies on a fluorescent probe that is activated by an exciting beam of appropriate wavelength and emits photons that will be acquired as images. Emission intensity depends on how many sensor molecules bind with the ion or molecule targeted. The photons are emitted

when an electron in the fluorophore drops to a lower electronic orbital, from an excited to a ground state. The difference of energy induces the emission of a photon, by the law of conservation of energy.

The mechanisms of photons generation and acquisition are described by an optical circuit as follows in figure 2.7. A titanium-sapphire laser (MaiTai) generates a short-pulsed polarised beam. A pockels cell modulates the beam to the needed power by phase-filtering the beam. The beam is then enlarged by a telescope to maximise the filling of the scanning mirrors which sweep in the X and Y-axis. The scan mirrors raster scan the beam onto each pixel of the field of view, scanning line by line. The scan lens and tube lens act as a further telescope to expand the collimated beam to slightly overfill the back aperture of the objective, which maximises spatial resolution. Each pixel in the FOV will in return emits photons if the fluorescent probe is activated, in a Ca^{2+} concentration-dependent manner.

Frames acquisition was controlled by the software ScanImage (Pologruto et al., 2003) run on Matlab. Laser power was usually set between 36.3 and 53.3 mW. Images were acquired at a 512x512 resolution and 30 frames per second. The zoom was adjusted to cover from 450 to 250 μm . The zoom and resolution were selected to acquire glomeruli as well as neurons activity while paying attention to get a variety of evoked responses. The compromise was also between the number of neurons and the ability to keep the stability of the FOV through the experiment. This was helped by using an x-y-z live motion correction implemented in ScanImage, which relies heavily on the presence of clear visual markers such as blood vessels as neurons footprints can appear and disappear as the experiment progresses.



<http://biomicroscopy.bu.edu/research/nonlinear-microscopy>

Figure 2.6 Comparison between 1-photon and 2-photon excitation. The Jablonski diagrams show energy bands corresponding to electron energy on different orbitals. The loss of energy after an electron returns to its ground orbital induces the emission of a photon. Two infra-red photons provide the same energy to a molecular probe as a single blue photon. The necessity of the two photons to hit the probe simultaneously constrains the excited volume to a thin plane. For one-photon microscopy, the fluorescence spatial distribution follows a quadratic distribution from the focal plane and adds out-of-focus acquired photons. In Maxwell's equations: λ : wavelength, ν : frequency, c : speed of light, E : photon energy, h : Planck's constant.

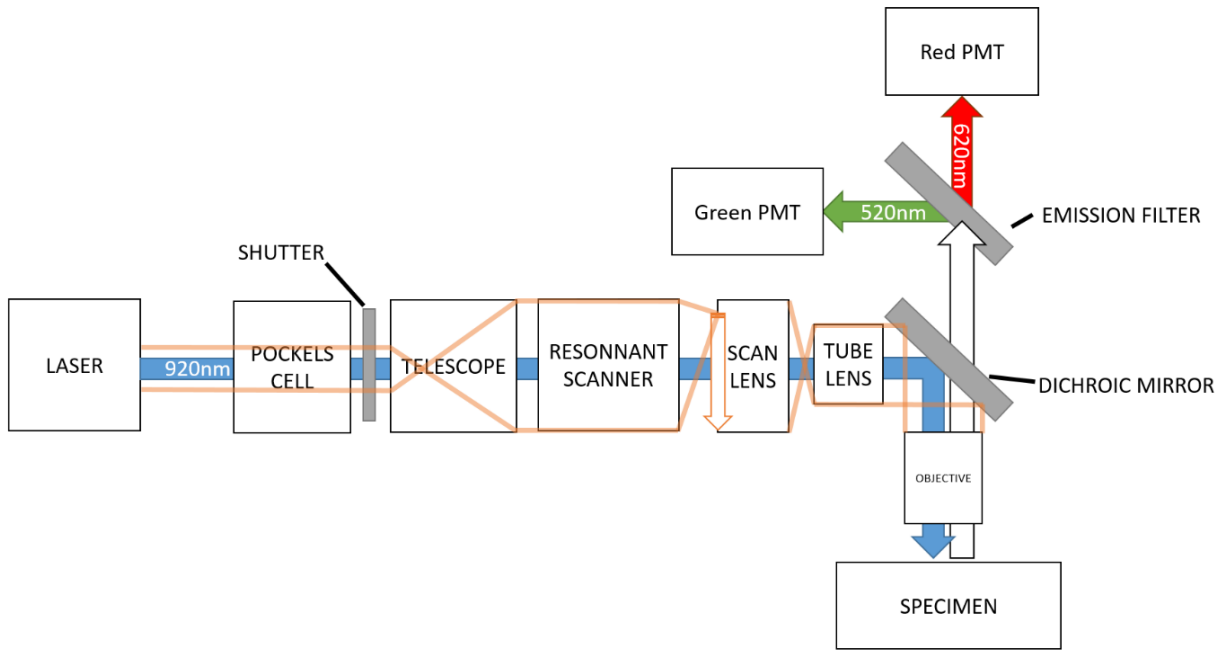


Figure 2.7 Two-photon microscope diagram. Schematic optical Beam path in orange. The laser generates pulses of polarised photons. The pockels cell controls the laser power. The telescope expands the beam to fill the scanner mirrors. The resonant scanner focuses the beam on each pixel by raster scanning each line of the FOV on the scan lens. The tube and scan lens fit the beam to the rear of the objective which condenses the beam onto the FOV in the specimen. Excitation of the tissue emits photons that are captured by photomultiplier tubes (PMT).

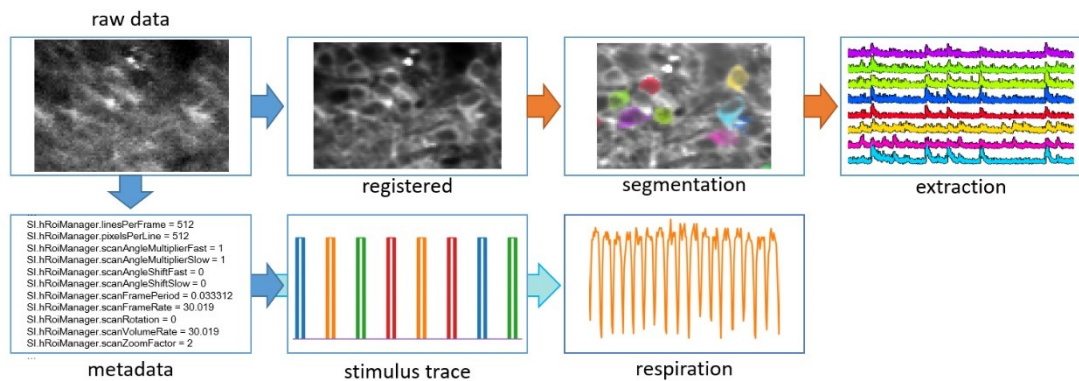


Figure 2.8 Calcium imaging data pipeline. Tiff image files are acquired with scanImage. Metadata about acquisition settings are extracted from the files headers. Stimulus and respiration traces are reconstructed from I2C data contained in each frame. Using suite2p, the movie is registered and semi-automatically segmented. After curation of ROIs, calcium traces are extracted and their background activity removed before applying a $\Delta F / F_0$ normalisation.

2.8 Calcium imaging data processing

Processing data from two-photon microscopy is a matrix factorisation problem. The matrices are movies of a 2D field of view containing active fluorescent cells. The movies are approximated or factorised in two components: the cells spatial footprints and their corresponding fluorescence activity traces.

From the scanImage-acquired tiff-file movies, I extracted hundreds of cells activity and footprint per animal using a semi-automated algorithm from the suite2p python package (Pachitariu, 2017, bioRxiv) (Fig. 2.8). First tiff metadata containing acquisition parameters, stimulus trace, and respiration recording were extracted. Then the tiffs were registered, the neuron regions of interest (ROI) detected, and the calcium traces extracted from the ROIs. Registration, ROI segmentation, and extraction were accomplished by custom python scripts using suite2p API. The suite2P graphical user interface (GUI) allowed for cells exploration and visual verification of images registration, detected cells, and extracted traces.

All movies of a single experiment are concatenated and registered, using suite2p registration module (Fig. 2.8). This method enables the correction of x and y non-rigid motions of the field of view (FOV) structures. Occurring Z motions were however not solvable and the affected frames were discarded. The alignment of frames is based on a reference template made of the best-correlated frames and iteratively updated through registration. The frames were divided by patches that were non-rigidly registered in the frequency domain, as phase-correlation is proven more efficient than cross-correlation. The patches are then glued back together and interpolation is applied at their junctions to suppress image smearing, to reform the frames.

Segmentation of neural components, would they be somata or neurite compartments such as dendrites or axons, consists of grouping pixels corresponding to these components on the image. The suite2p segmentation algorithm first reduces the dimensionality of the data by computing principal components which results in finding peaks in components. ROIs are extended around those peaks iteratively until newly added pixels don't correlate anymore with the ROI signal. Pixels located further from the component will be taken

as neuropile source and its signal will be subtracted from the component signal as a method of background removal. ROIs are non-binary. Each pixel of an ROI is weighted for its participation in the activity of the component, e.g. pixels of the cytosol have higher weights than ones of the nucleus. ROIs are allowed to overlap but overlapping pixels won't be used for trace extraction.

Segmented components were visually verified and manually curated (Fig. 2.8). Components with aberrant ROI or trace (too small amplitude or too noisy) were pre-emptively discarded. Merging of components was applied when components were visibly parts of the same neural compartment and had identical activity patterns. Glomeruli were manually segmented using ROI manager and polygons under the software imageJ. A python script generated ROI masks and traces from the saved imageJ polygons.

Calcium traces were extracted for each component as the pixel-weighted average value computed along the time axis (Fig. 2.8). The fluorescent traces had their background/neuropile signal removed by subtracting generally 70% of the background trace extracted from a doughnut-shaped surrounding the cells but not including other cells ROI. Finally, each calcium trace F was normalised by $\Delta F/F_0$ where $\Delta F=(F - F_0)$ and F_0 was the baseline estimated on the 3 seconds preceding each stimulus.

Additionally, I retrieved contextual information from the files required to analyse the data. I extracted metadata and external signals from the tiffs. The metadata contains information such as the zoom factor and spatial resolution of the movies configured during acquisition. The external signals are the stimuli delivery and respiration (Fig. 2.8). I used the I2C protocol that enables synchronous acquisition of these signals embedded into the frames headers. An I2C bus is monitored by the scanImage FPGA which acts as a slave in the I2C protocol. On that bus, an Arduino master broadcasts the external signals. The bus that connects the Arduino and the FPGA (SCB-19 AUX I/O Connector Bloc) is made of Serial Data Line (SDA) and Serial Clock Line (SCL). The communication is activated when an external trigger provided by a Labjack output determines the start of an acquisition.

The Arduino microcontroller receives signals such as the strain gauge, the olfactometer final valve state, and the olfactometer mass flow controllers,

and converts them from analog to digital before sending them to scanImage using the Wire library. ScanImage receives 3-4 packets containing each a value time point per signal. ScanImage will timestamp the incoming packets and log the data bytes to the header of each movie frame. The acquisition rate of I2C was set to 100Hz or 3-4 packets per frame if the movie is acquired at 30Hz. This precision is required to study time events like peaks of respiration.

2.9 Glucose tolerance test

Blood glucose was lowered by a 16 hours fasting overnight and subsequently increased by an IP glucose injection of 2g/kg. Glucose tolerance tests were conducted on 6 mice anesthetised with urethane. Blood glucose was measured every 10 minutes after the IP glucose injection. All blood glucose measurements were done with a glucometer (Accu-Chek Performa) using the blood from a cut in the tail. An identical paradigm was used during imaging experiments. I measured glucose in the fasted state before the IP injection, with values constantly below 10 mmol/l, and at the end of the experiment in sated state, when glucose was constantly measured at high values above 20 mmol/l.

2.10 Odour detection test

Olfactory sensitivity was determined by measuring how much a mouse sniffs a cotton bud saturated in different concentrations of isoamyl acetate versus a mineral oil control. Two cohorts of 12 fasted mice were tested twice. A first session where half received a saline injection and half a glucose injection and a second session a few days later (so their bodyweights get back to normal) with the saline and glucose injections switched up.

The test consisted of 4 consecutive 3 minutes runs where mice had to sniff either a cotton bud saturated with an increasing concentration of isoamyl acetate (10⁻⁶, 10⁻⁵, 10⁻⁴, 10⁻³ % in mineral oil) or another one situated at the opposite side of the cage containing only mineral oil as vehicle. The side of isoamyl acetate was randomised as well as the states of the mice. The test

arena was an empty regular cage with cotton buds hanging from a cap, slid inside a cut pipette to avoid chewing and contact with the odourised cotton buds. 2 or 3 cages were filmed at the same time, separated by sheets of paper to visually isolate the animals. Cages were cleaned and beddings were changed between each animal test.

I habituated the animals to the area with empty cotton buds for 10 minutes the day before the experiment. For the second cohort, I habituated the mice to handling and being scruffed during the week before the tests, so they are less stressed by the IP injections before the tests. I handled each mouse 3 times for 5 to 10 minutes.

The test score is the time sniffing at the odour minus the time sniffing the oil, divided by the total time sniffing both. Sniffing time was manually annotated with python video annotator (<https://github.com/video-annotator/pythonvideoannotator>). Subsequent analysis of locomotion was carried out using ANY-maze video tracking tools.

2.11 Statistical tests

The preferred baseline phases in reference to the inhalations were asserted with the Rayleigh test of uniformity. This test identifies non-uniform distributions, i.e. it detects a unimodal deviation from uniformity. The null hypothesis H_0 assumes the population is distributed uniformly around the circle while the alternative hypothesis H_1 indicates the opposite. The null hypothesis is rejected for small p-values. The test assumptions were that the distribution has maximally one mode and follows a von Mises distribution, or “circular normal” distribution. The data distribution was asserted by computing the Maximum Likelihood Estimator (MLE) for the parameters of the von Mises distribution. With these assumptions, a population not distributed uniformly around the circle implies it has a single peak.

The change in activity in cell and glomerulus odour responses following drug application or glucose injection was tested with a paired t-test if their distribution was normal, otherwise a one-sided or two-sided Wilcoxon signed-rank test was applied. Normality was tested with a D'Agostino-Pearson test

tested for normality. P-value below 0.05 was considered statistically significant (* denotes $p < 0.05$, ** $p < 0.01$, *** $p < 0.001$ and N.S. else). Similar analysis was applied for asserting changes in sensitivity thresholds and response maxima, in a cell/glomerulus.

Chapter 3

Odour-evoked periglomerular cells properties

3.1 Introduction

Periglomerular cells form the first layer of inhibition in the olfactory bulb where they modulate the afferent signal from the nasal epithelium. PGCs release GABA onto OSN axons, effectively dampening the glutamate transmission from OSN to MTC. This feedback inhibition is due to OSN releasing glutamate onto PGCs, which then release GABA onto OSN terminals. Therefore, odour stimuli activate PGCs which play a central role in shaping olfactory information processing. Afferent OSN axons merge in neuropil structures named glomeruli, based on the expression of the same olfactory receptor. PGCs distribute their dendrites into one or a few 'mother' glomeruli.

I investigated the odour-evoked response and properties of the dorsal glomeruli and PGCs against a panel of odours and concentrations. From the observed responses, characteristics of PGCs such as sensitivity or concentration-dependence were inferred. I questioned to which degree odours are encoded by PGCs in matter of amplitudes and oscillations. I compared the characteristics of odour encodings within and across groups of mother glomeruli. The similarity or difference in characterised responses may enlighten computational mechanisms of odour information shaping at the first synapse in the olfactory bulb.

The neural activity was measured through calcium imaging of PGCs somata and dendritic processes merged as glomeruli, in VGATxGCaMP6f anesthetised mice. The mice were fasted, as in chapter 5 the same mice were brought to satiety to study sensory-metabolic integration. The fluorescent calcium responses serve as a proxy for action potentials and are therefore a good reflector of neural activity. The measured neuropil activity made of a group of daughter PGCs dendrites will be referred to as glomeruli activity for clarification.

We expect a diversity of PGCs responses and heterogeneous groups of PGCs based on intrinsic properties, as they receive input not only from afferent OSN but also other PGCs, ETCs, and MTCs. Variations of characteristics and elicited responses will be overlaid to the known PGCs

subtypes for which the different connectivity preferences and response shapes have been observed.

Here below I investigated how the response properties of PGCs vary with increasing odour concentration and how this relates to the dendritic signal in glomeruli.

3.2 Results

To characterise PGCs and glomeruli odour-evoked responses, a computer-controlled olfactometer was used together with a respiration recording device (cfr. Methods). The latter is essential to measure inhalations during imaging as well for analysing PGCs respiration-related information. Both the final valve openings of the olfactometer and the respiration recordings were synchronized to the frame acquisition of the calcium imaging microscope to enable a real-time comparison with acquired neural activity (Fig 3.1 A).

To study the odour-evoked activity of PGCs, I required a diverse panel of odours and concentrations. This was to ensure that we capture a broad variety of PGC dynamics. The olfactometer stimulated the fasted animal with a series of odours presented in a pseudo-random order across a set of increasing concentrations (Fig 3.1 C). A selection of 4 odours was picked for an experiment. The panel of odours comprised of 2-heptanone, Isobutyl propionate, Ethyl tiglate, Isoamyl acetate, 2-phenylethanol, 2-isobutylthiazole and Trimethylthiazoline (TMT). The most commonly used odours were 2-phenylethanol, TMT, Ethyl tiglate and Isoamyl acetate.

The odours were chosen on 4 criteria. Only mono-molecular odours were selected because they assured that the concentration in particles per million remains reproducible between experiments. On the other hand, a mixture such as coffee would vary in concentrations as we could not assure the same composition each time. Secondly, they had to activate a high number of dorsal glomeruli since our calcium imaging protocol limits the field of view to that area. Furthermore, we wanted the odourant molecules to be as different as possible in their molecular features. This would improve the likelihood to activate more separated and less overlapping glomeruli. Lastly,

we chose odours to cover a range of ethological valences, attractive (2-phenylethanol), neutral (Isoamyl acetate), or aversive (TMT).

The four odourants were set in 8 vials, 4 vials diluted at 0.3% in mineral oil, and 4 vials in pure form. To establish a wide range of concentrations, the 2 sets of 4 vials were diluted in air at 0.1, 1, and 10%. This amounts to a total of 6 concentrations per odour. In some cases, Isoamyl acetate was only used with the 3 later concentrations. The odours were presented in 5 repetitions for each concentration, in an increasing manner. The odour stimulations were conferred in a pseudo-random order, under the constraint not to have 2 consecutive identical odours. The duration of the olfactometer valve opening was of 3 seconds and was spaced by 8 to 10 sec (Fig 3.1 A, 3.2 A). This spacing limited neuron response habituation. An experiment consisted of 120 stimulations (Fig 3.1 C).

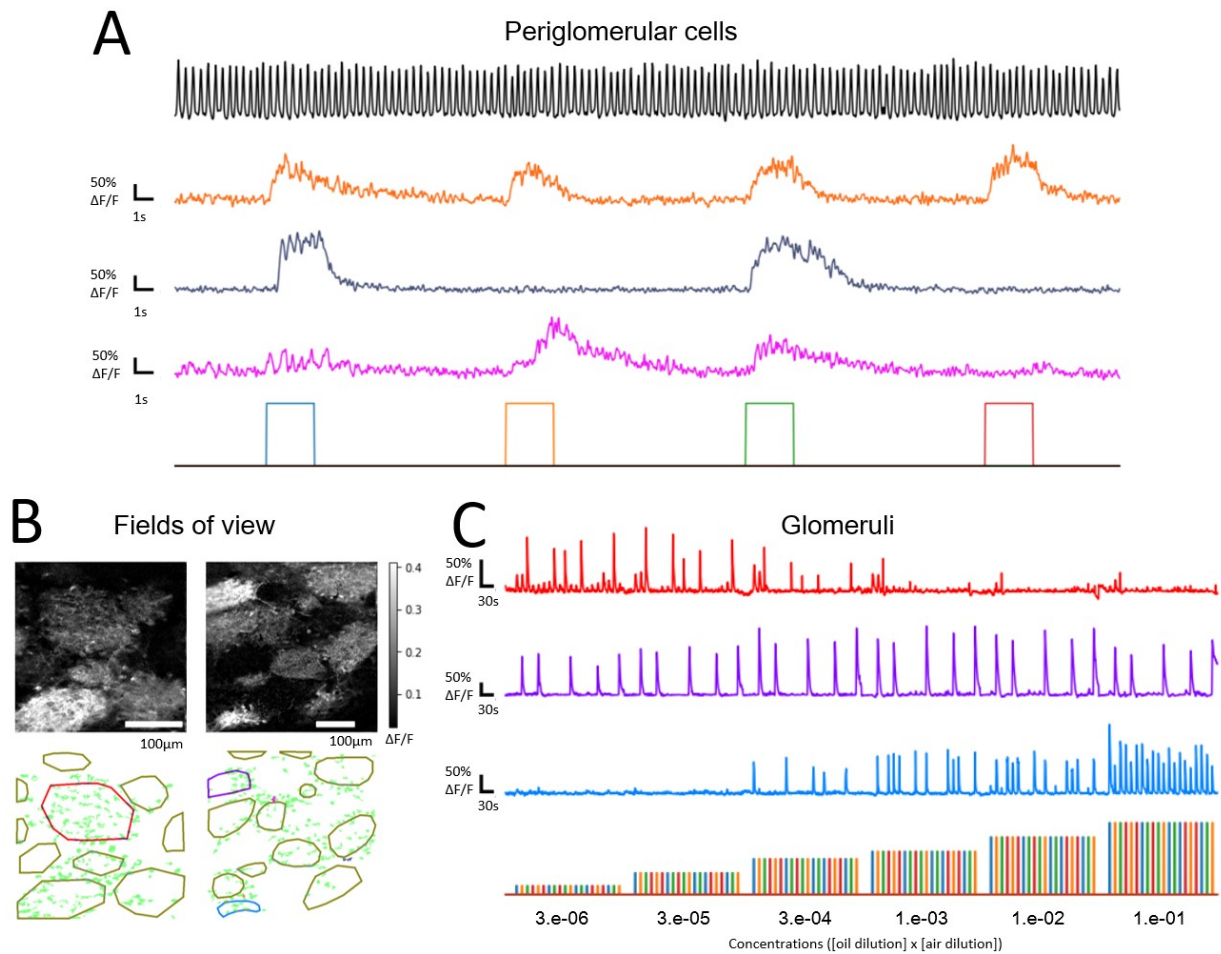


Figure 3.1 In vivo calcium imaging of PGCs under odour stimulations. a) Example calcium traces of 3 periglomerular cells under the course of 4 different odour stimulations depicted by the coloured pulses (bottom), odours: 2-Heptanone, Isobutyl propionate, Ethyl tiglate, Isoamyl acetate. Oscillations in the calcium traces are related to the respiratory signal that was recorded synchronously (top). **b)** Examples of fields of view, as the mean relative fluorescence during all stimulus frames of the movie (top). Segmented cells in green and glomeruli in yellow (bottom). Other coloured cells and glomeruli correspond respectively to example traces in a) and c). **c)** Example calcium traces of 3 glomeruli along with a recording subject to 4 odours stimuli, repeated randomly 5 times at each of the 6 increasing concentrations (dilution in oil x dilution in air). Bottom graph shows stimulations pulses with colours that correspond to the same odours as in a).

3.2.1 General overview of odourant-evoked calcium responses in PGC

I used *in vivo* 2-photon calcium imaging to record the changes in intracellular Ca^{2+} via the genetically encoded calcium indicator GCaMP6f

which was expressed in VGAT expressing cells. The figure 3.1 shows calcium traces of PGCs and the synchronous recording of the olfactometer final valve (Fig 3.1 A&C) and respiration (Fig 3.1 A). The figure 3.1 A displays traces of normalised fluorescence of calcium for 3 PGCs responding to 4 odours (2-Heptanone, Isobutyl propionate, Ethyl tiglate, Isoamyl acetate) depicted by the coloured pulses below. Respiration oscillations measured with a strain gauge (Fig 3.1 A) can be seen in the calcium traces. PGC timecourses were extracted from regions of interest (ROI) in calcium imaging movies (see methods, Fig 3.1 B). Each movie from an animal contained from 100 to 200 cells and 5 to 10 glomeruli. The figure 3.1 C shows 3 extracted glomeruli traces from the field of view in Fig 3.1 B that correspond to a full experiment subject to 4 randomised odours across 6 concentrations from a 3^{-5} to 10 % dilutions. Surprisingly, I observed not only glomeruli and cells that respond proportionally to the stimulus intensity but also some that respond inversely to the concentration (first trace on Fig 3.1 C). The two next traces are responding proportionally to the concentration. The purple trace is activated at the very first concentration and saturates quickly then starts to respond less on the last concentration. This might be due to the over-activation of neighbour PGCs which start to auto-inhibit. While the red and purple glomeruli show a tight tuning to a single odour as they show only 5 responses to the same odour in each concentration, the blue glomerulus is recruited by more odours as concentration increases until it responds to all 4 at 10% (Fig 3.1 C)

The figure 3.2 explains how odour-concentration averaged responses were extracted for a cell. To determine whether a PGC responds to an odour I averaged the 5 repetitions per concentration for each odour (Fig 3.2 A&B) and then calculated the signal-to-noise ratio (SNR) by calculating the mean response during stimulation, subtracting the mean during the 3 seconds preceding stimulation and dividing by the standard deviation of the 3 seconds baseline period (Fig 3.2C). To determine the SNR used to classify responses I performed the same SNR calculation on a region of baseline where there was no odour stimulus (Fig 3.2 C). I then took 40788 PGC and 2436 glomerulus odour stimuli recordings from all stimuli from 12 fasted animals, containing a total of 1619 cells and 105 glomeruli.

From this data set, I calculated the SNR threshold of acceptance that would result in a 0.001% false-positive rate of detecting a response (Fig. 3.2 D), with a receiver operating characteristic (ROC) analysis. The ROC establishes a trade-off between sensitivity and specificity and for this data set an SNR of 2 gave 6675 PGC responses and 1052 glomerulus responses. This threshold was used for all subsequent analyses.

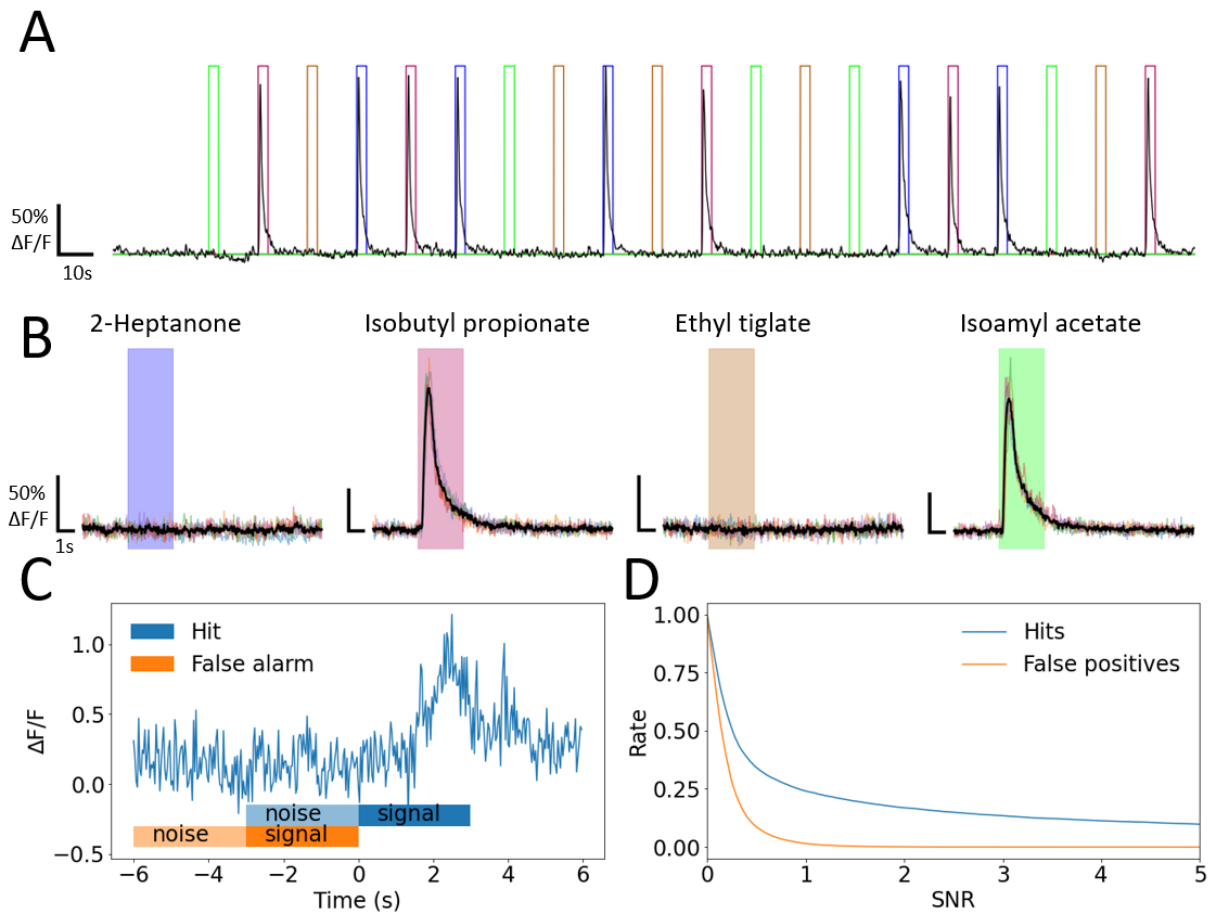


Figure 3.2 Parsing of odour-evoked responses. **a)** Example of a glomerulus relative fluorescence trace with 20 stimuli of pseudo-randomized odours at a dilution of 0.1%. Each colour pulse corresponds to an odour stimulus. **b)** Each bout of traces corresponding to a stimulus interval was parsed and shown overlaid in coloured traces for 2-heptanone, isobutyl propionate, ethyl tiglate and isoamyl acetate. Averaged response in black. Vertical band is odour onset. **c)** ROC analysis to determine the best signal-to-noise ratio that describes a true positive response by comparing 3 seconds of the signal with the 3 subsequent seconds. An example average response in blue, with the orange rectangle ranges, comparing the signal before odour onset ($t=0$) with prior noise shows a false alarm. With the blue rectangle ranges, the signal after odour onset is discernable from the prior noise. **d)** Analysis from the left box done on every trial-averaged responses. A threshold of 2 will give a false positive rate of 0.001.

These responses tell for which odour the cells/glomeruli are tuned. The calcium signal is a proxy for action potentials as each action potential evokes a fast-rising slow-decaying Ca^{2+} 'spike'. These Ca^{2+} spikes can overlap and summate. Therefore, the integral of the response will be proportional to the total spikes evoked by a stimulus. The intensity of the response is related to the area under the Ca^{2+} trace during odour stimulation. I used this area as a measurement for activity.

Furthermore, PGC responses are also composed of sub-threshold oscillatory activity, related to the breathing rhythm. The figure 3.3 A shows 2 responses from the same glomeruli to isobutyl propionate and ethyl tiglate with the synchronised respiration at the top. The oscillations in the calcium signals are a product of the mechano-sensitive properties of the OSN and are propagated in all neurons of the OB at the same frequency (Iwata et al., 2017). However, OB neurons can express a phase shift to the respiration cycle. The figure 3.3 B shows the overlaid respiration, where each peak in the black traces corresponds to the end of inhalation, and the calcium signal, during baseline and stimulation. That glomerulus showed different odour-dependent phase shifts during stimulation (Fig 3.3 B). The red isobutyl propionate curve rises at each inhalation as the purple ethyl tiglate curve rises later near the exhalation. This is an example of how PGCs/glomeruli encode odour signature in their odour-evoked responses through amplitude and phase shifts (Fig 3.2, Fig 3.3). Oscillations were not always visible (Fig 3.1A, Fig 3.3A baseline) in low SNR situations. The oscillations can be however magnified by averaging the signal over respiration cycles, as shown later in the chapter (Fig. 3.14).

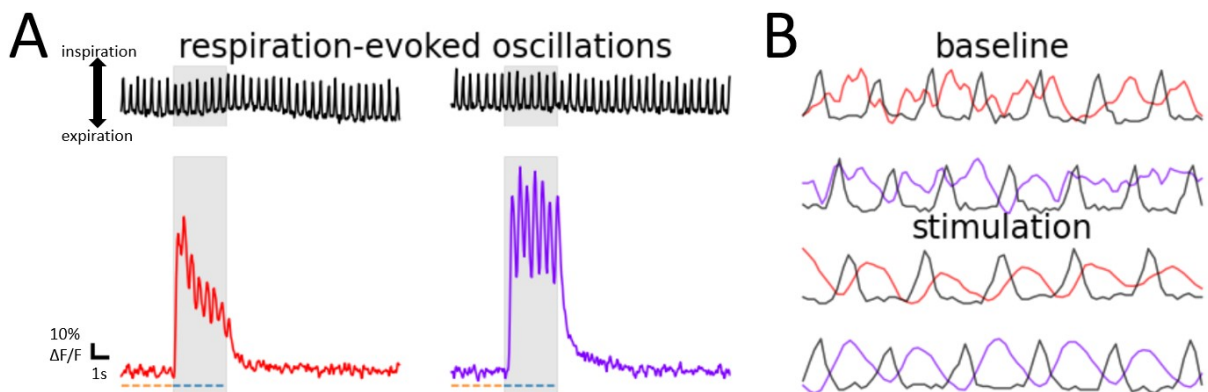


Figure 3.3 Respiration-evoked oscillations. Oscillations from the respiratory signal are reflected in PGCs calcium activity. This property is inherited from the mechano-sensitivity of OSNs that excite PGCs. **a)** Top: strain gauge resistance respiration recordings. Rising slopes correspond to inhalations. Bottom: odour-evoked responses to isobutyl propionate and ethyl tiglate, in a same glomerulus. **b)** Overlay of respiration (black) and calcium fluorescence (colour) traces. Baseline oscillation cycles are hardly visible due to low SNR. Cycles during stimuli show different shifts to the respiration onset, which is a feature of odour identity encoding. Top: baseline Parsed over the 3 seconds before stimulus onset (orange dotted line in a)). Bottom: Parsed over the stimulus onset (blue dotted lines in a)).

Odour-evoked activity in PGCs is therefore characterised by an intensity and a phase. The intensity was measured as the area under the curve of the calcium fluorescent signal during a stimulus. Phases were measured as an average phase across all responses to help with the low SNR of oscillations. Responses showed different shapes with the majority being a quick linear increase followed by an exponential decay. The next section covers the investigation of all these response dynamics and searches for any correlation with a concentration or an odour.

3.2.2 Characterisation of response dynamics

The PGCs odour-evoked responses displayed different dynamics (shapes) during and after stimulation (Fig 3.4). I used an unsupervised clustering algorithm to determine the types of response shape and their frequency. This will be used later to determine whether the response dynamic is related to the odour and/or concentration.

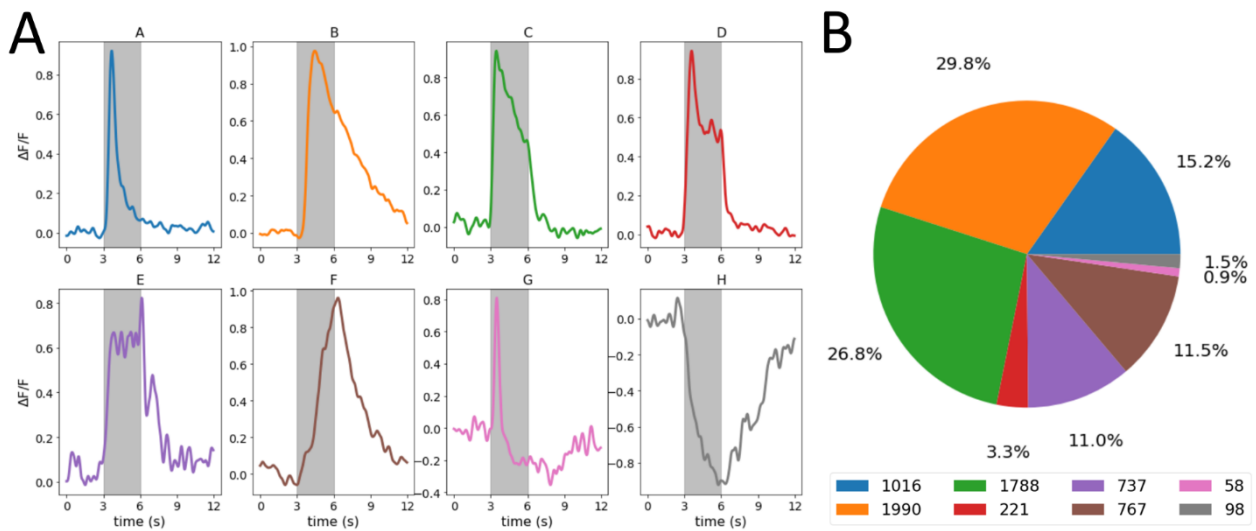


Figure 3.4 Clustering of odour-evoked PGC responses. Mean shift clustering done over 7727 responses (PGCs: 6675, glomeruli: 1052), odour-responses in 12 fasted animals resulted in 8 shape groups. **a)** Examples of calcium odour-responses for each group. Groups overlay as a spectrum, e.g. A switch to B with increase of input activity. Rarer G and H denote an inhibitory component. **b)** Groups repartition. The A/B/C clusters were the most observed.

To cluster the 7727 responses (PGCs: 6675, glomeruli: 1052), I first pre-processed them for better classification. The responses were normalised between -1 and 1 with the baseline at 0 and filtered with a rolling mean window of 200 ms. The 3 seconds during stimulation and 6 seconds after stimulation were resampled to 30 points. I then applied a mean shift algorithm from the python library sklearn with a bandwidth parameter estimated with a quantile of 0.001 to ensure disparity between groups. Mean shift was chosen for its characteristic of outputting groups of varying sizes. This resulted in 10 clusters. 3 of these clusters displayed similar fast peak shapes with different onset, which is explained by different times of inhalations after the odour valve opening. The 2 additional peak shape clusters were making only a few percent of the total. Merging these 3 short peak clusters, I ended up with 8 groups of response shapes (Fig 3.4 A, Fig 3.6 A).

The typical GCaMP calcium response pattern elicited by a single or few action potentials is formed by a quick rise followed by a slow decay (Fig 3.2 B & 3.4 A). This is the main transient shape of a response we observed, as shown by shapes A and B, and accounts for 45% of all responses (Fig 3.4 A). The B shape showed a continuous slow decay even after the offset of the odour stimulus (Fig 3.4 example B). The C shape is similar to the B shape except it decays rapidly at odour offset (Fig 3.4 example C). The F, G, H shapes may be subject to inhibitory inputs. In F, the late peak could be due to some delayed excitation while G and H clearly show a decrease in calcium activity.

The A, B, C shapes were the majority, accounting for 71.8% of the responses (Fig 3.4B). The square response E and late peak F (Fig 3.4 A) accounted for around 10% each. The square shape D made only 5% of the responses. Finally, the excitatory-inhibitory (G) and inhibitory (H) responses were very rare, accounting for 2.4% together (Fig 3.4 B). Sorting these shapes according to odours and concentrations can tell if they are expressed individually by a cell or do they evolve from one shape to another with stimulus intensity.

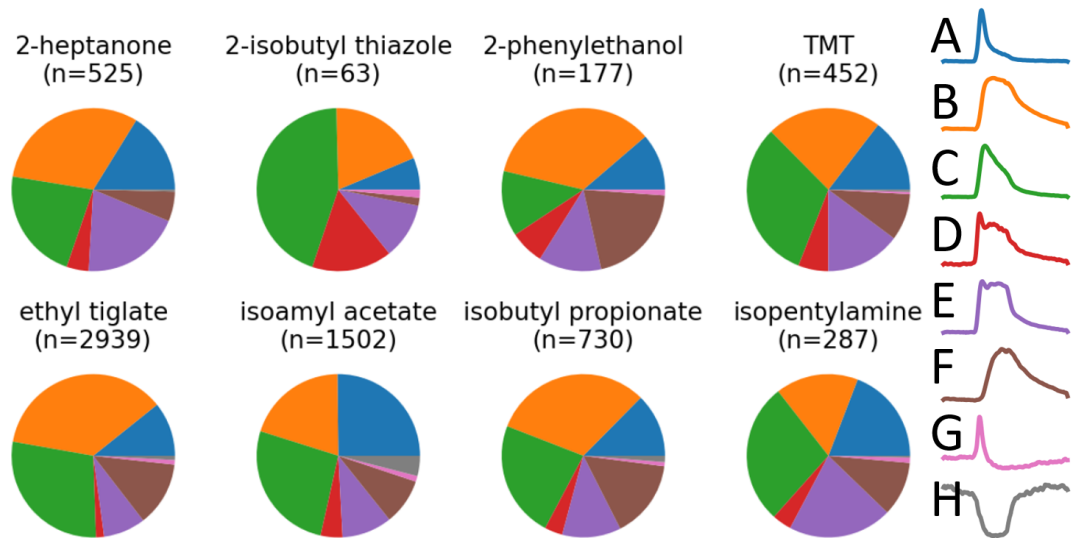


Figure 3.5 Repartition of shape clusters across odours. The repartition of response shapes across odours is heterogeneous with a predominance for A/B/C. Comparison is limited due to the disparity between the numbers of observations for each odour. Left: Pie representation of shape clusters by odours. Isoamyl acetate shows the highest proportion of inhibitory H but this is due to the relatively high number of responses to this odour. Although, the comparison is valid in regards to ethyl tiglate which odour-evoked responses amount in the same magnitude. Right: averaged responses as cartoon of different shape clusters.

The figure 3.5 shows how the shapes of response are spread across tested odours. The number of responses per odour varied largely. 2-isobutyl thiazole had only 63 responses while ethyl tiglate and isoamyl acetate had 2939 and 1502. Each odour elicited a heterogeneous set of responses clusters. The clusters A, B, C were dominant across all odours. The inhibitory response was found proportionally higher in isoamyl acetate. This might be due to the high number of isoamyl acetate responses detected. However, ethyl tiglate gave a comparable number of responses and no inhibitory responses. We cannot conclude that any shape is specific to an odour but would rather depend on the cells as the pie charts for each odour is likely to be composed of different cells.

To investigate any relation between response shape and concentration, I regrouped the responses from 1107 PGC-odour pairs in concentration sequences of activity (Fig 3.6 B & F). The activity was computed as the area under the curve during the 3s stimulation. The sequences ranged from 6 concentrations. The figure 3.6 B shows the sequences from 3 animals

where ethyl tiglate produced 3 and 5 activity-concentration points and isoamyl acetate a 4 points sequence. This variation comes as some odours only activated cells for a few concentrations as other odours activated the cells from the earliest concentration. The blue cell only responded to the 3 highest concentrations while the green cell responded to the 5 highest concentrations (Fig 3.6 B, left panel). The first concentration that elicited a response depends on the animal, cells sensitivity, and odour volatility. The major determinant will be the sensitivity of the OSNs giving the afferent input to the cell.

Therefore I standardised the concentrations relatively for each PGC-odour pair. The relative activations were enumerated from 1 to 6 relative to the concentration that gave the first response of the cell for an odour (Fig 3.6 B). Each consecutive relative activation corresponds to a jump of approximately one order of magnitude in concentrations (3^{-6} , 3^{-5} , 3^{-4} , 1^{-4} , 1^{-3} , 1^{-2} , 1^{-1} oil dilution x air dilution %) (Fig 3.6B, left panel). This approach accounts for differing sensitivity of the afferent inputs to different odours and allows a comparison of response dynamics corrected for the relative strength of activation (Fig 3.6 D).

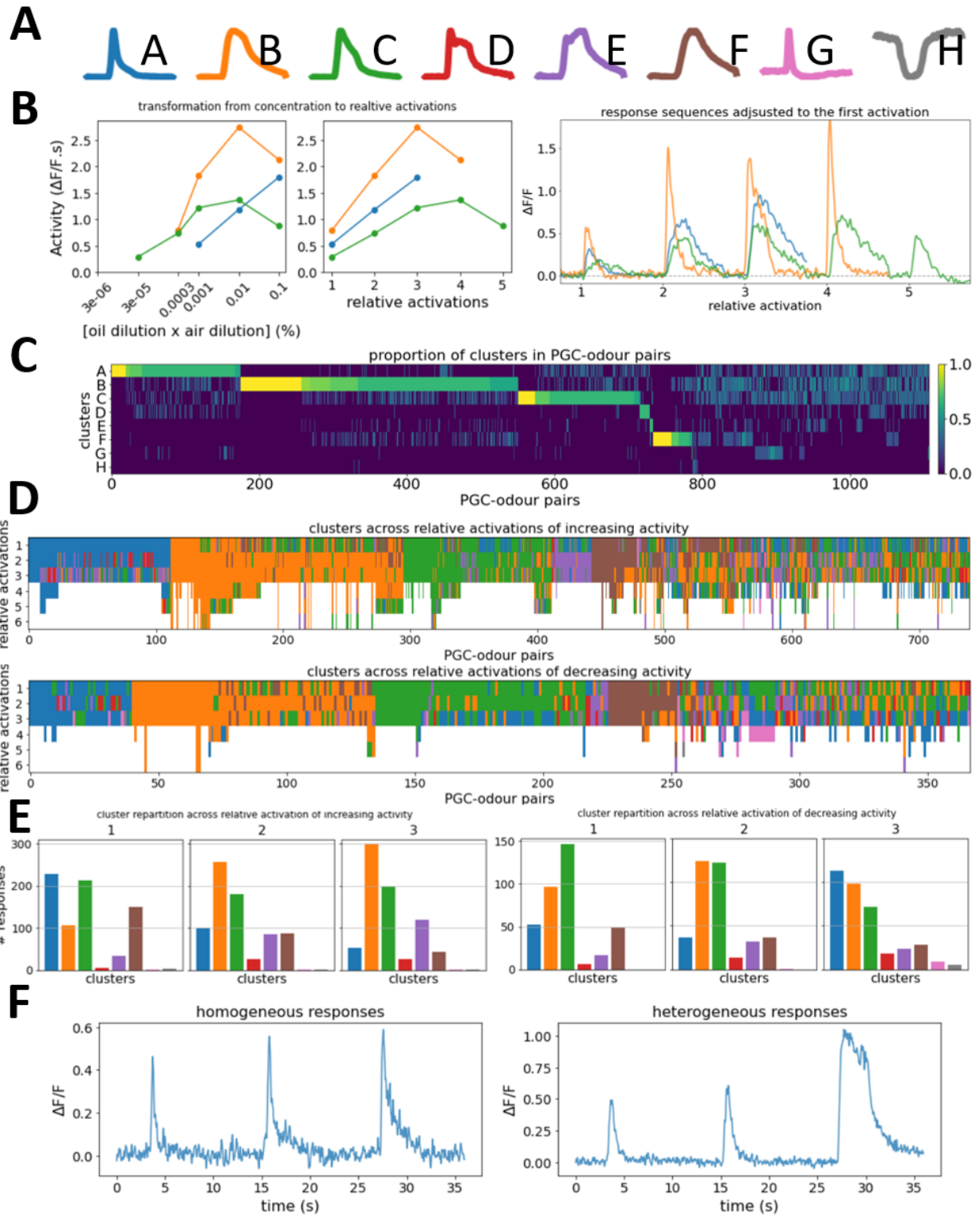


Figure 3.6 Repartition of shape clusters across relative activations.

Concentrations were transformed into relative activations starting at the first activation of the PGC to enable comparison across animals and odourants. The shapes appear to evolve on a continuous spectrum within a PGC-odour pair as concentration increases or decreases. **a)** Cartoon of response clusters found in (Fig 3.4). **b)** Transformations from dilution concentrations to relative activations for 3 PGC-odour pairs from 3 animals (blue: ethyl tiglate, orange: isoamyl acetate, green: ethyl tiglate). The relative activations grading permits the comparison of response shapes evolution between sequences, e.g. first activation of cells for different odours (left). Sequences of responses after transformation to relative activations (right). **c)** Proportion of shape appearing in each PGC-odour pair sequence. This array was sorted row by row until the proportion for the shape in a row reaches 50% (step-by-step sorting in appendix B) (n=1107 PGC-odour pairs). **d)** Shape across relative activations for each PGC-odour pairs colour-coded as A and sorted like C, for sequences increasing (top) and decreasing (bottom) activity with concentration. **e)** Distribution of shape in responses across the 3 first relative activations for increasing (left) and decreasing (right) response sequences. **f)** Examples of response sequences of a homogeneous set of shapes (A,A,A, left) and heterogeneous set of shapes (A,A,B, right).

Is the response shape a property of a cell or is it a property of stimulus strength? If it is a property of the cell the same response dynamic would be observed across different concentrations. To test this I first regrouped PGC-odour pairs by the criteria of the main shape they express, then observed if the shape changes with odour concentration and across odours the cell is responding to.

Figure 3.6 C shows the proportion of shapes in each PGC-odour responses sequences of relative activations. The array is composed of columns, each corresponding to a cell, in which each line gives the percentage of shape appearing in that cell response sequence, for example, the cell 1 here had 100% of response with a shape A. The initial array of the proportion of shapes per PGC-odour pair response sequences was sorted row by row, stopping when the shape cluster of that row appeared less than 50% in the response sequence then doing the next row on the left unsorted columns on the left to that stop column (see appendix B). Only clusters A, B, C, E, F appeared homogeneously in 140 sequences (A: 18, B: 53, C: 38, E: 2, F: 29) (Fig 3.6 E&F). However 737 sequences on 1107 have a majority of one type

of shape. This indicates that the shape of the response can change with relative activation within an odour-PGC pair.

Figure 3.6 D shows the shape clusters across relative activations for each PGC-odour pairs color-coded as the figure 3.6 A and sorted like the figure 3.6 C. It shows 4 main groups for the shapes A, B, C, E, F (blue, orange, green, purple, brown) and a group of mixed shapes. Figure 3.6 D concurs with the figure 3.6 C that the main shapes elicited in PGCs response sequences are A, B, and C. To better appreciate the transition between shapes, is the minimum response in the same shape if the response sequence decreases or increases? I separated the PGC-odour pairs according to their increase or decrease activity with concentrations (Fig 3.6 D). The shapes appeared to be on a continuum where the peak position and slope of decay move, as the strength of the stimulus increases. This can be seen in responses transitioning from one shape to another within a cell (Fig 3.6 D&F, Fig 3.7 A&B).

In the increasing sequences, the A group (blue) transits to the C (green) and D (red) shapes (Fig 3.6 D). In the same logic, the B group (orange) tends to switch from the C shape (Fig 3.6 D). Interestingly, in the decreasing response sequences, the A shape corresponds also to the lower activity coming from the C shape (Fig 3.6 D). This all shows that the shapes are on a continuum where the area under the curve decreases or increases with relative activation and that shape A correspond generally to lower activity.

In the increasing sequences, the shape A diminishes with relative activation in profit of B, D, E (Fig 3.6 E). This short peak A shape has a small area and relates a low activity. It is thus sensible that it appears earlier in relative activations. In the decreasing sequences, the A shape increases with relative activation while C decreases. For both increasing and decreasing sequences, the cluster F decreases. The excitatory-inhibitory G shape appears mainly in the pair that get inhibited with relative activation (Fig 3.7 B, Fig 3.6 E). I conclude that within a PGC-odour pair, elicited responses transit between shapes according to relative activation (Fig 3.6 F, Fig 3.7 A&B). Figure 3.6 F shows a homogeneous sequence of shapes A for ethyl tiglate and a heterogeneous sequence that transits from A to B for isobutyl propionate. However, it has to be taken into account that the shape clusters

are not purely distinct and a response can be miscategorised if ambiguous, like the shapes B and E. The apparent mixture in the four first groups (Fig 3.6 C&D) is partly due to the shapes belonging in-between two clusters.

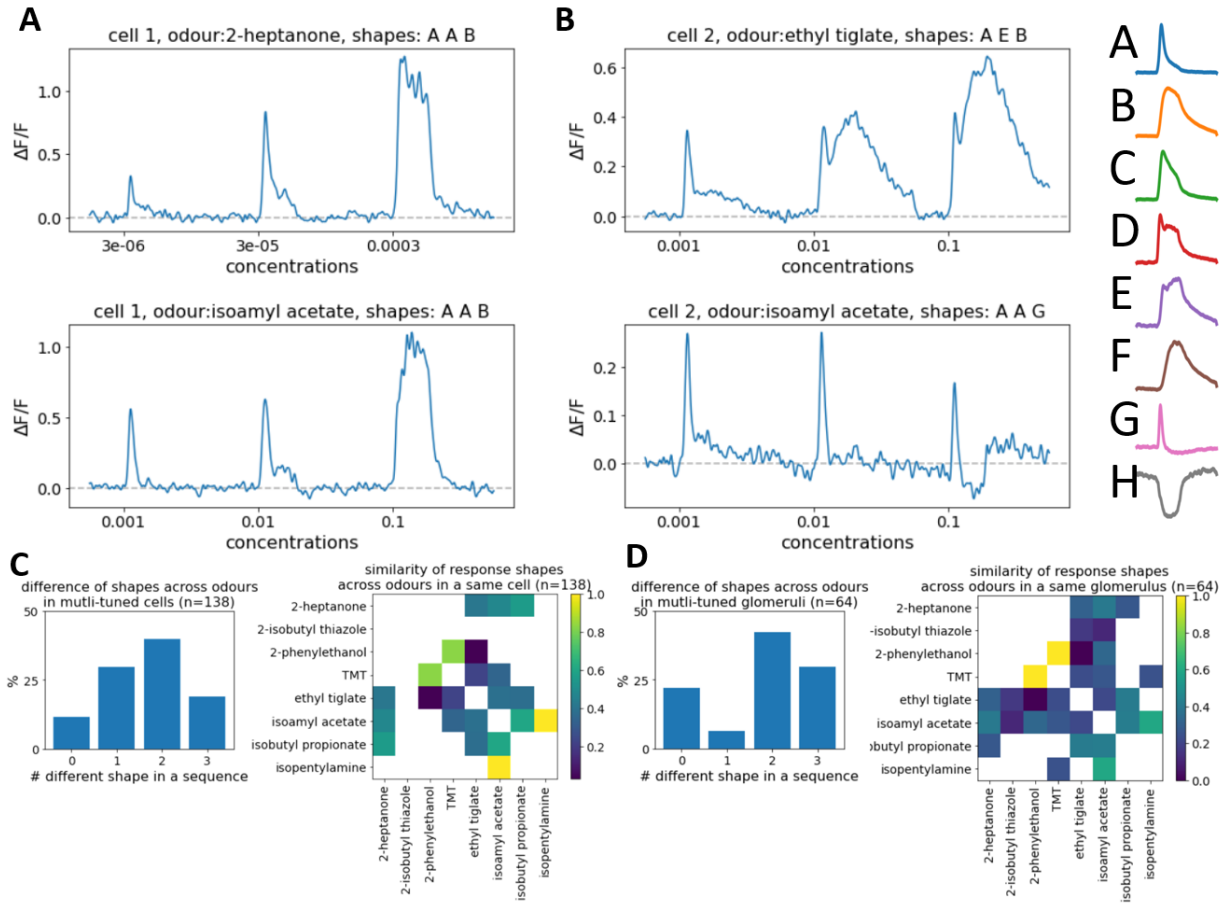


Figure 3.7 Repartition of shape clusters across odour in the same cell or glomerulus. The shapes of responses change not only with concentration but also with odours within a cell or a glomerulus. **a)** Example of a cell with an identical sequence of shapes for the 3 first relative activations to 2-heptanone (A,A,B) and isoamyl acetate (A,A,B). **b)** Example of a cell with a different sequence of shapes for the 3 first relative activations to ethyl tiglate (A,E,B) and isoamyl acetate (A,A,G). **c)** Distribution of the number of different shapes in the 3 first relative activations amongst 138 PGC-odour that are tuned to multiple odours (left). Array showing which pairs of odours elicited the same response shapes in PGCs (right) **d)** Distribution of the number of different shapes in the 3 first relative activations amongst 64 glomerulus-odour that are tuned to multiple odours (left). Array showing which pairs of odours elicited the same response shapes in glomeruli (right). Colourbars give the similarity (1: all shapes the same, 0: all different).

In figure 3.7, I investigated if, within a PGC, the patterns would change across odours. Figure 3.7 A shows a PGC that enacts the same response shapes for 2-heptanone and isoamyl acetate while the figure 3.7 B shows a cell that has different patterns for ethyl tiglate and isoamyl acetate. In cell 2, where the amplitude of the response is increasing for ethyl tiglate and decreasing for isoamyl acetate, the response shapes changes with these odours from A,E,B to A,A,G (Fig 3.7B). This means that the cell 2 might be involved in two separate circuits depending on the odour, and maybe receive inputs from two different glomeruli. I next regrouped PGC and glomeruli in the next section to address this question. So far, in the 138 PGC-odour pairs that are tuned for more than one odour, only a small fraction keeps the same response shapes during the 3 first activations (Fig 3.7 C left). To know which odour is more likely to activate cells with different patterns, I calculated the similarity of patterns as $1 - \text{the normalised average difference of shapes for the 3 first relative activations}$ (Fig 3.7 C right), that is to say, for each cell tuned for 2 odours, the similarity of patterns is 0 if no responses shapes are the same, $1/3$, if one is, $2/3$, if two are, and 1 if all 3 first responses in both odours have the same shape. The cells tuned for 2-phenylethanol and ethyl tiglate tend to express different patterns, as cells tuned for isoamyl acetate and isopentylamine are more likely to express the same patterns. Figure 3.7 D shows that glomeruli are either keeping the same patterns between odours around 25%, or are changing much of them. The similarity of response shapes across odours in the same glomerulus remained comparatively the same as in PGCs (Fig 3.7 C right, Fig 3.7 D right). Furthermore, glomeruli are more broadly tuned than the PGCs which may corroborate their closer position to the afference than the somata.

It remains intriguing if the similarity or dissimilarity of response shapes within the same cell is explained by connectivity to multiple glomeruli or just a glomerulus that also expresses different shapes. Therefore, I regrouped the PGCs and glomeruli to infer mono and multi-glomerular inputs to a PGC.

3.2.3 Estimating connectivity between PGCs and glomeruli

Some PGCs seem to maintain the same response shape across concentrations, maybe due to their intrinsic properties, while others seem to change their dynamics with increasing concentration. As concentration

increases more glomeruli become activated. This makes it possible that PGCs that change their shape with concentration are receiving input from other glomeruli. To examine this I had to infer which PGCs are connected to which glomeruli.

Glomeruli are spherical structures composed of intertwined dendrites of interneurons and TC/MTCs where afferent OSN axons form synapses. They are the point of connections between afference and the PGCs. A glomerulus and all the PGCs that innervate it can be made as a glomerulus-mother PGC-daughters group. Regrouping PGCs and glomeruli will help to tell about the multiplicity or uniqueness of afference to a PGC. To make the groups, I used the criteria that the PGCs and glomeruli must be tuned for at least one same odour and be within a short distance from each other. Then in these pre-groups, I looked at the similarity of shapes in the PGC-odours pairs and glomeruli-odour pairs (Fig 3.8 A). This estimated the likelihood for PGC-odour sequences to be originating from one or multiple glomeruli. The rationale for making the groups is to inspect the characteristics such as sensitivity, dynamic range, or phase in a family of PGC daughters and see if they all inherit properties from the glomerulus mother. This section will investigate the glomerulus-PGC relations with the point of view of glomeruli as a proxy for the averaged dendritic input, driven by OSNs and ETCs.

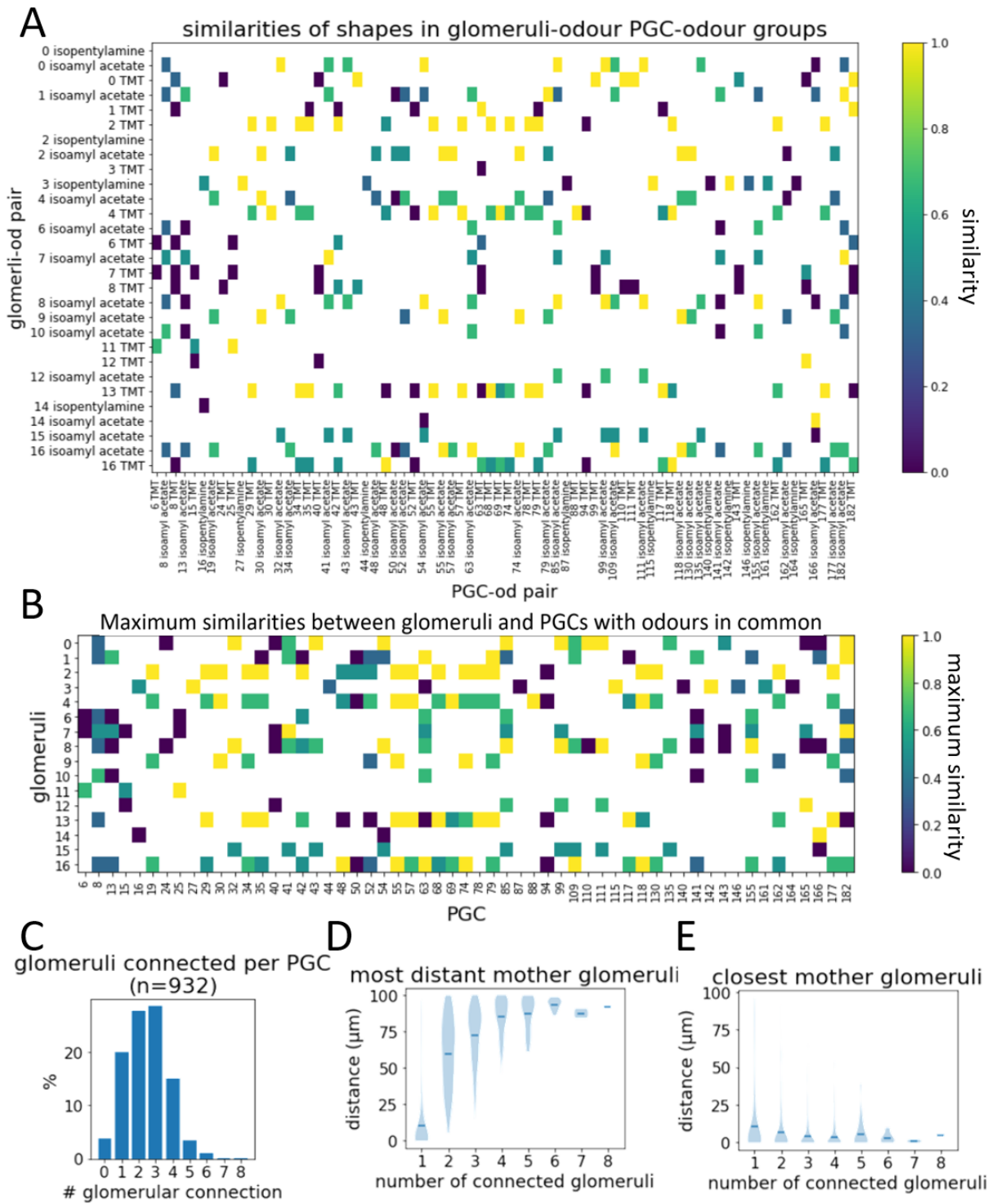


Figure 3.8 Glomeruli-PGC connectivity. Glomerulus-PGCs groups were estimated under the assumptions that the glomerulus mother and PGC daughter are: tuned for at least one same odour, distanced by less than 100µm, and have at least one response of the same shape for an odour in common. **a)** Similarity of shapes in the response sequences between the PGC-odours pairs and glomeruli-odour pairs. The colour indicates the similarity between shapes in responses sequences (1 means all the same shapes in the relative activations response between glomerulus and PGC, 0 means none). Blank pixels correspond to cases without the distance or odour-tuning verified. **b)** For a couple of glomerulus-PGC, the maximum of their odour responses shapes similarity (A) is used as a metric of the likelihood of connection. **c)** Distribution of the number of connected glomeruli per PGC (12 animals). A connection is established if the maximum similarity > 0. **d)** Distance to the most distant glomerulus against the number of connections made by PGCs **e)** Distance to the closest glomerulus against the number of connections made by PGCs.

I used 3 criteria to estimate the likelihood of a connection between a glomerulus and a PGC: 1) Distance, a PGC soma located on the edge of a glomerulus is likely to receive input from that glomerulus. I set a maximum distance of 100µm between a PGC soma and the edge of the glomerulus. 2) Odour tuning, the cell and glomeruli had to be responding to the same odour. 3) Response dynamics, the cell and glomerulus response shapes were taken into account, as a PGC is more likely to belong to a glomerulus if they exert the same patterns of activity. The similarity of the shapes within the first relative activations to an odour, at the same concentrations, between cells and glomeruli were computed (Fig 3.8 A) as follows for an odour o :

$$Similarity_{c,g,o} = \frac{\sum_i^{responses} (1 \text{ if } shape_{c,o}^i = shape_{g,o}^i \text{ else } 0)}{\sum_i^{responses} 1}$$

Where $Similarity_{c,g,o}$ is the similarity of response dynamics between the cell c and the glomerulus g for the odour o , $shape_{c,o}^i$ the shape category of i -th response of the cell c to the odour o , and $shape_{g,o}^i$ the shape category of i -th response to the odour o of the glomerulus g . A cell and a glomerulus are thus considered similar in response dynamics proportionally to the number of their responses that belong to the same shape cluster, 0 if all shapes are dissimilar, and up to 1 if all their responses share the same shape. This similarity formed a likelihood of connectivity between glomerulus-odour and PGC-odour pairs (Fig 3.8 A).

As this previous metric only worked with glomerulus-odour and PGC-odour pairs, I needed to reduce it to a metric between glomeruli and PGCs as the physical connections are between them and not abstract component-odour pairs. I inferred connectivity based on these reduced glomerulus-PGC similarities, defined as follows:

$$Similarity_{c,g} = \max_{odours\ o} Similarity_{c,g,o}$$

Figure 3.8 B thus compresses the component-odour pairs using the maximum of similarities from the glomerulus-PGC nodes (pixels belonging to the same glomerulus and cell) in figure 3.8 A. A node is the similarities for all odours between a glomerulus and a cell, for example, the intersections of the lines 2 and 3 with the 2 last columns of the figure 3.8 A correspond to the node between the glomerulus 0 (y-axis) and cell 182 (x-axis). Finally, The connection weight of a glomerulus-PGC is as strong as the most similar odour responses they share (Fig 3.8 B). A connection was counted for the rest of the analysis if the similarity was above 0, equivalent to at least one similar shape for a same odour between a glomerulus and a cell.

Based on those 3 criteria – distance, odour tuning, and response dynamics, the number of connected glomerulus per PGC was inferred for 932 PGCs (Fig 3.8 C). The number of connections per PGC ranged up to 8 with an average of 2.47. That fits the known view that PGCs form connections from one to multiple glomeruli and subdivide into as many as 4 subtypes (Tavakoli et al., 2018; Kosaka et al., 2019; Kiyokage et al, 2010; Bywalez 2017). Following Tavakoli et al. (2018) categories (Table 1.2), I can infer that 19.9 % of observed PGCs could be Microglomerular (1 glomerulus), 76.2 % Uniglomerular (1-3 glomeruli), 75.8 % Oligoglomerular (2–6 glomeruli), 0.3 % Polyglomerular (≥ 7 glomeruli) (Fig 3.8 C). 3.8 % of cells were not allocated to any glomerulus.

They may be either not connected to any glomeruli in the field of view or differing too much from glomeruli because their signal reflected other neural sources. It is complicated to discern between subtypes based on connectivity alone because these connection criteria overlap. As expected, the distance to the most distant glomerulus increase with the number of connection (Fig 3.8 D). The closest glomeruli are always within 25 μ m independently of the number

of connections (Fig 3.8 E). With all these connections, do PGCs reflect the multiple glomeruli they connected to in these groups?

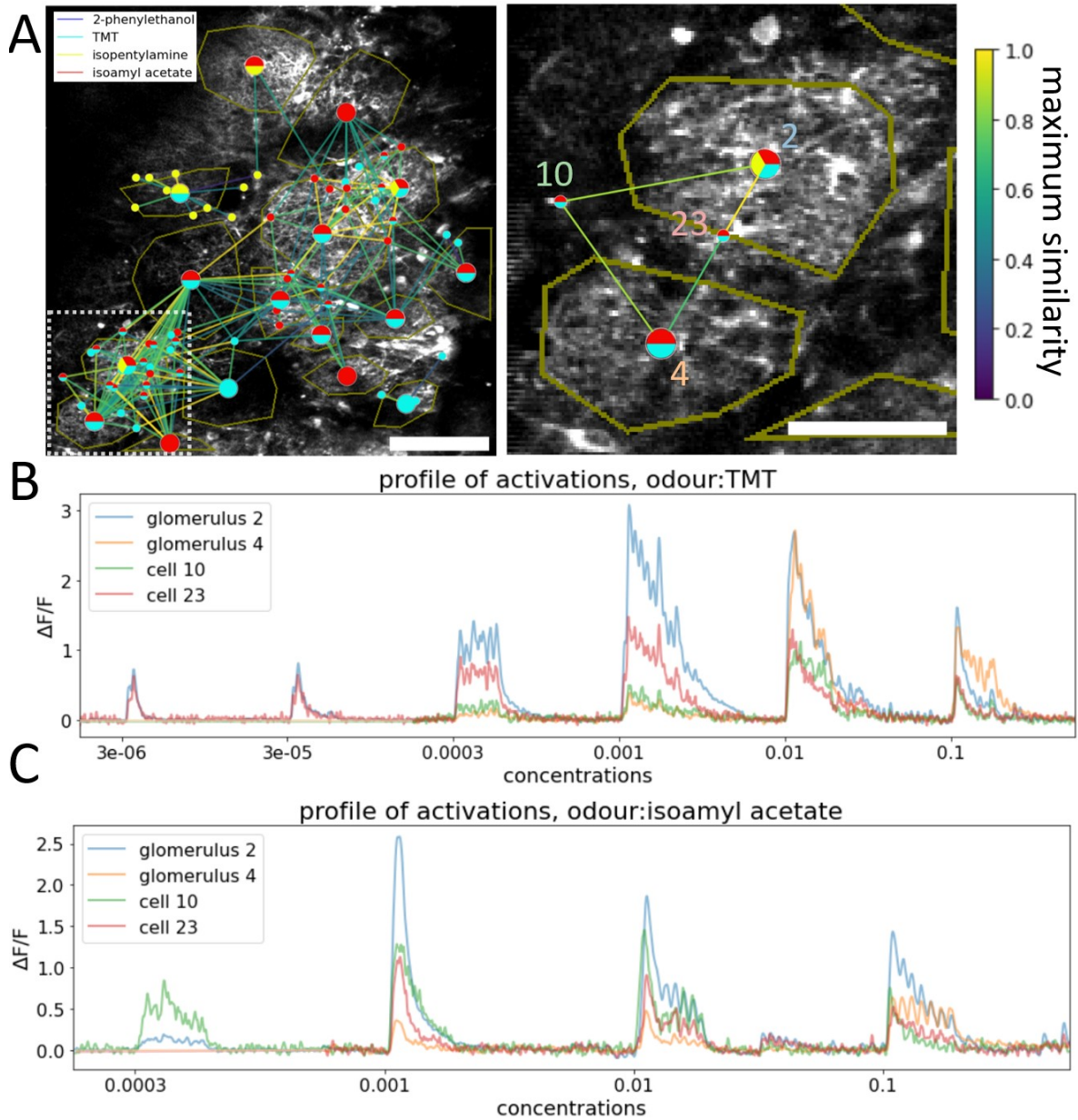


Figure 3.9 Comparison of response sequences within glomerulus-PGCs groups. PGCs connected to multiple glomeruli inherit similar shapes of odour-evoked responses. Connections were assumed if similarity > 0. **a)** Field of view. Maximum projection of all the frames when stimulation occurred. The large coloured circles represent the center of glomeruli, the small ones, PGCs. The colours in the pie describe which odours the PGC/glomerulus is responding to. The lines denote the PGC-glomerulus connections with a color based on the maximum similarity of responses shapes. Scale bar: 100 μm (left), 50 μm (right). **b)** Sequence of responses from the connected cells and glomeruli from the right panel in A, for the odour TMT.

Multi-connected PGCs follow their parent glomeruli in their calcium odour-evoked traces (Fig 3.9). On the left, figure 3.9A displays glomerulus-PGC groups corresponding to the figure 3.8 B. Each pie indicates the odour tuning of the component, as it had to respond to at least one concentration per odour. The connecting lines, with the colour representing $Similarity_{c,g}$, between glomeruli mother and PGCs based on previous calculations and corresponding colours (Fig 3.8 B). I show an example of two PGCs (10 and 23), both tuned for TMT and isoamyl acetate, with putative connections to two glomeruli (Fig 3.9 A, right). It appears cell 10 would be equivalently connected to glomeruli 2 and 4 as cell 23 would be more connected to glomerulus 2. In the figures 3.9 B&C) are overlaid the response sequence for two cells and glomeruli. It seems the cells (red and green) respond to both odour with a same dynamic as the glomeruli. However the two glomeruli (blue and yellow) start to diverge in their shape at the highest concentration (0.1 %) for both TMT and isoamyl acetate (Fig 3.9 B&C). This foretells more complex interglomerular interactions occur in the glomerular circuits at higher concentrations. PGC-PGC inhibition occurs at higher concentrations via gabaergic spillover (Murphy et al, 2005). This inhibition could be furthermore increased by the activation of mGluR(II) at higher concentrations (Zak et Schoppa, 2021). It is interesting to notice the two cells kept however a shared dynamic. This overall encourages validating my model of glomerulus-PGC groups.

To argue the validity of these groups and the assumption that the glomeruli can be seen as a proxy for the dendritic inputs, I asserted how much the glomerular responses were reflected in the PGC daughters during the first 3 relative activations (Fig 3.10), where saturating effects are less likely, e.g. the mGluR(II) and GABA spillover mentioned earlier. I represent two groups examples denoted as before (Fig 3.10 A) of two glomeruli, glomerulus 3 mainly tuned for isopentylamine and glomerulus 7 mainly tuned for isoamyl acetate. The spatial distribution of PGCs daughters around these glomeruli appears to be localised in the field of view (Fig 3.10 A). Figure 3.10 B shows the glomeruli response sequences in red, with the average of PGCs in black and individual PGCs in transparent colours. The glomerulus and PGC average traces overlay almost perfectly which means that the glomerulus can properly

reflect the average activity of PGCs. This is expected as the glomeruli are nothing but the sums of all the dendrites of PGCs daughters. Furthermore, across all the 220 groups in the 12 fasted animals datasets, the first 3 activations of the average of daughter cells are correlated with their glomerulus which validates the glomerulus as a source signal for PGCs (Fig 3.10 C).

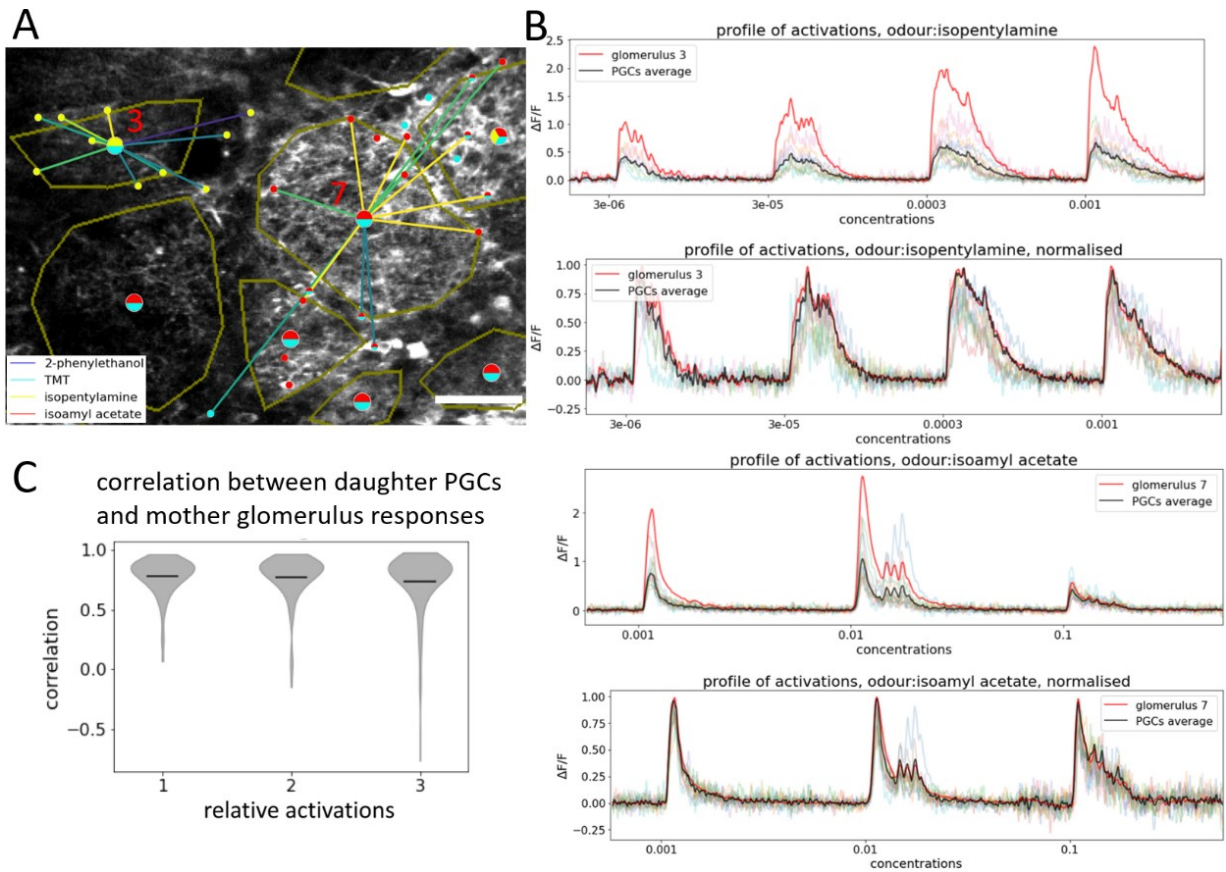


Figure 3.10 Glomeruli are the input sources to PGCs. The glomeruli are formed of dendrites of all the PGCs that innerve it and therefore express a fluorescent signal that reflects the average of the dendrites of PGC daughters. **a)** Field of view. Maximum projection of all the frames when stimulation occurred. The large coloured circles represent the center of glomeruli, the small ones, PGCs. The colours in the pie describe which odours the PGC/glomerulus is responding to. The lines denote the PGC-glomerulus connections with a colour based on the maximum similarity of responses shapes. Scale bar: 50 μm . **b)** Comparison of the sequences of odour-evoked responses of a glomerulus (red) and its PGC daughters (colours, average in black), for the group 3 with the odour isopentylamine (top) and the group 7 with odour isoamyl acetate (bottom). Normalised figures show the average of PGC shapes overlays with the glomerulus shapes. **c)** Coefficients of correlation between the averaged response of daughters PGCs and their mother glomerulus, for the first 3 activations ($n= 220$ glomerulus-PGCs groups, from 12 animals). Bars are means.

Now that groups are attested, I can look at the properties within these groups and how the PGCs properties differ from their parent glomeruli properties and also between PGCs within a same group. I showed that PGCs can be regrouped in one to multiple overlapping ensembles of glomerulus-PGCs based on distance, similarity of response shape, and odour tuning. I found PGCs making from 1 to 8 glomerular connections and responding from 1 to 4 odours. Computation-wise, monoglomerular PGCs are likely involved in contrast enhancement via feedback inhibition onto OSN axons. The multi-glomerular PGCs can be involved in more complex computations such as normalisation, taking into account broadly spread glomeruli for attenuating afferent signals on a larger scale. To further describe the relation between glomeruli and PGCs, I investigated odour-wise how the sensitivity, dynamic range, and phase shifts across PGCs sharing a same glomerulus are linked. PGCs and glomeruli activity can be characterised by dose-response curves from which I inferred metrics. Comparing these metrics in PGCs and mother glomeruli will provide insight into the heterogeneous or homogeneous inhibitory action of the PGC on the afferent signal.

3.2.4 Sensitivity of PGCs connected to a same glomerulus

OSN with the same receptor type is theorised to express different sensitivity (EC_{50}) to a same odourant (Cleland et al.,2012). These putative

variations in sensitivity in the afference lead to ask how different PGC sensitivity may arise due to differences in the synaptic weight they receive from the OSN, in addition to their intrinsic excitability. PGCs closely match the activations of these afferent axons, as they must provide feedback inhibition, while MTC/TC cannot be directly accounted for the dynamic of the sensory input (Short and Wachowiak, 2019). Therefore, the dose-response curves of PGCs may reflect the OSN curves. It is however unknown if all the PGCs innervated by a glomerulus work in unison or if their activation curve spread within a group to reflect the same spread of OSN sensitivities. Are the PGCs recruited simultaneously as soon as the glomerulus receives input or are they activated in different steps? That is to say, are the “same-glomerulus-odour” PGC sensitivities the same? To investigate this, I fitted the Hill equation to the dose-response curve of PGCs within glomerulus-PGC groups and observed the variation of their activation characteristics.

I used the Hill equation as a model to characterise the odour-activation of PGCs. The Hill equation defines traditionally the ligand binding to a molecule concentration but also characterises drug dose-sensory effect. The Hill equation is described by:

$$E = \frac{E_{max}}{1 + \left(\frac{EC_{50}}{[A]}\right)^n}$$

Where E is the response intensity of the effect of a dose of concentration $[A]$, E_{max} the maximum measured intensity, EC_{50} the dose that produces 50% of maximum response, $[A]$ the dose concentration and n the Hill coefficient.

I used this equation for the odourant activation of PGCs. E was considered as the odour-evoked activity and defined as the area under the calcium curve during stimulation. E_{max} denotes the maximum response elicited amongst concentrations. The dose $[A]$ was the odourant concentration presented to the animal. I used EC_{50} as a way to measure odour sensitivity. EC_{50} , the concentration that causes half of the maximum response, gives a qualitative idea of sensitivity as it relates to the point in the Hill function where the dosage starts to give a substantially bigger response. For better representation, I used the \log_{10} of EC_{50} as it ranges across multiple

magnitudes of concentrations. Comparing $EC_{50}s$ permits to determine how much PGCs spread their sensitivity in comparison to their connected glomerulus. There is an antagonism effect in case of a shift to the right, to higher concentrations, and a synergic effect to the left, to lower concentrations. The former implies inhibition amongst PGCs, the latter some sort of boosting synchronisation in the circuits at earlier concentration. The Hill coefficient n provides the steepness of the concentration-activity curve and inference of the dynamic range, which is the range of concentrations for which the cell/glomerulus starts responding to the point the response saturates. n is inversely proportional to the dynamic range, as high n values give a steeper slope. The dynamic range tells how much the PGCs can discern between concentrations.

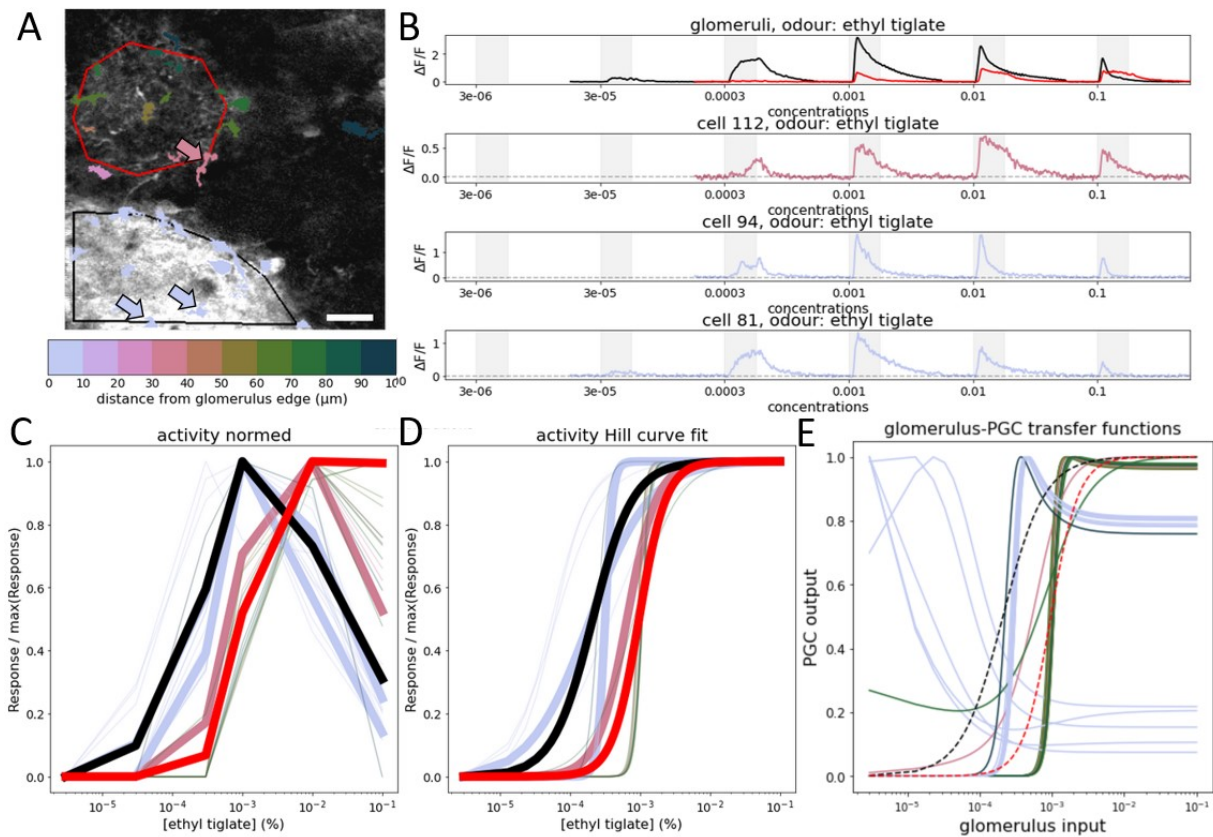


Figure 3.11 Sensitivity variation within glomerulus-PGC groups. Activity against concentrations varies between PGCs, but their activation profiles remain close to the nearest glomerulus. Sensitivity, approximated by the EC_{50} , of daughter PGCs straddles the glomerulus mother sensitivity. **a)** Maximum projection of all the frames when stimulation occurred. Two examples glomeruli (black and red). The PGCs belonging to the black glomerulus are coloured according to the distance to the glomerulus edge. All colours in A correspond in B, C, D and E. Scale bar: $25\mu\text{m}$ **b)** Sequences of responses evoked by ethyl tiglate in 2 glomeruli (first row) and 3 cells belonging to the black glomerulus. **c)** Activity, as the integral of the calcium trace during odour stimulation (grey rectangle in B), plotted against concentration (% in oil x % in air) **d)** Fitting a Hill function permits to transform discrete dosage-response curves from C into continuous curves, and extract the EC_{50} parameters for each curve. **e)** The transfer functions, or input-output functions, are the PGC activation curves divided by their glomerulus parent (black).

I first took only the components that showed an increase of activity with concentrations to have a positive slope (Fig 3.6 D). The measurements of sensitivity only make sense with increasing responses to concentrations. I gathered the responses sequence of 1860 PGC-odour and 153 glomerulus-odour pairs. Then I fitted the normalised concentrations-activity points of the

PGCs and glomeruli to the Hill equation using the python function `curve_fit` from the library `scipy` (Fig 3.11 C&D). To avoid aberrant values due to overfitting, as some sequences only have 3 points, I had to constraint the range of values for the Hill coefficient n from 1 to 15 and EC_{50} values from $1e-6$ to 0.1 as it is the range of concentrations used during the experiments. These boundary values were justified as they minimised the error of fitting (r-squared value) (see appendix C). Furthermore, some response curves decreased their activity after reaching a maximum (Fig 3.11 B&C, Fig 3.10 B, Fig 3.6 B). The increased concentration-dependent activity may induce self-inhibition of PGC via GABA spill-over or PGC-PGC inhibition via lateral neighbour inhibition (Murphy et al., 2005). Therefore, E_{max} was set to the maximum of the response curve. The histograms for n , EC_{50} and E_{max} of the 1860 PGCs fitted Hill curves and 158 glomeruli fitted Hill curves are shown in appendix C. The histograms had similar distributions for PGCs and glomeruli.

The hill equation permits the comparison of the concentration-dependent activation patterns to an odour across PGCs and glomeruli (Fig 3.11 D). The comparison of sensitivity and dynamic range was made within glomerulus-odour groups and its daughter PGC-odours pairs (Fig 3.11 A). The colour scheme specifies the distance to the edge of the glomerulus with the PGCs situated inside the glomerulus considered at a distance 0. Figure 3.11 B shows the responses sequences of the glomerulus in black and its daughter PGCs to ethyl tiglate from a concentration of 3×10^{-5} to 10 % dilution in oil x dilution in air. The neighbour glomerulus was depicted in red. The close PGCs tend to follow the trend of their mother glomerulus more (Fig 3.11 C, thick blue line) as the one situated further acts more similarly to the neighbour glomerulus (Fig 3.11 C, thick pink line).

The PGC daughters express different patterns of evoked activity that start to respond at different concentrations than the mother glomerulus (Fig 3.11 B). However, The PGCs activity curves seem close to the glomerulus one (Fig 3.11 C, D). PGCs situated between two glomeruli shows a sensitivity between the two glomeruli sensitivity (Fig 3.11 D, thick pink line). The activation properties of PGC daughters are therefore comparable to their mother glomeruli. I next constructed transfer functions to describe the input/output transformation of PGCs (Fig 5.11 E). I used the assumption of the

average glomerular activity being equivalent to the dendritic input to PGCs. The transfer function is then the PGC activation curve divided by the 'dendritic input', that is to say, the mother glomerulus activation curve. The dendritic input encompass ET and OSN drives. Figure 3.11 E shows different PGC dynamics in relation to concentration. This remains qualitative as the amplitudes of PGCs and glomeruli cannot be compared because the dendritic glomerular fluorescent signal is stronger due to higher Ca^{2+} concentrations achieved in the dendrites with a larger surface-area-to-volume ratio than the soma. There are 3 dynamics at play here: some cells display a decreasing transfer function, they are activated before the glomerulus and their gain falls as the glomerulus is more activated. Other cells have an input-output dynamic following the sigmoid of the activation curve of the glomerulus (Fig 3.11 E, black dotted line). Finally, we can observe a subset activated around the glomerulus EC_{50} which then decreases when the glomerulus activity plateau. This shows again that at higher concentrations, a self-inhibition phenomenon amongst the PGCs occurs, as described previously in acute slices (Murphy et al, 2005). Overall, PGC odour-evoked activation seems to either follow the activation of the glomerulus parent, follow but then receive inhibition at higher concentration, or globally decrease as the glomerulus activates.

Within the 153 glomeruli-odour groups, the odour-evoked activation characteristics of the PGCs varied (Fig 3.12 A&B). I looked at the glomerulus-normalised sensitivities, $EC_{50}/EC_{50\text{ glomerulus}}$, the dynamic ranges given by the relative Hill coefficients $n/n_{\text{glomerulus}}$, and the gains $E_{max}/E_{max\text{ glomerulus}}$ to tell how much the PGCs diverge in these properties from their common afference (Fig 3.12 A). The sensitivity of the PGCs is distributed around the glomerulus value (mean=1.06, stdev.=0.41) (Fig 3.12 A1) which means PGCs on average have the same EC_{50} as their parent. The PGC Hill coefficients were from 10 times smaller to 10 times bigger than the mother glomerulus coefficients with a majority of coefficients higher in PGC than in the glomerulus (mean=2.54, IQR = 0.91, 3.67) (Fig 3.12 A2). This means the PGCs have a steeper activation curve and a shorter activation range than the glomerulus.

PGCs have a limited dynamic range constrained by their membrane properties, i.e their ion channel repertoire (both ligand and voltage-gated), whereas the dendritic input, the glomerulus, is partly the pooled signal of

~5000 OSN which are thought to have varying sensitivities (Cleland et al., 2012). Therefore, PGCs are limited to steeper activation curves but their sensitivities span broader than the afferent input so at higher concentrations more PG cells will be active. Therefore, as PGCs are more active, GABA spillover is more likely, but only a subset of PGCs are affected by the presumed spillover or more generally speaking “a gain reduction” at higher concentrations.

However, comparing maximum amplitudes between PGCs and glomeruli to evaluate the input-output gain is not adequate because of their difference in calcium fluorescence intensity (Fig 3.12 A3). If the fluorescence intensities were comparable, these measurements would show an amplification in the PGCs stomata activity compared to the input dendritic activity (mean=4.03, stdev.=5.94).

I used the coefficients of variation to characterise the spread of the sensitivity, range, and gain within all glomerulus-PGCs-odour groups across animals (Fig 3.12 B). Each circle tells the animal identity by its colour and the radius reflects the size of the group. The sensitivity and gain diverged less than one standard deviation while the Hill coefficient shows the most divergence. This tells the grouped PGCs do not vary much in their sensitivity and gain. The spread in the Hill coefficient, which is inversely proportional to the dynamic range, allows for greater contrast in grades of activations and foretells an ability to play a diversity of computational functions. In the case of contrast enhancement, an elongated range of activation would enable the PGCs to provide feedback inhibition earlier in concentrations and therefore attenuate low-intensity stimuli while letting pass higher intensities (Fig 1.7).

Figure 3.12 C represents the same data as in the figure 3.12 A plotted against the distance to the edge of the glomerulus. They all show a shallow slope and low regression coefficient (sensitivity: reg. coef.=0.09, p-val.=9.71e-5; range: reg. coef.=0.11, p-val.=1.09e-6; gain: reg. coef.=0.23, p-val.=3.69e-24), indicating that proximity to a parent glomerulus was not correlated with having a similar EC_{50} . The normalised range and gain showed the most change with distance respectively changing mean values from 2.18 to 3.12 and 2.42 to 6.57 in the linear regression. These distance-dependent variations

might relate to the involvement of connection to multiple glomeruli, like the subtypes of PGCs situated further away, namely oligoglomerular cells (OGC) and polyglomerular cells (POGC) aka short-axon cells (SA) (Table 1.2).

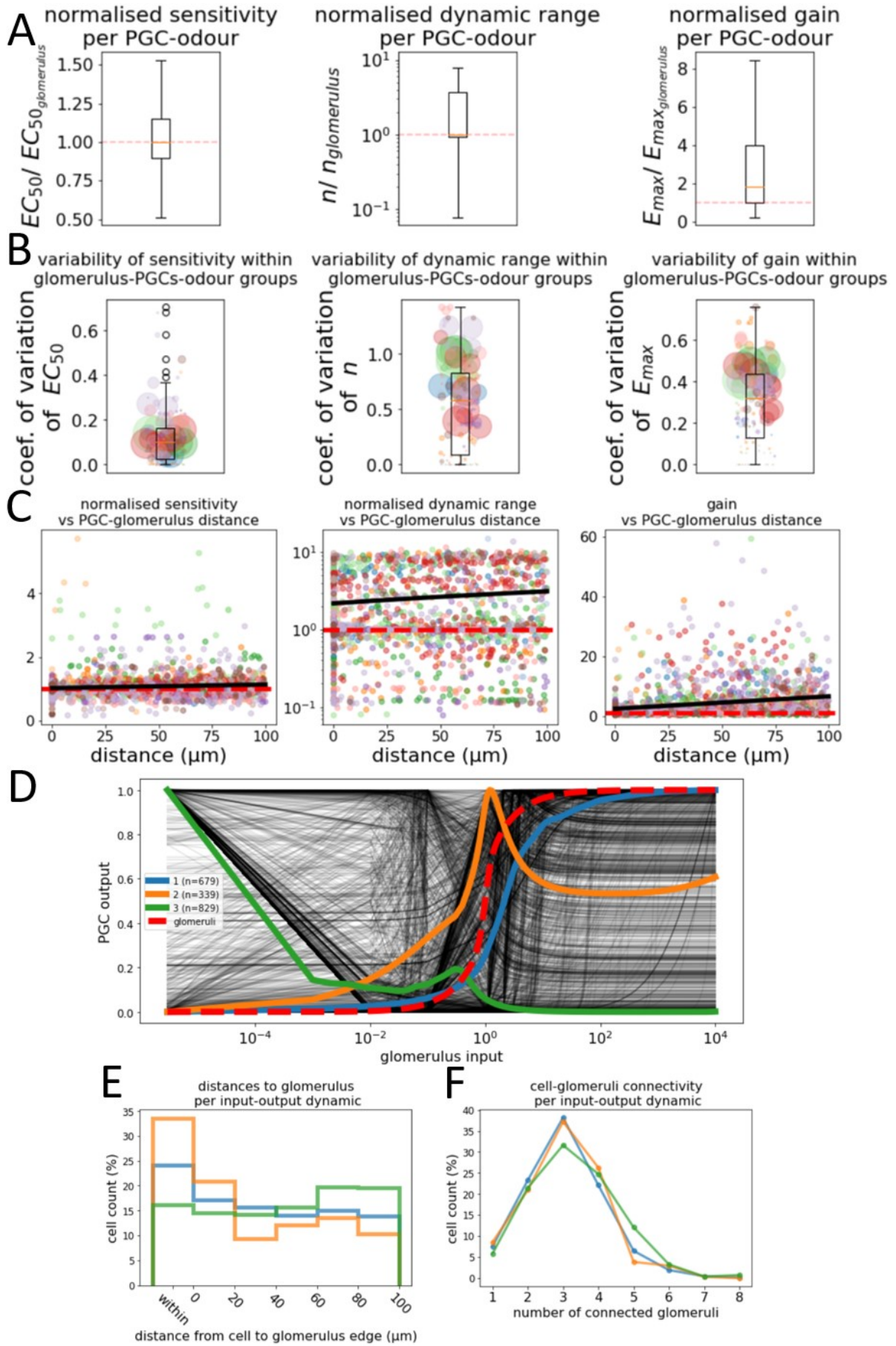


Figure 3.12 Hill function parameters variations within glomerulus-PGC groups. A Hill function was fitted on sets of 3 to 6 responses of 1847 PGC-odour pairs from 153 glomeruli-odour groups in 12 fasted animals. Each function is characterised by 3 parameters: the EC_{50} , an estimation for sensitivity, n , the Hill coefficient, an estimation for the dynamic range, and E_{max} , the maximum response. Here is shown how these properties vary across PGCs in a same glomerulus-odour group. **a)** Boxplots of EC_{50} , n , and E_{max} for each PGC-odour pairs, relatively to its parent glomerulus value. **b)** Coefficients of variation within PGCs of each glomerulus-pgc groups. Circles represent the size of groups and the colour the animal. **c)** Linear regressions of the 3 Hill parameters (from (A)) for all PGC-odour pairs in function of the distance to the edge of the glomerulus parent. **d)** Input-output dynamic of PGC-odour pairs (black), defined as the Hill function of PGC divided by the Hill function of the parent glomerulus. All curves are normalised so the glomeruli Hill curve have an EC_{50} of 1 and E_{max} of 1. The blue, orange, and green curves are the centroids from a k-means clustering ($k=3$). The red dotted curve is the average of all glomeruli normalised Hill functions. **e)** Histogram of the distances to parent glomeruli for the PGCs belonging to the 3 groups resulting from the k-means clustering of the transfer functions in (D). **f)** Distribution of estimated connected glomeruli for the PGCs from the 3 transfer functions groups (Fig 3.8). Boxplots: Orange bars are medians. The box delimits the lower and upper quartiles. The whiskers show the range of the data. Flier points represent outliers.

The transfer functions describe the input-output dynamics of the PGCs (Fig 3.12 D). The red dotted line shows the average glomerulus activation function centred on a EC_{50} of 1 (red dashed line). All the black lines are the PGCs transfer functions. The blue, orange, and green curves are the main patterns of PGCs transfer functions. To compute them, I took all the 1847 PGC-odours pairs Hill functions and associated glomerulus-odour Hill functions. Then I shifted all these functions so the glomeruli EC_{50} are centred at 1. The transfer functions are the PGCs dose-response functions divided by the functions of their mother glomeruli. Following that, I used the k-means algorithm with $k=3$ (number k chosen based on the elbow method, see appendix B) to extract 3 groups of transfer functions (blue, orange, green) of 679, 339, and 829 glomerulus-PGC-odour samples. Amplitudes were not considered in this analysis as they cannot be directly compared, amplitudes were therefore normalised to 1.

3 types of PGCS input-output dynamics are shown in figure 3.12 D. The decreasing ones (green) means PGC-odour pairs responded before the

glomeruli. They might be more sensitive than the glomerulus or activated by another part of the circuitry. This dynamic decreased with glomerulus input so they could be inhibited by other PGCs as the glomerulus activity rises. Another type of transfer function in orange shows higher sensitivity than the glomerulus as well but then get inhibited after reaching the glomerulus EC_{50} . The gain reduction at higher concentrations is likely implemented using mechanisms that have been described in experiments with acute slices, e.g. self-inhibition via spillover (Murphy et al, 2005), mGluR(II) activation at high concentrations (Zak et Schoppa, 2021). The last blue transfer function follows the glomerulus trend with a delay. The green and orange curves have higher output activity values before the glomerulus EC_{50} . This dynamic relates to contrast enhancement (Fig 1.7). If we consider the glomerulus as afference, the green and orange functions would dampen lower sensory inputs by acting as a high-pass filter.

I then linked back the 3 transfer functions to the cells distances to the glomerulus and their number of connected glomeruli computed in the previous section (Fig 3.12 E&F). The PGCs whose function decreased with glomerulus activation (green) had a higher likelihood to be positioned far from the glomerulus. The PGCs expressing a transfer function activated earlier than the glomerulus then inhibited at higher concentrations (orange), or following glomerulus activity (blue) tended to appear close to the glomerulus, especially in the orange case (Fig 3.12 E). The estimated number of connected glomeruli for the PGCs corresponding to each transfer function appeared similar, with a peak of a bell-shaped distribution on 3 connected glomeruli (green: 31.56%, orange: 37.16 %, blue: 38.20%). The green group was slightly more connected (few more PGCs with 5, 6, and 8 connections than the 2 other groups) (Fig 3.12 F). Based on connectivity and distance, PGC with different transfer functions cannot be classified in distinct groups, but rather on a continuum with the orange and blue ones more likely to be mono/uni-glomerular due to a close distance to the glomerulus, green more likely to be poly/oligo-glomerular due to a longer distance.

PGCs characteristics of odour-evoked activity across concentrations differ from their parent glomeruli. I found so far that PGCs followed 3 different types of transfer functions, have generally steeper hill curves than their glomerulus, and express a range of EC_{50} s that straddle the parent glomerulus EC_{50} , with the average of all PGC daughters EC_{50} s close to their glomerulus EC_{50} . All the characteristics were closer to the parent glomerulus ones as the cells were nearer. The observed spread of PGCs characteristics plays a role in shaping the afference via feedforward inhibition and creating the diversity of MTC activity. Groups of glomerulus-PGCs code for odour identity and concentration based not only on the amplitude of responses but also on a respiration-linked oscillatory dynamic. All OB neuron populations' activity oscillates at a unique frequency that takes root in the periphery where OSNs capture breathing rhythm via mechanosensation.

3.2.5 Oscillatory activity and phase coding

Airflow-driven mechanosensation by the OSN synchronises the OB neuron populations. The respiration frequency of 2-4Hz in anaesthetised mice is reflected in the calcium and membrane potential activity of OB neurons (Ackels et al., 2020; Iwata et al., 2017). The OSNs generate this respiration-linked oscillatory signal (Iwata et al., 2017). Inhalation-linked activity arises from OSNs and is then modified by feedforward inhibition of JGCs, creating a diversity of phase shifts coding in second-order neurons of OB. It is the basis of the temporal coding of olfactory information. Odour identities are coded by phase-locked respiration (Gire et al., 2013; Dhawale et al., 2010).

Mice can discriminate an odour identity within one breath. The phase shift to the inhalation onset encodes odour identities in glomeruli MTC dendrites (Iwata et al., 2017). During a respiration cycle, different latencies of activity onset occur in a same glomerulus across the neurons types projecting their dendrites into it (Short and Wachowiak, 2019). The phase shift changes between pure air-flow and odours applications (Iwata et al., 2017). Therefore, the phase shift discriminates the presence of an odour from none. Phase shift coding has other properties than the signature for an odour. It is invariant to airflow and concentrations changes (Iwata et al., 2017). A glomerulus can express different phase shifts for odours and an odour elicit various phase

shift across glomeruli. The phase complements the amplitudes and the selection of activated glomeruli for encoding odours in the OB.

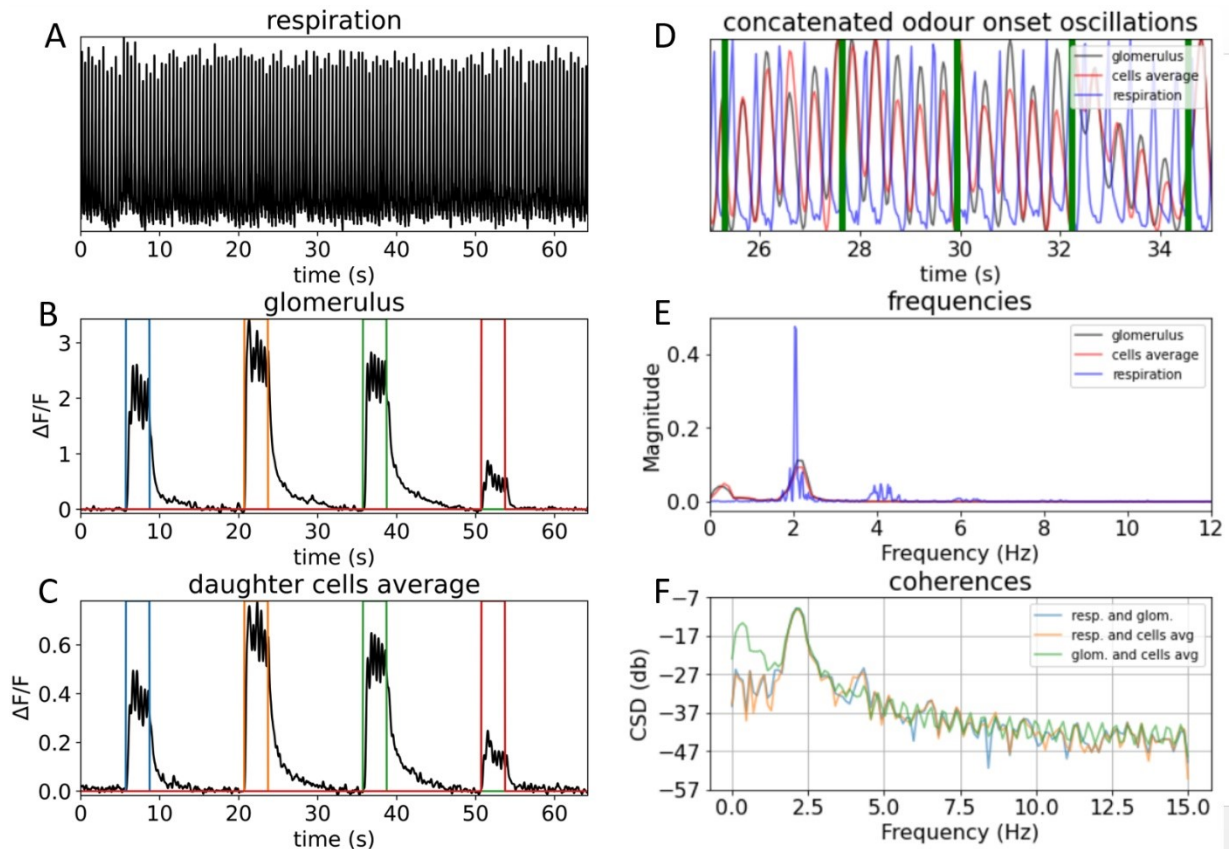


Figure 3.13 PGCs reflect OSN breathing mechano-sensitivity. The PGCs inherit the respiration-evoked activity from the OSNs. The evoked oscillations are synchronised between the PGC somata and the parent glomerulus. **a)** Strain gauge recordings of the respiration **b)** 4 odour-evoked responses in a glomerulus showing oscillations concurring with the respiration in a). 2-heptanone, isobutyl propionate, ethyl tiglate, and isoamyl acetate at 10% dilution in air. **c)** Average of odour-evoked responses of the daughter PGCs of the glomerulus in b). **d)** Concatenation of parsed odour-evoked oscillations in the parent glomerulus (black), the average the daughter PGCs (red), and the respiration signal (blue). Only 4 bouts are shown. The green line is where bouts were connected. **e)** Fast Fourier Transform of the 3 whole traces in (D). A 2Hz respiratory frequency appears in the glomerulus and the PGCs **f)** Cross-spectral density of the traces in d). The glomerulus and PGCs are coherent between each other and with respiration.

Phases are ordered amongst OB populations. All cells types MTC/TC/OSN/JGCs vary in latencies (Short and Wachowiak, 2019). OSN phase is the earliest to the inhalation onset. Juxtglomerular cells, including

PGCs, mirror sensory inputs oscillations (Short and Wachowiak, 2019). In the second-order neurons, MTC shows a large diversity of phase latencies (Ackels et al., 2020). Even sister MTCs from a same glomerulus are not identical in their phases. Otherwise, TCs phases tend to be locked together as they play a role of reference pace in the OB. Both MTCs and TCs phases are shifted later than in glomerular layer interneurons.

The phases are delayed by inhibition, therefore, PGCs oscillations play a major role in the diversity of MTC phases. Sister MTCs innervated by a single glomerulus show different spike timing during odour stimulation relative to respiration (Dhawale et al., 2010). Odour-evoked phase shifts amongst sister MTC diverge. Furthermore, air-flow-driven phase responses are variable across OSN axons in the glomerular layer which leads to different phase shifts for air-flow across glomeruli (Fig 3.14 D). This means glomerulus-specific phases are likely produced in the OB by inhibition shaping from PGCs.

To measure oscillations in a signal, the Fast Fourier Transformation (FFT) is the method usually applied. The FFT transforms any temporal function into a sum of weighted sinus functions of a series of frequencies. The weights give which frequencies are present in the signal. Figure 3.13 demonstrates, using FFT, that the oscillations occurring in PGCs calcium activity reflect the inhalation frequency. The respiration signal was acquired via a strain gauge apposed against the mouse thorax. This flexible resistance transduced the flexion into a voltage we measured (cfr. methods). Figure 3.13 A shows a minute of mouse respiration. Anesthetised mice breathe at a rhythm from 1 to 4 Hz. I observed similar oscillations in glomeruli (Fig 3.13 B) and PGCs (Fig 3.13 C) evoked responses. The oscillations were not always observable in cells due to low SNR. Therefore I averaged daughter PGCs traces to reduce the noise (Fig 3.13 C). Furthermore, oscillations are rarely explicit in the baseline (Fig 3.14 A) and are not picked up by FFT. It requires an averaging over respiration cycles to make it appear (Fig 3.14 B). In figure 3.13 D, for FFT purpose, I thus only looked at the concatenated odour-evoked oscillations, taken from periods of stimulation on the calcium traces. As expected, the same frequency of 2Hz for that animal was found both in the respiration signal and the glomerulus, as well in the PGCs daughters (Fig 3.13 E). To assess the coherence in frequencies between the glomerulus and its

PGCs, I used a cross-spectral density (CSD) plot (Fig 3.13 F). It shows the mutual resonant frequencies in a pair of signals. There is a peak of coherence for all pairs between respiration, glomerulus, and cells. This shows the same oscillations are effectively shared in a glomerulus-PGCs group.

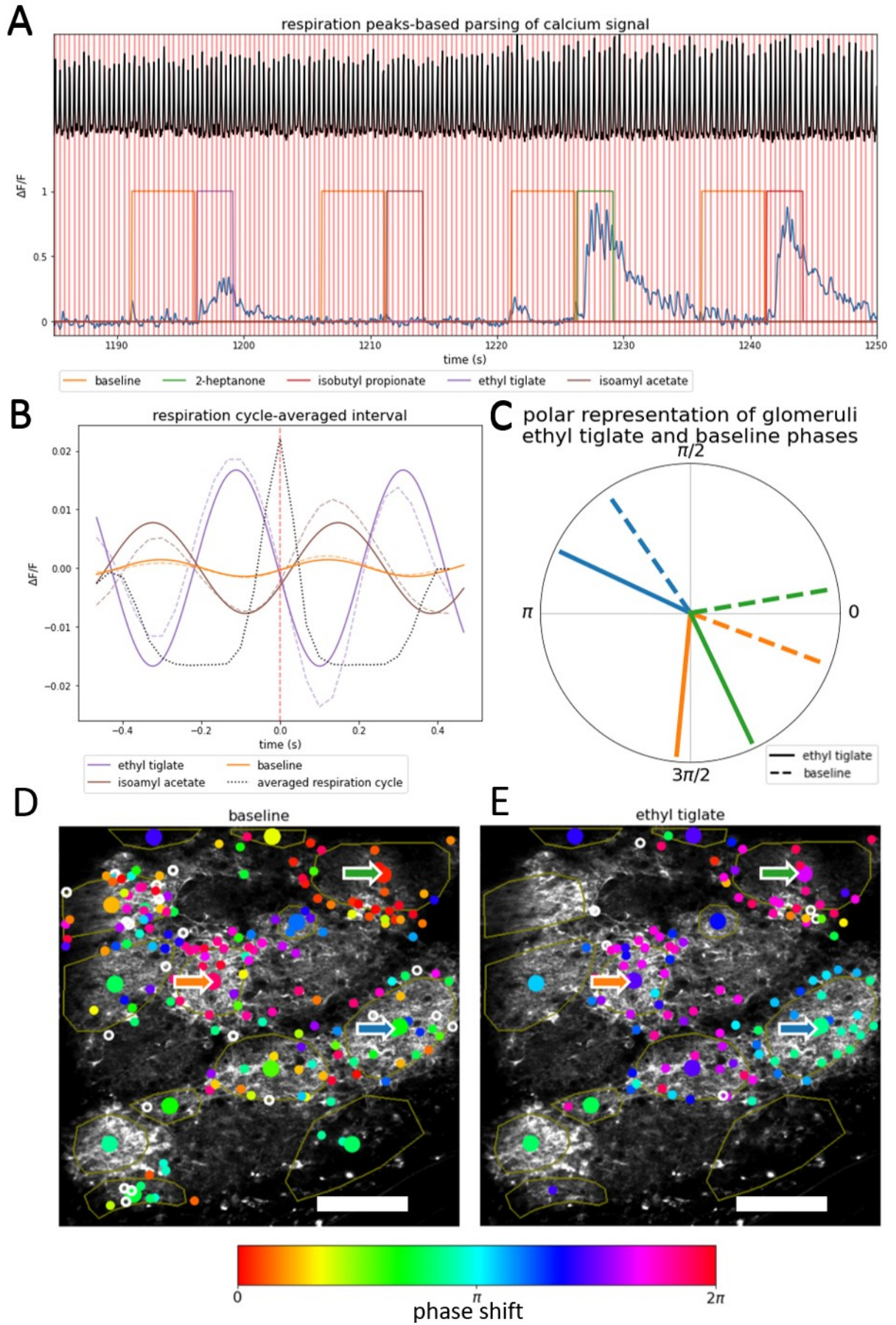


Figure 3.14 Respiration-triggered averaging and phase coding. Interval-triggered average (ITA) enhances oscillations in a signal by averaging bouts made from points before and after an inhalation peak. The phase of oscillations is shifted in relation to the respiration inhalations. Furthermore, odour-evoked oscillation phases shift from that baseline phase. **a)** In a low SNR trace, oscillations are not visible. Intervals are made from points before and after inhalation peaks (red lines). Baseline ITAs are taken from the 5 seconds before stimuli (yellow), and odour ITAs during the 3-seconds stimuli (colour-coded odours). **b)** ITAs, averages of all the bouts from (A), for the baseline and 2 odours. Dotted lines are data. Full lines are fitted cosinus. Black dotted line is the averaged respiration cycle centred on the inhalation peak. **c)** Phase shifts relative to the respiration peak for the baseline (dotted) and ethyl tiglate (full line) for 3 glomeruli in (D,E). **d)** colour-coded baseline phase shifts for PGCs (small circle) and glomeruli (large circles) **e)** colour-coded ethyl tiglate-evoked phase shifts for PGCs (small circle) and glomeruli (large circles). FOV background is the maximum projection of all the stimulation frames. Scale bar: 100 μm .

As calcium imaging has a temporal resolution and signal-to-noise ratio too low to see oscillations in the baseline or to apply FFT, I used inhalation-trigger average (ITA) to extract oscillatory information. First, I detected the peaks in the respiration that correspond to the end of inhalation (Fig 3.14 A). I created intervals by adding points before and after these peaks (Fig 3.14 B). I used these intervals to split the calcium signal into bouts that I averaged together (Fig 3.14 B). For the baseline airflow, only bouts occurring out of odour stimulations and ignoring 7 seconds after odour onsets were taken (Fig 3.14 A). This avoids any contamination of odour phases as it is known odour-evoked after-image can persist after the cessation of odour stimulation (Patterson et al., 2013; Matsumoto et al., 2009) and because I too observed tails of responses still appearing after odour offset (Fig 3.14 A, green pulse train). As for the odours, only bouts occurring during odour valve openings were averaged (Fig 3.14 A).

I then extracted phase shifts from these ITAs. The coloured dotted lines in figure 3.14 B show the ITAs for the baseline, ethyl tiglate and isoamyl acetate. The black dotted line represents the averaged respiration cycle centred on the end-of-inhalation peak. To improve the accuracy of time delay measurements, as the low temporal resolution only enable only increments of 33ms (imaging at 30Hz), I fitted a cosinus function using the python library

scopy. The function was $r \cos(2\pi ft + \varphi)$ where r is the amplitude, f the frequency and φ the phase. The peak of the phase shift-less cosine coincides with the respiration peak. The advantage of the cosine fitting is that I can gather parameters without further measurements like peak to peak and such. To enforce good fitting, I constrained f to be between 0.75 and 1.25 times the frequency of respiration, as that frequency lightly varies through an experiment. The ITAs were rejected if the standard deviation error on f was above 0.1 (see appendix C). This ensures ITAs were periodical signals. Thus, φ gave a time delay between the peak of the respiration signal and the peak in the ITA. The phase shift was then calculated as φ divided by the respiration period, making it independent of respiration frequency and comparable across animals.

Figure 3.14 C shows for 3 glomeruli, their phase shifts for baseline and ethyl tiglate. The activating odour can be discerned from the airflow by a change in the phase shift. The 3 glomeruli are shown by arrows in phase-coloured maps (Fig 3.14 D&E). The phases change from airflow to odour for the PGCs as well. In both cases, phases tend to cluster per glomerulus-PGCs groups. However, baseline phase shifts show more heterogeneity than the odour-evoked ones.

PGCs tend to express the same phase shift as the parent glomerulus (Fig 3.15). Here I show an example of a glomerulus-PGC group. The glomerulus and its cells have a preferred phase shift in the absence of odours (Fig 3.15 A). This phase shift will change when the glomerulus is responsive to an odour (Fig 3.15 B), as ethyl tiglate displaced the phases lightly earlier (going from red to pink on the phase colour bar) compared to baseline (Fig 3.15 A). The PGCs baseline phase shifts tend to diverge as they go further from the glomerulus (Fig 3.15 A), as they are likely connected to other glomeruli with different phase shifts (Fig 3.14 D). The average ITA oscillation during baseline in the cells coincides with the glomerulus (Fig 3.15 C). For ethyl tiglate, the average of cells is slightly delayed. As seen in the figure 3.15 C, D, E&F, the PGCs phase shifts are heterogeneous but on average close to the glomerulus value. Fig 3.15 E&F shows the phase of the glomerulus and the histogram of PGCs phases. For both airflow and the odour, the phase of glomeruli seems lightly in advance of the phase of the PGCs.

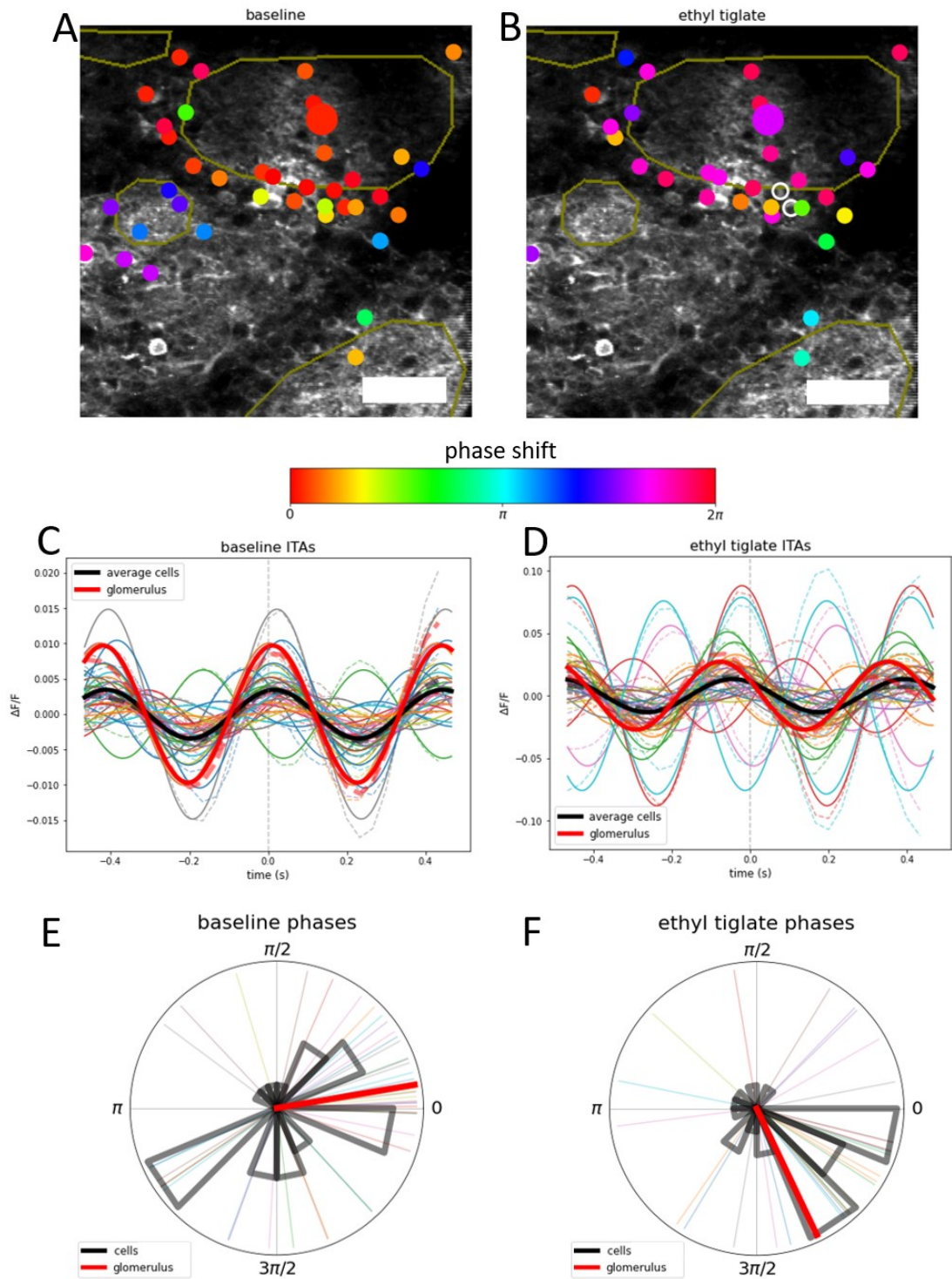


Figure 3.15 Phase shift variability within glomerulus-PGCs groups. PGCs tend to follow the phase shifts of their glomerulus parents, in baseline and during odour stimulation. Baseline phase shifts amongst PGCs are spread while their odour-evoked phase shifts are more centred around the glomerulus value. Odour-evoked phase shifts are slightly delayed compared to the glomerulus. **a)&b).** Colour-coded phase shifts for PGCs (small circle) and a glomerulus (large circle) of the same group, for baseline oscillations (A) and ethyl tiglate (B). The empty circles denote the inability to fit a cosine on the ITA. **c)&d).** Interval triggered averages of 2 respiration periods for baseline (C) and ethyl tiglate (D). Average of all daughter cells in black, glomerulus in red, individual cells in other colours. Dotted lines are the raw

data, filled lines are fitted cosinus. 0 denotes the inhalation peak. **e)&f).** Circular histograms of the baseline and ethyl tiglate-evoked phase shifts in the daughter PGCs (black) and mother glomerulus (red). individual cells in other colours. FOV background is the maximum projection of all the stimulation frames. Scale bar: 50 μm .

In figure 3.16, I extended these results to the total of the data of 8 fasted animals, containing 1152 glomerulus-PGCs pairs (for airflow analysis) and 1269 glomerulus-PGC-odours triplets (for odour-evoked analysis). I plotted all the differences between the phase shifts of a PGC and its glomerulus for the baseline (Fig 3.16 A) and all the odours (Fig 3.16 B). The one and the other show a mean around 0. The PGCs are close in phase to their glomerulus in any case. However, in the airflow case, values are more widespread. This could be due to OSN glutamatergic inputs driving PGCs commonly during odour stimulation in an active mode, while during baseline they would remain less constrained in a passive mode. The more compact distribution of differences in odour phases can be due to OSN-driven external tufted cells (ET) that excite PGCs. ETs are by default spontaneously bursting but during odour stimulation they play a role in the OSN->ET->PGC circuit which may reinforce PGCs oscillatory synchronisation (Shao 2009).

Both PGCs and glomeruli phases change from airflow to odour. The difference of odour-baseline phase shifts between cells and glomeruli ($odour_{cell} - baseline_{cell}$) - ($odour_{glomerulus} - baseline_{glomerulus}$) shows that both discern airflow and odour in a similar manner (Fig 3.16 C). Figure 3.16 D shows phase histograms for different odours. In general, PGCs phases are later than glomeruli phases. For each odour, multiple phases occur, so these plots might not be totally representative. For example, in my data, ethyl tiglate elicited at least 3 different phases across glomeruli (Fig 3.14 C).

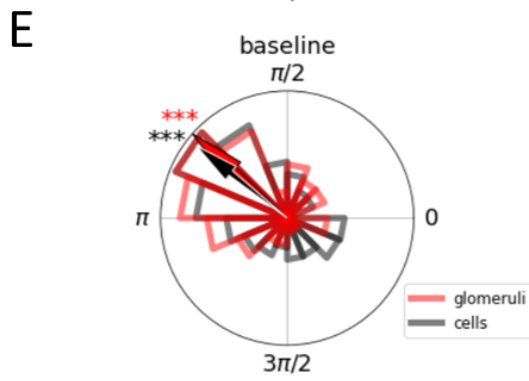
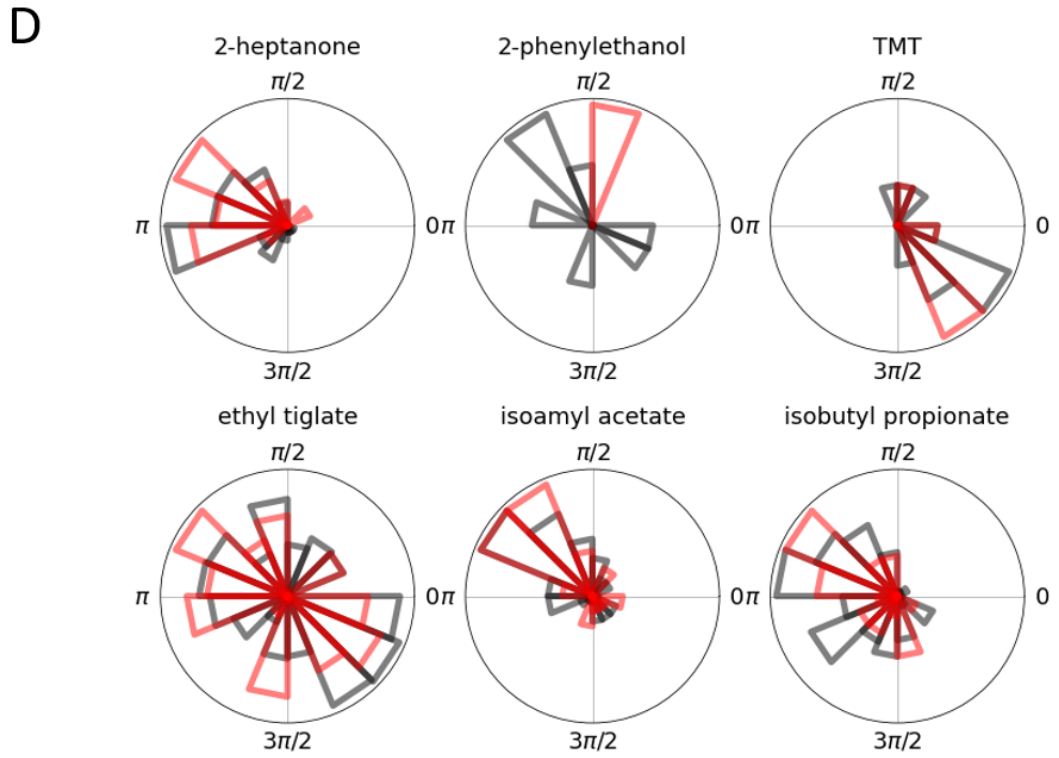
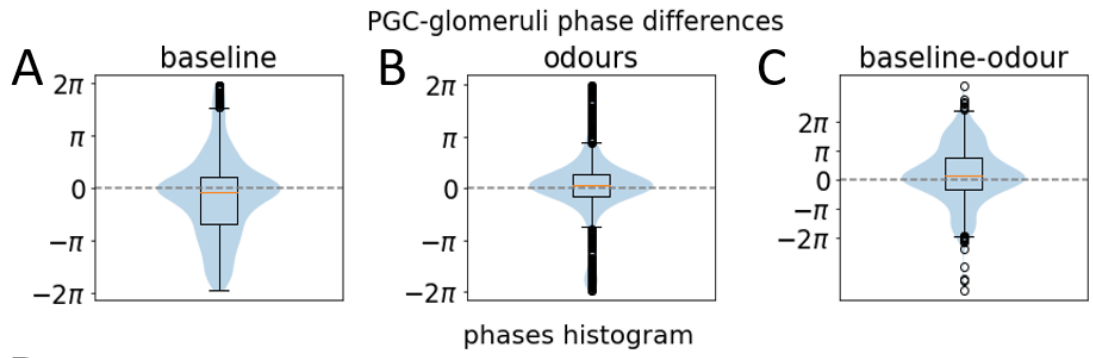


Figure 3.16 Phase shift variability within glomerulus-PGCs groups.

Difference between the phase shift of glomeruli mothers and their PGC daughters from a dataset of 8 fasted animals and 6 odours. PGCs elicit similar phase shifts as their glomeruli, especially during odour stimulation. **a)** Distribution of baseline phase shift of a PGC subtracted by its glomerulus. 1152 glomerulus-PGCs pairs. **b)** Distribution of odour-evoked phase shift of a PGC subtracted by its glomerulus. 1269 glomerulus-PGC-odours triples. **c)** Difference between cells and glomerulus of change of phase shifts between baseline and odour: $(odour_{cell} - baseline_{cell}) - (odour_{glomerulus} - baseline_{glomerulus})$. 790 glomerulus-PGC-odours triples. **d)** Circular histograms of odour-evoked phase shifts in individual cells (black) and glomeruli (red). **e)** Circular histogram of baseline phase shifts in individual cells (black) and glomeruli (red). Red arrow shows circular mean of glomeruli. Black arrow shows circular mean of cells. Boxplots: Orange bars are medians. The box delimits the lower and upper quartiles. The whiskers show the range of the data. Flier points represent outliers.

PGCs and glomeruli preferred phase orientation was by default between $\frac{\pi}{2}$ and π with the glomeruli slightly advanced (Fig 3.16 E; Rayleigh test: cells: $n=749$, $mean=0.786\pi$, $p=5.75e-12$, glomeruli: $n=60$, $mean=0.769\pi$, $p=0.0002$). This is close to OSN baseline phases measured under anaesthesia spreading from $\frac{\pi}{2}$ to $\frac{3\pi}{2}$. Tufted cells (TC) are also known to have a preferred phase around $\frac{3\pi}{2}$ (Ackels et al., 2020; Jordan et al., 2018). This makes sense that PGCs phase is close to OSNs and before TCs. MTCs however show a more diverse phase distribution which is likely due to GC and PGC inhibitory shaping.

I showed that PGCs have their phases similar between them within a glomerulus-PGCs group. The heterogeneity of phases around the glomerulus value may play a role in orienting phase in second-order neurons, which show more diversity (Fantana et al., 2008). PGCs phases were delayed compared to the glomerulus as expected (Short and Wachowiak, 2019). Interestingly, the baseline phase has a main orientation like TCs and that orientation is within range of what is known for OSNs (Ackels et al., 2020; Jordan et al., 2018). The predilection of PGCs aligning in phase with a glomerulus, along with other metrics, could help infer PGCs subtypes.

3.2.6 PGC subtypes inference from function and connectivity

After grouping PGCs in glomerulus-PGCs groups and computing metrics, I can attempt to look for PGC subtypes using these metrics. The idea was that, for example, a cell eliciting a plateau response (shape B in Fig 3.4), having a single glomerulus parent and at a close distance would be a microglomerular cell (cfr. Introduction). A cell at a larger distance with more connections would end up being a polyglomerular cell or oligogglomerular cell. A PGC showing a biphasic response (shape G in Fig 3.4) may be an ET-driven PGC because ETs are known to have biphasic responses. Unfortunately, due to a lack of data and limitation in observations, a clear inference was not possible. The field of view restricts the number of observable cells and calcium imaging is limited to only one neural population. In an effort, I agglomerated and normalise metrics for PGCs relatively to the parent glomerulus to see if groups would appear sharing common metrics.

The main predictors of PGC subtypes are their size and their connectivity to glomeruli. It ends up to 4 overlapping PGC categories spread on a continuous spectrum of the number of connected glomeruli: Microglomerular (1 glomerulus), Uniglomerular (1-3 glomeruli), Oligogglomerular (2–6 glomeruli), and Polyglomerular (≥ 7 glomeruli) (Tavakoli et al., 2018; Kosaka et al., 2019; Kiyokage et al, 2010; Bywalez 2017). From the estimated number of connected glomeruli (Fig 3.8 C), I inferred which percentage of cells could belong in each category (Fig 3.17 A). These classes are overlapping which makes the classification difficult. Most PGCs fit both Uniglomerular and Polyglomerular types. I assumed a broader odour tuning would correlate with glomeruli connectivity. Only a minority of PGCs were tuned for more than one odour (Fig 3.17 B). Connectivity and tuning broadness is indeed correlated (linear regression with $r=0.16$, $p\text{-value}=1.15e-06$) (Fig 3.17 C). This makes sense as more glomeruli connected increases the possibility of broader odour tuning.

The characteristics I used are either PGC-wise or glomerulus-PGC-odour-wise metrics. PGC metrics were the cell diameter, based on a 2D Gaussian fit on the ROI (estimated by suite2p), the number of glomeruli (Fig 3.8 C), the tuning broadness, The number of averaged responses in each shape cluster, and the baseline phase. Glomerulus-PGC-odour metrics were

all relative to the glomerulus parent value and included sensitivity (EC_{50}), dynamic range (hill coefficient), gain (EC_{max}), baseline phase, and odour-evoked phase.

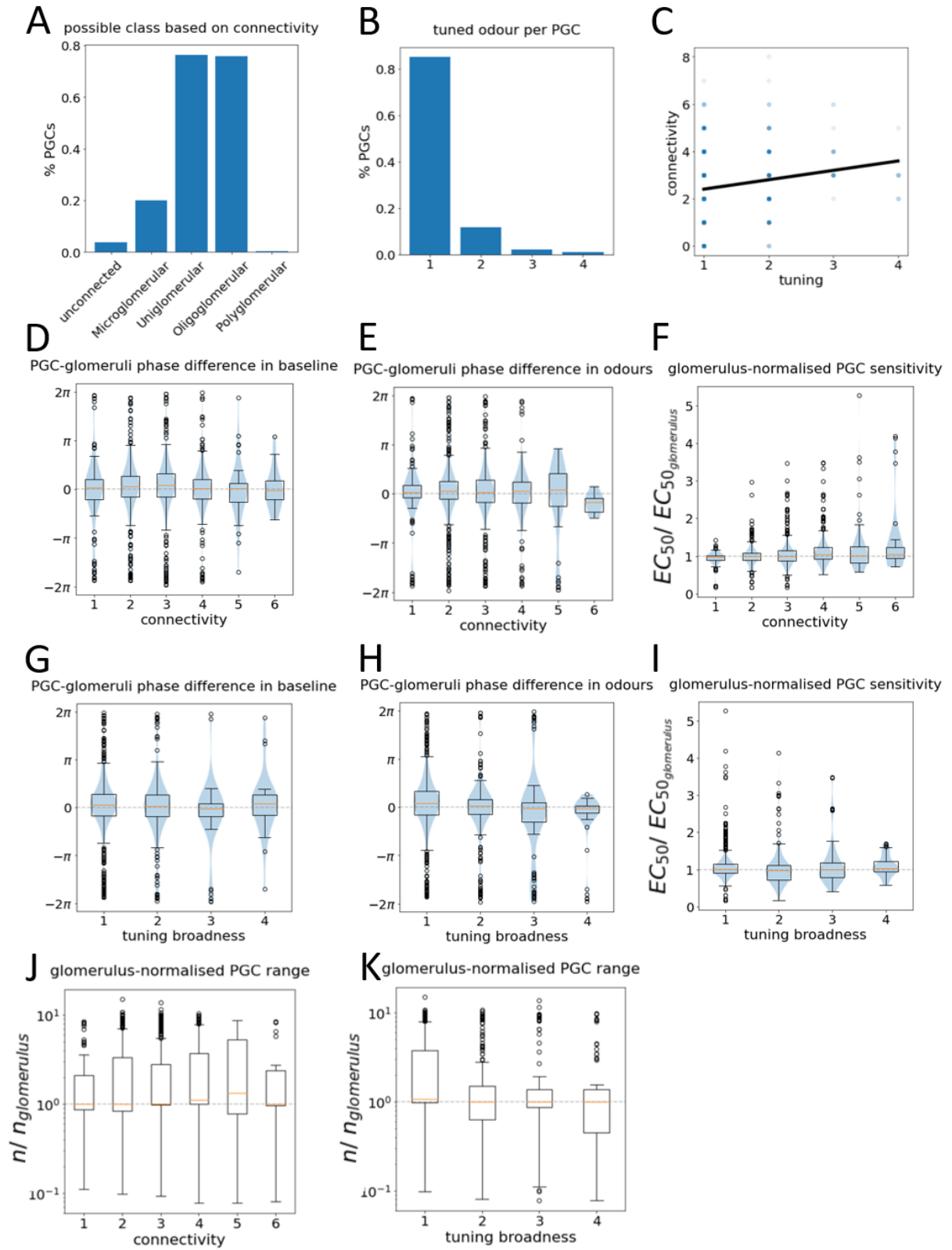


Figure 3.17 Relation of PGCs and PGC-odour pairs metrics to connectivity and odour tuning. Investigation of links between PGCs characteristics and their estimated glomerular connectivity and their repertoire of responding odours. **a)** Distribution of PGC subtypes based on estimated connectivity (Fig 8.C): Microglomerular (1 glomerulus), Uniglomerular (1-3 glomeruli), Oligoglomerular (2–6 glomeruli) and Polyglomerular (≥ 7 glomeruli). (n=932 PGCs). **b)** Distribution of number of responding odours per PGC. **c)** linear regression between odour tuning and connectivity ($r = 0.16$, $p = 1.15e-06$) **d)** Difference of baseline phase shift between PGC daughters and glomeruli mothers against connectivity. **e)** Difference of odour-evoked phase shift between PGC daughters and glomeruli mothers against connectivity. **f)** Glomerulus-normalised sensitivity against connectivity. **g)** Difference of baseline phase shift between PGC daughters and glomeruli mothers against odour tuning. **h)** Difference of odour-evoked phase shift between PGC daughters and glomeruli mothers against odour tuning. **i)** Glomerulus-normalised sensitivity against odour tuning. **j)&k)** Glomerulus-normalised Hill coefficients of PGC-odour pairs against connectivity and odour tuning. Connectivity: number of estimated connected glomeruli; Tuning broadness: number of responding odours. Boxplots: Orange bars are medians. The box delimits the lower and upper quartiles. The whiskers show the range of the data. Flier points represent outliers.

In figure 3.17 D-K, I looked at how glomerulus-PGC-odours measurements were related to the glomeruli connectivity and the tuning broadness. Overall, these metrics did not change with connectivity or tuning broadness and stayed close to the parent glomeruli values. The sensitivity and ranges tended to vary slightly more with connectivity (Fig 3.17 F&J). It is likely because higher connectivity encompass more various EC_{50} and Hill coefficients values from more glomeruli. However, tuning broadness seemed to slightly lower the Hill coefficient which corresponds to higher dynamic ranges (Fig 3.17 K)

I attempted to show correlations between the PGC-wise metrics mentioned above using PCA (n=529) (Fig 3.18 A). The explained variances were low for the two first components (12.42%, 18.28%). This analysis is thus not conclusive of any clear groups. I only found that tuning broadness and connectivity were gradually distributed along 45 degree axis and the baseline phase along -45 degree axis (appendix B). The shapes or cell sizes did not show any oriented or clustered distribution. Therefore connectivity and tuning broadness are parallel and both are orthogonal to the baseline phase. Neither had relations to size or shapes.

A second PCA on the Glomerulus-PGC-odour metrics was barely more fruitful (Fig 3.18 B). For each PGC, I averaged the EC_{50} , Hill coefficients, gain, baseline phase difference, and odour-evoked phase differences (n=262). Explained variances were a bit higher with 37.41% and 19.26% for the two first components. Here I found the first component represented the increasing continuum of the hill coefficient (96.02% explained variance) and the second component explained mostly the gain (87.45%) and EC_{50} (47.2%) (appendix B). Phase differences did not exhibit any relationships. The gain and EC_{50} were not linearly correlated ($r=0.08$, $p\text{-value}=0.2$). The limited number of samples in these two PCAs is because the Hill function parameters restrict the data to only concentration-increasing responses and phases metric only the data with respiration signal available.

I conclude there is a distinct possibility that PG cells don't exist in discrete groups but are on a continuum. It might require more data. More odours tested would help for a better assertion of PGC-glomerulus connections. Different airflow patterns of olfactory stimulations could also help evaluate cells and glomeruli responding with similar shapes.

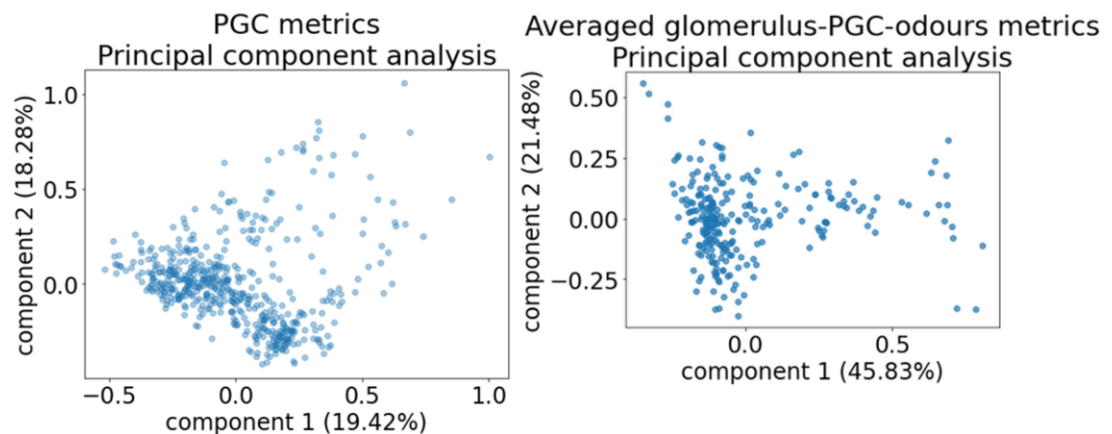


Figure 3.18 Principal Component Analysis of PGC and PGC-odour metrics. **Left:** Cloud of PGC points in a space determined by the two first components of a PCA. The metrics used are the cell diameters, the estimated number of connected glomeruli (Fig 3.8 C), the tuning broadness, The number of responses in each shape cluster, and the baseline phase shift. **Right:** Cloud of PGC points in a space determined by the two first components of a PCA. The metrics used, normalised to the glomerulus parent, are the sensitivity (EC_{50}), dynamic range (Hill coefficient), gain (EC_{max}), baseline phase shift and odour-evoked phase shift.

3.3 Conclusion

In this chapter, I identified and characterised odour-evoked responses in PGCs and glomeruli, in fasted anaesthetised mice. PGCs code for an odour in a matter of amplitude of the response and the phase shift to the respiratory rhythm. No difference in characteristics was found across odour activations. The cells did in general increase activity with concentrations with a minority expressing concentration-decreasing activity. A diversity of response shapes were observed, indicating complex neural interactions occurring in the glomerular layer. PGCs formed groups linked to a glomerulus. PGCs form connections from 1 to multiple glomeruli and can respond to multiple odours. PGCs within a glomerulus-PGCs group share on average the properties of the glomerulus like the sensitivity and dynamic range in an odour concentration-activity curve. Airflow phases and odour-evoked phase were similarly close within neighbouring PGCs. PGCs phases were however delayed to the glomerulus. PGCs have a default preferred phase in absence of odour. PGCs subtypes could not be inferred based on the computed metrics. This would require more data and more diverse stimuli to record with. To estimate connectivity, a ground truth using a tracing method would be ideal. Furthermore, despite sharing a same odour tuning, groups were biased by the choice of a distance (100 μ m) and the choice of having at least one similar response only. Consequences are that the properties within a glomerulus-PGC-odour group are more spread than reality.

Considering the glomerulus as a partial proxy for afference is debatable. The glomeruli also reflect the activity of other neurons that synapse into that neuropile, especially TC/MTC which provide feedback excitation. However, the literature says the PGCs activity is the first to respond to the afference, because of the high membrane resistance of PGCs, so the assumption that glomeruli partially reflect axonal inputs holds. This calls for a multi-populations recording method. Imaging simultaneously the OSN and PGCs would solve that problem.

Chapter 4

OMMI: Optical multi-modal imaging

4.1 Introduction

Brain imaging using fluorescent probes often limits itself to a single neuronal population with GECI bound to specific cell-types promoters. This limits our understanding of neural circuit function as only a single population can be imaged simultaneously. The activity of targeted neurons is measured against stimuli intensity while neglecting sensory, relay, or interneuron inputs. In this study case, PGC activity is reported to the odour stimuli concentrations; allegedly well corresponding to the actual PGC inputs that are OSN afferent axons. While PGC activity is correlated with odour concentration as shown in the previous chapter, once the connections in the OSN-PGC circuit are disrupted or dissected, this assumption may not hold anymore. Knowing the individual OSN inputs to each glomeruli becomes necessary. In a broader view of the study of neural circuits, having a means of imaging simultaneously multiple populations confer a greater advantage to play with the dynamics of the circuit and decipher its mechanisms.

To achieve multi-population imaging of the olfactory bulb afference and the first layer of inhibitory interneurons, I first attempted using two-photon imaging by complementing the green emission of GCaMP6f in PGCs with a functional red calcium dye for the OSNs (Cal-590). Given the low rate of success of the dye injection, I preferred to switch to a regular microscope and combine two imaging modalities for each neuron population. We, therefore, developed an optical multi-modal imaging (OMMI) widefield microscope rig that enables a combination of different wavelength illumination to the surface of the brain and allows recording of fluorescent, intrinsic and hemodynamic signals in a quasi-simultaneous manner. This system gives possibilities to not only perform multi-population imaging experiments but also measure the neuronal activity coupling with blood flow dynamics.

Imaging OSNs and PGCs simultaneously permit to study of the feedback loop they take part in. I did observe differential modulation of activity in OSNs and PGCs following the application of pharmacological tools. I showed a case study example of manipulating a micro-circuit using OMMI

which is a low-cost efficient method to observe the dynamics of two neuronal populations.

4.2 Multi-population imaging

Multi-population imaging enables the measurement of activity from several neuron-type populations. In calcium imaging, the fluorescent probe often targets a specific cell type. Then the neuron responses are recorded in relation to externally applied stimuli. This method does not take into account the activity of all intermediate neurons to the periphery and neurons downstream. For example, I recorded activity from PGCs while varying odour stimuli and concentration. Secondly, on a more local scale, interactions between neuron types in microcircuits are hidden. In the glomerular layer, the activity of ETCs which participate in circuits with PGCs is not observed. These are two reasons why multi-population imaging is useful to study a neuron population activity in the light of the activity of input or output neurons relatively to that population, or in regards to the neuronal local populations activity. Multi-population imaging helps to investigate the structure of neural circuits. For example, simultaneous measurement of the olfactory bulbs input with that of PGCs could reveal lateral interactions and feedback loops. Multi-population imaging procures a great advantage to reveal the dynamics of a whole layer in a given experiment context of applied stimulus and brain state.

To achieve multi-population imaging using fluorescence microscopy, we require the use of fluorescent reporters of neural activity emitting at different wavelengths to discern between the populations. The usual green calcium indicator GCaMP can for example be complemented with a red-emitting RCaMP (Akerboom et al, 2013; Han et al, 2019). It is even possible to image with quadri-colour blue, red, yellow, green calcium indicators XCaMP (Inoue et al., 2019). Multi-colour imaging increases the complexity of the protocol to put in place as it involves additional techniques such as virus or dye injection, or breeding of animal lines expressing GECI. Furthermore, supplementary optical hardware might be necessary and add a heavy cost, in the case of multiple excitation laser sources.

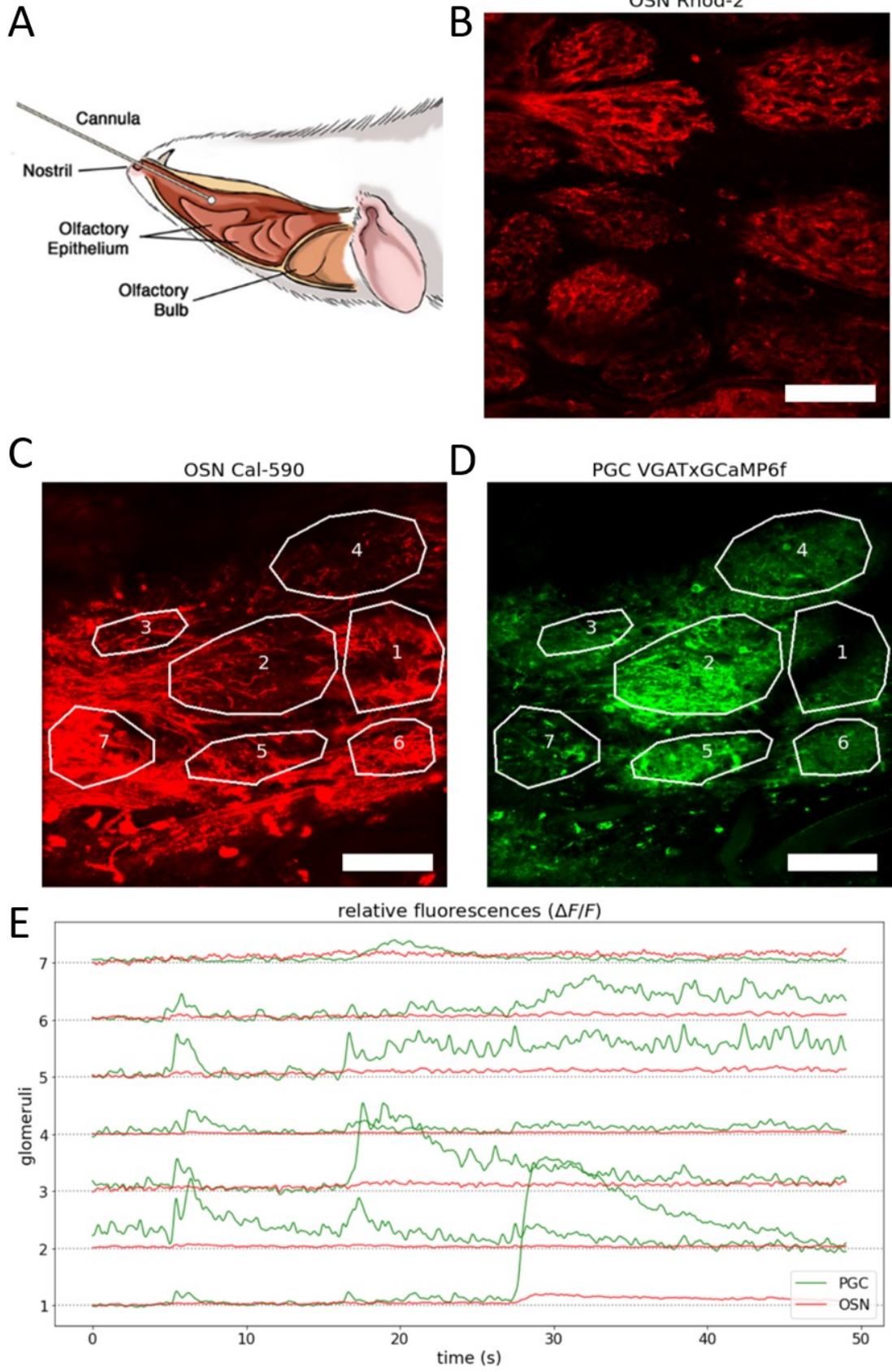


Figure 4.1 two-photon multi-population imaging. Simultaneous recordings of OSNs and PGCs in the glomerular layer of the olfactory bulb. The many attempts to have the OSN well responding were not fruitful. The best cases are shown here. **a)** A calcium dye aimed at staining the OSN terminals was injected nasally via a cannula, in an anesthetized mouse put on its back. (adapted with permission from Uyttingco C., Martens J., “Adeno-Associated Virus Vectors: Design and Delivery”, p. 283-297, Springer, 2019). **b)** Calcium indicator Rhod2 in the OSN glomeruli imaged with a two-photon microscope in a wild-type mouse. **c)&d).** calcium-sensitive dye Cal-590 targeting the OSN in a VGATxGCaMP6f mouse expressing GCaMP in PGCs. Average projection of 1-minute recording. Scale bar: 100µm. **e)** Normalised fluorescence traces of 7 glomeruli identified in C&D, subject to 3 stimulations of 3 seconds of ethyl tiglate, 2-heptanone, and isoamyl acetate. The signal-to-noise ratio of the OSNs was too low, a small response is perceptible in the glomerulus 1.

Multi-population imaging is useful for my project because I wanted to record from OSNs and PGCs simultaneously as they form a feedback inhibition circuit where OSNs release glutamate into PGCs and PGCs proportionally inhibits OSNs. In the last chapter, I only imaged PGC somata and the average neuropil of PGCs cells in glomeruli, in regards to olfactory stimulation of the periphery (Fig 3.1). The transfer functions of PGC were based on the assumption that the average neuropil signal from the glomeruli will reflect the input to PGCs (Fig 3.11E, Fig 3.12E). Recording simultaneously from the OSN side of glomeruli can help verify this assertion.

The first approach to record from OSN in addition to the PGC was to add a functional marker on OSN in our VGATxGCaMP6f mice. This way, we could record both populations with two-photon microscopy and use 2 photomultiplier tubes for the red and green emitted signals. I tried different calcium indicators injected nasally to reach the OSNs somas in the olfactory epithelium (Fig 4.1 A). After the injection, the OSN axons would be imaged in the olfactory bulb glomerular layer (Fig 4.1 B&C).

The nasal loading protocol followed that of Wachowiak and Cohen (2001). The mice were temporarily anesthetized with a surgical dose of ketamine and xylazine then put on their back. A cannula was inserted through the nostril of the same side of the olfactory bulb we wanted to target (Fig 4.1 A). Once at a depth of 9-10 mm, 8µl of a mixture containing the dye was

injected with a hamilton syringe at a slow rate. The dye preparation consisted of 10 ml of physiological solution, 20 μ l of Triton X-100, and 1 mg of dextran conjugated dye. The role of triton is to break the cell membrane for the dye to enter. The animal was kept on its back for 1 to 2 hours and then awakened with antisedan. The mice could be imaged 3 to 10 days post-injection.

This protocol was however proven inconsistent through many trials. I either had no cells stained, or all cells stained but unresponsive (Fig 4.1). First, I used alexa-594 and Calcium green on 3 wild mice to test my injection technique. I could not see any OSN marked. I then tried injecting Rhod2 indicator on another cohort of 3 mice while keeping them on their back for a longer time for the dye to properly impregnate the OSNs. Either there were no cells marked or they were saturated and thus not useful for functional imaging (Fig 4.1 B). Finally, to assert the non-responsiveness was not due to damages in the epithelium or other variables, I injected Cal-590 in a cohort of 5 VGATxGCaMP6f mice. This allowed to verify the responsiveness of the glomerular layer on the GCaMP green channel (Fig 4.1 C). Again, only a couple of these assays worked. Even when I had OSN labeled they weren't always responsive, while the PGCs were clearly activated, excluding any nose occlusions or damages to the periphery (Fig 4.1 E).

The rate of success of this method is known to be hit or miss, The possible reasons for failures are the triton can destroy cells in the epithelium or the dye didn't reach cells in the cavity properly. It results in OSNs being too much stained, destroyed, or partially marked. As nasal loading of OSN proved unreliable we developed an alternate method to measure OSN activity along with PGCs.

4.3 OMMI: Optical Multi-Modal Imaging

OMMI started as an upgrade of our current intrinsic imaging setup and aims at recording multi-modal brain signals (Fig 4.5 A). Intrinsic signal optical imaging (ISOI) allows the acquisition of neural signals in relation to the opacity of brain tissues. This is done by measuring the absorption of infra-red light at the surface of the brain (Fig 4.2 B) (cfr. methods). In the case of the olfactory bulb, activated glomeruli show increased absorption which is due to the movement of water in the olfactory afferents (Vincis et al., 2015; Gurden et al.,

2006). We decided to couple ISOI and one photon fluorescent imaging, using a set of LEDs gated alternatively with each frame (Fig 4.3 B). This would therefore give the ability to simultaneously record the OSN afference through ISOI and the PGC interneurons via GECI imaging (Fig. 4.5 B&C). Furthermore, this method is widefield and therefore allows a larger FOV comprising both bulbs compared to the 2 photon microscopy.

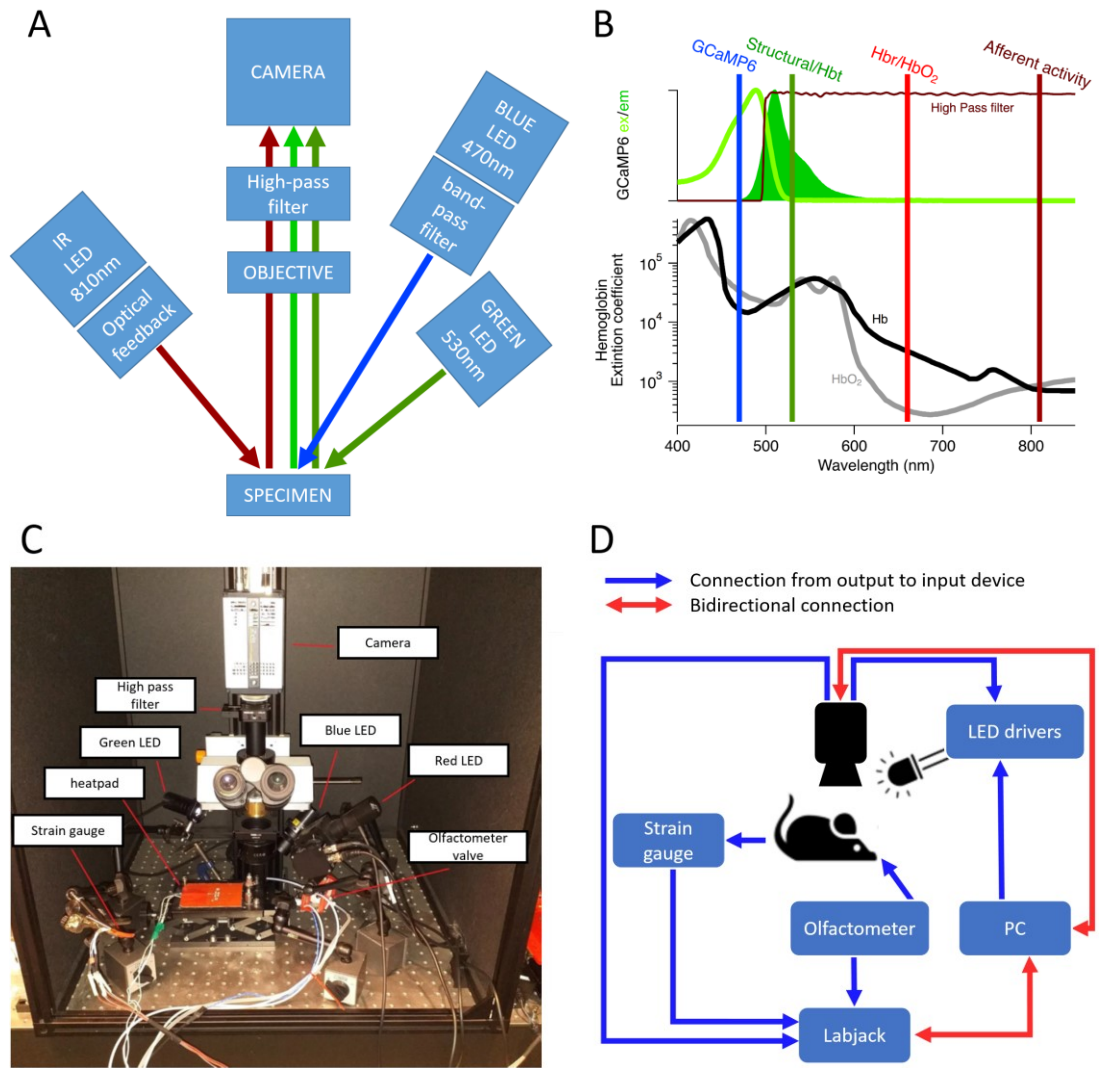


Figure 4.2 OMMI setup and control of equipment. Optical Multi-Modal Imaging (OMMI) is a low-cost solution for in vivo imaging of multiple neural populations. It provides simultaneous calcium and intrinsic optical imaging. **a)** Schematic of the light paths. The infrared 810nm LED is stabilised with an optical feedback photodiode to enhance intrinsic signals. High-pass filter cuts wavelengths below 500nm. The blue light is band-pass filtered at 457.5 \pm 2nm to limit Hbr/HbO₂ contamination. **b)** Wavelengths of illuminating lights for different imaging modalities: GCaMP6 (470nm), Structural (530nm), Hbr/HbO₂ (660nm), intrinsic (810nm). Excitation and emission spectrum of GCaMP6 (top). The absorption spectrum of oxygenated and deoxygenated blood (bottom). **c)** picture of the OMMI microscope rig. **d)** Connections schematic. The PC configures the camera and the LED drivers, and acquires frames from the camera. The Labjack sends the respiration and the olfactometer finale valve signals to the PC. The olfactometer is managed by a separate laptop.

4.3.1 Description of necessary Hardware

The OMMI rig consists of a camera and a set of LEDs corresponding to each modality required (Fig 4.2 A). ISOI requires a high well depth and high-speed camera because the variations in intrinsic signals are 1:10000. Therefore the OMMI rig uses a 16-bit Andor Zyla camera (Fig 4.2 C). Any similar featured camera compatible with the micro-manager software can be installed.

The default acquisition channels are defined by infra-red (810nm), blue (470nm), and green (530nm) LEDs respectively to provide ISOI, GCaMP, and structural movies (Fig 4.5 A, Fig 4.2 B). As intrinsic optical signals are very small, it is important to have a stable light source. We took advantage of the optical feedback functionality of cyclops LED drivers (open ephys) which embed a FET (field effect transistor) that acts as a precision voltage-controlled resistor. A glass slide was used to pick off ~4% of the light intensity which was measured with a photodiode (Thor labs, PDA36A-EC) to adjust the LED current to a constant intensity (Fig 4.2 A) by compensating for the temperature dependence and current/irradiance nonlinearities of the LED. This optical feedback enables a precise and fast onset of the LED with very short rise and fall times of 0.53 and 0.46 μ s, compared to a regular LED driver (Plexon LD-1) with times of 49 and 39 μ s. Additionally, it enhanced the driving accuracy to 0.41% vs 8.29 % for a regular driver (Test signal: 1 kHz 500 mA offset, 1A peak-to-peak sine wave, <https://open-ephys.org/cyclops>). The accurate reactivity is required as the infra-red LED is switched on and off in small periods during the camera shutter opening, and therefore need to quickly reach its light intensity to have a stable signal acquisition and shut down fast to not contaminate the next frame using another LED illumination.

We used a clean-up filter for the 470nm blue LED used to excite the GCaMP, bandpass filter (457.5 \pm 2nm) to limit the contamination of Hbr/HbO₂ ratio of absorption (Fig 4.2 B). Finally, the 530nm green LED provides a structural reference for FOV preview and motion correction. It can also be used as a corrective signal for deeper regions contaminated by blood dynamic. The system remains flexible as any LED can be set up to fill the need for specific fluorescent indicators or tissue optical properties. Furthermore, the hemodynamic can be recorded through the Hbr/HbO₂ ratio

of oxygenated and deoxygenated blood (Fig 4.2 B) which provides traces similar to an MRI BOLD signal.

Different wavelength signals are emitted from the brain and recorded on alternative frames (Fig 4.3 D, Fig 4.5 A). The light paths go through a CANON AF 50mm EF 1:1.8 objective which enables a FOV > 4.7mm (Fig 4.2 A). The high pass filter (Thor labs, cut am WL 500nm) rejects the blue light during GCaMP stimulation. Therefore, green and infrared lights reach the camera sensor. OMMI does not need a motorised filter optic changer for each modality but instead relies on controlled exposure widths through high-precision Cyclops LED driver (Fig 4.2 D). The open-source Cyclops make sure the LEDs are on only during their allocated frames (Fig 4.3 B).

The Labjack, a low-cost data acquisition device (Table 4.1), can record additional physiological signals. The Labjack analog inputs acquire the voltage values from an instrument, and these values are saved in a text file alongside frame timestamps. For monitoring, the respiration signal was recorded from a strain gauge but an oximeter designed for mice (Starr, MouseOx Plus) can be used as well.

material	price
Cyclops LED Driver (x3)	465£ (545€)
LabJack U3-HV - USB Multifunction Data Acquisition Unit	130£
M530L4 - 530 nm, 370 mW (Min) Mounted LED, 1000 mA	222.38£
M470L4 - 470 nm, 760 mW (Min) Mounted LED, 1000 mA	222.38£
M810L4 - 810 nm, 363 mW (Min) Mounted LED, 1000 mA	191.25£
FL457.9-10 - Ø1" Laser Line Filter, CWL = 457.9 ± 2 nm, FWHM = 10 ± 2 nm	81.16£
FELH0500 - Ø25.0 mm Premium Longpass Filter, Cut-On Wavelength: 500 nm	98.25£
PDA36A2 - Si Switchable Gain Detector, 350 - 1100 nm, 12 MHz BW	260.52£
total	2600.94£

Table 4.1 OMMI materials. The required equipment to custom-build and run an OMMI system. Any camera compatible with the micro-manager camera-controller python library will suit the system, given minor changes to bring.

4.3.2 Control of equipment

The OMMI system is controlled on the PC via a GUI implemented in python that uses mainly the micro-manager and PyQt libraries (Fig 4.3 A). The PC controls the LED drivers and the camera for the different modes of alternated illuminations and the exposure time of the LEDs and the shutter. The PC receives frames from the camera and signals from the Labjack, saving it all with common timestamps. The camera sends its shutter signal to the Labjack and the LED drivers so illumination and data acquisition are synched with frame acquisition (Fig 4.2 D). The Labjack acquires the signal of each frame exposure from the camera (FIRE signal), with another signal such as the olfactometer final valve and the respiration recorded through a strain gauge (Fig 4.5 D). The Labjack allows to start or/and stop a "Run and Save" acquisition with an external Sync/trigger signal (TTL). The imaging bouts of the experiment can start with a rising edge and stop with a falling edge. 30 seconds of imaging separated by 1 minute helps reduce bleaching of the fluorescent indicator. Overall, 5 USB ports are required on the PC for the 3 LED drivers, Labjack, and camera. This excludes another Labjack to generate a sync/trigger signal and the olfactometer, which were both set on a separate laptop, from which the stimulation protocol was managed.

A OMMI

Run and Save File Splitting Odour Map Creation

Camera Settings

Exposure : 10.07 **1**

Real exposure : 10.071

Approx Framerate **2** 43.11 Test Framerate **3** 48.19

Bit depth : 16-bit (low noise & high) **4**

Binning : 4x4

Shutter mode : Global

Overlap : Off

Live Histogram Crop **5**

LEDs

GREEN 0.50

RED 0.70 (%exp)

BLUE 1.00 **6**

7 Default Settings **8** Load Settings **10**

9 load Zyla Unload Zyla

Acquisition Settings

Duration (s) 50.00 **11**

Sequential **12**

R-B **14**

Green 0 **13**

Red 0

Blue 0

Green frame each (nb frames) : 5 **15**

Red and Blue **16**

Saving folder : E:/OIS Data/191029/test Browse... **17**

Name : DefaultName **18**

Frames per file : 512 Max file size (GB) : 0.35

19 ARDUINO SYNC Max duration per file (s) : 10.24

Start Trigger **22**

Stop Trigger

20 RUN AND SAVE **21** LOOP

23 ABORT

24 **25** 29%

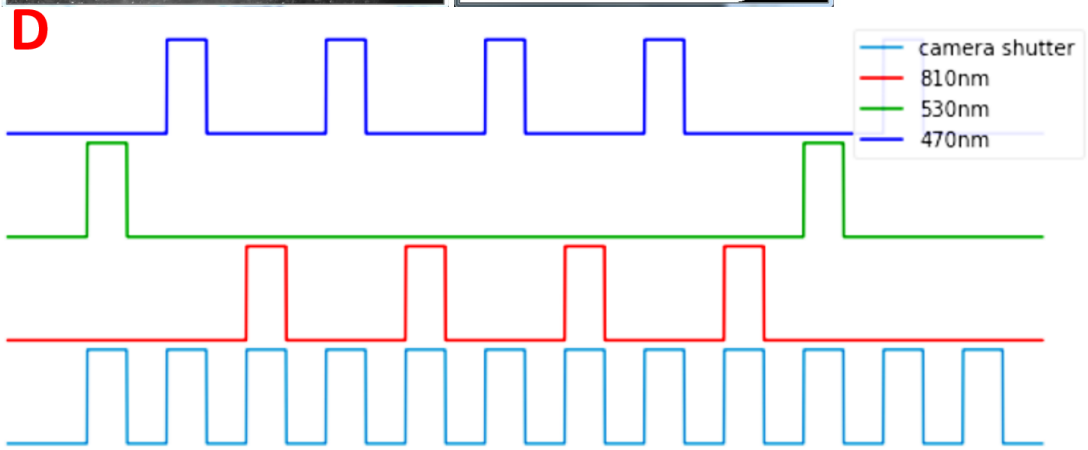
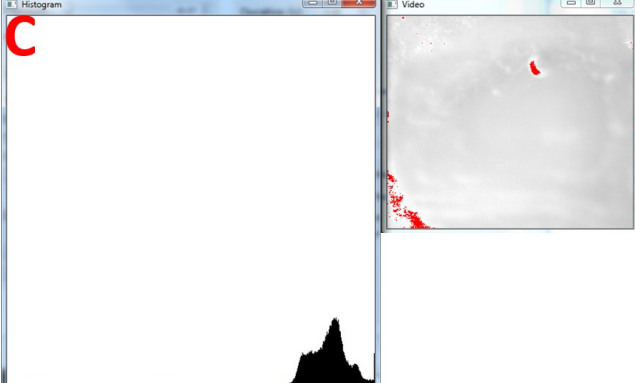


Figure 4.3 OMMI Graphical User Interface. An experiment is initialised and run in the GUI. The user inputs camera and LEDs settings, focus on the animal brain then runs an imaging protocol. **A.** "Run and Save" panel of the OMMI GUI. 1. Exposure slider and spin box: set the exposure of the camera (ms). The text label displays the actual exposure of the camera. Note that there is always a difference between them. 2. Calculate and display an approximation of the framerate based on the documentation of the camera 3. Test the framerate of the camera with the current settings. It launches an acquisition of 5 frames and displays the average frequency between these frames. Note that (2) and (3) are in frame per second (fps). 4. Display a live video from the camera and plot the histogram of the frame displayed. 5. Display an image snapped by the camera and the user can draw an ROI to modify the actual ROI of the camera. 6. The thick box allows the user to choose which LED is ON. The spin box determines the illumination time of the LED in a ratio of the exposure. 7. Reset the settings to the default settings. 8. Allows the user to choose a .json file that contains the settings of a previous experiment/test. 9. Load the Zyla camera 10. Unload the Zyla camera. 11. Estimated duration of the experiment. It is used to create the right number of .tif files to feed images during acquisition. A good practice is to use a larger duration estimate. 12. Thick box to check if you want to use the Sequential mode. Sequential mode creates a LED sequence containing the number of green, red and blue frames specified in (3). During the acquisition, it will loop through this list of LED in the following order : [nb of red, nb of green, nb of blue]. 13. Allows the user to choose the number of frames for each channel. Used in Sequential mode only. 14. Thick box to check if you want to use the R-B mode.) R-B mode creates a LED sequence containing an alternation of a red and a blue frame ("Red and Blue") or red frames only ("Red only") or blue frames only ("Blue only"). Afterward, a certain number of green frames are inserted in this sequence at a constant interval. 15. Spinbox that determines the interval (in number of frames) between 2 green frames. 16. Allows the user to choose between "Red and Blue", "Blue only" or "Red only". 17. Opens a pop-up window to select a folder where to save all the experiments files. 18. Names the experiment. Later this will create a folder containing all the files related to an experiment. 19. Sets the number of frames saved per .tif file. Base on this number, the file size is estimated based on ROI and the duration of recording in a file is estimated based on framerate. 20. Synchronises the Arduinos of each LED driver with the current acquisition settings. 21. Starts a "Run and Save" acquisition which will last the duration specified in (11). 22. Allows to start or/and stop a "Run and Save" acquisition with an external signal (TTL). It will start with a rising edge and stop with a falling edge. 23. Starts a "Loop" acquisition. 24. Aborts any ongoing acquisition. 25. A progress bar for a "Run and Save" acquisition. (Adapted with permission from Louis Vande Perre's manual). **B.** 'Crop' window **C.** 'live histogram' window (left). The saturated pixels appear in red on the cropped FOV (right). (OB surgery from Mark Conway). **D.** Pulse trains of the 3 LEDs and the camera shutter in R-B mode with a green frame every 5 frames.

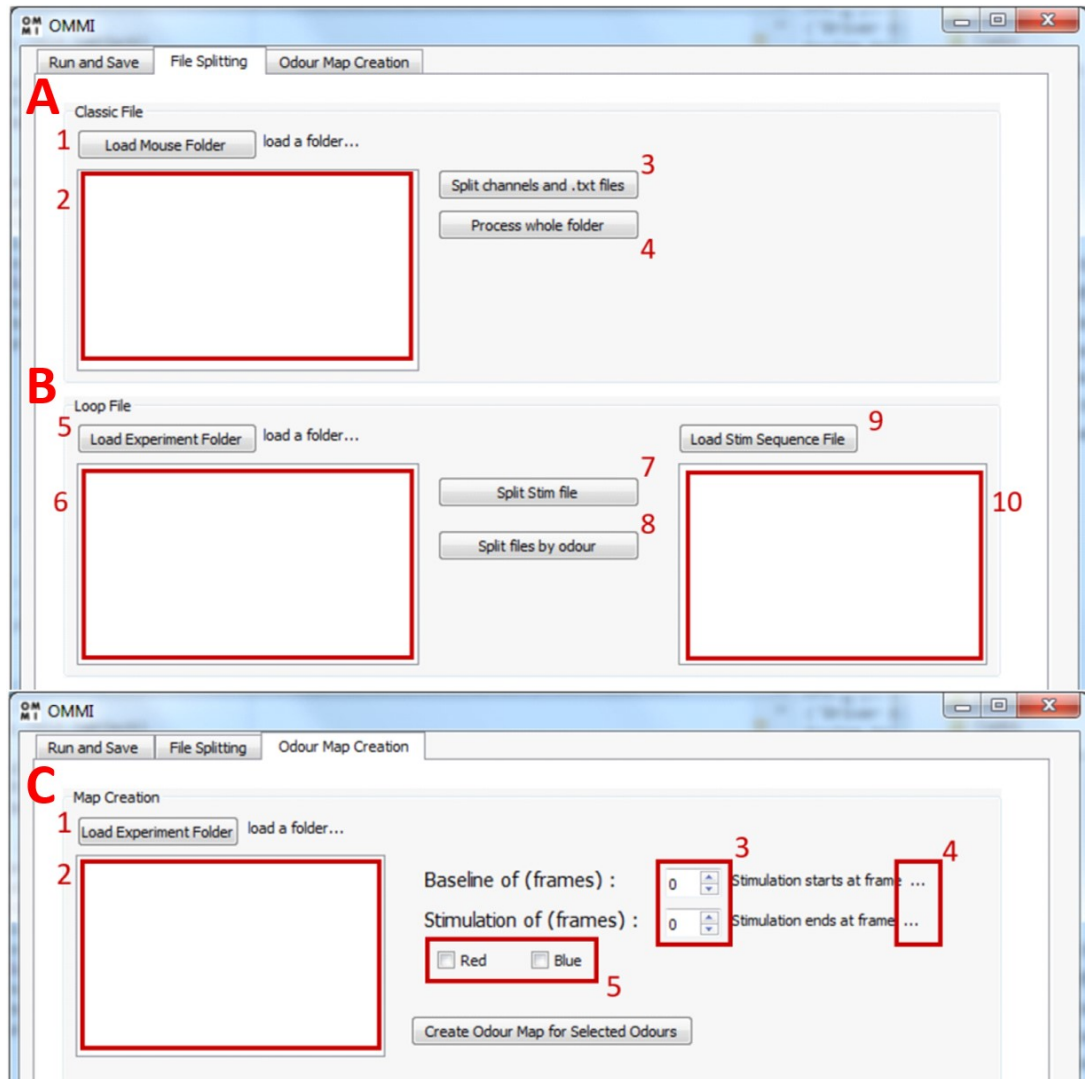


Figure 4.4 File splitting and odour map creation in the GUI. Tools to preview results. The channels in the files are demixed. Stimulus maps are then created. **A.** Classic File (generated by "Run and Save" acquisition). 1. Opens a pop-up window to select a mouse folder. 2. Displays the experiment folders within the mouse folder. 3. Creates a "Processed" folder (inside the experiment folder selected) with the .tif and .txt for each colour channel. 4. Does the same as (3) for all the experiment folders displayed in (2). **B.** Loop File (generated by "Loop" acquisition). 5. Opens a pop-up window to select an experiment folder. 6. Displays the .txt contained in the experiment folder. It corresponds to the number of "sync pulses" that triggered a continuous acquisition 7. Creates a "#stimName_processed" folder (inside the experiment folder loaded) within the .tif and .txt for each colour channel. 8. Creates a "OD#odNumber_processed" folder for each odour specified in the stim sequence file. In one "odour" folder you will find the split files for each stimulation associated with the odour of this folder. 9. Opens a pop-up window to select a .json file generated by the olfactometer program. This file contains the sequence of odours used to stimulate the mouse. 10. Displays the

sequence of odours. To use (8), the number of actual stimulations recorded (6) must be equal to the number of stimulations in the stim sequence (10). **C.** Tool designed to create an odour map for a single stimulation recording. 1. Opens a pop-up window to select an experiment folder. 2. Displays the folders that are inside the experiment folder. The user will need to use the File Splitting tool first. 3. Allows the user to choose the number of frames that are used to average the baseline and the stimulation frame. 4. Indicates at which frame the stimulation ends and starts. 5. Allows the user to create a red channel and/or blue channel odour map.

4.3.3 Experimental design: A walkthrough of an experiment

The GUI allows the control of the camera and set up of experiment protocol (Fig 4.3 A). It permits to choose which modalities of imaging to use and in which proportions. For example, the figure 4.3 D shows an alternation of blue and red frames while doing a structural green frame on every 5 frames. The left side of the GUI gives control of the camera settings such as the shutter exposure bit depth, binning, shutter mode, and overlap (Fig 4.3 A). On the right side, acquisition settings give LED order configuration and saving options. The configuration and start of an experiment go as follows:

- 1) **Focus the animal:** To record from glomeruli at the surface of the brain, the focal plane must be adjusted so the superficial blood vessels appear sharp. The 'live histogram' button (4) opens a live video window from the camera. The green LED is ticked on (6 in Fig 4.3 A), as it is the most adapted wavelength to identify vasculature (Fig 4.2 B). The user can adjust the height of the platform (Fig 4.2 C) while looking at the display to focus on the brain.
- 2) **Crop the FOV:** There is an option to crop the FOV in a smaller region of interest (5 in Fig 4.3 A, Fig 4.3 B), which can increase the frame rate and save storage space, as the camera sensor scans fewer pixels. It also helps for adjusting the LED intensity only on the region of interest.
- 3) **Histogram to set LED intensities:** The live histogram permits adjustment of the intensity of the LED to maximise the range of

acquired values (Fig 4.3 C, left). The saturated pixels appear in red (Fig 4.3 C, right). This is particularly relevant for the ISOI channel (red LED) where the user wants to spread the histogram to the highest values, to increase sensitivity for measuring changes in intrinsic optical signals.

- 4) **Set up LED stim protocol:** The acquisition settings panel (12-16) controls which LEDs to utilise and at which frequency. I used the R-B mode (14), alternating red and blue illuminations of frames, with a green illumination every 5 frames, as a structural frame for movie registration purposes. An alternative sequential mode (12) lets the user decide on any combination of LEDs. Usually, a framerate of 50Hz is divided across the red, blue, and green channels (R-B mode gives ~25Hz per channel). The 'Arduino Sync' button synchronises the Arduino of each Cyclops LED driver with the current acquisition settings (20). The drivers listen to the camera shutter and their programming tells them which pulses to activate for (Fig 4.3 D). Furthermore, the exposure times of each LED can be adjusted as a ratio of the frame acquisition exposure (6). Smaller values can be inputted to avoid light leaks between frames of different modalities, while higher values enhance the signals.
- 5) **Set up saved files:** The user sets a saving folder named after the date and the animal (17) that will be filled with experiments named in (18), for example, 'fasted', 'drugs', then 'glucose'. Movies containing the interleaved frames from all channels are saved as tiff files. The number of frames per file can be set, according to the preferred size or duration per file (19). If using loop mode, it is suggested to make one file per stimulus.
- 6) **Triggered start:** Acquisition can be set as a continuous movie ('run and save') recording or by movie bouts ('loop') (Fig 4.3 A). For the loop mode, the Labjack listens to a trigger input that signal starts and ends of acquisitions of movies bouts (22). The stimuli sequences are delimited by the rising and falling edges of a sync signal generated by another Labjack. I embedded it in my olfactometer protocol script (appendix A), which ran on a separate laptop. The 'loop' mode enables to record only around stimulations times, which saves memory storage

and reduces the fluorophore photobleaching. The sole advantage of the continuous mode is to gather measurements of baseline between stimuli, which can be used for baseline correction, and to measure spontaneous activity.

- 7) **Run experiment:** A 'Run and Save' acquisition is a continuous acquisition mode where a single .txt contains all the frame-related data and multiple tiff files contain the images data. On the other hand, a 'Loop' acquisition is a discontinuous acquisition mode made of multiple acquisitions. These small continuous acquisitions are triggered by an external signal. All experiments used in this thesis used the 'loop' mode.
- 8) **Saved data:** The data is saved as tiff files because they are easy to examine with FIJI/imageJ. The tiff files are saved with one or multiple associated text files containing in each row the information linked to a frame: the channel (R/G/B), a timestamp, the olfactometer finale valve opening state, and the respiration signal value. A JSON file with all the GUI parameters is also saved.
- 9) **Preview results:** Post-experiment, the user can visualise each channel movie after deinterleaving the frames using the 'File Splitting' panel (Fig 4.4 A&B). Another 'Odour Map Creation' panel allows generating stimulation maps (Fig 4.4 C). These odour maps are obtained by the division of the stimulation frames average by the baseline average.
- 10) **Example results:** After registration and processing, afferent input (red channel) and interneurons (blue channel) odour-evoked signals are extracted (Fig 4.5).

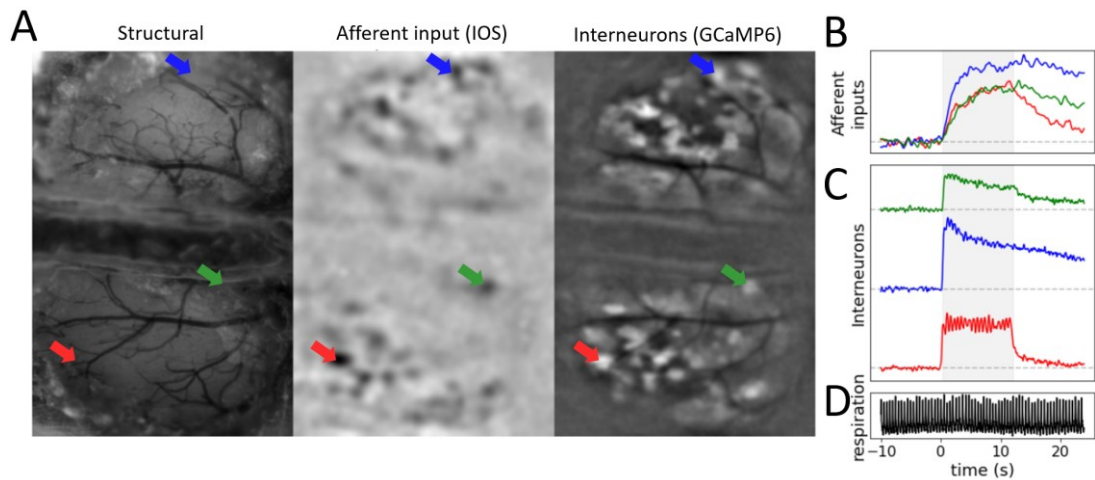


Figure 4.5 OMMI results. OMMI produces odour-evoked responses for two neuron populations: the olfactory sensory neurons (OSN) with intrinsic signal optical imaging and the periglomerular cells (PGC) with one-photon calcium imaging. **a)** The average projection of all the green frames serves as a structural picture (left). Odour response maps for ethyl tiglate (average of 5 presentations) for the OSNs (center) and PGCs (right). **b)&c).** Normalised responses to a 10-second stimulus of ethyl tiglate for the glomeruli OSNs (B) and PGCs (C) referred by the arrows in a). **d)** respiration signal of a single trial.

4.3.4 Analysis of Experiment

All the OMMI experiments followed the same protocol depicted in chapter 3 but with stimuli of 10 sec spaced by 1 minute (Fig 3.1), each experiment consisted of movie bouts corresponding to 4 odours and 3 concentrations, repeated 5 times. I processed the ISOI and GCaMP movies (Fig 4.5 A) using a custom python pipeline and then extracted glomeruli traces from them for both OSNs and PGCs (Fig 4.5 B&C). The whole experiment was registered using a spatial phase alignment method using only the structural frames (Fig 4.6 A), which provides substantial time-saving. The FOV should however not move, except if the animal is injected or withdrawn, which is the case when drugs had to be applied under the coverslip.

The movies were normalised by removing the average baseline image before stimuli and then divided by that same image. This gives $\Delta F/F$ and $\Delta R/R$ movies, respectively for GCaMP and ISOI. The reflectance $\Delta R/R$ movies were inverted to a relative absorption $\Delta A/A$ (Fig 4.5 B, Fig 4.7 C). For manual segmentation purposes, a spatial band-pass filter was then applied between 10 and 100 μm to get rid of the global diffuse signal that encompasses

background activity such as the granule cells activity in the deeper layer. I then averaged all 5 trial movie bouts of a same stimulus together to create a high SNR concatenated movie where I could easily inspect glomeruli activity in FIJI/imageJ (Fig 4.6 B&D). The movie was enhanced by downsampling 10 times in time then applying a Gaussian filter with a $\sigma=3$ in Z. I segmented the glomeruli with ovals, using the FIJI ROI manager, and saved them in a zip file (Fig 4.6 C). This method permits to segment ROIs while verifying both GCaMP and intrinsic signals spatially (Fig 4.6 B) and temporally (Fig 4.6 D).

I extracted glomeruli OSN and PGC responses (Fig 4.5 B&C, Fig 4.7 C&D) using the ROIs previously segmented. From the raw movies, the averaged pixels value across time was extracted from each ROI and a 10 pixels surrounding annulus. The surrounding signals were removed from the ROI signals with a coefficient of 0.9, to remove background contamination. The normalised signal ($\Delta F/F$ or $\Delta A/A$) was then computed for each response as the trace minus the mean of the 3-second baseline, divided by the mean of the baseline. The integral of a 5-trials averaged response was used as a measure of activity. Only responses with an SNR above 2 were kept for further analysis.

In my case study, I recorded simultaneous OSN and PGC responses to 4 odours (2-heptanone, isobutyl propionate, ethyl tiglate, isoamyl acetate) at 3 concentrations (0.1%, 1%, 10% air dilution). Both OSN and PGC glomeruli showed a similar concentration dependence. Figure 4.8 A shows highly correlated linear least-squares regression between OSN and PGC activity, for 2 glomeruli. Across 7 animals, OSN and PGC activity linear regressions were well correlated with a mean correlation coefficient of 0.85 ($n= 271$ glomeruli, $\text{mean} \pm \text{SEM} = 0.85 \pm 0.00842$) (Fig 4.8 B). This shows that the OSN and PGC sides of a glomerulus activate similarly along with concentrations.

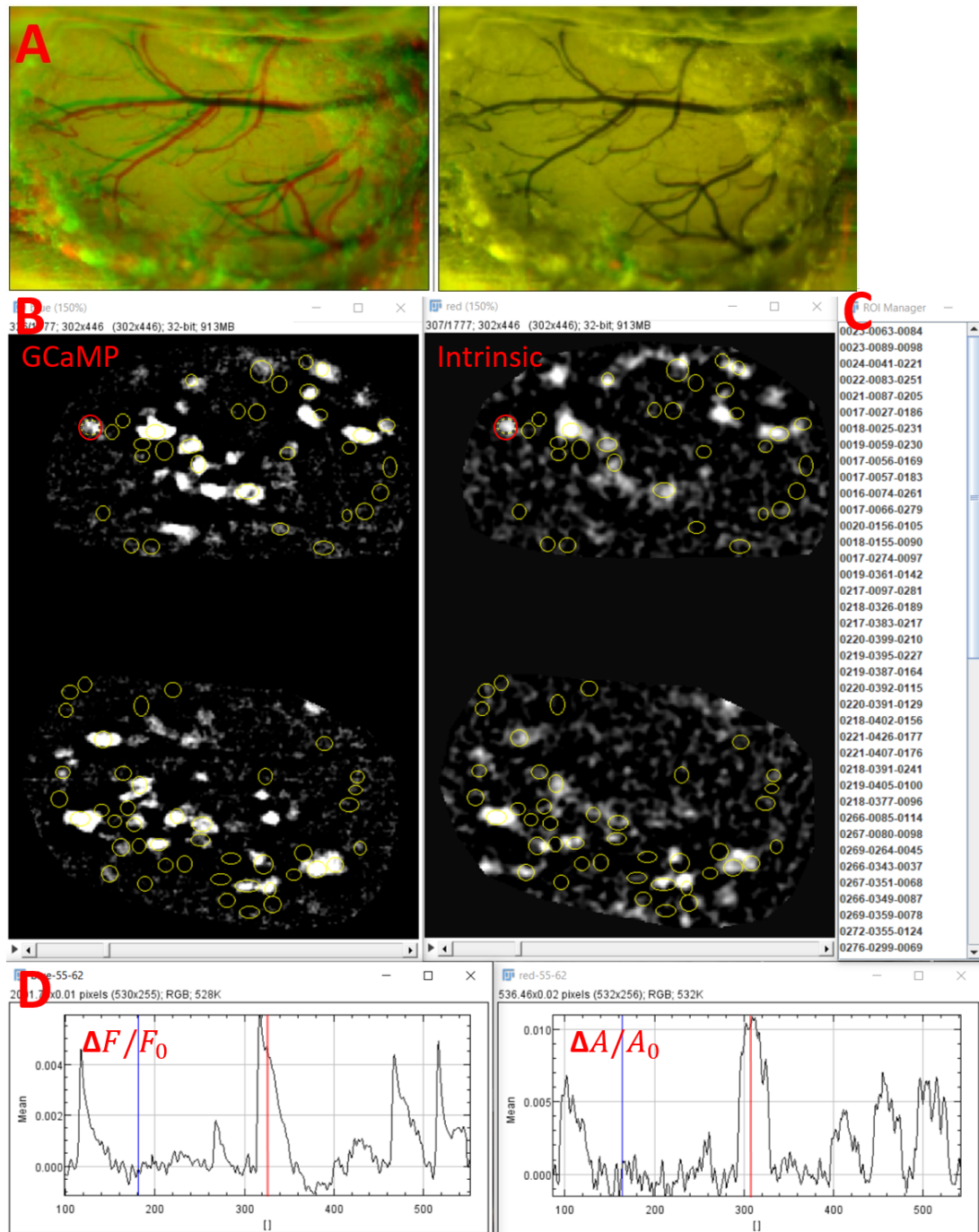


Figure 4.6 preprocessing and segmentation of glomeruli. The OMMI data is processed in a python notebook, then segmented manually in FIJI with the help of an enhanced movie. **a)** Average of structural frames (control session in red, drugs in green) before (left) and after (right) phase-base registration. **b)** Yellow ovals are manually apposed glomeruli ROIs. 5-trials averaged downsampled movies of the calcium imaging channel (left) and intrinsic optical imaging channel (right). **c)** ROI manager in FIJI. **d)** Z-axis profiles of the red ROI in b) to verify the consistency of temporal activity in both channels.

4.4 Circuit manipulation: blocking afferent glutamatergic inputs

OMMI gives the possibility to investigate neural circuits with simultaneous measurements from multiple populations. Here I disrupted the feedback inhibition implemented by OSNs and PGCs. By blocking AMPA and NMDA glutamatergic receptors in PGCs, I expected a higher OSN activity and a lower PGC activity. Vincis et al. (2015) already showed diminution of the afference intrinsic signals following application of glutamatergic antagonist.

To manipulate the circuit under OMMI, I developed a method to remove the cover glass mid-experiment and apply a drug topically on the dorsal olfactory bulb. Instead of using dental cement or glue to seal the coverslip after a craniotomy, I used quick-drying silicon rubber (wagnersil 22 NF, wagner dental) which is easy to peel off. The rubber must be carefully chosen to not be fluorescent under any of the LED lights. After the control recordings, I could peel off the window, suck up the ACSF gel above the bulb and add back the ACSF gel mixed with drugs. The brain was then again covered by a 5mm cover glass, and terminally sealed with glue. An alternative would be to make a small chamber above the bulb and perfuse the drugs with a Luer syringe. This was revealed impractical as it is difficult to not induce pressure upon the brain.

Applying glutamate intake blockers in the glomerular layer enables to isolate the PGCs circuitry from the sensory afference. It also blocks the feedback excitation from MTCs. To put in evidence the feedback inhibition provided by the PGCs to the OSNs, I applied the AMPA receptor antagonist NBQX with the NMDA inhibitor D-AP5. The ACSF gel applied after the fasted-control imaging was made of agar ACSF with 1 mM of D-AP5 and 0.1 mM of NBQX. In one animal, the figure 4.7 A&B shows the maximum of all odour responses map of the dorsal olfactory bulb in control versus glutamate blockers, respectively for OSNs and PGCs. As expected, I observed an increase in OSN activity (Fig 4.7 A) and a decrease in PGC activity (Fig 4.7 B). The PGCs are less activated because the afferent glutamatergic transmission is reduced (Fig 4.7 D). The OSNs activity is heightened as a result of less PGC feedback inhibition (Fig 4.7 C). Across 206 glomeruli, the glutamate blockers seemed less effective at higher concentrations due to the competitive aspect of the glutamatergic antagonist, as more glutamate

released by the OSN with odour concentration is competing with a fixed amount of iGluR blockers (Fig 4.7 E). This is reflected in the reduced effect of the drug on PGCs while concentration increases (0.1%, 1%, 10% oil dilutions: $100 \pm 4 \%$ versus $31 \pm 1 \%$; $100 \pm 3 \%$ versus 41 ± 1 ; $100 \pm 2 \%$ versus $53 \pm 1 \%$; one-sided Wilcoxon signed-rank tests: $p < 0.001$) (Fig 4.7 F). The OSN activity shift between control and drugs also decreases with concentration (0.1%, 1%, 10% oil dilutions: $100 \pm 4 \%$ versus $215 \pm 5 \%$; $100 \pm 3 \%$ versus 142 ± 3 ; $100 \pm 2 \%$ versus $133 \pm 2 \%$; one-sided Wilcoxon signed-rank tests: $p < 0.001$) (Fig 4.7 F).

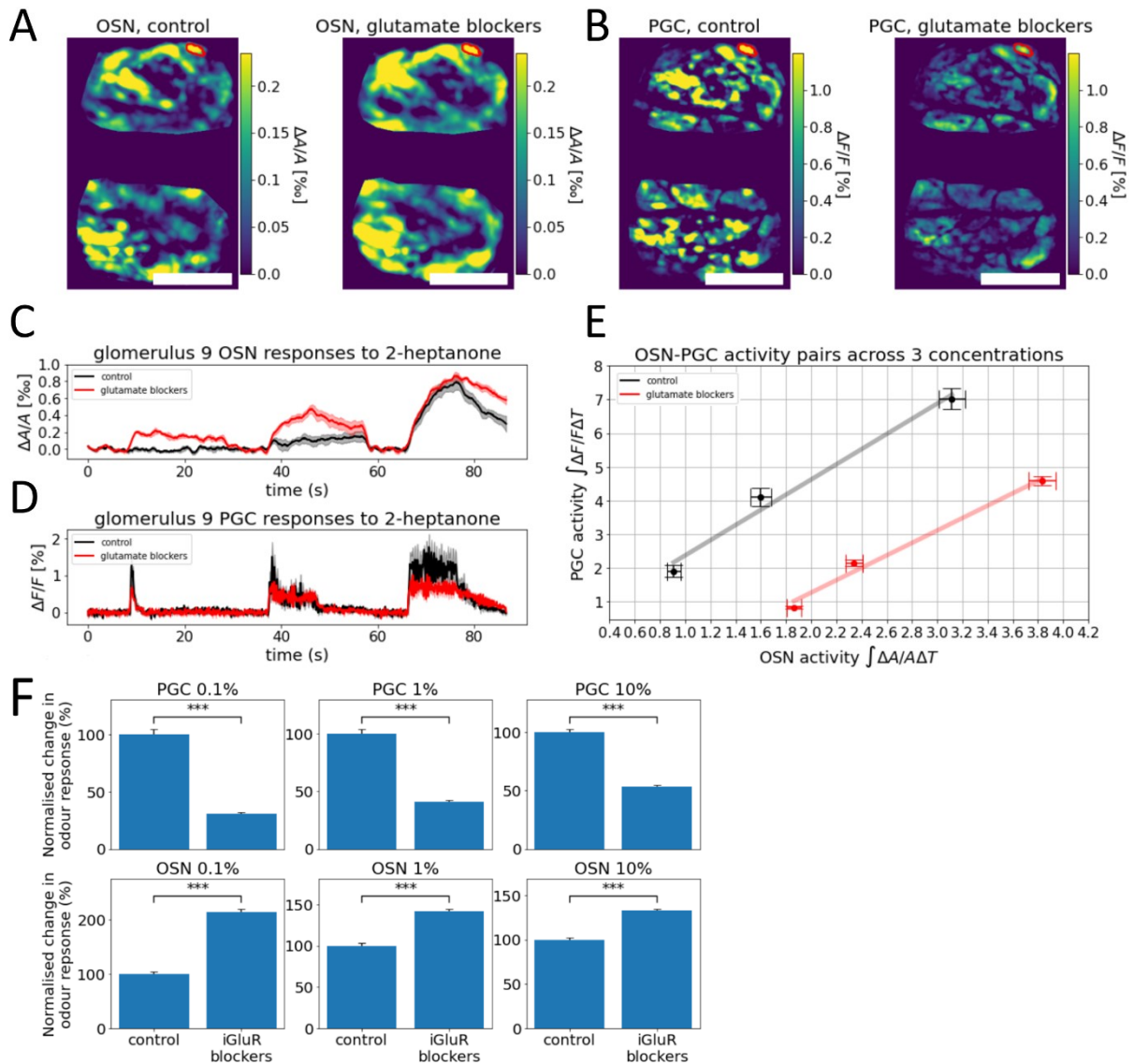


Figure 4.7 Changes of activity in olfactory sensory neurons and periglomerular cells following iGluR blockers. Imaging of OSNs and PGCs under OMMI before and after topical application of 0.1 mM NBQX and 1mM D-AP5 in a fasted animal. OSN activity decreases as the PGCs provide less feedback inhibition due to reduced glutamate intake. 2-heptanone, isobutyl propionate, ethyl tiglate, and isoamyl acetate were delivered to the animal 5 times for 10 seconds, spaced by 1 minute. This was repeated for the odour diluted in air at 0.1, 1, and 10%. **a)** Maximum of all the frames of the OSN channel when any odour was provided at 10% before and after glutamate blockers. **b)** Same as a) for PGCs. **c)&d)** Example of glomerulus responses to 2-heptanone diluted at 0.1, 1 and 10% in air for the red ROI in (a), b). **e)** PGC activity of all responses across the 3 air dilutions plotted against the OSN activity of the same glomeruli. The activity is defined by the integral of the signal during a stimulus. (264 glomerulus-odour pairs from 74 glomeruli). **f)** Changes in odour-evoked responses in PGCs and OSNs per concentration, normalised to control responses. Bars are the standard error of the mean. Scale bar: 1mm.

Across 699 glomeruli-odours pairs from 206 glomeruli in 3 mice, the figures 4.8 C and D respectively show the difference of activity for PGC and OSN glomeruli with the application of glutamate blockers. The red lines represent the mean of these distributions. PGCs overall decreased in activity and OSNs increased. In PGCs the decreasing difference grows with concentrations (means for 0.1, 1, and 10%: -0.137, 0.0248, -0.308). In OSNs, the increasing effect diminishes with concentration (means: 0.01, 0.007, 0.008), which is expected from the competitive nature of the glutamate antagonist. The NBQX and D-AP5 change in an opposite manner the OSNs and PGCs activity. This means the OSN-PGC feedback inhibition computation is effectively well targeted by this circuit manipulation.

This manipulation proves the utility of OMMI and the removable coverslip method for investigating neural circuit computations in vivo.

4.5 Conclusion

OMMI provides a reliable and low-cost solution that enables multi-population imaging with only one fluorescent indicator. The system is adaptable to updates for any changes of excitation wavelengths, parallel acquired signals, or awake mice experiments. Any dorsal brain region can be imaged. However, deeper neurons can be imaged given the use of the green LED signal to correct for blood dynamic contamination. Finally, OMMI can provide an easy mean to study neurovascular coupling by setting one modality on hemodynamic and another one or two on neural activity.

This method is ideal for the study of how the state affects a circuit by its ability to measure both neural population activity and the population that provides its input. Across the different stages of the OB, the afferent OSN and interneuron PGC, the glycemia state may affect dynamic uniquely. Furthermore, we can observe how a state or context affects the feedback micro-circuit.

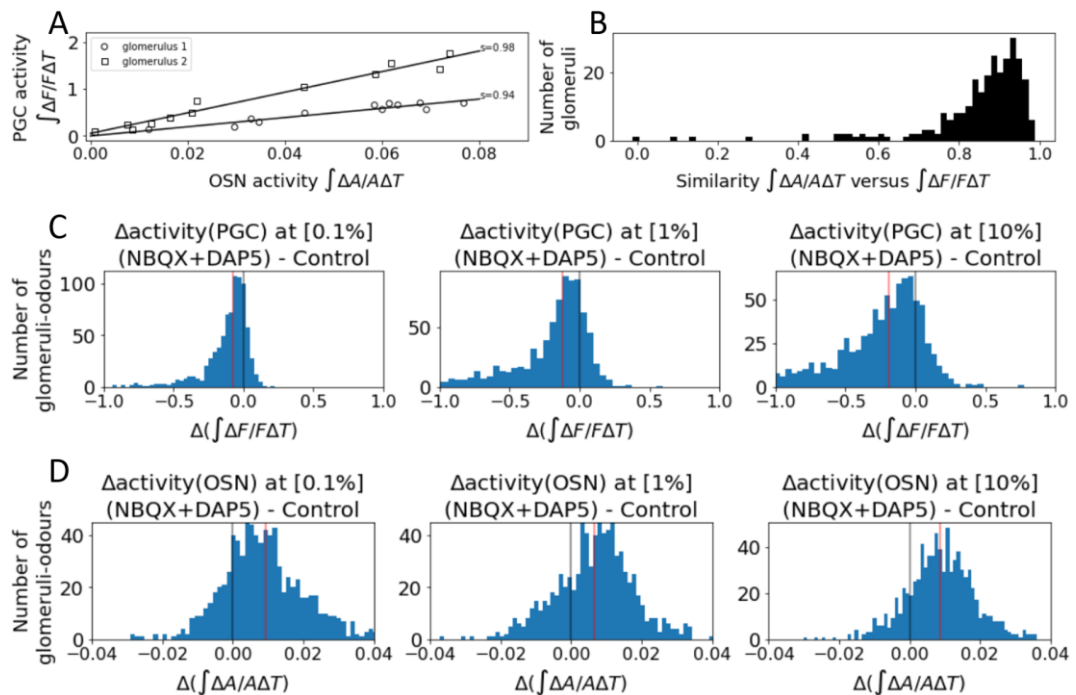


Figure 4.8 PGC-OSN feedback inhibition reduces following iGluR blockers. Effect of topically applied glutamate blockers (0.1 mM NBQX,

1mM D-AP5) on OSN and PGC neurites in glomeruli. **a)** linear least-squares regressions of OSN-PGC activity couples from 2 glomeruli, using 4 odour responses at 3 concentrations. OSN and PGC neurites activity in glomeruli are well correlated. **b)** Histogram of all correlation coefficients of OSN-PGC activity linear regression for 271 glomeruli in 7 mice (mean \pm SEM= 0.85 \pm 0.00842). **c)** Histograms of difference in PGC activity for all odours across the three air dilutions. red bar is the mean. (means \pm SEM= -0.13716 \pm 0.00788, -0.24843 \pm 0.01278, -0.30815 \pm 0.01346). **d)** Histograms of difference in OSN activity for all odours across the three air dilutions. red bar is the mean. (means \pm SEM=0.01013 \pm 0.00048, 0.00701 \pm 0.00043, 0.00898 \pm 0.00037). 699 glomerulus-odour responses per concentration in 3 mice.

Chapter 5

The effect of blood glucose on olfactory sensitivity

5.1 Introduction

Olfactory sensitivity is modulated by the satiety state which is conveyed in the organism by specific nutrients (Soria-Gómez et al, 2014; Aimé et al, 2007; Berg et al, 1963). The olfactory bulb is known to be a centre of nutrient-sensing (Julliard et al, 2017; Tucker et al, 2013). This enables the olfactory bulb to integrate both the internal metabolic state and exterior food cues. A satiated mouse would have a lower ability to detect a food source and a fasted mouse would have a heightened ability. Secondly, to minimise computations, this adaptation of olfactory sensitivity should happen early in the sensory circuit rather than in several regions downstream. Multiple neuron populations in the OB are sensitive to different nutrients. In particular, the MTC has been shown to sense changes in extracellular insulin and glucose (Tucker et al., 2013). Here, I investigate if increased blood glucose would affect the inhibition of the very first synapse of the OB, in the glomerular layer, via the first interneurons in the olfactory information pathways, the periglomerular cells.

There are a few hints for metabolic-sensing occurring in glomeruli, as in the presence of the glucose transporter GLUT4 (Al Koborssy et al., 2014) and the glucose and insulin-sensitive potassium channel Kv1.3 (Tucker et al., 2013; Fadool et al, 2000). These were found heterogeneously in glomeruli so I expect heterogeneity in glucose-modulation in regards to activated glomeruli. The question I am asking is whether increased blood glucose modulates the activity of PGCs and therefore modulates transmission at the first synapse in the OB.

To tackle these questions, we investigated the odour-response characteristics of PGCs using two photons imaging. Protein expression in PGCs was gathered with immunostaining. In a corollary to the two-photon imaging, and to record the afference, I used widefield one-photon imaging combined with intrinsic imaging under the OMMI system described in the previous chapter. To study the effect of glycemia, I imaged the mice with low and high blood glucose using stimuli determined to elucidate any changes in the sensitivity. I expected to see the PGCs more activated with heightened

glucose which would then result in increased inhibition to the afferent input. The OSN-PGC feedback inhibition would be up-regulated by a glucose increase and therefore lessen olfactory sensitivity to odours.

5.2 Sensory-metabolic integration

5.2.1 Expression of metabolically sensitive proteins

We began by examining the presence of two metabolically active proteins, GLUT4 and Kv1.3. We used GAD-67 GFP mice to label inhibitory interneurons and labelled thin sections of their olfactory bulbs with a GLUT4 mouse antibody with a donkey anti-mouse 594 secondary antibody, and a Kv1.3 mouse antibody with goat anti-mouse 555 secondary antibody.

With corroboration to Koborssy et al (2014) finding of the heterogeneous presence of GLUT4 in glomeruli, we found that most PGCs expressing GAD-67 were also expressing GLUT4 (817/926) (Fig 5.1 B&D). The GLUT4 seems spread across the cytoplasm. We used GAD67 GFP mice and GLUT4 antibodies. However almost half of the GLUT4 stained neurons were not GAD67 (972/1789) (Fig 5.1 B&D). Figures 5.1 C and E show the immunostaining for Kv1.3 potassium channel in GAD67 GFP mice. About half of the GAD67+ cells colocalized with Kv1.3 (435/741). However, a vast amount of Kv1.3+ cells were not GAD67 (741/1176). In both GLUT4 and Kv1.3 cases, the cells lacking GAD67 are likely GAD65 PGCs or ETCs. The observed GAD67+ PGCs make up roughly half of the PGCs (Kiyokage et al., 2010). Kv1.3 seems present in loci of the membrane or proximal primary dendrite (Fig 5.1 E, left). Kv1.3 seems implicated in insulin and glucose-sensing (Tucker et al., 2013; Fadool et al., 2000). GLUT4 enables the transport of glucose inside the cell and translocates to the membrane in response to insulin receptor activation. Thus, Figure 5.1 indicates the OB glomerular layer is an ideal place for sensing glucose as the latter reaches it and there are neurons with the machinery to sense it.

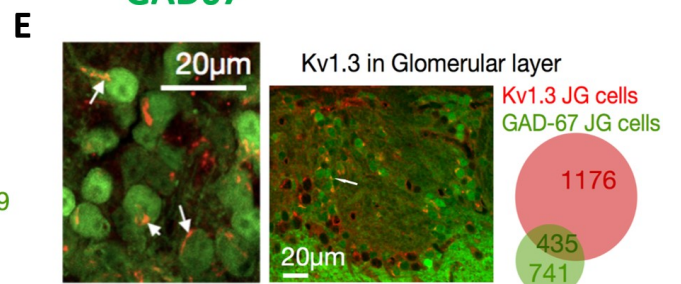
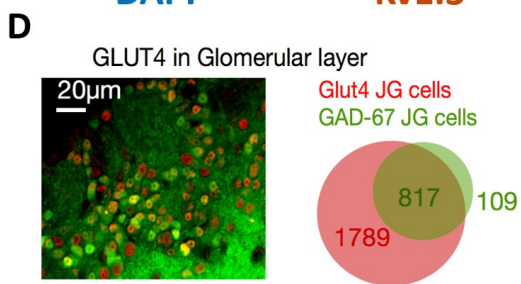
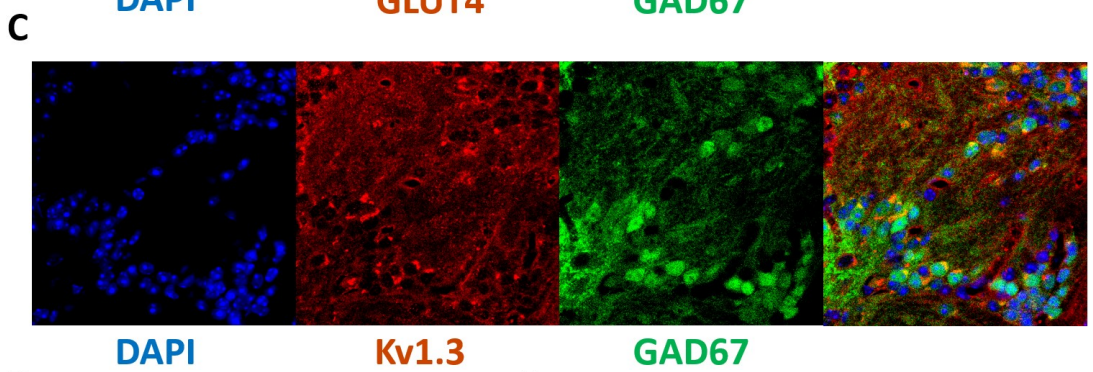
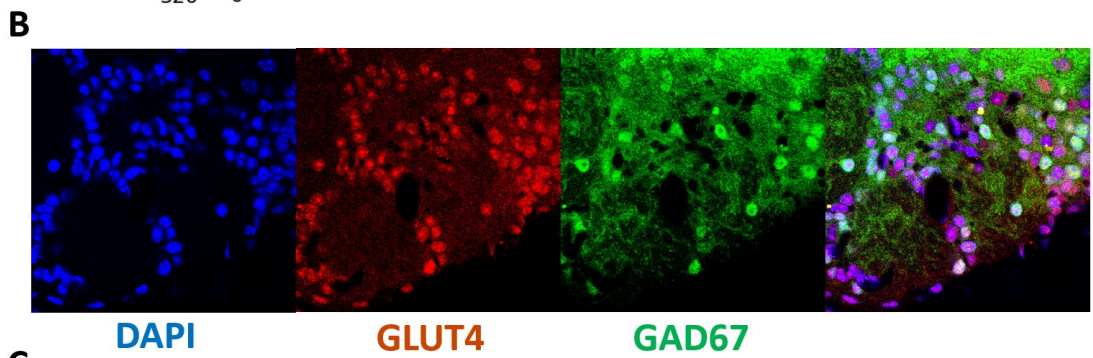
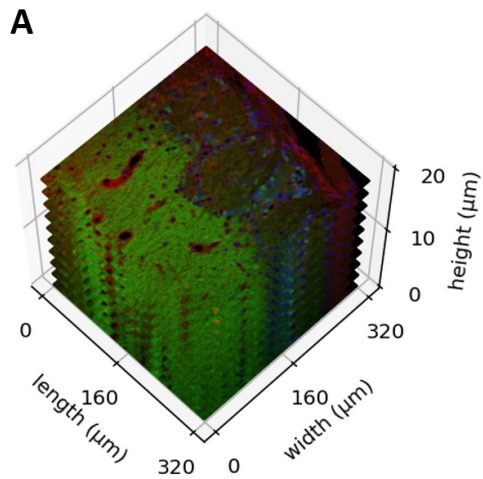


Figure 5.1 Expression of GLUT4 and Kv1.3 in the olfactory bulb glomerular layer. GLUT4 is greatly more present in the GAD67+ periglomerular cells than Kv1.3. GAD67+ periglomerular cells only represent a subset of periglomerular cells that can also be GAD65+. **a)** confocal imaging was done on 5 to 10 320x320um planes, spaced by 2um. **b,d)** Immunostaining of GLUT4 in GAD67-GFP mice. A large part of GAD67+ periglomerular cells colocalised with GLUT4 within the cytoplasm. **c,e)** Immunostaining of Kv1.3 in GAD67-GFP mice. A small subset of GAD67+ periglomerular cells had Kv1.3 stained in their membrane. Scales for b and c: 128x128um. Circle diameters are proportionate to the number of detected cell stainings.

5.2.2 Modulating blood glucose levels

The satiety states were emulated by fasting the mice overnight before the experiments. The effectiveness of the fasting was shown in a consistent bodyweight loss following 16 hours of fasting ($n=50$, $\text{mean}\pm\text{SD}=-11.35\pm 3.28$) (Fig 5.2 A). To induce 'satiety' through hyperglycemia an intraperitoneal injection of glucose (2g kg^{-1}) was given to fasted mice, this increased glycemia from 10 to 30 mmol/l ($n=12$, Fasted $\text{mean}\pm\text{SD}=9.62\pm 1.76$, Glucose $\text{mean}\pm\text{SD}=31.08\pm 4.13$) (Fig 5.2 C), all glucose measurements were made with a glucometer using blood from a cut in the tail in anesthetised mice. We then carried out a simple behavioural paradigm to test whether this hyperglycemia protocol reduced food intake. I compared how much saline and glucose injected fasted mice ate in % of their lost body weights ($n=8$, Saline $\text{mean}\pm\text{SD}=0.39\pm 0.1$, Glucose $\text{mean}\pm\text{SD}=0.3\pm 0.1$; one-sided Wilcoxon signed-rank test: $p<0.05$) (Fig 5.2 B). The amount of food eaten by fasted (saline) mice spread from 27 to 57% of their lost body weight while the amount eaten by sated mice was rather centred around 30%.

To obtain a time course of the change in blood glucose after the IP injections I performed a glucose tolerance test on a cohort of 6 anesthetised mice (Fig 5.2 D). 15 to 20 minutes after the IP, a 30 minutes blood glucose plateau was reached and gave enough time for measurements with a constant glycemia (Fig 5.2 D). Using this paradigm of low and high blood glucose corresponding to both satiety states, we were able to image neurons and

effectuate behavioural tests to observe state-dependent changes. From here on, we referred to the high glycemic state as satiated, as it closely mimics that metabolic state.

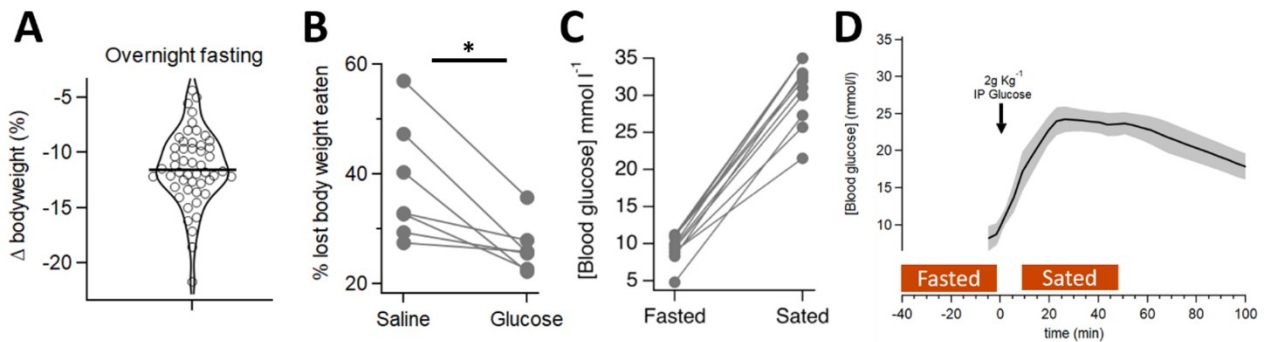


Figure 5.2 Modulating blood glucose levels and hunger. Blood glucose was lowered by a 16 hours fasting overnight and subsequently increased by an IP glucose injection of 2g/kg. The modulated level of glucose reflects the satiety state. **a)** Following overnight fasting, mice consistently lost weight ($n=50$, $\text{mean} \pm \text{SD} = -11.35 \pm 3.28$). **b)** Fasted mice receiving a saline IP ate more than the ones receiving a glucose IP ($n=8$, Saline $\text{mean} \pm \text{SD} = 0.39 \pm 0.1$, Glucose $\text{mean} \pm \text{SD} = 0.3 \pm 0.1$). The mice were left in an empty cage for 10 minutes with 3 food pellets and the amount of lost body weight eaten was given by the weight of the remaining food. **c)** Blood glucose was measured before and after an imaging session where an IP glucose injection was given mid-session ($n=12$, Fasted $\text{mean} \pm \text{SD} = 9.62 \pm 1.76$, Glucose $\text{mean} \pm \text{SD} = 31.08 \pm 4.13$). The mice were therefore imaged in fasted and satiated states. **d)** Time course of a glucose tolerance test in anesthetised mice ($n=6$). Blood glucose was measured every 10 minutes after the IP glucose injection. All blood glucose measurements were done with a glucometer using the blood from a cut in the tail.

I next wanted to corroborate previous behavioural experiments showing a satiety-induced decrease in olfactory sensitivity (Julliard et al, 2007; Aimé et al, 2012). The aim was to measure the olfactory detection threshold of mice in fasted versus satiated states. I designed the experiments to be paired with both fasted and satiated measurements made from all mice. A cohort of 12 mice was used with a 50/50 split between fasted then satiated on the first trial which was reversed for the second trial a week later, so the mice could recover their lost body weight. The test consisted of 4 consecutive 3 minutes runs where mice had to sniff either a cotton bud saturated with an increasing concentration of isoamyl acetate (10^{-6} , 10^{-5} , 10^{-4} , 10^{-3} % in mineral

oil) (Fig 5.4) or another one situated at the opposite side of the cage containing only mineral oil as vehicle (Fig 5.3 A). The side of isoamyl acetate was randomised as well as the states of the mice. 2 or 3 cages were filmed at the same time, separated by sheets of paper to visually isolate the animals. I habituated the animals to the area with empty cotton buds for 10 minutes the day before the experiment. The test arena consisted of an empty regular cage with cotton buds hanging from a cap, slid inside a cut pipette to avoid chewing contact with the odourised cotton bud (Fig 5.3 A).

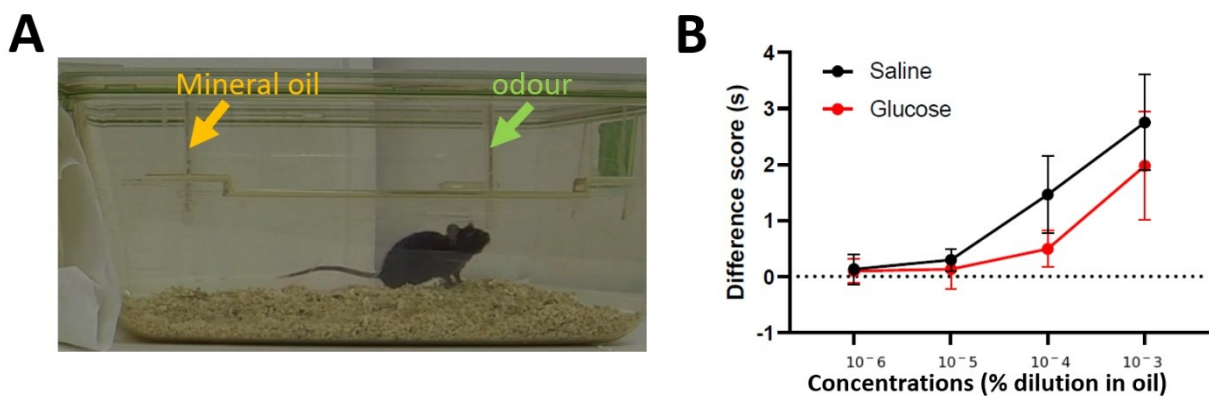


Figure 5.3 Olfactory sensitivity test. Olfactory sensitivity was measured by counting how much a mouse sniffs a cotton bud saturated in different concentrations of isoamyl acetate versus a mineral oil control. A cohort of 12 fasted mice was tested twice. A first session where half received a saline injection and half a glucose injection and a second session a few days later (so their bodyweights get back to normal) with the saline and glucose injections switched up. **a)** The test arena was made of the regular mouse cage with bedding. The position of the odour and control were randomly placed on the left or right side of the cage. They were also randomly switched as new higher concentrated odour cotton buds were introduced. **b)** Fasted mice (saline) scored slightly better than sated ones (glucose). The test score is the time sniffing at the odour minus the time sniffing the oil, divided by the total time sniffing both. Sniffing time was manually annotated. Bars are the standard error of the mean

Sniffing times were annotated manually using python video annotator (<https://github.com/video-annotator/pythonvideoannotator>). The sensitivity of the mouse was related by a difference score calculated for each odour concentration as $(t_{odour} - t_{oil}) / t_{total}$ where t_{odour} is the time spent sniffing the odour cotton bud, t_{oil} the control and t_{total} their sum (Fig 5.3 B). In the first cohort of 12 mice the data appeared to show the expected difference, with

a higher sensitivity in the fasted (saline) injected mice, however, due to large variability between mice this was not significant (Fig 5.3 B). With this experiment, I found that fasted mice could detect Isoamyl acetate at a 10^{-4} dilution similar to previous reports (Breton-Provencher et al., 2009; Abraham et al., 2014). These results in figure 5.3 B remained problematic as the scores were very variable. Behavioural tests are prone to the variation of participation of the animals. They might have been stressed by the IP before the experiment. Some animals even stayed in a corner during the test. At least, their performance was increasing with the concentrations whatever the satiety (Fig 5.3 B). The largest difference in scores was for the 10^{-4} dilution. The 10^{-6} dilution seemed to be unrecognisable for both fasted and satiated mice as the 10^{-5} dilution showed a slightly better score only for the fasted ones. To accentuate the differences between fasted and satiated states (Fig 5.3 B), I prepared a second cohort of experiments with improvements to try to minimise score variability.

For the second cohort of 12 mice, I habituated the animals to handling and scruffing so they would be less disturbed by the IP injection before the test. I handled each animal for several minutes 3 times the week before the tests. It proved successful as they were more relaxed and less resistant to the IP during the tests. It was hoped that this would improve the participation to the test. Because of the immobility issues with the first cohort, I added the use of a tracking system (Fig 5.4, Fig 5.5 E). The video of an additional camera positioned above the cages was processed through the ANY-maze video tracking software. This allowed drawing of the paths traveled by the mice (Fig 5.4) and the extraction of locomotion metrics (Fig 5.5 C&D). The sniffing annotation remained manual.

The locomotion activity of the mice varied. All the tracking maps are similar, except the mice 1 and 2 that showed less motion (Fig 5.4). The presence of mice on the odour target in green compared to the control side is hard to tell only by these maps most of the time. It can however be clearly seen that mice 7 and 9 succeeded in the strongest concentration (Fig 5.4). The behaviours of the mice in the arena were diverse. Some mice seemed to have a priori preferences for one side of the cage. Mouse 1 (glucose) on the left side, mouse 3 (saline) on the right side. This might be due to a bias of the

positions of the cages in the room, with one side of the cage closer to the edge of the table. Mouse 2 (saline) shows immobility during the third concentration. Overall, despite the proof that the mice were active during the 3 minutes tests, their motions seemed to not be only motivated by finding the odour source. Of course, the tracking cannot infer the mice were sniffing. Therefore I assessed the sniffing manually on the lateral camera video.

Sniffing was calculated similarly to the previous cohort (Fig 5.5 A). Unfortunately, results worsened with a score even more similar in both states. Only the highest concentration shows a mean score of fasted mice superior to the satiated ones in average (Fig 5.5 A). I used the presence of animals in a 5 cm radius around the cotton buds as a secondary signal of interest for the odour source (Fig 5.5 B). The radius was drawn around the green (odour) and grey (control) targets (Fig 5.4). It showed like figure 5.5 A a similar behaviour between fasted and satiate mice using the same scoring method as for sniffing (Fig 5.5 B). No change in mobility or distance traveled was observed (Fig 5.5 C&D). Fasted slightly moved more which could be explained by an exploration enhanced by the need for food (Fig 5.5 C&D). While the individual-wise behaviour was quite variable, the animals moved more with increased concentrations, by the look of the overlaid paths of all animals (Fig 5.5 E). There are more tracks around the targets on either side with the progression of concentrations (Fig 5.5E). This means more investigation occurs along with concentrations but fasted looked more efficient at finding the source of the odour (arrow) (Fig 5.5 E).

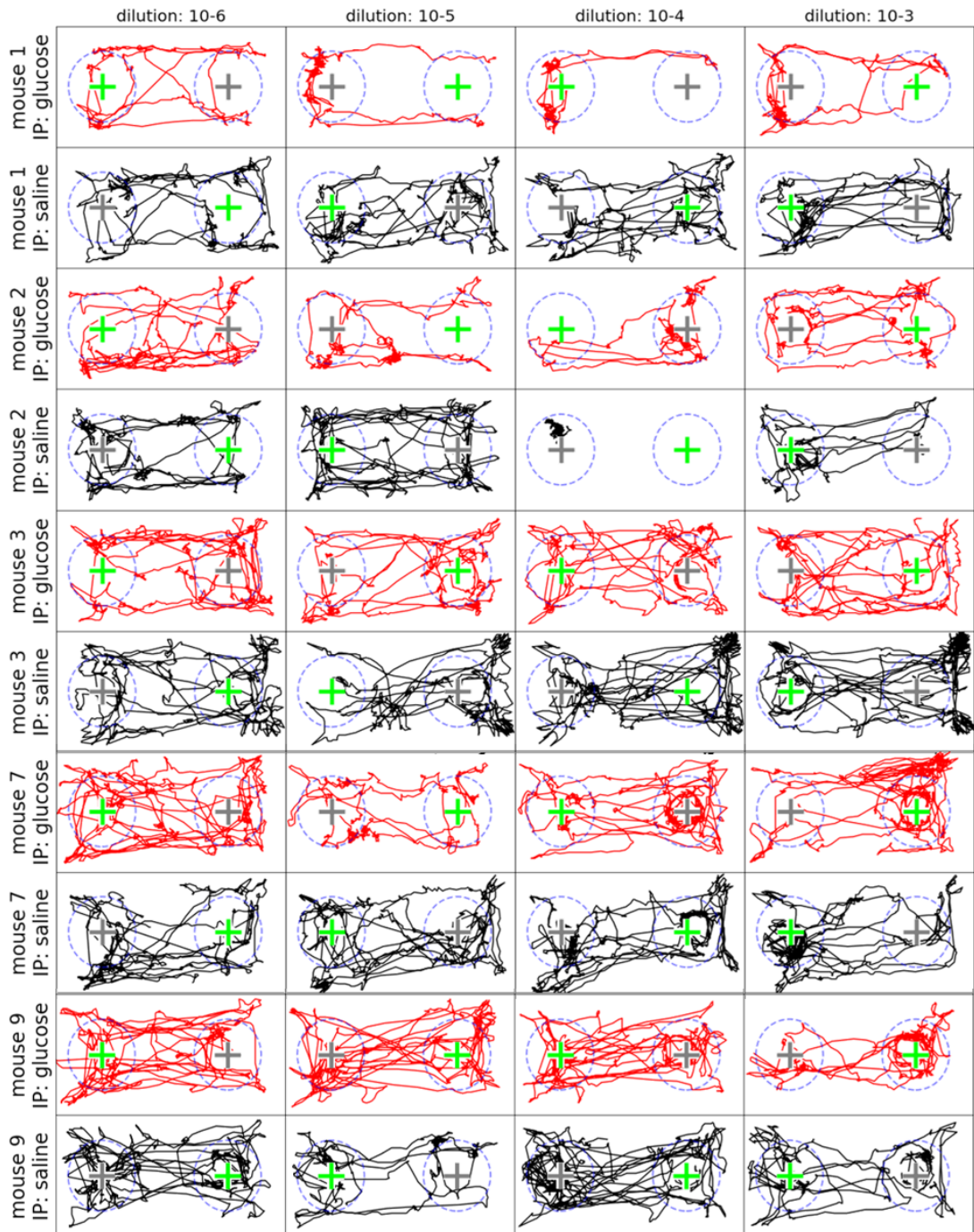


Figure 5.4 Locomotion tracking. Paths taken by mice (n=12) fasted and sated during the olfactory sensitivity test (ANY-maze video tracking software). The green cross is the isoamyl acetate source (the odour target) and the grey cross is the mineral oil (control). The dotted circles are the areas used in figure 5.5 B to measure the presence around the targets. The variability in distance traveled is great. Mice 1 and 2 did move less for example. The mouse presence around the odour target also varied a lot. Mice 7 and 9 showed they particularly succeeded in the test at the latest concentration.

Unfortunately, the results were not improved compared to the previous cohorts (Fig 5.5) with the fasted mice score still overlapping with the satiated ones (Fig 5.5 A). However, the additional measurements helped to investigate how mice variably performed in the test (Fig 5.4, Fig 5.5 C, D&E). The tracks show a huge variability between animals in their behaviours in the test (Fig 5.4). Overall, fasted and satiated mice behaved similarly with fasted mice moving slightly more (Fig 5.5 C&D). Both metabolic states were more active with the increasing concentrations (Fig 5.5 A&E).

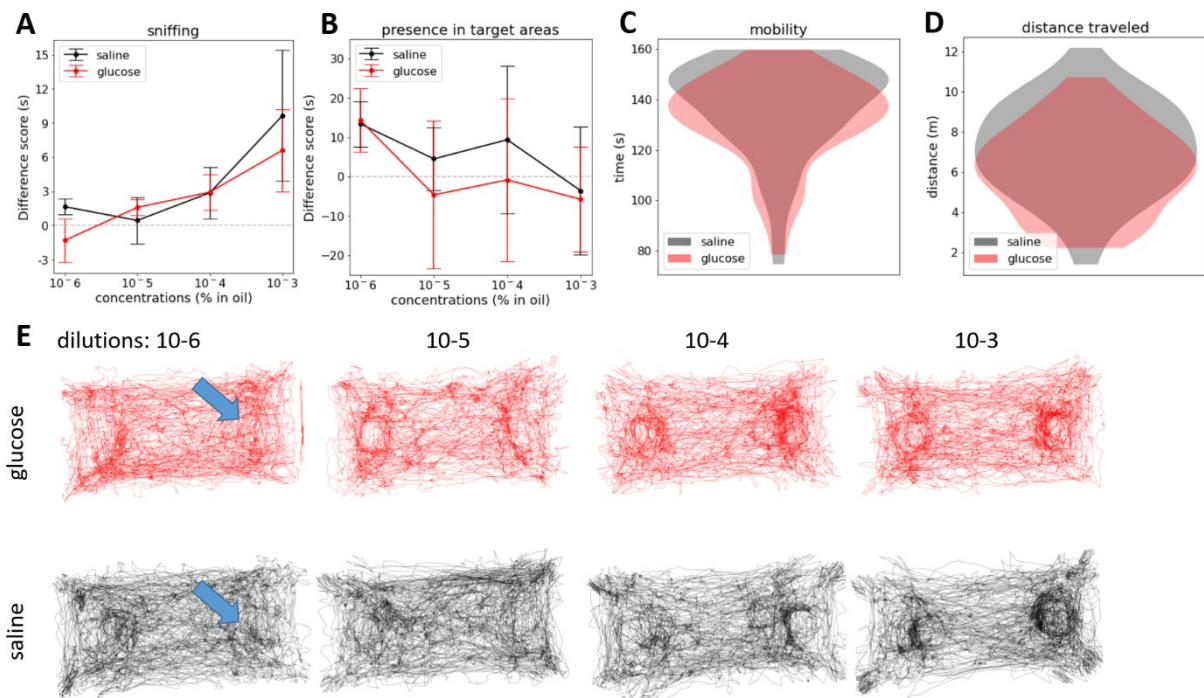


Figure 5.5 Olfactory sensitivity test with tracking. A second cohort of 12 mice did the same test as in figure 5.3 except they were handled 3 times for several minutes the week before and a tracking software was used. Fasted mice are only a little bit more active and better at scoring than satiated mice. **a)** Same as figure 5.3 B. The fasted and satiated mice performed similarly with a slightly better score for the fasted mice at the latest concentration. **b)** Same score as figure 5.3 B but using time spent in 5 cm radius of the targets. Fasted mice did slightly better. **c)** Time spent moving for all concentrations tests in fasted and satiated mice. Computed from data from ANI-maze tracking software. **d)** Distance traveled during all concentrations tests. Fasted mice moved slightly more than satiated ones. **e)** Overlay of the tracked paths of all mice when they received saline or glucose IP injections. Arrow indicates the isoamyl acetate cotton bud. Glucose-injected mice seem more mistaken given the tracks around the control side. The fasted mice (second row) show more and more drawing around isoamyl acetate target as the concentration increases. Bars are the standard error of the mean.

Overall, figure 5.5 shows the mice participated more as concentration increased but no difference of score was established between fasted and satiated mice. This does not conclude in higher sensitivity for food odour in fasted mice compared to satiated. These tests (Fig 5.3 B, Fig 5.5 A) suggest that fasted mice are more olfactory sensitive but the behavioural tests are subject to a large amount of variability. Examining the tracks of individual mice it can be seen that many do not seem motivated to investigate the odour even at the highest concentration (Fig. 5.4). Although the odour used (isoamyl acetate) is the major component in the odour of bananas it does not appear to be an attractive odourant for mice naive to bananas/isoamyl acetate. Consistent with this idea, a subsequent cross habituation experiment was carried out.

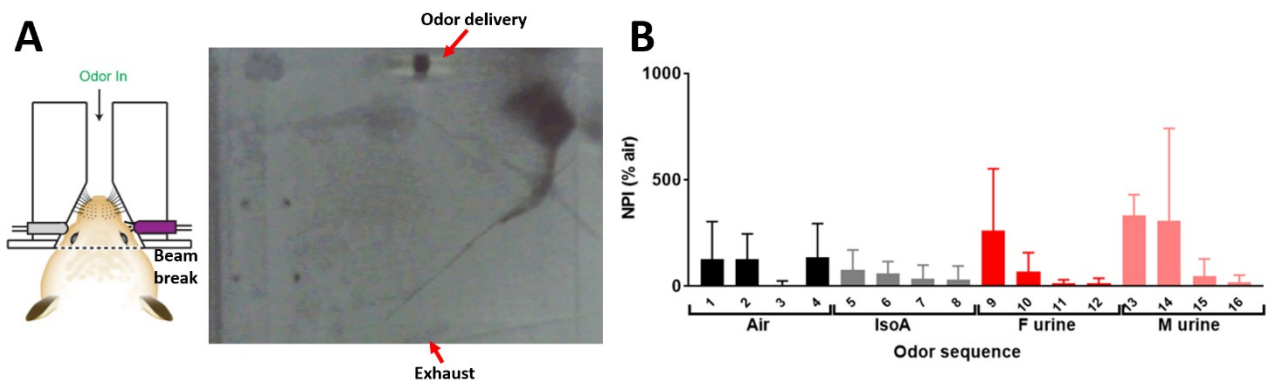


Figure 5.6 Naïve olfactory preference test. Using an automated olfactory testing arena, mice were shown to not interact much with isoamyl acetate in comparison to air puffs control. **a)** The transparent box works with an odour delivery port which embeds a beam break sensor and an exhaust vacuum to clear out the odourised air. **b)** Nose poke investigation in percentage of the air delivery investigation. The time of investigations was determined by the durations when the sensor was activated. The protocol was 4 stimulations of 1 minute of air, then isoamyl acetate, then female and male urines. The urines were expected to elicit interest. The naïve mice (n=5) did not reliably interact with isoamyl acetate.

Andreea Pantiru, using an automated olfactory testing arena based on the work of Qiu et al. (2014) showed that naive mice do not reliably interact with isoamyl acetate (Fig 5.6). We built an automated behavioural test box that contains an odour port equipped with a beam sensor (Fig 5.3 C). We used the same olfactometer (206A, Aurora Scientific) as in the imaging experiments. The signal from the nose poking into the odour port was acquired through an Arduino simultaneously with the odour delivery signal. The protocol

consisted of 4 series of 4 repetitions of air, isoamyl acetate, female urine, and male urine. The stimuli lasted 60 sec separated by 60-seconds intervals. Within 5 wild-type mice (3M, 2F), the nose poke investigation relative to the investigation time of air was measured (Fig 5.3 D). The results show less investigation for isoamyl acetate than for air. Isoamyl acetate is therefore rather a neutral odour. Showing no preference, isoamyl acetate lacks interest by default, and the act of seeking it wouldn't be influenced by hunger. A food odour pairing paradigm before sensitivity testing may solve this problem.

This behavioural study of integration between the olfactory sensitivity and the metabolic state is inconsistent. I did not find a difference in sensitivity between fasted and satiated mice. I wanted to prove the modulation of sensing food odour based on metabolic need. However, isoamyl acetate is not considered as a food odour because it is neither learned as appetitive nor innately preferred (Fig 5.3 D), which is a limitation of these sensitivity tests. The changes in behaviour remained difficult to assert but at least the paradigm of satiation control via glycemia seemed reliable (Fig 5.2 B). While behavioural variability is too high, I hoped to find more consistent changes looking at olfactory neurons in anesthetised animals.

I next will describe a study of the changes in the olfactory sensory neurons and the first neurons that could modulate their activity, the periglomerular cells. Anesthetised mice have the advantage to have a reproducible behavioural state and no troubles of IP injection-induced stress or traits of personality biasing the measures.

5.3 The effect of increased blood glucose on olfactory sensory neurons and periglomerular cells at the first synapses of the olfactory bulb

With PGCs being the first candidate for modulating olfactory sensitivity in the olfactory pathway, I decided to record odour-evoked activity of PGCs and the neurons receiving their inhibition, the OSNs. Using OMMI, explained in the previous chapter, I simultaneously imaged both at the glomeruli level. This is to say, the neuropile structures where OSN axons and PGC dendrites

meet and operate a feedback inhibition circuit. This circuit was investigated in the same mouse, fasted and satiated, as described in the paradigm above. We expected a lowered OSN activity due to a higher PGC activity in satiated animals. This dynamic may be originated from a supposed increased excitability of PGCs following heightened blood glucose. This chapter will aim to unveil how OSNs and PGCs evoked activity varies with glycemia.

For all experiments of this chapter, I used the odours 2-heptanone, isobutyl propionate, ethyl tiglate, and isoamyl acetate because these odours elicited the most dorsal responses. The experiments were similar to those described in the previous chapter, imaging simultaneously OSNs and PGCs in the dorsal olfactory bulb of anesthetised mice. I used 3 air dilutions 0.1, 1, and 10 % of odour compound vapour mixed in air. Every 4 odours were presented 5 times randomly in a sequence of a total of 20 presentations. The stimuli lasted 10 seconds and were separated by 1 minute. This protocol was repeated for each air dilution. 60 stimulations were therefore provided in a fasted state. I then measured glycemia with blood from a tail cut, injected glucose IP, recorded another 60 stimulations, and verified that glycemia was high at the end of the experiment. The glucose measurements were always below 10 mmol/l in fasted mice and above 20 mmol/l at the end of the experiment, consistent with my continuous measures (Fig 5.2 D). Since I started recording 10 minutes after the IP, I assumed that that part of the experiment was on a glycemc plateau. The glomeruli were segmented and their activity extracted as defined in the OMMI chapter. I only kept responses with a signal-to-noise ratio above 2 and where signals from both OSN and PGC were detectable.

I observed increases of both OSN and PGC with glycemia (Fig 5.7, Fig 5.8) in fasted mice. Figure 5.7 shows an example animal with 220 glomerulus-odour pair responses of OSN-PGC couples in 60 identified glomeruli (Fig 5.7 E). On average, across all odours, OSN glomeruli increased their activity in the satiated mouse (Fig 5.7 A&C). Similar observation can be seen for the PGC glomeruli (Fig 5.7 B&D). Across concentrations, the difference of activity seemed to increase with the concentration (Fig 5.7 E). The changes were more remarkable in PGCs than in OSN (Fig 5.7 F&G). The effect tended to diminish with concentration for both PGC (0.1%, 1%, 10% oil dilutions: $100 \pm$

4 % versus 152 ± 6 %; 100 ± 3 % versus 130 ± 4 ; 100 ± 2 % versus 121 ± 3 %; one-sided Wilcoxon signed-rank tests: $p < 0.001$) and OSN (0.1%, 1%, 10% oil dilutions: 100 ± 3 % versus 144 ± 3 %; 100 ± 2 % versus 129 ± 3 ; 100 ± 2 % versus 107 ± 2 %; one-sided Wilcoxon signed-rank tests: $p < 0.001$) (Fig 5.7 H).

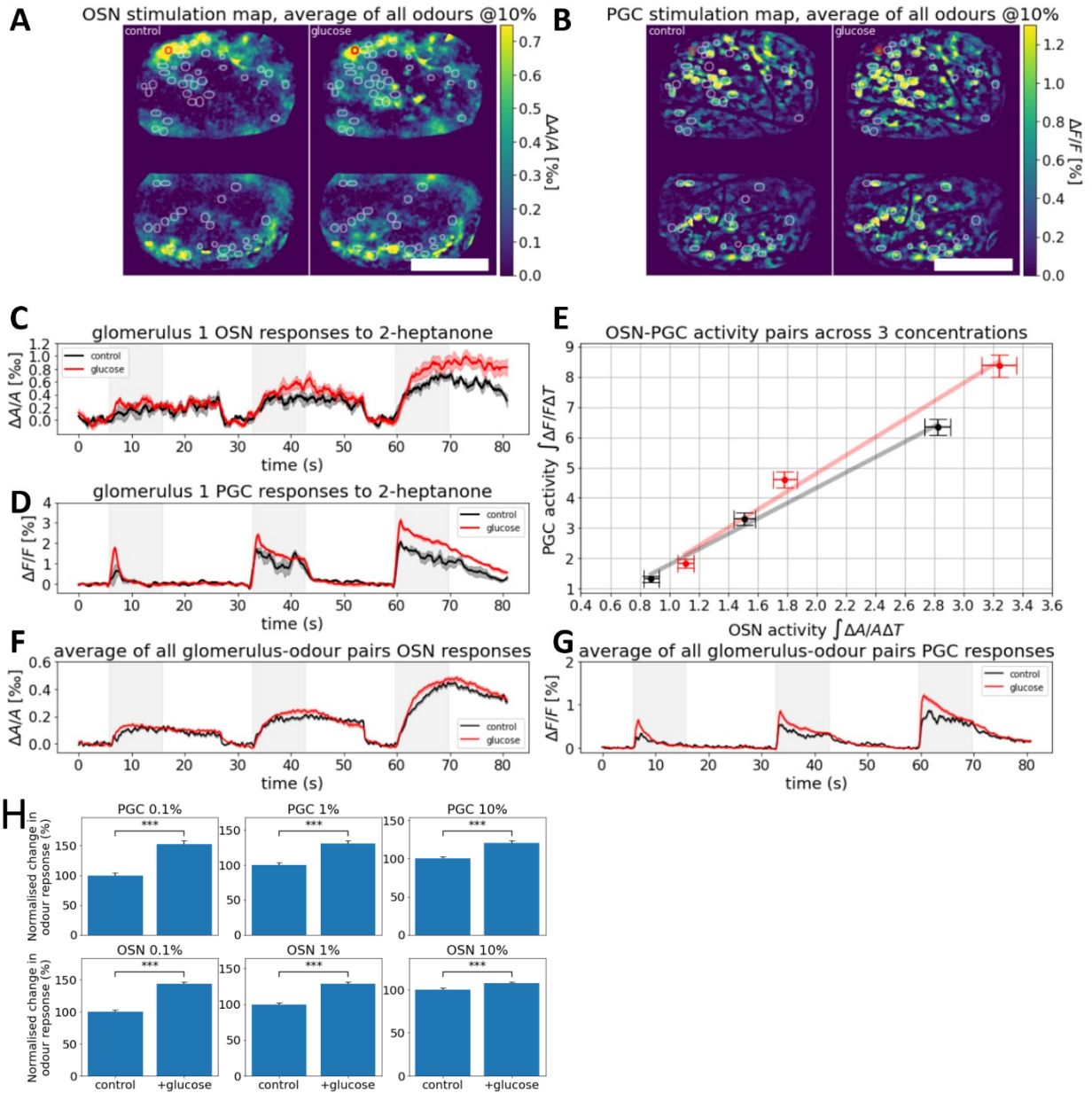


Figure 5.7 Changes of activity in olfactory sensory neurons and periglomerular cells following heightened blood glucose. Imaging of olfactory sensory neurons and periglomerular cells under the optical multi-modal imaging system in the fasted and satiated state in a single animal. 2-heptanone, isobutyl propionate, ethyl tiglate, and isoamyl acetate were delivered to the animal 5 times for 10 seconds, spaced by 1 minute. This was repeated for the odour diluted in air at 0.1, 1 and 10%. The activity is defined by the integral of the signal during a stimulus. **a)** Maximum of all the frames of the OSN channel when any odour was provided at 10% in the fasted (control) and satiated (glucose) states. The activity mostly increased. **b)** Maximum of all the frames of the PGC channel when any odour was provided at 10% in the fasted (control) and satiated (glucose) states. The activity mostly increased. Ovals are manually annotated ROIs. The red ROI is the example shown in c) and d). **c) & d)** example of glomerulus responses to 2-heptanone diluted at 0.1, 1 and 10% in air. Both OSN axons and PGC dendrites glomerular activity increased with blood glucose. **e)** PGC activity of all responses across the 3 air dilutions plotted against the OSN activity of the same glomeruli (220 glomerulus-odour pair responses from 60 glomeruli). Glucose displaces the resulting curve positively in both OSN and PGC axis. **f) & g)** average responses at 0.1, 1 and 10% dilution of all OSN and all PGC for all odours. The average responses for both OSN and PGC at all dilutions showed an increase with blood glucose. **h)** Changes in odour-evoked responses in PGCs and OSNs per concentration, normalised to control responses. Bars are the standard error of the mean. Scale bar: 1mm.

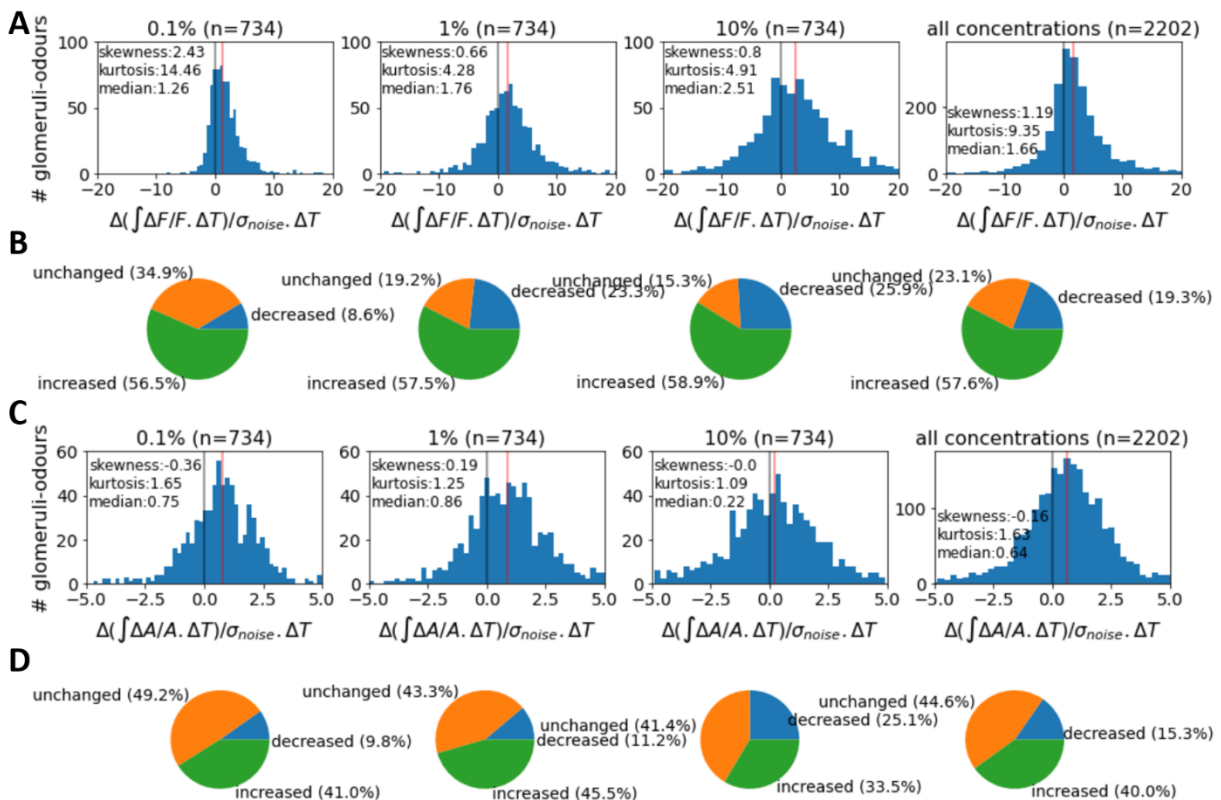


Figure 5.8 Distribution of changes in OSN-PGC glomeruli activity following heightened blood glucose. Changes in activity were normalised by noise to take into account variation of signal quality across animals and glomeruli. In the glomeruli imaged during the plateau of high blood glucose, both OSN and PGC component mostly increased their activity (n=4 mice, 734 OSN-PGC-odour responses per air dilution from 199 glomeruli). Activity was considered decreased or increased if the normalised change was below -1SD or above 1SD (b and d). **a)** Histograms of normalised difference in PGC activity for all odours across the three air dilutions. The distribution has a positive median that increases with concentration which can be due to a better detected signal with stronger stimuli. On average, the sated state increased PGC glomerular activity. **b)** Discrete distribution from a) data. The majority of changes are increases in all concentrations. A part of decreased change grows with concentration. Overall (last panel), the PGC glomeruli largely increased in activity. **c)** Histograms of normalised difference in OSN activity for all odours across the three air dilutions. The changes are less detectable than in PGC due to the intrinsic signal optical imaging method but slightly positive. **d)** Discrete distribution from c) data. Half of the OSN glomeruli did not change with glucose. The rest of changes are mainly increases with a small component of decreases that grows with concentration. Overall (last panel), OSN glomeruli activity was half increased, half unchanged with a minor component of diminutions. Red vertical line shows the median of the distribution.

In 4 animals, from which I extracted 734 OSN-PGC-odour from 199 glomeruli, similar trends were observed (Fig 5.8). The majority of changes were an increase in both OSN and PGC responses, with a change defined by a difference of activity greater than 1SD of the signal noise (Fig 5.8 B&D). In both cases, the decreased differences appeared with higher concentrations (Fig 5.8 B&D). The histograms of relative changes in PGCs demonstrate a distribution around 0 with a median slightly to the right (Fig 5.8 A). The detected changes tended to spread with concentrations but the median remained positive globally. The part of PGC glomeruli that increased their activity remained constant across the 3 concentrations (56.5%, 57.5%, 58.9%) (Fig 5.8 B). A decreased change of activity component grew from 8.6% in the smallest concentration to 25.9% at the highest concentration. Overall most PGC activity was enhanced by blood glucose increase with a minor decreasing effect that could be due to interglomerular inhibitory effects (Fig 5.8 B, last panel).

Between 41.4 and 49.2% of OSN-odour pairs activity did not change across concentrations (Fig 5.8 D). The activity changes in OSN were 4 times smaller than in PGC because OSN optical intrinsic signals are noisier (Fig 5.8 C). The part of changes that increased in OSN was rather constant across concentrations (41%, 45.5%, 33.5%) while a small part of decreasing changes expanded from 3.8% to 25.1% along with the concentration (Fig 5.8 D). Overall, intrinsic signals of OSNs showed to be half unchanged, half increased, with a minority of decreased activity (Fig 5.8 D, last panel).

The concentration range that I had to use for OMMI was higher than the one for the two-photon imaging experiments. I needed to use the strongest concentrations here because the intrinsic optical signals are weak. That however recruits a lot of the bulb glomeruli and induces a gain reduction in PG cells as discussed in chapter 3. Therefore, I tried an approach to maximise the OSN signal but limit any gain reduction in the PG cells. This was achieved by blocking postsynaptic receptors receiving glutamate from the OSNs, 0.1 mM NBQX and 1 mM D-AP5 were added to the craniotomy to block AMPA and NMDA receptors respectively (as described in chapter 4).

This glucose experiment was done completing the iGluR blockers experiment done in chapter 4. After the 60 stimulations in the fasted mouse and 60 stimulation post glutamate blocker, I injected glucose and recorded the same 60 stimuli again. Figure 5.9 shows data from 74 glomeruli recorded from a single animal. Panel A and B show the response images (see methods) before, after iGluR blockers, and after IP glucose, for OSNs and PGCs. Application of iGluR blockers increased the OSN response and decreased those of PGCs and this can be seen in the time courses of 2 individual glomeruli in C and D. Subsequent application of glucose IP reduced the OSN signal but increased that in PGCs as it can be seen for the average data from this animal (Fig 5.9 E-G). The glucose injection resulted in increased PGC odour-evoked activity and decreased OSN odour-evoked activity. The effect tended to diminish with concentration for both PGC (0.1%, 1%, 10% oil dilutions: 100 ± 4 % versus 130 ± 4 %; 100 ± 3 % versus 132 ± 3 %; 100 ± 2 % versus 122 ± 2 %; one-sided Wilcoxon signed-rank tests: $p < 0.001$) and OSN (0.1%, 1%, 10% oil dilutions: 100 ± 3 % versus 66 ± 2 %; 100 ± 2 % versus

96 ± 2 ; 100 ± 2 % versus 88 ± 1 %; one-sided Wilcoxon signed-rank tests: $p < 0.001$ except dilution 1% $p < 0.05$) (Fig 5.9 H).

While the PGCs reacted similarly as in absence of glutamate blockers (Fig 5.7 E), the OSNs did the opposite as in the naïve case. A possible explanation is that reducing the afferent signal is equivalent to using lower concentration stimuli. In this case, the glucose-induced heightened PGC activity can increase the feedback inhibition onto OSNs. This means that in figure 5.7 the stimuli were too strong for the increased inhibition action of PGC to be reflected on OSNs. Keep in mind that OSN measurements are at a lower resolution than PGCs and give lower precision in changes.

In 3 animals, I identified 206 glomeruli responding to the stimuli (Fig 5.9,10). The part of increased changes in PGC activity was reduced compared to the previous case without iGluR blockers (Fig 5.10 A&B) while the OSN glomeruli reduced more their activity (Fig 5.10 C&D). Blocking glutamate reduced excitatory inputs not only from OSNs but also reduce the excitatory contributions to PGC from MTC and ETC. The major changes were increases for PGCs and decrease for OSNs (Fig 5.10 B&D). Across concentrations, PGC glomeruli expressed a constant part of decreased activity (13.9%, 11.8%, 15.8%) which may correspond to a similar part of positive changes in OSN glomeruli (14.5%, 24.6%, 15.6%) (Fig 5.10 B&D). The OSN-PGC relationship was more apparent here than in figure 5.8, as their changes in activity seem linked in opposition.

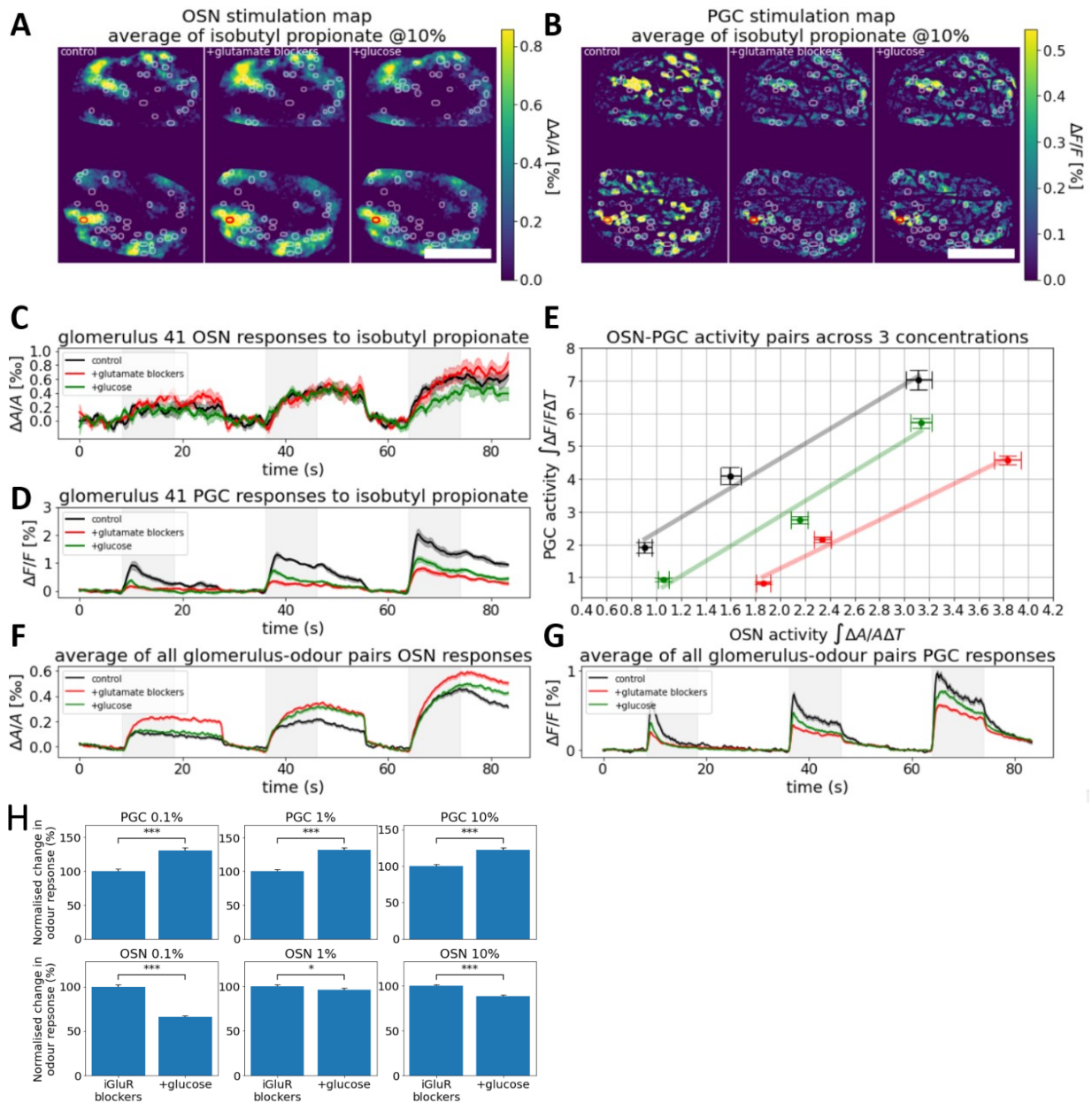


Figure 5.9 Changes of activity in olfactory sensory neurons and periglomerular cells following heightened blood glucose with reduced glutamatergic inputs. This is the same experiment as figure 5.7 except the protocol was applied for an animal in the fasted state, then after topical application of NMDA and AMPA blockers (0.1 mM NBQX, 1mM D-AP5), ending with a recording session after glucose injection. **a)** Maximum of all the frames of the OSN channel when isobutyl propionate was provided at 10% in the fasted (control), glutamate blockers and glutamate blockers + glucose states. The activity globally increased by blocking glutamate because of a reduction of the feedback inhibition provided by PGCs. Following the glucose injection, the activity decreased, maybe due to an amplification of feedback inhibition. **b)** Maximum of all the frames of the PGC channel when isobutyl propionate was provided at 10% in the same states mentioned here before. The activity decreased following the blocking of afferent glutamatergic inputs. The heightened blood glucose correlated with an increased activity thereafter. Ovals are manually annotated ROIs. The red ROI is the example shown in c) and d). **c) & d)** example of a glomerulus responses to isobutyl propionate

diluted at 0.1, 1 and 10% in air. **e)** PGC activity of all responses across the 3 air dilutions plotted against the OSN activity of the same glomeruli (264 glomerulus-odour pair responses from 74 glomeruli). Blocking glutamate reduced PGC activity and increased OSN activity. Subsequent glucose injection decreased OSN activity and increased PGC activity. These opposite effects in OSN and PGC are corresponding to the feedback inhibition they implement. **f) & g)** average responses at 0.1, 1 and 10% dilution of all OSN and all PGC for all odours. This shows the same results as e). **h)** Changes in odour-evoked responses in PGCs and OSNs per concentration, normalised to control responses. Bars are the standard error of the mean. Scale bar: 1mm.

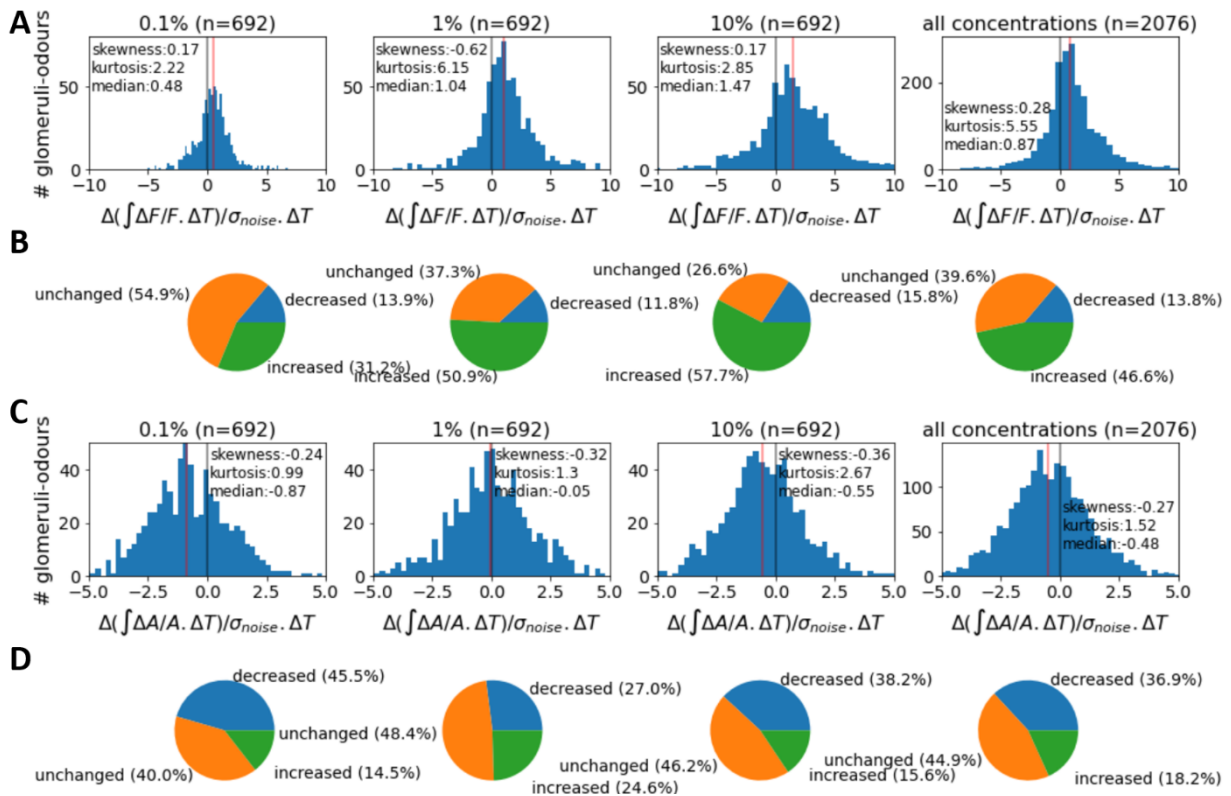


Figure 5.10 Distribution of changes in OSN-PGC glomeruli activity following heightened blood glucose with reduced glutamatergic inputs. These are the difference in activity between the glutamate-blocked fasted state and the sated state. Changes in activity were normalised by noise to take into account variation of signal quality across animals and glomeruli. Topical application of glutamate blockers NBQX (0.1 mM) and D-AP5 (1mM) changed the previously observed modulations following heightened blood glucose (Fig 5.9). (n=3 mice, 692 OSN-PGC-odour responses per air dilution from 206 glomeruli). Activity was considered decreased or increased if the normalised change was below -1SD or above 1SD (b and d). **a)** Histograms of normalised difference in PGC activity for all odours across the three air dilutions. **b)** Discrete distribution from a) data. **c)** Histograms of normalised difference in OSN activity for all odours across the three air dilutions. **d)** Discrete distribution from c) data. Red vertical line shows the median of the distribution.

Adding glutamate blockers reinforced the effects of glucose on the PGC-to-OSN feedback. Figure 5.11 B denotes more OSN inhibition following glucose administration (12.2%) than without iGluR blockers (1.7%) (Fig 5.11 A). The feedback inhibition circuit cannot be studied alone because of external inhibitory and excitatory inputs such as interglomerular inhibition between PGCs and feedback excitation from MTCs to PGCs. More PGC-to-PGC inhibition is recruited with the strength of the stimulus. A part of the PGC glomeruli decreased activity was reduced from 9.9% to 4.5% by limiting the OSN glutamatergic afference (Fig 5.11). It is complicated because if PGCs increase activity, it means these activity-increased PGCs inhibit more other PGCs, participating in a decreasing component of the PGC glomeruli population. As increased activity is observed in PGC glomeruli, a smaller decreasing component follows proportionally (Fig 5.8 B, Fig 5.10 B).

Here I showed pieces of evidence that heightened glycemia increased the excitability of PGCs in anaesthetised mice, for strong afferent inputs (Fig 5.7,8) and reduced afferent inputs (Fig 5.9,10). The expected attenuation of OSNs activity matching the increased excitability of PGCs was only met in the second case, with the iGluR blockers (Fig 5.10 B). The increased activity of OSNs in the naïve case does not fit with the hypothesis of blood glucose reinforcing PGC-OSN feedback inhibition via PGC glucose-sensing (Fig 5.8 D). However, OSNs activity appeared to be more decreased after glucose administration when iGluR blockers were applied (Fig 5.10 D). The study of how the circuit dynamic might have changed within and across glomeruli

necessitates an interpretation of coupled changes of both PGC and OSN activity of the same glomeruli. Generally, it is important to mention that the increased activity in PGCs is rather one of the several potential contributing factors to decreased activity in OSNs.

In the two experiments, without and with iGluR blockers, similarly, 12.3% and 17.8% of the glomeruli did not change activity in either of their PGC or OSN components (Fig 5.11). The amount of increased PGC activity without OSN change remained the same with 23.4% and 22.3% of the glomeruli of each experiment (Fig 5.1). In the “fasted → glucose” experiment (Fig 5.11 A), the largest group of OSN-PGC activity changes within glomeruli was OSN \nearrow , PGC \nearrow with 27.5% (Fig 5.11 A). This type of change goes against the logic of feedback inhibition and may signify that OSN intrinsically increased their activity with glucose. This type of change was reduced to 10.5% when applying iGluR blockers (Fig 5.11 B). In the “fasted + iGluR blockers → glucose” experiment (Fig 5.11 B), OSN \searrow , PGC \nearrow and OSN \searrow groups emerged with 15.4% and 13.8%. The OSN \searrow , PGC \nearrow changes are clearly explained by an enhanced feedback inhibition while the OSN \searrow glomeruli, lacking a change in PGC, may have their activity change due to lateral inhibition. However, the 22.3% of PGC \nearrow does not match with the 15.4% of OSN \searrow .

Overall, the PGCs activity was essentially heightened in both cases with only a clear enhancement of the feedback inhibition into OSN visible when iGluR blockers were applied. Feedback inhibition does not seem influenced at the strong concentrations given the absence of neither OSN \searrow , PGC \nearrow , and OSN \searrow groups in the “fasted → glucose” case.

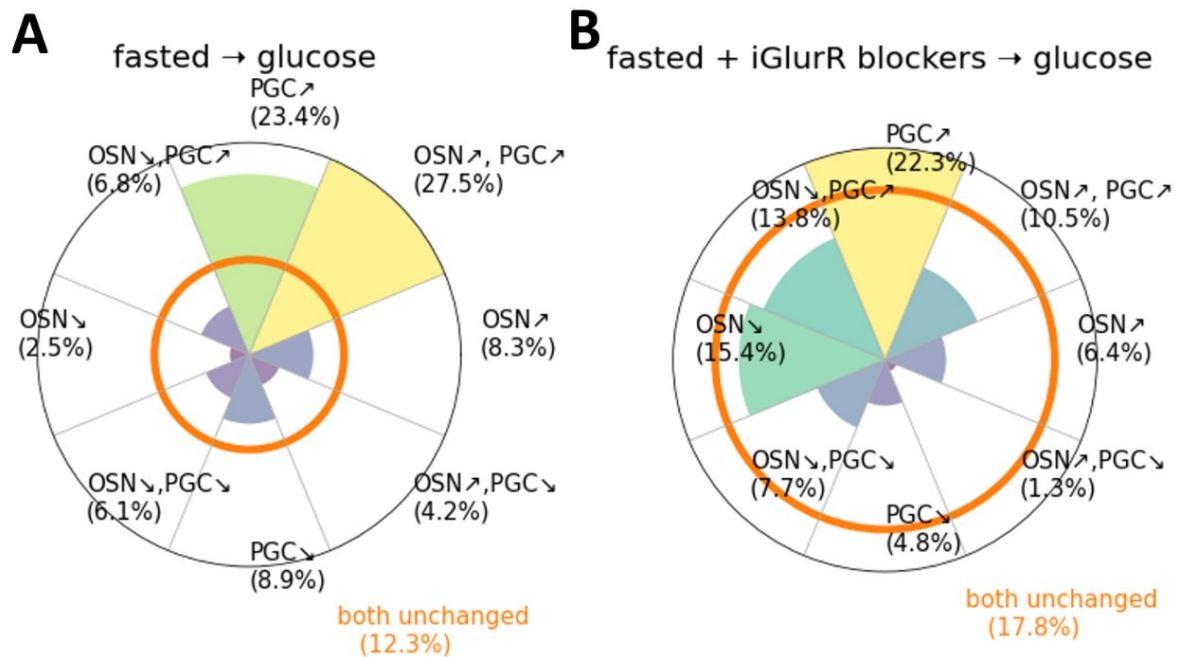


Figure 5.11 Summary of change of activity in OSN-PGC-odour pairs following glucose administration. Change of activity in glomeruli after an intraperitoneal injection of glucose ($2g\ kg^{-1}$). Percentage of all OSN-PGC-odour responses that had either their OSN component increased/decreased, PGC component increased/decreased or both unchanged, based on the last panels of figure 5.8 B&D and 5.10 B&D. **a)** Change of glomeruli activity between fasted and sated states (4 mice, $n=2202$ responses), data from figure 5.8. **b)** Change of glomeruli activity between fasted with glutamate blockers and sated states (3 mice, $n=2076$ responses), data from figure 5.10.

The noise inherent to intrinsic optical imaging in OSN signals being in the same order as the change I wanted to study is a substantial shortcoming of intrinsic signal optical imaging. This limitation requires the use of strong stimuli to detect changes reliably but then that would elicit PGC-PGC inhibitions rather than the PGC-OSN inhibition I wanted to observe. More odour presentation repeats would fit better to reduce noise. In this section, using only 3 points of concentration also limited the study of PGC excitability. We must have first activating concentration responses and responses at saturating concentrations to have a good idea of glucose-induced changes

along the dose-response curve. A broader range of concentrations can be used under two-photon imaging because it enables faster measurements by stimulating only 3 seconds with 10-seconds intervals, compared to the 10 seconds stimulation and 1-minute interval of the OMMI system.

5.4 Glycemia-driven transformation of PGC dose-response curve in somata and glomeruli

Glycemia exerts an effect on the PGC activity as seen in the previous section. However, the concentrations tested were on the high extremum which stops from appreciating the change in the activation dynamic. Knowing how the activation curve changes from the first response to the max response would help determine underlying mechanisms. In the case of odour detection, I wanted to investigate any shift in the olfactory sensitivity threshold. That is to say, what is the earliest concentration for which a PGC is activated?

The hypothesis is that PGCs would acquire an earlier sensitivity in a satiated state because heightened blood glucose would reduce detection of food odourants at a lower concentration by increased feedback inhibition from the PGC to the OSN afference. The subtle olfactory detection would be disregarded because the metabolism state dictates the organism that seeking food source is no more relevant. PGC would be thus activated early on due to glucose increase. As the PGCs become more excitable, they would have a lower maximum response due to PGC-PGC inhibitions occurring earlier.

This experiment aimed to produce dose-response curves for the fasted and satiated states and fit them with a Hill function. Then I would compare the dynamic of these curves in both states for PGCs and the glomeruli. The hill curve fitting was done as mentioned in chapter 3. The recording in the satiated state started 10 minutes post IP injection of glucose to be in a high glycemic plateau (Fig 5.2 D). Like all experiments in this thesis, the blood glucose was systematically measured in the fasted state below 10 mmol/l and at the end of the experiment above 20 mmol/l.

I used measurements in the same cells and glomeruli, from 4 animals used in chapter 3, where I was successfully able to record an additional session in a satiated state after an IP injection of glucose, while not losing the

same field of view. I had an additional 2 animals where the FOV had moved before and after glucose injection.

The stimuli were 4 odours amongst 2-heptanone, ethyl tiglate, isoamyl acetate, isobutyl propionate, 2-phenylethanol, TMT, or 2-isobutyl thiazole, at 6 different concentrations as defined in chapter 3 but presented twice, in each state (Fig 5.12 B&C). All along the recording and especially after the injection, I took care to conserve the same field of view to track cells and glomeruli. I only considered glomeruli and somata with an increasing profile of responses with concentration and a successful fitting of hill curve to ensure data quality (Fig 5.12 C&D). As for detecting a positive or negative change, 2 standard deviation of noise was the threshold for admitting a difference (Fig 5.13).

In the figure 5.12 examples, on average, we can see glomeruli responding earlier in the satiated state, and elicit a higher maximum amplitude in later concentrations, in concordance with the previous section measurements under OMMI (Fig 5.8 B). I looked at the change in the earliest and maximum responses in 47 glomerulus-odour pairs and 252 cell-odour pairs, across 4 animals (Fig 5.13). The difference of activity was normalised by noise SD to be comparable across cells/glomeruli and animals. A change was detected if its absolute value reached above 2 SD.

A difference between cells and glomeruli appeared when comparing maximum responses (Fig 5.12 C&D). The comparison was made between the maximum responses in the fasted state and the satiated state, not necessarily at the same concentration. Glomeruli showed the third part unchanged, a third increased, and a third decreased (Fig 5.13 C), close to the PGC glomeruli OMMI measurements (Fig 5.8 B), despite the smaller sample here. On the other hand, PGC activity was mainly reduced (Fig 5.12 D). The distribution of normalised changes is centred on -5. This indicates PGCs are submitted to an increase of lateral PGC-PGC inhibition.

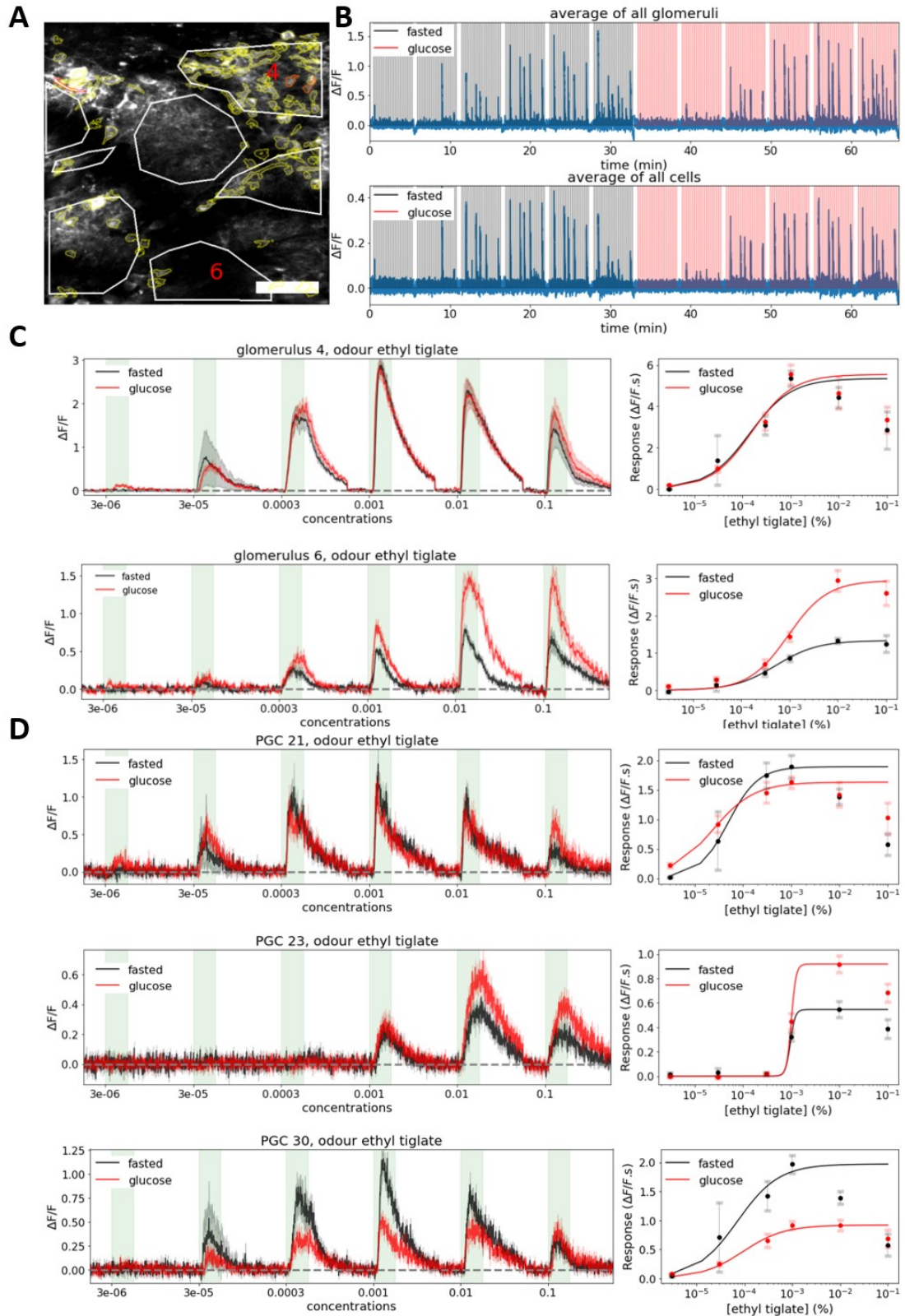


Figure 5.12 Profile of activation of periglomerular cells in fasted and sated states. In this example animal, blood glucose correlates with heterogeneous effect on PGCs activity in their somata and the glomeruli they project their dendrites onto (104 cells, 7 glomeruli). **a)** Field of view containing ROIs of PGCs in yellow and glomeruli in white. The background is the maximum projection of all the frames where odour stimulation occurred. The

red ROIs denote the examples of c) and d). **b)** Averaged fluorescence traces of all cells/glomeruli. The stimuli protocol was given in the fasted state (black) and after glucose administration (red). The protocol consists of 4 odours presentations, repeated randomly 5 times at each of the 6 concentrations. **c) & d)** Left: example of a set of responses across 6 concentrations in the fasted (black) and sated (red) states. Each response is an average of 5 repetitions. Right. Hill function (dose-response curve) fitted over activity points extracted from the 3 to 6 responses on the left. Scale bar: 50 μ m.

The first responses were shown to have changed less in the first responses (76.2% unchanged for the glomeruli, 67.6% for the cells) (Fig 5.13 A&B) than in the maximum responses (33.3% unchanged for the glomeruli, 17.2% for the cells) (Fig 5.13 C&D). However, the changes in first activations may be not comparable to the maximum response changes as the former is likely to surpass 2SD and thus will be less detectable. Overall, the first activation responses are mostly unchanged with a small bimodal effect similar in PGCs (15.2% increasing, 17.2% decreasing) and glomeruli (9.5% increasing, 14.3% decreasing) (Fig 5.13 A&B).

Cells and glomeruli expressed heterogeneous changes in their first and maximum responses (Fig 5.13). 26.2% of glomerulus-odour responses showed no changes (glomerulus 4 Fig 5.12 C, Fig 5.13 E). 26.2% of glomerulus-odour and 16.8% of cell-odour had a higher maximum response (Fig 5.12 C, glomerulus 6, Fig 5.12 D, cell 23, Fig 5.13 F). Overall in somata, a lower activation in all concentrations was the most common with 39% (Fig 5.12 D, cell 30, Fig 5.13 F). Finally, the cases where a change occurred in both first and maximum responses were a minority. In glomeruli, 14.2% of detected changes had both first and maximum responses increase (7.1%) and decrease (7.1%) together (Fig 5.13 E). In cell-odour pairs, it was higher with 11.9% of both responses decreasing (example cell 30, Fig 5.12 D, Fig 5.13 F). Opposite changes in early and maximum responses were rare. Not seen in glomeruli, there was 8.2% of cell-odour pairs with increased first response and a lowered maximum response (Fig 5.13 F), as the example of cell 21

denotes (Fig 5.12 D). This case was surprisingly not present in glomerulus-odour pairs.

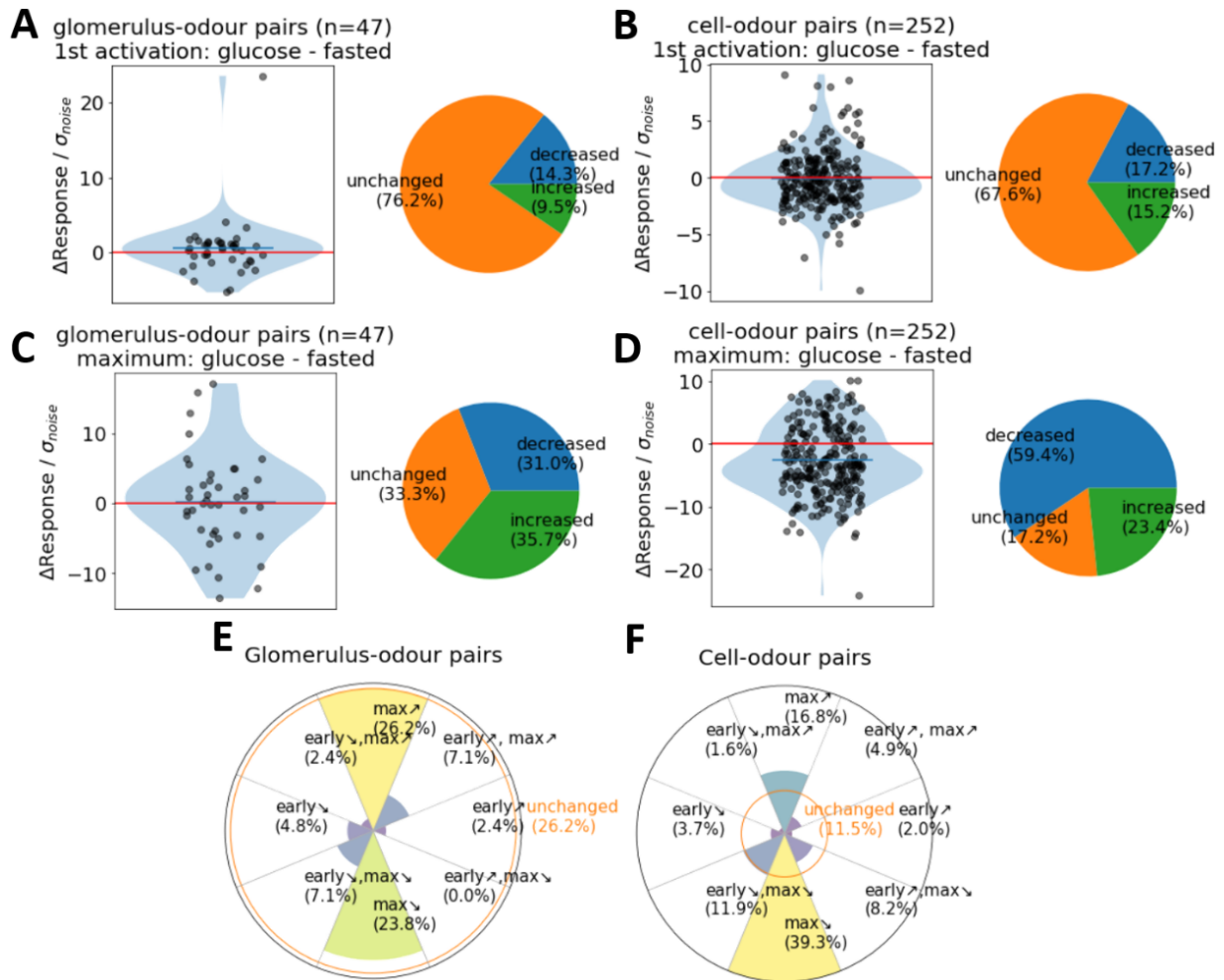


Figure 5.13 Changes in earliest and maximum responses of PGCs somata and glomeruli. Changes of activity, normalised by the SD of noise, of the first and maximum response across concentrations, for 47 glomeruli-odour pairs and 252 cell-odour pairs (n=4 animals) between fasted and sated states. In the pies, activity is considered decreased or increased if the difference of activity is below -2SD or above 2SD. **a)** Normalised differences of glomeruli activity for the responses given by the first activating concentration for an odour. **b)** Normalised differences of cell activity for the responses given by the first activating concentration for an odour. **c)** Normalised differences of glomeruli activity for the maximum responses for an odour. **d)** Normalised differences of cell activity for the maximum responses for an odour. **e,f)** Repartitions of earliest/maximum response changes in glomerulus-odour and cell-odour pairs.

Figure 5.13 showed that differences were mainly detectable above 2SD in the maximum responses and appeared to be bidirectional in glomeruli while showing a preference in decrease for the PGCs. This might imply PGCs are receiving more glucose-induced inhibition by neighbouring PGCs than the glomeruli that are directly receiving OSNs excitatory inputs. The 35.7% of maximum responses that increased in glomeruli (Fig 5.13 C) may relate to the OSN increased activity noticed earlier under OMMI (Fig 5.8 D).

Using 6 concentrations limits the accuracy in detecting a blood glucose-induced sensitivity shift. Fitting Hill functions to concentration-response data resolve this limitation by interpolating a continuous range of concentration from 10^{-6} to 10^{-1} (% air dilution x % oil dilution), based on the assumption that PGC activation follows a ligand-receptor activation dynamic regarding the strength of the stimulus. A Hill function is defined, as in chapter 3, by 3 parameters: the Hill coefficient n , which describe the dynamic range, with a high value of n corresponding to a steeper curve and smaller dynamic range, the EC_{50} , the concentration that produces half of the maximal response, and EC_{max} that I refer here as the maximum response, where the Hill curve saturates.

Furthermore, fitting a hill curve makes it possible to align all the curves around an EC_{50} of 1 figures 5.14 A&B, done by a normalisation by the EC_{50} and maximum of the fasted state, which permits the comparison of the changes from the first response to maximum, across animals, cells, glomeruli, and odours despite the diverse EC_{50} s. With all the fasted curves centred, we can observe the shift of the dosage-response function relatively. Figures 5.14 A&B show the average of all fitted Hill functions both in fasted and sated states, with all the EC_{50} s normalised to the fasted EC_{50} s and all the maximums normalised by the fasted maximums.

The observations in figure 5.14 were tentative as the Hill functions were fitted on only 3 to 6 points in different somata and glomeruli. Secondly, glomerular activity originated from signals averaged over more pixels than the somata which have small ROIs. Somata data contained more noise and thus likely fewer data points to fit. Therefore, these arguments must be taken into

account for the interpretation of differences between the results in somata and glomeruli.

The dosage-response curve in glomeruli shifted lightly upward with glucose (Fig 5.14 A). The response gain appeared to be positive across all concentrations. However, the differences between the fasted averaged Hill curve and sated Hill curve were only around 1 to 10% of the response as shown on the right y-axis. The glomeruli seemed more excited across all concentrations but there was no sensitivity shift along the concentration axis as the EC_{50} s remained mostly unchanged (Fig 5.14 C, left). The change in dynamic range is centred on 0 with a positive tail (Fig 5.14 C) which would indicate a smaller responding range of odours in a satiated state.

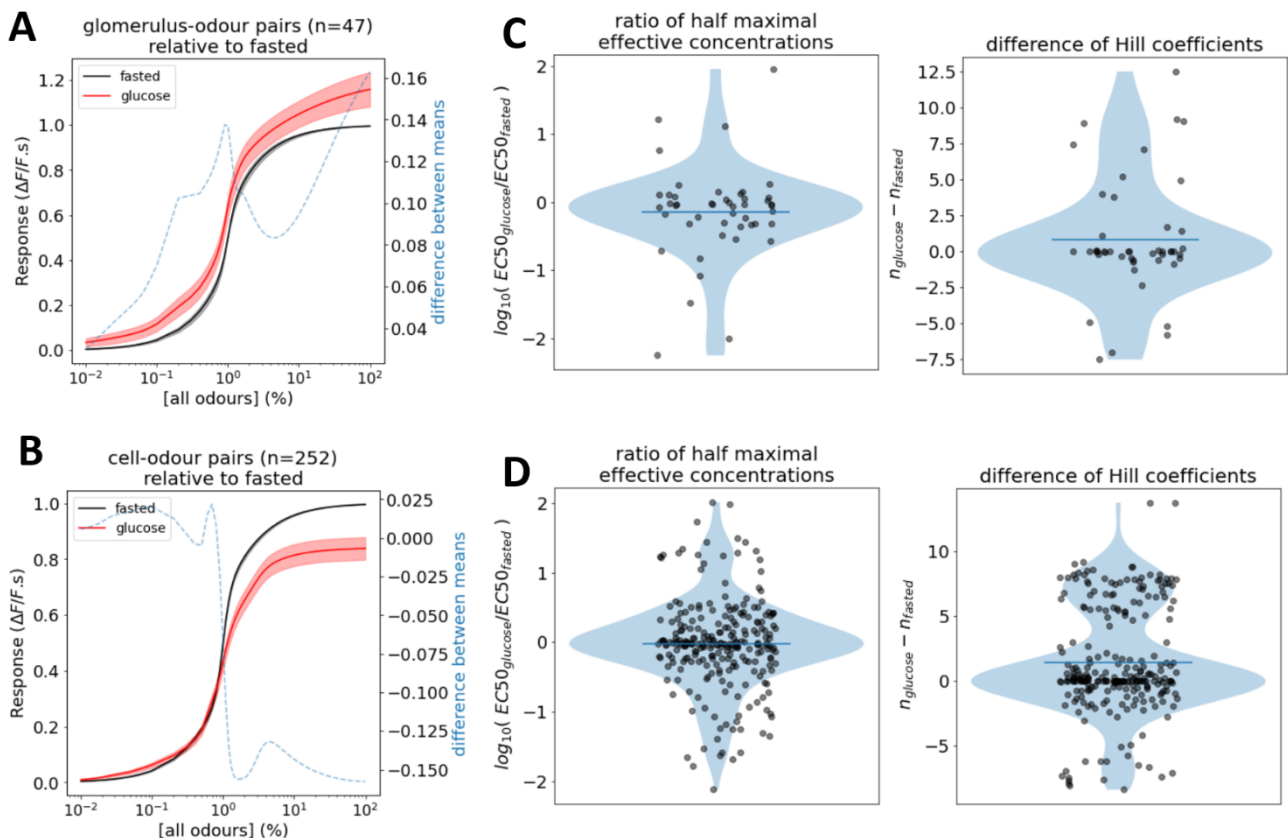


Figure 5.14 Transformations of Hill functions of PGCs somata and glomeruli. Dosage-responses curves are defined by Hill function which have EC_{50} , the half-maximal effective concentration, and n , the Hill coefficients, as parameters. **a)** Hill function of 47 glomeruli-odour pairs and **b)** 252 cell-odour pairs from 4 animals, in fasted (black) and sated (red) states. Both curves are normalised by the EC_{50} and the maximum of the fasted state curves. **c)** Changes of EC_{50} and the Hill coefficients between the fasted and sated states for **c)** glomerulus-odour pairs and **d)** cell-odour pairs.

PGCs seemed to express a reduced response only for concentrations past the EC_{50} (Fig 5.14 B). However, the changes were 10 times smaller than the responses (right y-axis). This possible reduction of activity in PGCs at higher concentrations might be due to the recruitment of neighbouring PGCs providing PGC-PGC inhibition. The EC_{50} did not seem to have moved in average (Fig 5.14 D, left) which shows like for the glomeruli that the changes are rather in gain (variation of DF/F) than sensitivity (shift on the concentration axis). The changes in dynamic ranges possess two modes (Fig 5.14 D, right). One encompasses PGCs that did not expand their responsive range, with a delta around 0, and the second, around 7.5, tells that a proportion of them make the dosage-response curve steeper. Therefore, PGCs dynamic range would tend to become smaller in the satiated state.

The glycemia-induced changes were heterogeneous and are potentially different for PGCs somata and glomeruli dendrites. While the EC_{50} -related sensitivity appears unchanged for both, glomeruli would rather change the response gain positively across all concentrations and the PGCs negativity only at higher concentrations. While using the Hill function as a trick to have a continuous range of responses, it remains difficult to observe the change in the earliest activations and calls for a better method to measure any change in excitability at lower concentrations.

5.5 Displacement of the PGC activation thresholds in regards to blood glucose time course

The resolution given by the incremental stimuli tested limits the study of sensitivity threshold shift. When using a discrete set of stimulus intensities, the threshold will fall within a range. To determine precisely at what

concentration a neuron begins to activate and how that threshold shifts with the metabolic state, I implemented a ramp stimulus that continuously stimulates across a range of concentrations. This innovation affords 2 advantages, it gives the ability to measure activation thresholds with a single stimulus that covers a continuous range of concentrations instead of stimulating many times with a discrete set of concentrations, and a full range of concentrations can be tested more rapidly.

Furthermore, thanks to this method of scanning a range of stimulus strengths shortly I could do time series to observe changes in neural activity along with the temporal dynamic of the blood glucose (Fig 5.2 D). That is to say during the rise of glycemia and its plateau. I was wondering if the PGCs would react to the change of glycemia or just its effect at its plateau value. More generally, this experiment would be a chance to observe the expected increased excitability of PGCs in the satiated state. I would expect an earlier activation and end a lower maximum response due to hyper-excited PGC-PGC inhibition.

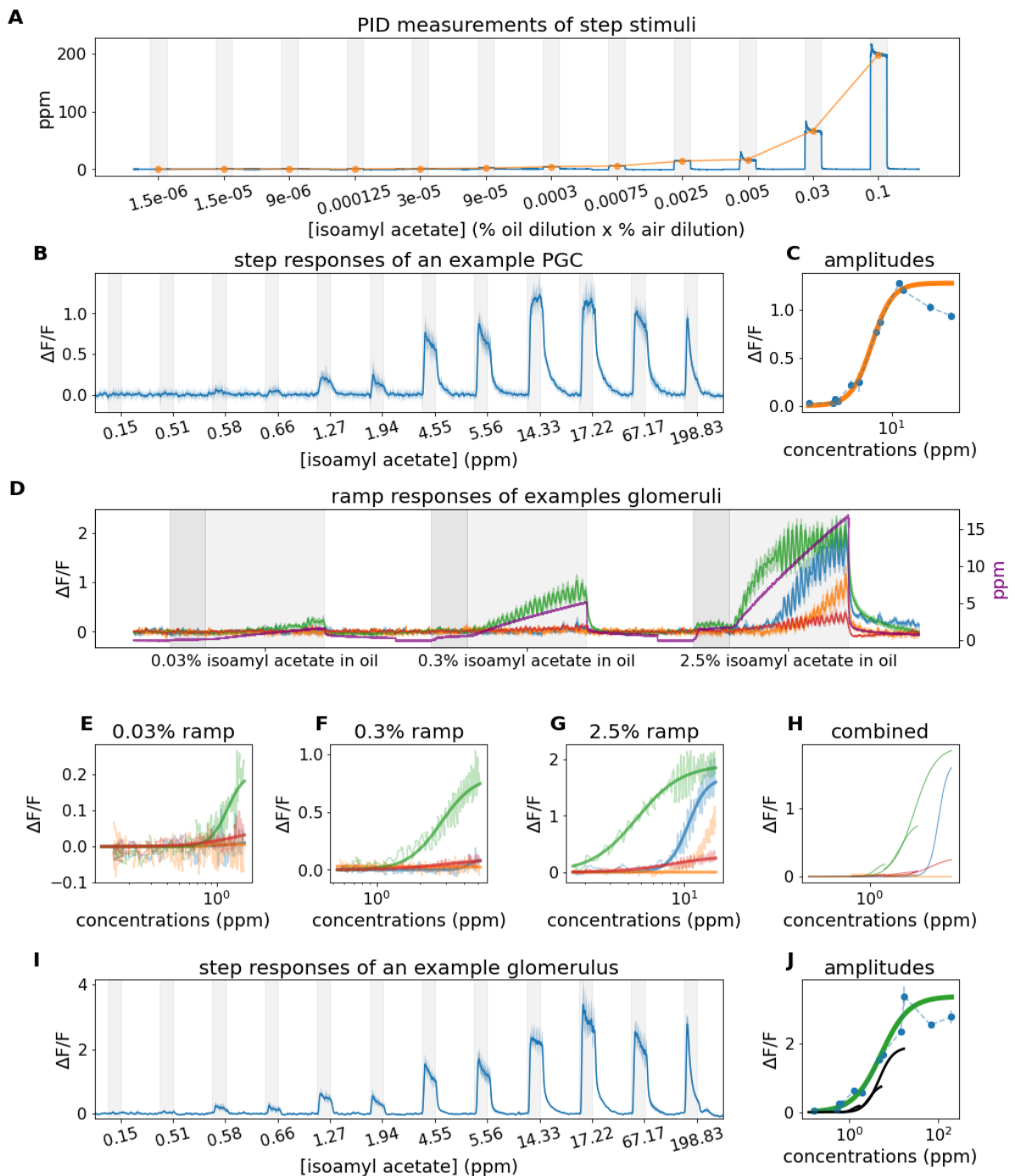


Figure 5.15 PID calibration and ramp stimulus. **a)** Calibrations of 12 different dilutions of isoamyl acetate, measured in ppm by a photoionisation detector (Aurora, miniPID Fast Response Gas Sensor (200B)) (cfr. methods). **b)** Fluorescent responses to step stimuli, in a periglomerular cell for each concentration defined in b). Average from 5 repetitions per concentration. **c)** Hill curve fitting on the amplitudes from the responses in b). **d)** Example of 4 glomeruli responding to 3 ramp stimuli (averages of 5 repetitions) from 3 oil dilutions of isoamyl acetate: 0.03%, 0.3% and 2.5%. Each ramp starts in the greyed area and is composed of 3 seconds of the odour vapour diluted 0.5% in air, then during 10 seconds increases up to 10% dilution in air. The purple trace gives the ppm measurement from the PID along the ramp. Each ramp PID value respectively ranges from 0.11 to 1.68, 0.44 to 5.18, and 1.43 to 16.86 ppm. **e-h)** Hill curve fittings from the 10 seconds of increasing

concentration in the ramps responses (light grey area in d)). **i**) Fluorescent responses to step stimuli, in a glomerulus for each concentration defined in b). Average from 5 repetitions per concentration. **j**) Hill curve fitting on the amplitudes from the responses in i) (green). Hill curves provided by the 3 different ramps for the same glomerulus (black).

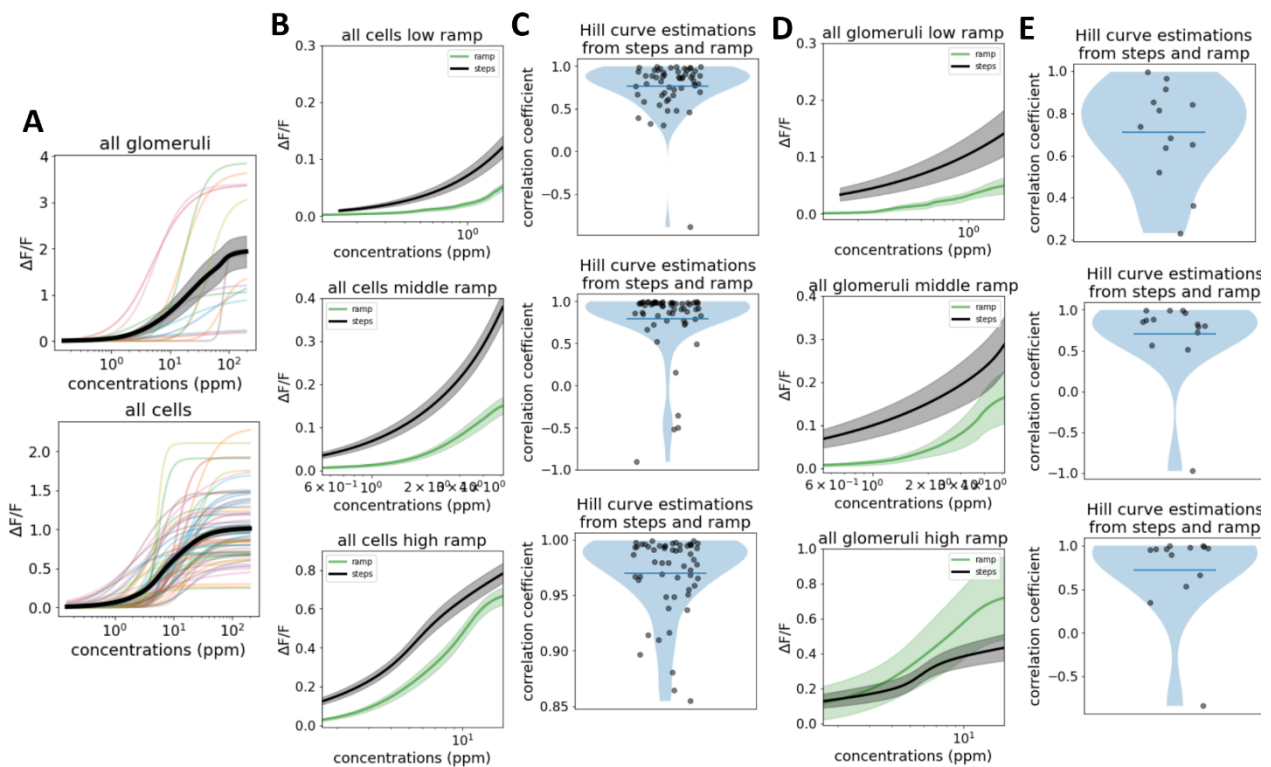


Figure 5.16 Ramp stimuli as a tool to estimate dose-response curves. The ramp stimulus allows testing a range of doses (concentrations in ppm) during 10 seconds. The relation between the isoamyl acetate concentration (ppm) and the PGC/glomeruli activity ($\Delta F/F$) (Fig 5.17) creates a dose-response curve on which a Hill function is fitted. The Hill functions generated from 12 steps stimuli match closely the ones estimated from fewer ramp stimuli. **a**) Hill functions of 17 glomeruli and 304 cells from 3 animals estimated from 12 steps responses (Fig 5.15 A). Average in black. **b**) for 304 PGCs, average of Hill functions fitted on 12 steps responses points (green) and the ramp responses (green). **c**) Correlation between the Hill function bout estimated from a ramp stimulus response and the corresponding truncated bout estimated from step responses. **d**) For 17 glomeruli, average of Hill functions fitted on 12 steps responses points (green) and the ramp responses (green). **e**) Correlation between the Hill function bout estimated from a ramp stimulus response and the corresponding truncated bout estimated from step responses. All the data here is in the fasted state.

To generate the ramps, I modified my custom script that controlled the olfactometer to be able to provide any temporal pattern of varying concentrations or flow rate. I made a loop that updates at 20Hz the value of the mass flow controller responsible for the % dilution of odour vial with air while maintaining a constant total flow rate (included in appendix A).

The ramps consisted of an initial 3 seconds plateau at the lowest 0.5% air dilution (because it cannot be set lower than that value) to start the stimulus without an immediate concentration jump. It was then increased from 0.5 to 10% air dilution in a 10 seconds ramp. The ramp stimuli were separated by 30 seconds. I used 3 different ramps using 0.03, 0.3, and 2.5% dilutions of isoamyl acetate in oil that I referenced as low, middle, and high ramps (Fig 5.15 D). A continuum of concentrations from 0.11 to 16.86 ppm was covered by these stimuli, with each ramp PID values respectively ranging from 0.11 to 1.68, 0.44 to 5.18, and 1.43 to 16.86 ppm.

As an example of the utility of ramps, I could observe 4 glomeruli with a different threshold of activation (Fig 5.15 D). I could as well infer bouts of dose-response function from these ramp responses (Fig 5.15 E, F, G&H). I then compared the dose-response obtained with ramps to that obtained with steps to verify the method, ramps gave similar dose-response functions to steps despite being lightly shifted (Fig 5.15 J, Fig 5.16), likely due to the delay in odour delivery. It strongly suggests that the ramps can be used to compare the concentration-response dynamic between fasted and satiated states.

The concentrations in ppm for 12 different step stimuli and the 3 ramps were measured with a photoionisation detector (Aurora, miniPID Fast Response Gas Sensor (200B)) (Fig 5.15 A, Fig 5.15 D). I used the PID measurements to sort the steps stimuli in an increasing ppm manner (Fig 5.15 A, B&I). From the 12 step stimuli, I extracted the amplitudes of the normalised fluorescence and used these to fit Hill curves remarkably well (Fig 5.15 C&J). The PID also gave the continuous ppm values of the 3 ramps (Fig 5.15 D). For each ramp, low, middle, and high, I recreated bouts of dose-response curves (Fig 5.15 E, F, G&H). Figure 5.15 J shows a dose-response curve gathered from step responses versus the ramps for a glomerulus. To assert the reliability of the ramps, I plotted the average bouts of Hill curves fitted from

the ramp responses from all cells and glomeruli in the fasted state and compare them with the curves calculated from the steps (Fig 5.16 A). It returned a good fit of the dosage-response curve for the cells, especially with the high ramp which gave a mean correlation between 0.95 and 1 (Fig 5.16 B&C). As for the glomeruli, the limited amount of samples made the correlation coefficient poor but still above 0.5 (Fig 5.16 D&E). Overall, the dose-responses curves estimated from ramp responses are a viable method of measurement of activity against a continuous range of concentrations and permit a precise detection of the concentration for which a PGC begins to activate.

The sensitivity threshold was measured as the first concentration that elicits an activation in a ramp response. I defined an activation as where the $\Delta F/F$ value rose above 2SD of the noise, which coincides with the inflection point where the trace starts rising (vertical dotted lines in figure 5.17). I then found back the ppm corresponding value on the ramp recording of the PID (blue trace, right y-axis, Fig 5.17 D). If no value above that threshold was detected, the data point was ignored. Furthermore, maximum amplitudes were also extracted from the ramp responses (left y-axis, Fig 5.17 D) as a measurement of maximum response. These measurements were proved useful to compare changes between fasted and sated states, in maximum responses, that is to say, responses to high concentration stimuli (ΔMAX , Fig 5.17) and changes in sensitivity threshold (ΔTHD , Fig 5.17), which tells the change in excitability of the PGCs.

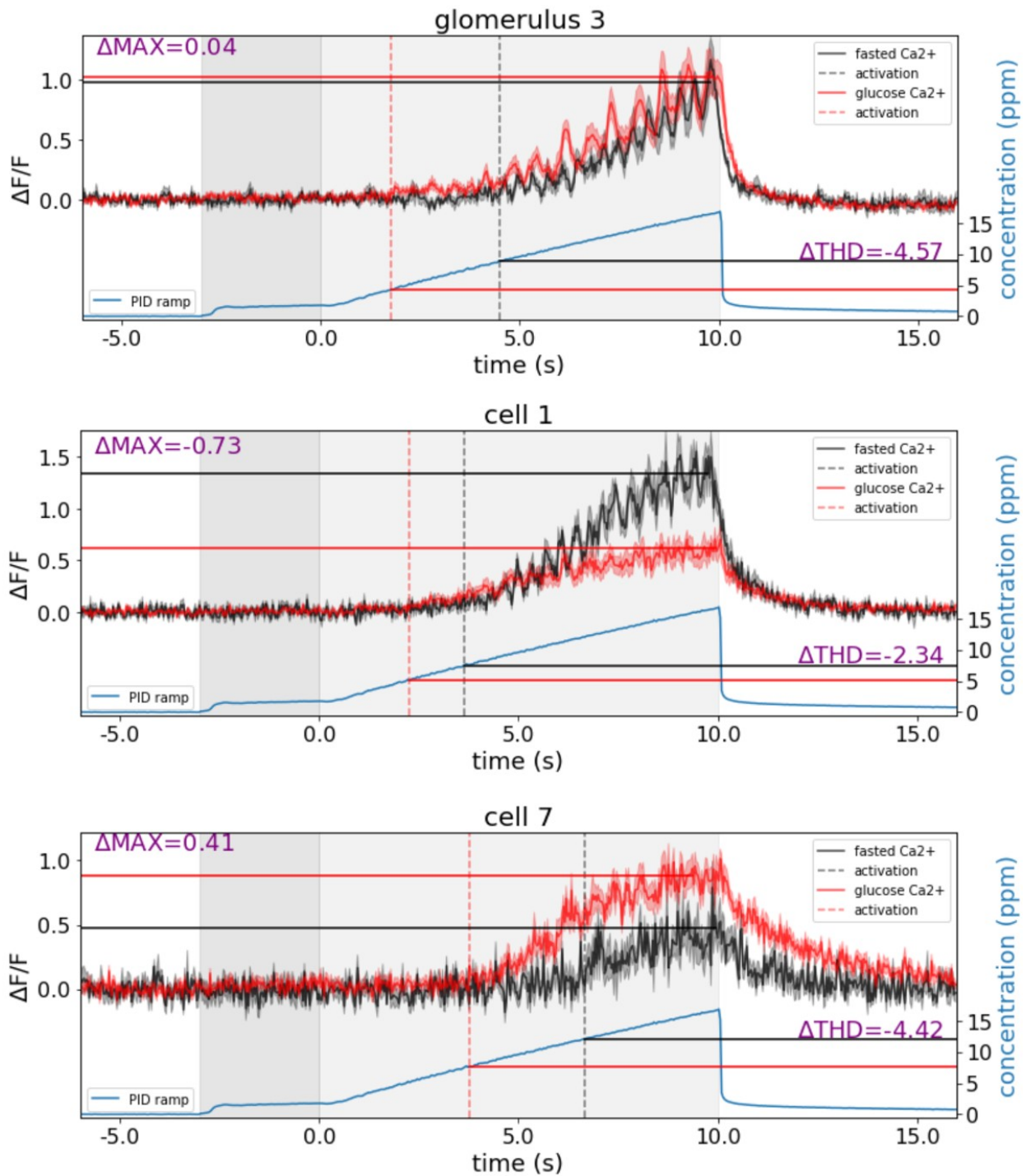
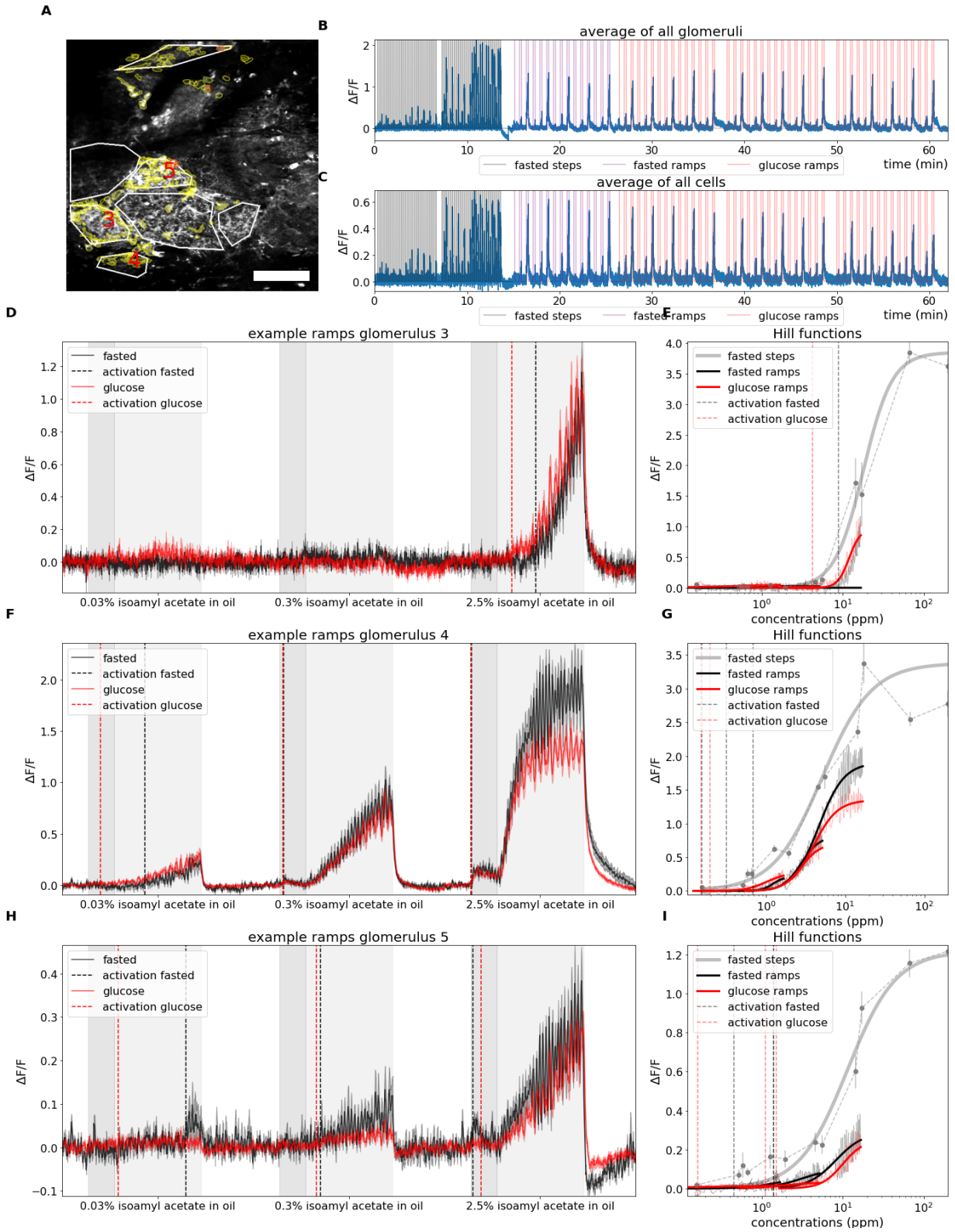


Figure 5.17 Ramp stimuli as a tool to estimate sensitivity threshold. The threshold corresponding to the first concentration (ppm) that activates a cell or a glomerulus was determined by a time point (vertical dotted lines) where the activity ($\Delta F/F$) (red and black traces) goes above 2 SD of the noise, which is estimated on 3 seconds of the baseline. That time point is then reflected on the PID trace (blue) which gives the corresponding ppm concentration on the right y-axis. Using This method allows the comparison of sensitivity (ΔTHD) between different states (sated in red, fasted in black). A difference of maximum (ΔMAX) responses was also computed on these ramp responses using the maximum of $\Delta F/F$ traces, under the criteria of being at least 2 SD above the noise.



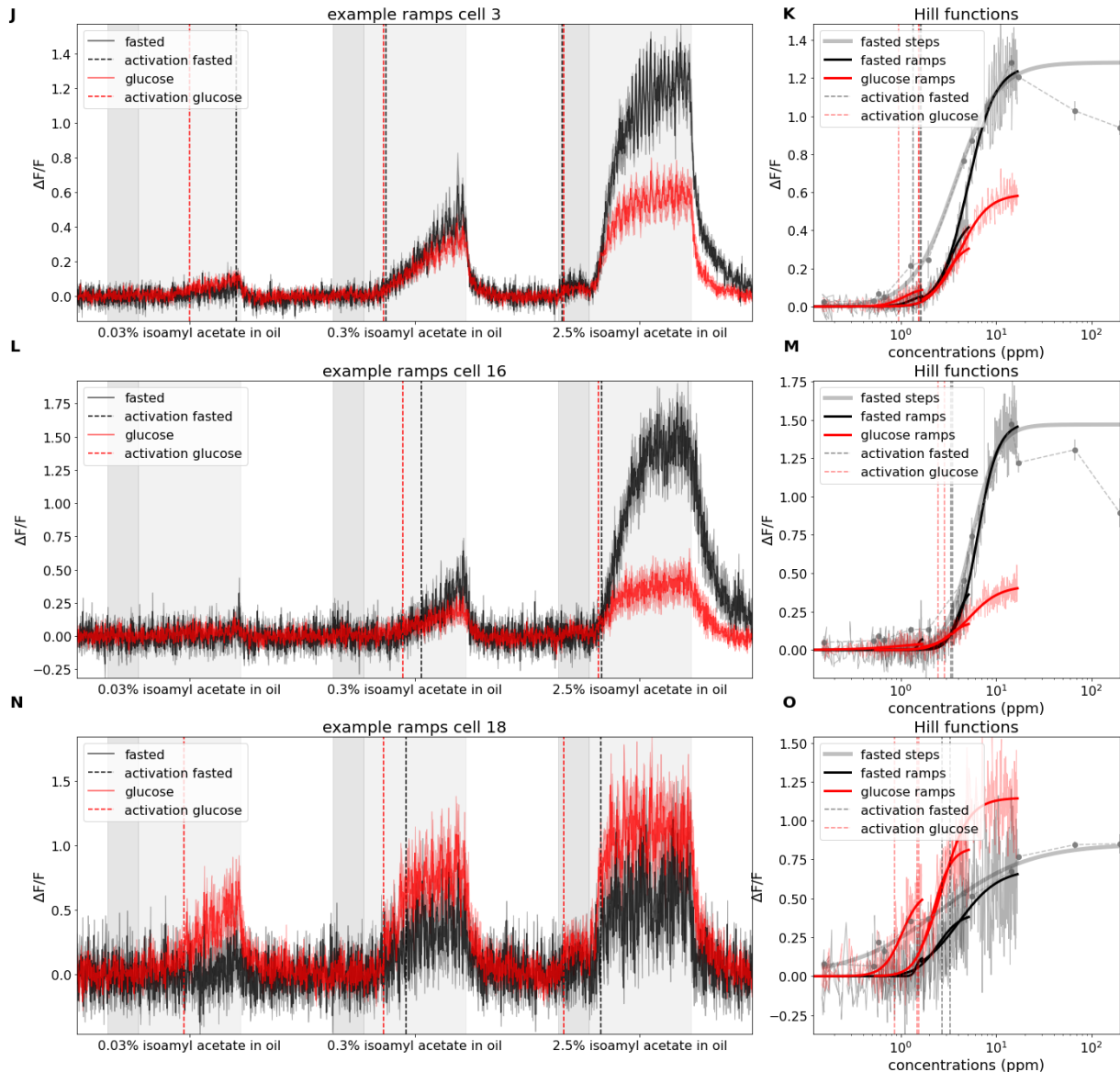


Figure 5.18 ramps experiment. Example of a ramp experiment in one animal. These experiments consisted in comparing the Hill functions estimated from step stimuli with ramp stimuli and observing the effect of blood glucose across time post-IP injection of glucose (2g kg^{-1}) using ramp stimuli to measure a shift in activation and a difference in maximum response. **a)** Field of view under two-photon microscopy. 108 cells ROIS in yellow. 7 glomeruli in white. **b&c)** concatenated average $\Delta F/F$ traces of 7 glomeruli and 108 cells (blue), with the overlaid protocol of the ramp experiment composed of 12 steps stimuli on increasing concentrations each repeated 5 times (black), followed by the 3 intensities ramps (0.03%, 0.3%, 2.5% isoamyl acetate in mineral oil, rising from 0.5% to 10% air dilution) (Fig 5.15 D) repeated 5 times (purple). After glucose administration, the 3 ramps are presented 15 times (red). **d,f,h,j,l,n)** Examples of responses to the 3 ramp stimuli, averaged of 5 responses in the fasted state (black), averaged of 15 responses in the sated state (red). Detected activations denoted by the vertical dotted lines, based on figure 5.17 method. **e,g,i,k,m,o)** Hill function fittings, from the 12 steps stimuli (grey), from the fasted ramps (black) and sated ramps (red). Vertical dotted lines from the panels on the left. Scale bar: $100\ \mu\text{m}$.

With this new method of sensitivity measurement established, I designed an experiment where I stimulated with the ramps before and after glucose administration. The stimulation protocol was as follows. I first stimulated with 12 different concentrations of step stimuli. They were made using isoamyl acetate at 0.03, 0.3, 2.5, and 100% dilution in oil. Each of these dilutions was then diluted in the airflow at 0.5, 3, and 10%. These 12 concentration steps were stimulated in 5 repeats in the fasted state (Fig 5.18 B&C) and used as a comparison with the ramps (Fig 5.15, Fig 5.16) as mentioned above. The steps lasted 3 seconds and were spaced by 10 seconds. Then I stimulated, still in the fasted state, with 3 or 5 repeats of the ramps of low, middle, and high intensities (Fig 5.15 D). 1-2 minutes after the glucose IP injection, I recorded again 15 repetitions of these 3 ramps for up to 60 minutes post-injection. I picked 3 different phases of the glycemc curve: 0-20, 20-40, and 40-60 minutes intervals to look at changes in the ramps, earliest activation, and maximum amplitude responses (Fig 5.18, 5.19, 5.20). The glucose measured before IP was below 10 mmol/l and above 20 mmol/l by the end of the session. The first interval of time gave data points corresponding to the rising glycemia while the rest reflected the plateau level (Fig 5.2 D).

In an example animal (Fig 5.18), the glomeruli ramps responses retained relatively constant amplitudes through the timecourse (Fig 5.18 A) while PGC ramps decreased with time (Fig 5.18 B). The blood glucose-induced changes were heterogeneous (Fig 5.18 D-O). The activation threshold was reached earlier in the satiety states mostly in the low ramp (Fig 5.18 F,J,N). Figure 5.18 M shows that a high ramp can be identical to the dosage-response curves generated from steps. In some cases, the activity was higher across all concentrations in the satiated state (Fig 5.18 N&O). Keep in mind these examples were done with 3 to 5 repeats of stimuli for the fasted component and 15 for the glucose one.

The ramp experiment was done with 3 animals from which I identified 304 PGCs and 17 glomeruli. Similarly as in chapter 3, only ramp responses with an SNR above 2 were accepted. Low, middle, and high ramp averaged responses in fasted and sated states are shown in figure 5.19 (cells) and figure 5.20 (glomeruli). For the cells, 20 low, 112 middle, and 267 high ramps

responses were accepted, each time in both fasted and satiated states (Fig 5.19). The activation in PGCs always came earlier in the sated state with the low ramp stimulus, whether the activation was computed globally over the average of all stimuli (first row) or by 20 minutes intervals (Fig 5.19). The middle and high ramps maximum responses were similar to the fasted state in the first 20 minutes but then decreased more and more during the 40 next minutes. The glomeruli responses were in a lower amount with 7 low, 12 middle, and 17 high ramps responses only accepted (Fig 5.20). Here there seems to be no differences between the fasted and sated states. However, the satiated state still seems to make glomeruli respond earlier in the small ramp as shown by the vertical dotted lines. These observations might indicate increased excitability of PGCs at the lower concentrations of stimulus. However, these detections of activations are computed on cells/glomeruli-averaged traces and must be computed on individual PGCs and glomeruli.

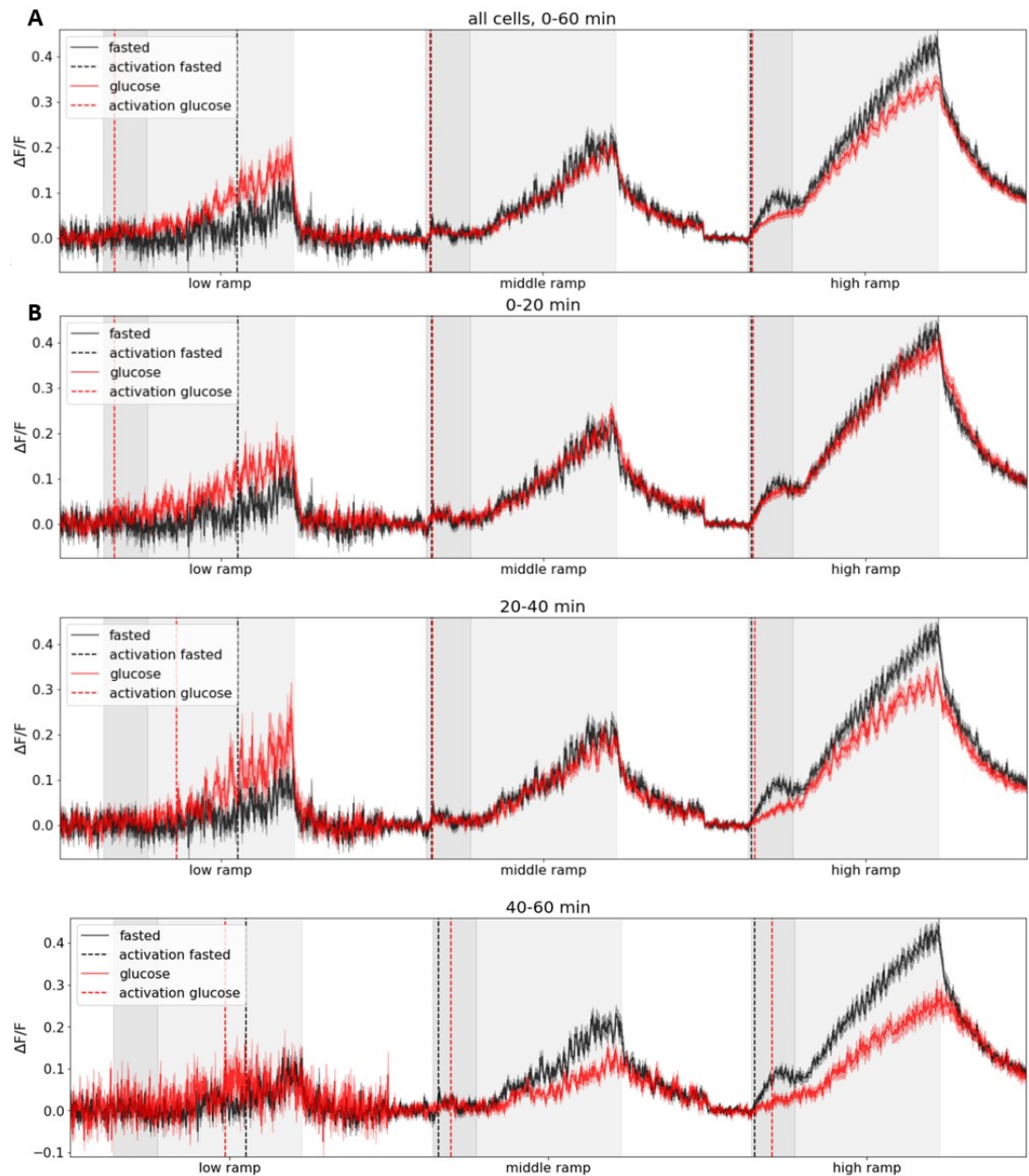


Figure 5.19 Average ramp responses and activation detection in PGCs following glucose administration. Averaged responses to the 3 ramp stimuli (low: 0.03%, middle: 0.3%, high: 2.5% isoamyl acetate in oil, rising from 0.5% to 10% air dilution). Detected activations denoted by the vertical dotted lines, based on (Fig 5.17) method. Activation is detected in point of response trace that reaches above 2SD of noise, this is used as a measure of sensitivity threshold. **a)** Average of 3 to 5 responses in the fasted state (black), average of 15 responses in the sated state (red). **b)** time series using the average within the 0-20, 20-40, and 40-60 minutes post glucose administration. Average of 3 to 5 responses in the fasted state (black), average of 3 to 5 responses in the sated state (red) in each time interval. (from 3 animals, low ramp: n=20 cells, middle ramp: n=112 cells, high ramp: n=267).

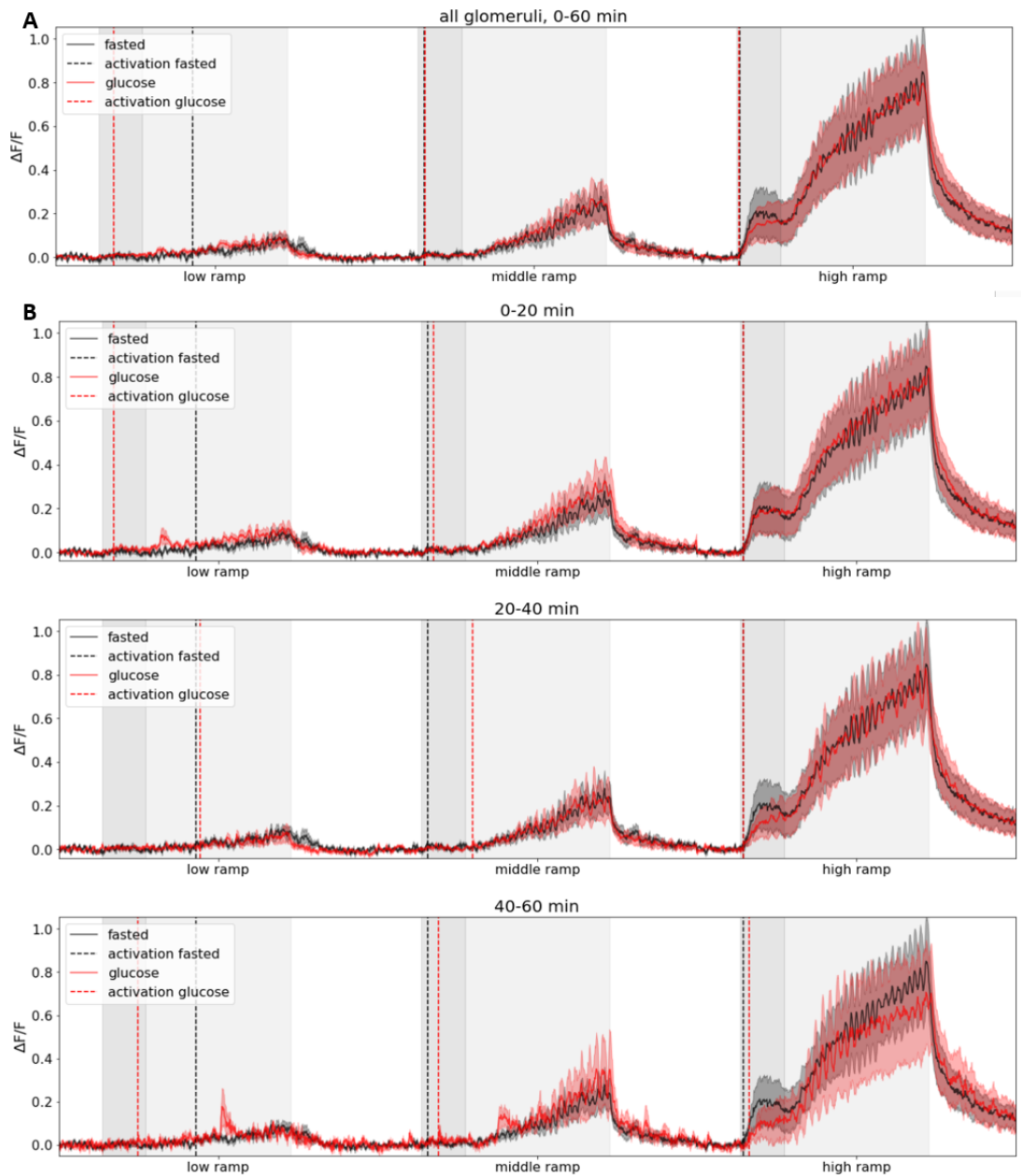


Figure 5.20 Average ramp responses and activation detection in glomeruli following glucose administration. Averaged responses to the 3 ramp stimuli (low: 0.03%, middle: 0.3%, high: 2.5% isoamyl acetate in oil, rising from 0.5% to 10% air dilution). Detected activations denoted by the vertical dotted lines, based on (Fig 5.17) method. Activation is detected in point of response trace that reaches above 2SD of noise, this is used as a measure of sensitivity threshold. **a)** Average of 3 to 5 responses in the fasted state (black), average of 15 responses in the sated state (red). **b)** time series using the average within the 0-20, 20-40, and 40-60 minutes post glucose administration. Average of 3 to 5 responses in the fasted state (black), average of 3 to 5 responses in the sated state (red) in each time interval. (from 3 animals, low ramp: n=7 cells, middle ramp: n=12 cells, high ramp: n=17).

For each 20 minutes segments post glucose administration, I computed the sensitivity threshold (Fig 5.21 A&B) and maximum response (Fig 5.21 C&D) difference as defined in figure 5.17. The difference of maximum responses was again normalised by the standard deviation of noise to take into account detectability across any noise levels. The number of differences measured for each time segment varied due to the presence or not of detected activations or if the maximums were above twice the SNR. Therefore, the low ramp tended to generate fewer data points.

The difference of sensitivity threshold in PGCs was negative in the first 20 minutes, that is to say the PGCs were excited at a smaller concentration in the sated state than in the fasted state, and especially for the low ramp (n= 7, mean±SEM=-0.44 ± 0.14) (Fig 5.21 B). After 40 minutes post-injection, the PGCs became to be excited at a later ppm concentration than in the fasted state, especially in the high ramps (n=131, mean±SEM=1.85±0.28). This trend of difference in sensitivity threshold (ppm), earlier activation in the first 20 minutes then later and alter afterwards, was visible in cells in all low, middle and high ramps (Fig 5.21 B) (across 20 minutes segments (0-20,20-40,40-60 min): **low ramp**: n= 7, mean±SEM=-0.44 ± 0.14; n= 4, mean±SEM=-0.06±0.12; n= 1, mean=0.77; **middle ramp**: n=79, mean±SEM=-0.55±0.13; n=60, mean±SEM=-0.31±0.19; n= 27, mean±SEM =0.57±0.3; **high ramp**: n=258, mean±SEM =-0.85±0.15; n=239, mean±SEM=0.74±0.22; n=131, mean±SEM=1.85±0.28).

All the low ramp responses in glomeruli showed an earlier activation at any time after the glucose IP injection (across 20 minutes segments (0-20,20-40,40-60 min): **low ramp**: n=7, mean±SEM= -0.57±0.17; n=5, mean±SEM= -0.38±0.2; n=3, mean±SEM= -0.09±0.15) (Fig 5.20 A, first panel) and even activated slightly earlier than cells in the first 20 minutes (glomeruli: -0.57ppm, cells: -0.44 ppm) (Fig 5.20 A). The stronger stimuli middle and high ramps gave responses with a globally later activation than in the fasted state (across 20 minutes segments (0-20,20-40,40-60 min): **middle ramp**: n=12, mean±SEM= 0.03±0.45; n=11, mean±SEM= 0.46±0.38; n=6, mean±SEM= 0.12±0.3; **high ramp**: n=16, mean±SEM= -0.4±0.45; n=16, mean±SEM= 1.15±0.83; n=9, mean±SEM=3.32±1.94) (Fig 5.20 A, second and last panel).

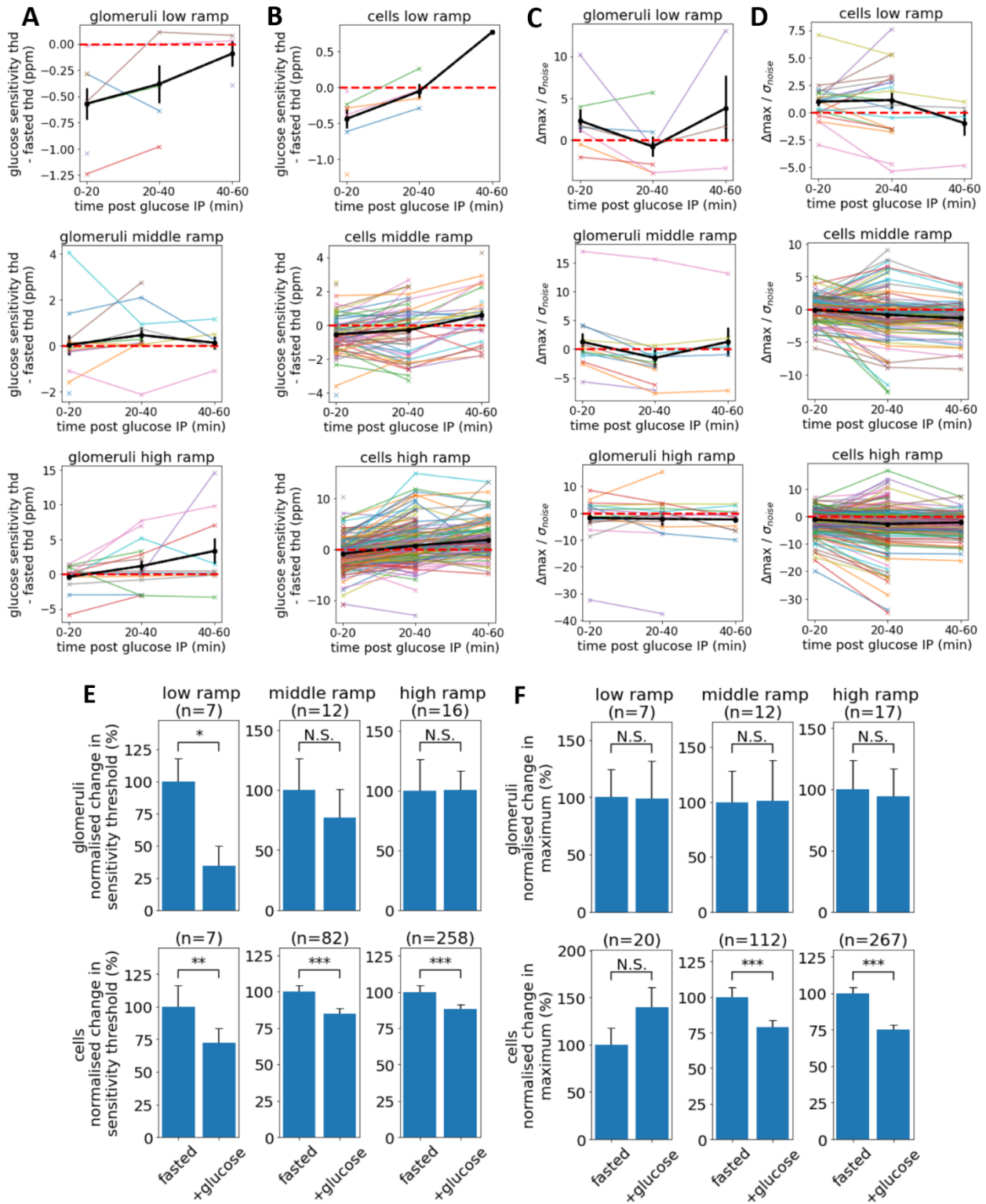


Figure 5.21 Change in sensitivity and maximum responses following glucose administration across 3 time periods. For all 3 periods of 20 minutes after the glucose IP injection, the difference (sated – fasted) of sensitivity threshold and maximum responses were computed (as defined in figure 5.17, for each ramp stimuli). Each time period comprises 3 to 5 repetitions of a ramp stimulus. The amount of samples is reduced with the low ramps, as it was more unlikely for the trace to reach a change of 2SD from the baseline, and therefore these samples were not added. **a)** Difference of sensitivity threshold in glomeruli between the

sated and fasted state (0-20,20-40,40-60 min: low ramp: n=7, mean±SEM= -0.57±0.17; n=5, mean±SEM= -0.38±0.2; n=3, mean±SEM= -0.09±0.15; middle ramp: n=12, mean±SEM= 0.03±0.45; n=11, mean±SEM= 0.46±0.38; n=6, mean±SEM= 0.12±0.3; high ramp: n=16, mean±SEM= -0.4±0.45; n=16, mean±SEM= 1.15±0.83; n=9, mean±SEM=3.32±1.94). **b)** Difference of sensitivity threshold in PGCs between the sated and fasted state (0-20, 20-40, 40-60 min: low ramp: n= 7, mean±SEM=-0.44 ± 0.14; n= 4, mean±SEM=-0.06±0.12; n= 1, mean=0.77; middle ramp: n=79, mean±SEM=-0.55±0.13; n=60, mean±SEM=-0.31±0.19; n= 27, mean±SEM =0.57±0.3; high ramp: n=258, mean±SEM =-0.85±0.15; n=239, mean±SEM=0.74±0.22; n=131, mean±SEM=1.85±0.28). **c)** Difference of maximum responses in glomeruli between the sated and fasted state (0-20, 20-40, 40-60 min: low ramp: n= 7 , mean±SEM= 2.32 ± 1.49; n= 7 , mean±SEM= -0.77 ± 1.28; n= 3 , mean±SEM= 3.78 ± 4.84; middle ramp: n= 12 , mean±SEM= 1.28 ± 1.63; n= 12 , mean±SEM= -1.53 ± 1.75; n= 6 , mean±SEM= 1.28 ± 2.71; high ramp: n= 17 , mean±SEM= -1.79 ± 2.17; n= 17 , mean±SEM= -2.2 ± 2.55; n= 10 , mean±SEM= -2.38 ± 1.4). **d)** Difference of maximum responses in PGCs between the sated and fasted state (0-20,20-40,40-60 min: low ramp: n= 20 , mean±SEM= 0.98 ± 0.43; n= 20 , mean±SEM= 1.12 ± 0.73; n= 4 , mean±SEM= -0.97 ± 1.32; middle ramp: n= 112 , mean±SEM= -0.08 ± 0.18; n= 112 , mean±SEM= -0.84 ± 0.37; n= 76 , mean±SEM= -1.38 ± 0.27; high ramp: n= 267 , mean±SEM= -1.13 ± 0.22; n= 267 , mean±SEM= -2.75 ± 0.41; n= 166 , mean±SEM= -2.21 ± 0.27). **e)** Normalised changes in sensitivity threshold in cells and glomeruli between fasted and the hour following glucose injection. **f)** Normalised changes in maximum response in cells and glomeruli between fasted and the hour following glucose injection. Coloured lines denote cells and glomeruli differences of sensitivity and maximum. black lines are the average. vertical black bars are SEM.

Overall, the concentration needed to activate a PGC in its response to a ramp is smaller in the sated state than in the fasted state, but only in the 20 first minutes after IP, which corresponds to the initial increase of blood glucose. As blood glucose reaches a plateau, the PGCs start to activate later than in the fasted state.

Is that earlier activation in the first 20 minutes joined by an increased maximum response? The hypothesis tells that since PGCs are getting more excitable with glucose, my expectation is they will reach a lower maximum response due to the PGC-PGC inhibition that comes earlier as well.

In cells, the glucose-fasted difference in maximum responses generally decreased along the time post IP and the size of the ramp (across

20 minutes segments (0-20,20-40,40-60 min): **low ramp**: n= 20 , mean±SEM= 0.98 ± 0.43; n= 20 , mean±SEM= 1.12 ± 0.73; n= 4 , mean±SEM= -0.97 ± 1.32; **middle ramp**: n= 112 , mean±SEM= -0.08 ± 0.18; n= 112 , mean±SEM= -0.84 ± 0.37; n= 76 , mean±SEM= -1.38 ± 0.27; **high ramp**: n= 267 , mean±SEM= -1.13 ± 0.22; n= 267 , mean±SEM= -2.75 ± 0.41; n= 166 , mean±SEM= -2.21 ± 0.27)(Fig 5.21 C&D).

Parsing responses over periods of 20 minutes limited the number of samples for sensitivity due to noise. There were not many points for low ramps, that give the highest resolution of tested concentrations, because a very low activation is hidden in noise and difficult to detect. It was therefore preferable to increase the number of repeats averaged using a whole 60 minutes period. I detected changes in the sensitivities and maxima for cells and glomeruli, in the fasted state vs 1-hour after glucose injection. The sensitivity threshold to isoamyl acetate in glomeruli tends to be reduced with glucose, only significantly with the low ramps but with a small sample (low, middle, high ramps: 100 ± 18 % vs 34 ± 15 %, 100 ± 26 % vs 77 ± 24 %, 100 ± 26 % vs 89 ± 16 %; Wilcoxon signed-rank tests) (Fig 5.21 E). In cells, the threshold significantly diminished with glucose for all ramps (low, middle, high ramps: 100 ± 16 % vs 64 ± 11 %, 100 ± 4 % vs 80 ± 4 %, 100 ± 4 % vs 86 ± 4 %; Wilcoxon signed-rank tests) (Fig 5.21 E). Glucose did not affect the maximum of the responses in glomeruli (low, middle, high ramps: 100 ± 24 % vs 99 ± 32 %, 100 ± 28 % vs 101 ± 37 %, 100 ± 24 % vs 94 ± 22 %; Wilcoxon signed-rank tests) (Fig 5.21 F). In cells, the maximum of responses tended to decrease with glucose, however no significant changes were detected with the low ramps (low, middle, high ramps: 100 ± 17 % vs 140 ± 21 %, 100 ± 7 % vs 79 ± 5 %, 100 ± 4 % vs 75 ± 3 %; Wilcoxon signed-rank tests) (Fig 5.21 F).

This diminution in maximum responses in cells confirm the observations of reduced activity at the highest concentration on the normalised Hill functions (Fig 5.14B) and in the set of 6 concentrations step stimuli responses (Fig 5.13 D&F). Only with the low ramp, at 0-20 and 20-40 minutes intervals, the maximum responses appeared bigger than in the fasted state (Fig 5.21D, first panel) possibly because the PGC-PGC inhibition would be less likely recruited with a such low intensity stimulus (across 20 minutes

segments (0-20,20-40,40-60 min): **low ramp**: n= 20 , mean±SEM= 0.98 ± 0.43; n= 20 , mean±SEM= 1.12 ± 0.73; n= 4 , mean±SEM= -0.97 ± 1.32).

The glomeruli vary slightly from the cells behaviour in the difference of maximum responses. The low and middle ramp responses expressed a greater maximum response in the sated state (20 minutes segments (0-20,20-40,40-60 min): **low ramp**: n= 7 , mean±SEM= 2.32 ± 1.49; n= 7 , mean±SEM= -0.77 ± 1.28; n= 3 , mean±SEM= 3.78 ± 4.84; **middle ramp**: n= 12 , mean±SEM= 1.28 ± 1.63; n= 12 , mean±SEM= -1.53 ± 1.75; n= 6 , mean±SEM= 1.28 ± 2.71) (Fig 5.21 C, first and second panel). The high ramp stimulus resulted in lower response maximum for all time points (**high ramp**: n= 17 , mean±SEM= -1.79 ± 2.17; n= 17 , mean±SEM= -2.2 ± 2.55; n= 10 , mean±SEM= -2.38 ± 1.4). These measures only match with the increase of activity across all concentrations shown in the Hill curve fittings gathered in figure 5.14 A for the low and middle ramps.

Overall, during the rise of blood glucose, in the 20 minutes following the glucose IP injection, the PGC somata and glomeruli were excited at a lower concentration than in the fasted state. After that time, the concentration required for activation increased. As for the maximum amplitude of the responses, they tended to decrease during the hour following the injection. By dividing the set of sated responses into 3 time intervals, the detectability and accuracy to measure sensitivity and maximum from the averaged response from each interval decreased as they were fewer repetitions to be averaged. The detection of maxima and sensitivity thresholds harvested little amount of data points, especially with the low ramp stimuli. Therefore, I decided to look at the average of all responses in the sated state, without regard to relation in time, to enhance the detection of the earliest activating concentrations and the maximum responses. I also fitted hill functions to the sated state ramps responses so I could compare them with previous hill function fittings (Fig 5.14), which were estimated from 6 concentrations steps stimuli that were measured during the blood glucose plateau.

I fitted bouts of Hill curves on the averaged of repeated ramp responses both in fasted (3 or 5 repeats) and satiated state (15 repeats) (cells: **low ramp**: n= 54, **middle ramp**: n= 59, **high ramp**: n= 55; glomeruli: **low ramp**: n= 12, **middle ramp**: n= 14, **high ramp**: n= 13). In the cells, I found that the hill curves bouts displayed a similar pattern of difference with a sated-related decrease at the higher concentrations (Fig 5.22 A, left) than in the 6 concentrations steps experiment (Fig 5.14 B). The difference in glomeruli fitted Hill curves did not seem to change much (Fig 5.22 B, left). However, for both PGCs and glomeruli, we can see an increase of the gain at the lowest concentrations (Fig 5.22 A&B, right). This difference at lower concentrations would encourage the hypothesis of PGCs early excitability in the satiated state.

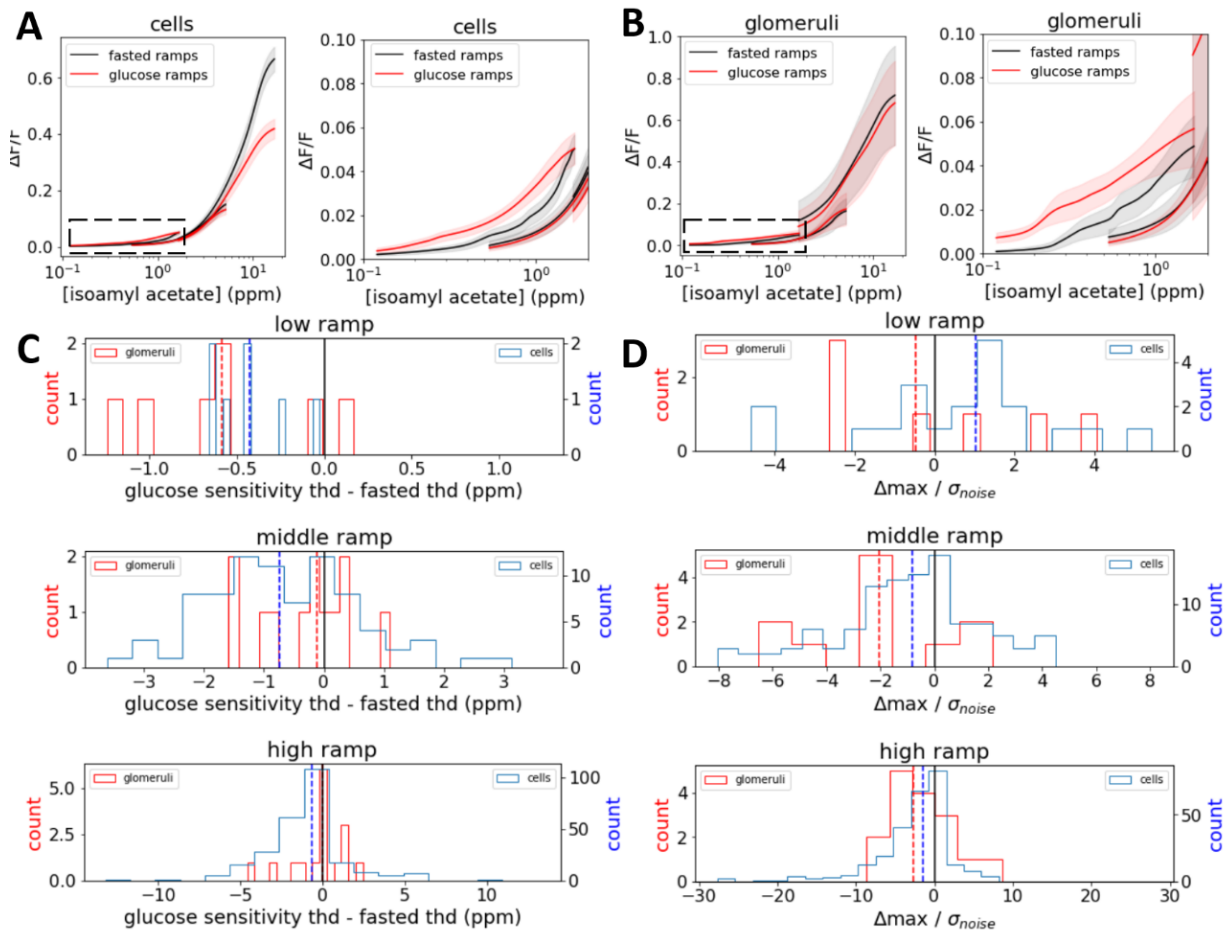


Figure 5.22 Difference in sensitivity threshold and maximum responses between the fasted state and the 60 minutes following glucose administration. **a)** average Hill functions of cells derived from the 3 ramps responses in fasted (black) and sated (red) state, right: zoom on the bout of Hill function fitted on low ramp responses. (low ramp: n= 54, middle ramp: n= 59, high ramp: n= 55). **b)** same as a) for glomeruli.(low ramp: n= 12, middle ramp: n= 14, high ramp: n= 13). **c)** Histograms of the difference of sensitivity for cells and glomeruli between the fasted state (3 to 5 repeats of stimuli) and

the sated state (15 repeats) for the low, middle and high ramps stimuli (glomeruli: low ramp: $n=7$, $\text{mean}\pm\text{SEM}=-0.02\pm 1.02$; middle ramp: $n=12$, $\text{mean}\pm\text{SEM}=-0.97\pm 1.48$; high ramp: $n=17$, $\text{mean}\pm\text{SEM}=-3.34\pm 2.35$), (cells: low ramp $n=20$, $\text{mean}\pm\text{SEM}=0.63\pm 0.55$; middle ramp $n=112$, $\text{mean}\pm\text{SEM}=-1.0\pm 0.26$; high ramp: $n=267$, $\text{mean}\pm\text{SEM}=-2.59\pm 0.3$). **d**) Histograms of the difference of maximum response for cells and glomeruli between the fasted state (3 to 5 repeats of stimuli) and the sated state (15 repeats) for the low, middle and high ramps stimuli (glomeruli: low ramp: $n=7$, $\text{mean}\pm\text{SEM}=-0.56\pm 0.19$; middle ramp: $n=12$, $\text{mean}\pm\text{SEM}=-0.31\pm 0.23$; high ramp: $n=16$, $\text{mean}\pm\text{SEM}=-0.22\pm 0.45$), (cells: low ramp: $n=7$, $\text{mean}\pm\text{SEM}=-0.42\pm 0.09$; middle ramp $n=82$, $\text{mean}\pm\text{SEM}=-0.66\pm 0.14$; high ramp: $n=258$, $\text{mean}\pm\text{SEM}=-0.95\pm 0.16$). Vertical dotted lines are the medians of the distributions.

The histograms of differences in sensitivity thresholds show for both PGCs and glomeruli earlier response activations in small ramps with a smaller effect as the ramp height increases (dotted lines show the median of the distributions, Fig 5.22 C). The low ramp activated cells and glomeruli with a concentration up to 1 ppm lower (cells: $n=7$, $\text{mean}\pm\text{SEM}=-0.42\pm 0.09$; glomeruli: $n=7$, $\text{mean}\pm\text{SEM}=-0.56\pm 0.19$), the middle ramp up to 3 ppm lower (cells: $n=82$, $\text{mean}\pm\text{SEM}=-0.66\pm 0.14$; glomeruli: $n=12$, $\text{mean}\pm\text{SEM}=-0.31\pm 0.23$), and the high ramp up to 10 ppm lower (cells: $n=258$, $\text{mean}\pm\text{SEM}=-0.95\pm 0.16$; glomeruli: $n=16$, $\text{mean}\pm\text{SEM}=-0.22\pm 0.45$) (Fig 5.22 C). The noise-normalised changes in maximum responses were positive only for the cells stimulated by the low ramp (cells: $n=20$, $\text{mean}\pm\text{SEM}=0.63\pm 0.55$; glomeruli: $n=7$, $\text{mean}\pm\text{SEM}=-0.02\pm 1.02$) (Fig 5.22 D, first panel). For the middle (cells: $n=112$, $\text{mean}\pm\text{SEM}=-1.0\pm 0.26$; glomeruli: $n=12$, $\text{mean}\pm\text{SEM}=-0.97\pm 1.48$) and high ramps (cells: $n=267$, $\text{mean}\pm\text{SEM}=-2.59\pm 0.3$; glomeruli: $n=17$, $\text{mean}\pm\text{SEM}=-3.34\pm 2.35$), the changes in maximum response were rather negative (Fig 5.22 D, second and last panel).

By extracting the difference in sensitivity thresholds and maximum responses using all the responses during the 60 minutes post IP, I showed that PGCs could be more excitable with an increase of blood glucose, as they activate at an earlier concentration, and subsequently more inhibited at higher concentrations, as their maximum response reduced.

The earlier activations of PGCs in a satiated state corroborate the hypothesis of reducing small intensity stimuli. This effect is mostly present up

to 20 min after the glucose injection, during glycemia increase. After that and by the end of the blood glucose plateau, PGC activity decreased.

5.6 Conclusion

I identified heterogeneous effects induced by heightened blood glucose in the glomerular layer of the olfactory bulb, in OSN and PGCs. I only observed an evident effect on the OSN-PGC feedback inhibition circuit while applying iGluR blockers under OMMI, where increased excitability of PGCs led to a decreased OSN activity within glomeruli.

While behaviour sensitivity tests resulted in a non-significant conclusion of sated mice being more olfactory sensitive, PGC somata and glomeruli demonstrated a mix of down and up modulation. The heightened sensitivity witnessed in behaviour partially reflected the increase of PGC glomeruli activity, observed under OMMI and two-photon imaging. However, at the level of the somata, a contradiction with the glomeruli appeared as the somata activity diminished at higher concentrations. This brought a new question about the different actions of glycemia in the dendrites and the somata. This may foretell implications of complex circuits in the glomerular layer with multiple PGC subtypes that meet their dendrites in glomeruli.

Chapter 6

Summary discussion, future perspectives and Conclusion

6.1 Characterisation of odour-evoked PGC properties

In chapter 3, I investigated the odour-evoked properties of the PGCs somata and glomerular dendrites. I observed a similar odour-evoked dynamic between the PGCs and their parent glomeruli, and attempted based on the connectivity alone to classify subtypes of PGCs. All experiments were conducted in fasted mice, as they were used as a control hungry state before a glucose injection.

6.1.1 odour-evoked periglomerular cells properties

Different shapes of responses were observed, corroborating with previous observations of inhibitory and excitatory onset responses, and excitatory offset responses (Homma et al., 2013). While Homma et al. (2013) highlight 3 response shapes, I found about 8. The majority was composed of short and long excitatory transients. Some rarest ones were biphasic: excitatory-inhibitory and inhibitory-excitatory. Some were activated at odour onset and others at odour offset. The inhibitory responses were a minority, but it is partly due to the limitation of suite2p, software to segment neurons in calcium imaging data, to detect them, as the common assumption is to look for positive responses.

Cells and glomeruli did not elicit only one type of shape, but sometimes different ones depending on the odour presented, e.g. an inhibitory response for isoamyl acetate and an excitatory response for ethyl tiglate. Therefore the shapes were properties of an odour-cell rather than a cell. Furthermore the shapes tended to change with the concentration of the stimulus.

Odour-evoked activity of PGCs is known in literature, as observed with calcium imaging in vivo (Homma et al., 2013). In this thesis, the novelty was to test a panel of 6 concentrations for 8 odours. The aim of using that spread of concentrations was to build dosage-concentration curves. The curves allowed to determine metrics such as sensitivity or EC50. PGCs belonging to a same glomerulus tended to share their odour-evoked properties. Kovalchuk et al. (2015) found as well that adult-born PGCs have the same sensitivity as their parent glomeruli.

I found finally 3 types of dosage-response curves, two were typical sigmoids, with one kind closely relating to the glomerulus input, and the last one had the particularity to respond at the lowest concentration then show a decreased activity while increasing concentration. Furthermore, a PGC that was very sensitive as described above, could be for one odour but would have a regular sigmoid dosage-response curve for another odour. The mechanism behind the high sensitivity decreasing response profiles remains elusive.

Furthermore, I observed in the increasing response profiles, that after reaching a saturated maximum, the cell/glomerulus started to respond less to the subsequent higher concentration. A mechanism of PGC-PGC inhibition might be responsible for that observation. It has been shown in slices that MgluR (ii) participates in intraglomerular strong reciprocal inhibition (Zak and Schoppa, 2021). The mGluR (ii) is recruited at higher stimulation in PGCs (Zak et al., 2015). Another self-inhibition mechanism would be PGC-PGC GABA spill-over, previously shown in slices (Murphy et al, 2005; Najac et al., 2015; Shao et al., 2019). One manner to demonstrate the implication of GABA in that reduced gain after saturated response would be to see if it disappears after applying GABA blockers topically.

6.1.2 PGC inheritance of mechano-sensitive signals from OSN

I investigated the oscillatory activity and phase coding of PGCs. PGCs inherit the respiration-induced mechano-sensitive signals from the OSNs (Iwata et al., 2017). The phase shifted when an odour was presented, showing that phase plays a role in coding odour identity (Gire et al., 2013; Dhawale et al., 2010). I observed a similar odour-evoked phase between the PGCs and their parent glomeruli. Furthermore, I showed that the basal preferred phase of glomeruli and PGCs is the same, and close to the OSN phase reported in the literature (Ackels et al., 2020). As for the odour-evoked phases that deviate from that basal value, I suggest they might be involved in shaping the large diversity of phases observed in MTCs (Iwata et al., 2017).

6.1.3 determining PGC subtypes based on odour-evoked activity

The PGC subtypes can be classified by their number of connections to glomeruli. Estimating connectivity between PGCs and glomeruli was done based on the criteria of a common responses shape, a same odour tuning, and a close distance. Visually, the connections seemed realistic, as the asserted cells were found in a close vicinity of the parent glomerulus. Functionally, The average activity of the daughter PGCs was well correlated with the parent glomerulus.

The number of connections per cell was however overestimated because a connection was considered valid if the cell was sharing only one odour-response shape at the minimum. Another bias is the constrained distance of 100um, which is a conservative assumption but will get the most of the linked PGCs. The attributed subtypes based on connections were largely overlapping with 80% of PGCs being either uniglomerular (1-3 connections) or oligoglomerular (2-6 connections). The left minority were allocated as microglomerular (20%) and almost none to the polyglomerular type.

This distribution has similarity with the latest study done with electrophysiology means in slices (Tavakoli et al., 2018), even if these slice experiments were also restrained to only 64 measured PGCs. Tavakoli et al. (2018) found the largest group was also oligoglomerular with 35% then uniglomerular cells with 25%, and lastly microglomerular cells with around 15%. They also inferred the polyglomerular cells to be around 20%, which I could not infer in my experiments. 10 to 16% of the JGCs in the glomerular layer are indeed dopaminergic, that is to say, OGC or POGC (McLean and Shipley, 1988; Panzanelli et al., 2007).

Polyglomerular cells were not easily detectable in this thesis, due to the limited field of view of the two-photon microscopy, as POGC can extend their dendrites to glomeruli up to 500um. Also, the 100um constraint limits the finding of connected POGCs. The microglomerular cells, which are CR+, were also under-represented in my study. CR+ PGCs are supposed to be abundant, but since they are not OSN-driven I did not detect them much through odour stimulation.

The microglomerular cells have a physiotype that elicits slow plateau responses (Tavakoli et al., 2018) which might relate to my observations of long bumps of spontaneous activity in cells that were not activated by odourants and therefore were not included in my study.

I attempted to determine PGC subtypes only based on the odour-evoked response profiles of PGCs, while knowing that the best differentiator would be their neurochemistry. My findings were limited as the categorised subtypes were largely overlapping. With the same method as in chapter 3, using a larger panel of odours might help refine the connectivity estimation. The use of more complex patterns of stimuli may be also beneficial to elude connectivity. For example, a long stimulus would elicit different kinds of adaptation responses that would help link PGCs to their parent glomeruli. A higher speed recording to measure the onset delays of activation could be also a powerful manner to estimate connection, as cells and glomeruli are closely activated in time.

The ideal estimation of connectivity would be the use of a tracing method to construct a ground truth. One could pipette a dye into a PGC and observe the dendritic ramifications into glomeruli. The properties of these ramifications and the PGC morphology could also play a role in determining the subtype (Tavakoli et al., 2018; Kosaka et al., 2019; Kiyokage et al., 2010; Bywalez 2017). On the other hand, injecting a retro-tracing agent in a glomerulus would highlight all the daughter PGCs. Ultimately, the solution is staining post-imaging for CR+, CB+, and TH+ cells. It remains difficult to assert PGC subtypes just by observing odour-evoked activity of VGAT expressing cells in the glomerular layer of the olfactory bulb.

6.2 Optical Multi-Modal Imaging for simultaneous recording of OSN and PGC

We developed a method for simultaneous imaging of two neural populations, here the OSN and PGC, called optical multi-modal imaging (OMMI). The advantage of this method is that it does not require additional injections of fluorophores; a modified mouse that expresses a GECI suffices. The GECI, such as GCaMP6, permits the observation of a first neural population under the one-photon microscopy modality of OMMI. A second

population can be measured through intrinsic signal optical imaging; in the olfactory bulb, the OSN axons terminals.

Intrinsic signal optical imaging (ISOI) presents similar results and resolution as a BOLD MRI signal. Depending on the wavelength used, intrinsic signals can tell about the blood oxygenation, the blood volume, or some neural activity. This modality can also be used in the field of vision, wherein the visual cortex, after doing a Fourier analysis, one can observe the visual stimuli frequency for example (Schwartz, 2003). A similar logic permits investigation in the auditory cortex (Teichert and Bolz, 2017). In the olfactory bulb, I validated the intrinsic signals for the OSN as I showed a correlation with the GCaMP odour-evoked activity of the glomeruli, against increasing concentrations.

The main interest of the OMMI system is the ability to test drugs or state effects on multiple populations at the same time, and investigate the function of neural circuits. I showed by applying iGluR blockers, a disruption of the inhibitory feedback loop between OSN and PGC. Following topical drug application of NBQX and DAP5, PGCs were less activated by the OSNs glutamate, and in return, the OSNs were less inhibited by the PGCs. The attenuated intrinsic signals under drugs confirm previous experiments (Vincis et al., 2015; Gurden et al., 2006). OMMI adds the novelty of having PGC signal recorded simultaneously.

Previous study of the input-output of the olfactory bulb, aimed at recording both OSN and MTC (Storace et Cohen., 2017, Storace et Cohen., 2019). However, these methods are inconsistent because they always depend on the success of the second population staining after injections of an additional calcium or voltage indicator (Storace et Cohen., 2017, Storace et Cohen., 2019). For instance, nasal injection for functionally staining the OSN takes time and is uncertain. OMMI solves that issue with the use of ISOI which does not require any injection, and even works in a wild mouse.

The two modalities I used under OMMI, Wide-field one-photon imaging and ISOI, have limitations. ISOI of olfactory responses works best at higher concentrations because it gives a quite noisy signal. Alternatively, smaller stimuli responses can be recorded using more repeats. Increasing the

framerate for ISOI is another solution to reduce noise. ISOI depends on tissue osmolarity (vincis et al., 2015), therefore one must be aware that edema post-surgery and drying of tissue in long non-recovery experiments may affect the signals. One-photon imaging is limited by emitted light scattering and thus biased towards the activity of superficial brain layers.

GCaMP and ISOI have different resolution and response scales. ISOI is at lower spatial and temporal resolution. The user must pay attention that ISOI changes are in 1:10 000, as the fluorescence responses are rather in 1:10. Changes are harder to detect in ISOI. These two modalities have therefore to be cautiously compared one to the other, e.g. one cannot simply summarise both channels as excitation/inhibition ratio, in the case of imaging an excitatory and and inhibitory population.

We established an open-source low-cost and consistent method for dual population imaging, with up to 3 channels, and the possibilities to study neurovascular coupling, olfaction, audition, and vision. It is provided with an open-source graphical user interface that enables to run an experiment protocol and preview results. Furthermore, it can be adapted for studies in awake animals. OMMI is compatible with any micromanager camera, coupled to open-ephys cyclops optical controllers. Finally, a python pipeline to process the acquired data with that GUI can be found on the Johnston lab Github.

6.3 Effect of blood glucose on OSN and PGC in glomeruli

In anaesthetised fasted mice, the emulation of satiety via a glucose intraperitoneal injection disturbs the odour-evoked activity of olfactory sensory neurons axon terminals and periglomerular cells. The effect diverges for low and high concentrations stimuli and is therefore bimodal. It results in reduced afferent activity at low concentrations likely due to the PGC dendrites increased activity (Fig 6.1).

The glycemia-induced changes in PGCs are heterogeneous and unexpectedly different for PGCs somata and glomerular dendrites (Fig 6.1). While the EC_{50} -related sensitivity remains unchanged for both, glomeruli rather amplified their response across all concentrations while the somata decreased in activity at high concentrations. Only when using the ramps stimuli, an increased somatic activity could be observed at low concentrations

(see 5.5). The heterogeneous effect of blood glucose on PGCs (Fig 5.12 C&D, Fig 5.13) could relate to the only partial occurrence of Kv1.3 and GLUT4 (Fig 5.1) in PGCs. To further demonstrate the modulation of the olfactory afference via glucose-sensing PGCs, an experiment of GABA and Kv1.3 blockers topically applied should be conducted in vivo, following the same protocols as in chapter 5.

However, overall some major dynamics come out. The changes in the activity of PGC somata recorded through 8 odours with 6 concentrations steps stimuli (Fig 6.1, 2P steps, left) concord with the observations using only isoamyl acetate with ramp stimuli (Fig 6.1, 2P ramps, left). The increased activity across all concentrations of PGC dendrites was also confirmed in both OMMI (Fig 6.1, OMMI, right) and 6-step experiments (Fig 6.1, 2P steps, right). Interestingly, OSN activity changes (Fig 6.1, OMMI, left) are opposed to the ones in PGC somata, for the low and high concentrations. This suggests an enhancement of the feedback inhibition of PGC somata onto OSN terminals (based on 2P ramps somata and OMMI OSN measurements, Fig 6.1).

A model could be that the glucose-sensing happens in the PGC dendrites (based on 2P steps and OMMI PGC measurements, Fig 6.1) as they have more surface to sense nutrients in the extracellular space, while somata would auto-inhibit due to over-excitation at higher concentrations.

Finally, the measurements in the PGC somata ramp responses (Fig 6.1, Fig 5.22 A) gave a dosage-response curve post-glucose that tends to match the hypothesised change of activity, summarised in figure 6.2. The heightened blood glucose made the somata more excitable at the lowest concentrations and induce PGC-PGC inhibition at higher concentrations. However, the sample size for these low ramp stimuli measurements was small and only tested on isoamyl acetate, despite being more accurate to detect a concentration of the first activation than the Hill curve fitted over 6 steps responses.

6.4 Future suggestions

I used glycemia as a proxy for satiety while bypassing other aspects of satiety such as stomach distention and enteric secretions involved during food intake. Increasing blood glucose does not take into account other satiety

signaling pathways to PGC and OSN. There is a plethora of other satiety signals that the olfactory bulb can detect, that could be investigated (Julliard et al. 2017). Glucose was the easiest satiety signal to modulate. The olfactory afference, and therefore olfactory sensitivity, can also be modulated but centrifugal fibres such as noradrenergic fibres from the locus coeruleus (Eckmeier and Shea, 2014) or serotonergic inputs (Petzold, Hagiwara, and Murthy, 2009). Finally, the vagal nerve communicates the mechanosensation of stomach distension.

The rationale of metabolic sensing modulating olfaction implies that the odour represents an opportunity for caloric intake. Yet, isoamyl acetate was not per se a food-odour, despite smelling like banana. Isoamyl acetate attractiveness to mice appears inconsistent in literature, with increased olfactory performance when fasted (Aimé et al. 2007; Prud'homme et al. 2009) to just a neutral interest (Wu et al. 2020).

The study of olfactory-metabolism integration would make more sense using an odour paired to food. One manner to pair is to soak the cage food pellets with isoamyl acetate. Another way is to reward the detection of the odour with food but then it would become an operant learning and might rather associate the odour more with a task than with the food. Using food deprivation repetitively to force mice to associate the odour with food may be a viable solution.

Furthermore, anesthetised animals cannot manifest so much the mechanisms of satiety. The glucose and insulin tolerance tests differ between awake and anesthetised mice. Anesthetics impair glucose tolerance test and insulin secretion, inducing hyperglycemia, as it is shown with ketamine or isoflurane (Andrikopoulos et al. 2008; Windeløv, Pedersen, and Holst 2016; Zuurbier et al. 2014). Adjunction of atropine for urethane anesthesia also affects glucose tolerance (Zuurbier et al. 2014).

This calls for chronic imaging in awake animals with a glucose-monitoring system via a subcutaneous device (Klueh et al. 2006). This would bring an additional advantage of conducting behavioural tests and imaging in the same mice to compare the olfactory sensitivity in tests in regard to the measured neural activity, and gives the possibility to investigate the learning of food-odour pairing.

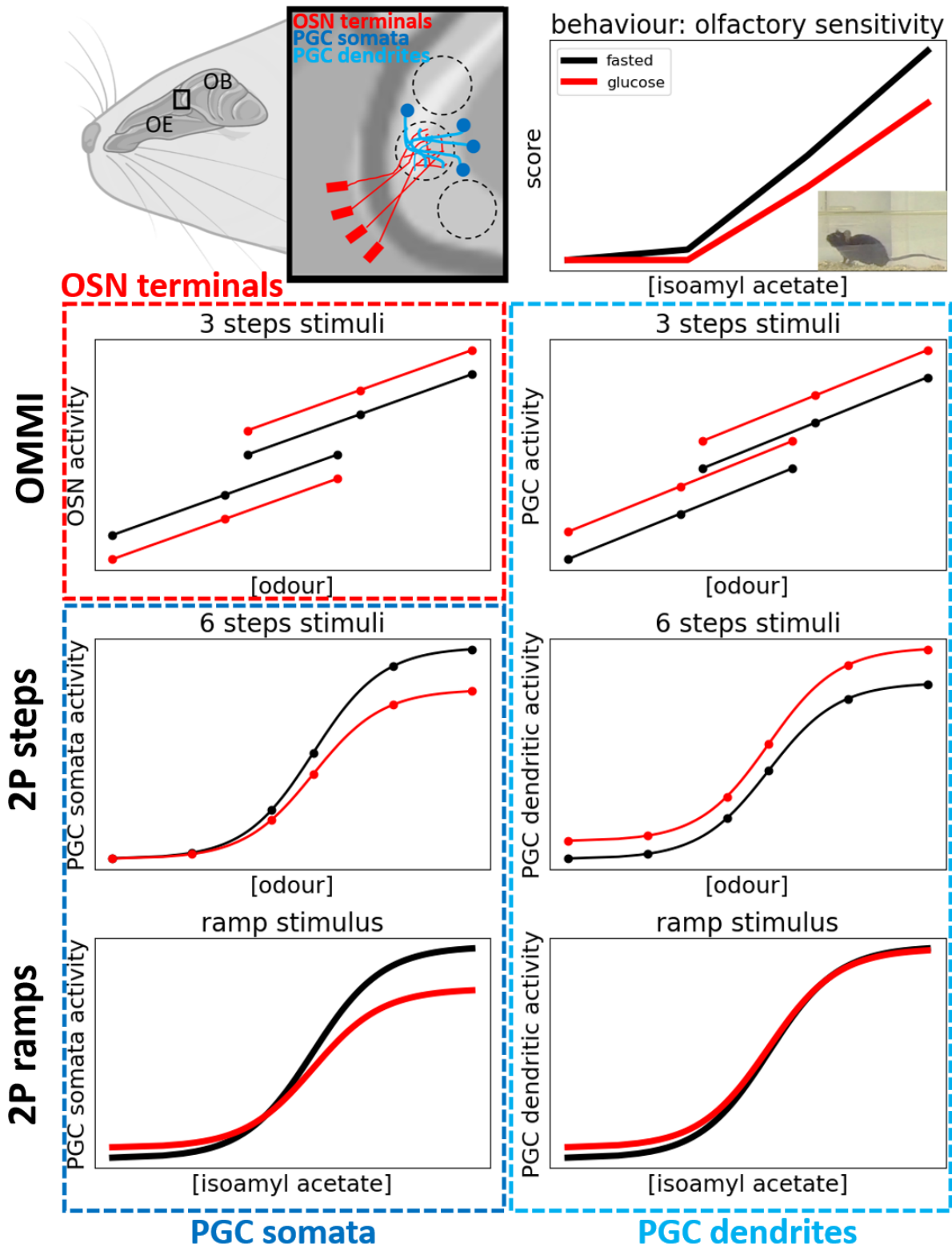


Figure 6.1 Graphical summary of glucose experiments. The influence of satiety on olfactory sensitivity was investigated in behaviour and the neural circuit at the first synapses in the olfactory bulb. The first neural computation occurs as a feedback inhibition of the inhibitory interneurons PGC into the OSN terminals in the glomerular layer of the olfactory bulb. To emulate satiety states, mice fasted overnight to induce hunger, and an i.p. injection of glucose (2g/kg bodyweight) mimicked the satiated state. The plots depict the results from chapter 5, with a behaviour detection test and 3 imaging experiments: OMMI (OSN and PGC glomeruli), 2P steps (PGC somata and glomeruli), and

2P ramps (PGC somata and glomeruli). In the 2P experiments, glomeruli consist in the sum of the local PGC dendrites. Black curves represent the fasted state and the red the sated state. **Behaviour**: fasted mice scored better in an isoamyl acetate detection test than the sated ones. **OMMI**: OMMI simultaneously records OSN and PGC glomeruli through 1P and ISOI imaging methods. The 2 first lines represent points from iGluR blocker experiments, attenuating glutamate intake from the afference works as a proxy for using lower concentrations stimuli. OSN terminals activity was decreased with glucose at lower concentrations but increased at higher concentrations. PGC glomeruli activity was increased along with all concentrations. 4 odours were used: 2-heptanone, isobutyl propionate, ethyl tiglate, and isoamyl acetate. **2P steps**: Hill functions were fitted on the activity of 6 steps stimuli of increasing concentrations. PGC somata only change was a decreased activity at higher concentrations. The glomeruli activity was globally enhanced. 8 odours were used: 2-heptanone, 2-isobutyl thiazole, 2-phenylethanol, 2,3,5-trimethyl-3-thiazoline, isobutyl propionate, isopentylamine, ethyl tiglate, and isoamyl acetate. **2P ramps**: Using a continuously increasing stimulus over 10 seconds, precise dosage-response curves were produced. This improved stimulus resolution enabled us to see increased excitability of both PGC somata and glomeruli at the lowest concentrations. Only isoamyl acetate was used. OE: olfactory epithelium; OB: olfactory bulb; 2P: two-photon calcium imaging; 1P: one-photon widefield calcium imaging; ISOI: intrinsic signal optical imaging. Adapted from “mouse head (lateral)”, by BioRender.com (2021).

Blood glucose \nearrow \Rightarrow $Kv_{1.3}$ \searrow \Rightarrow PG excitability \nearrow & OSN inhibition \nearrow

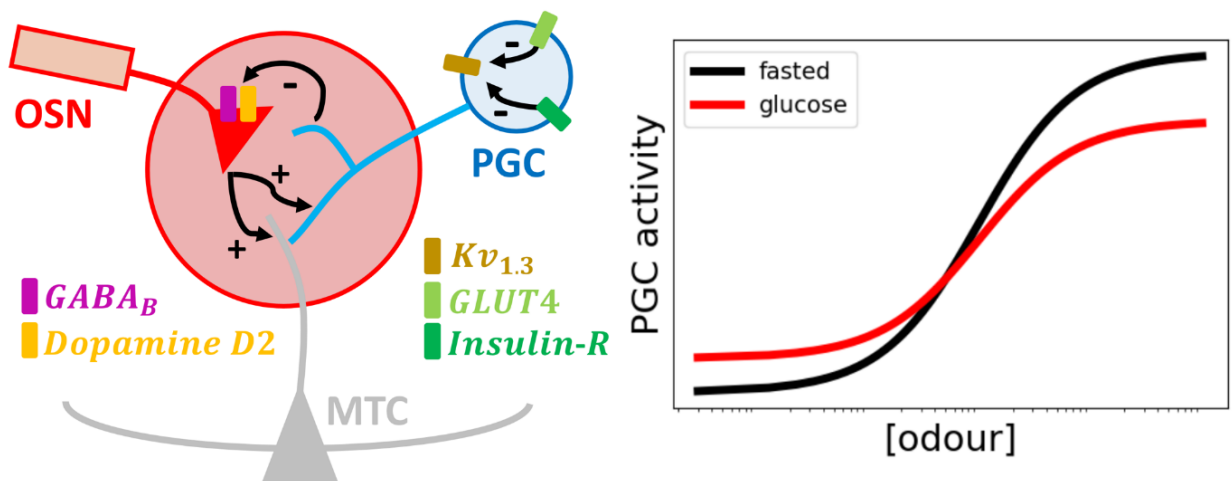


Figure 6.2 Hypothesis of glucose-mediated inhibition of the olfactory afference. Satiety reduces olfactory sensitivity. I hypothesised the loss of olfactory sensitivity occurs in OSN by increased feedback inhibition at the first synapses in the glomerular layer of the olfactory bulb, given that PGCs are glucose-sensitive. **Left:** Glomerulus OSN-PGC micro-circuit. OSN releases glutamate into PG and mitral cells. OSN activity is dampened through feedback inhibition by the PG cells. Hypothesis for the mechanism: Kv1.3 channels expressed by periglomerular neurons become inhibited by insulin and glucose, which may be transported by GLUT4, a glucose transporter. This would result in increased release of GABA and/or dopamine which would act on GABA_B and/or D2 receptors present on the olfactory afferent synaptic terminals. Both GABA_B and D2 receptors decrease glutamate release from the afferent synapse. This results in reduced olfactory sensitivity for food detection, which fits the rationale of a satiated state. **Right:** Expected changes in the dosage-response curve of PGC following heightening of glucose. PGCs would become more excitable at earlier concentrations but auto-inhibition by PGCs would be increased at higher concentrations. OSN: olfactory sensory neuron; PGC: periglomerular cell; MTC: mitral cell.

6.5 Overall conclusion

The satiety state influences olfaction. Mice are less able to detect isoamyl acetate when their glycemia is high compared to when they have fasted. These behaviour changes rely on a perturbation of the feedback inhibition onto the olfactory afference in the olfactory bulb glomerular layer. The transmission of olfactory information is dampened in the sated state. Heighten blood glucose results in increased excitability of the inhibitory periglomerular interneurons which then contribute to reduce furthermore the release of glutamate from the olfactory afferent terminals to the olfactory bulb

This study reconciled behavioural tests of olfactory sensitivity and neural activity measurements both in the afferent signal of the olfactory sensory neurons (OSN) and the inhibitory periglomerular cells (PGC). The OSN-PGC neural circuit was investigated in the intact brain by imaging the dorsal olfactory bulb *in vivo* in anaesthetised mice. A combination of widefield one-photon calcium imaging, intrinsic signal optical imaging, and two-photon calcium imaging enabled the study of the circuit at local and broad bulb scales. Therefore, I recorded from PGC somata and dendritic neuropile, as well as

OSN axon terminals. I expected that the OSN-PGC feedback inhibition would be amplified due to the PGC sensing of blood glucose during satiety.

I could not confirm the putative role of Kv1.3 and GLUT4 as the mechanism for glucose sensing but only their relative presence in PGCs. Nevertheless, I found blood glucose modified odour-evoked activity of PGC dendrites and somata differently. The effect on dose-response profiles of PGCs was heterogeneous. The putative attenuation of OSNs by PGCs was bimodal with only low odourant concentration being dampened by increased inhibitory feedback. The adjacent odour detection behavioural tests tended to confirm literature findings of satiety reducing olfactory sensitivity.

This study contributed to narrowing the gap between the behavioural phenomenon and the underlying neural mechanism. It completed the work done in *ex vivo* studies and corroborates results of satiety-dependent olfactory performance in behavioural experiments. It confirms assumptions of the olfactory bulb as a metabolism sensing hub and brings a step forward to solving the problem of integration of olfaction and metabolism state at the first sensory synapses.

Bibliography

- Adam, Yoav et al. 2014. "Functional Transformations of Odor Inputs in the Mouse Olfactory Bulb." *Frontiers in Neural Circuits* 8.
- Aimé, P. et al. 2007. "Fasting Increases and Satiation Decreases Olfactory Detection for a Neutral Odor in Rats." *Behavioural Brain Research* 179(2): 258–64.
- Andrikopoulos, Sofianos et al. 2008. "Evaluating the Glucose Tolerance Test in Mice." *American Journal of Physiology - Endocrinology and Metabolism* 295(6): 1323–32. <http://www.ajpendo.org> (November 22, 2021).
- Antal, Miklós, Mark Eyre, Bryson Finklea, and Zoltan Nusser. 2006. "External Tufted Cells in the Main Olfactory Bulb Form Two Distinct Subpopulations." *European Journal of Neuroscience* 24(4): 1124–36. <https://onlinelibrary.wiley.com/doi/10.1111/j.1460-9568.2006.04988.x> (November 22, 2021).
- Aroniadou-Anderjaska, V., M. Ennis, and M. T. Shipley. 1997. "Glomerular Synaptic Responses to Olfactory Nerve Input in Rat Olfactory Bulb Slices." *Neuroscience* 79(2): 425–34.
- Aroniadou-Anderjaska, Vassiliki et al. 2000. "Tonic and Synaptically Evoked Presynaptic Inhibition of Sensory Input to the Rat Olfactory Bulb Via GABA_B Heteroreceptors." *Journal of Neurophysiology* 84(3): 1194–1203. <https://www.physiology.org/doi/10.1152/jn.2000.84.3.1194> (November 22, 2021).
- Aungst, J. L. et al. 2003. "Centre-Surround Inhibition among Olfactory Bulb Glomeruli." *Nature* 426(6967): 623–29. www.nature.com/nature (November 22, 2021).
- Balu, Ramani, R. Todd Pressler, and Ben W. Strowbridge. 2007. "Multiple Modes of Synaptic Excitation of Olfactory Bulb Granule Cells." *Journal of Neuroscience* 27(21): 5621–32. <https://www.jneurosci.org/content/27/21/5621> (July 14, 2020).
- Banerjee, Arkarup et al. 2015. "An Interglomerular Circuit Gates Glomerular Output and Implements Gain Control in the Mouse Olfactory Bulb." *Neuron* 87(1): 193–207.
- Benito, Nuria et al. 2018. "A Pool of Postnatally Generated Interneurons Persists in an Immature Stage in the Olfactory Bulb." *Journal of Neuroscience* 38(46): 9870–82. <https://doi.org/10.1523/JNEUROSCI.1216-18.2018> (November 22, 2021).
- Berg, H. W., R. M. Pangborn, E. B. Roessler, and A. D. Webb. 1963. "Influence of Hunger on Olfactory Acuity." *Nature* 197(4862): 108.
- Berkowicz, D A, and P Q Trombley. 2000. "Dopaminergic Modulation at the Olfactory Nerve Synapse." *Brain research* 855(1): 90–99. <http://www.ncbi.nlm.nih.gov/pubmed/10650134> (April 3, 2020).
- Bonino, Michela, Dario Cantino, and Marco Sassoè-Pognetto. 1999. "Cellular and Subcellular Localization of γ -Aminobutyric Acid(B)

- Receptors in the Rat Olfactory Bulb." *Neuroscience Letters* 274(3): 195–98.
- Boyd, Alison M., Hiroyuki K. Kato, Takaki Komiyama, and Jeffry S. Isaacson. 2015. "Broadcasting of Cortical Activity to the Olfactory Bulb." *Cell Reports* 10(7): 1032–39.
- Bracci, Enrico, and Stefano Panzeri. 2006. "Excitatory GABAergic Effects in Striatal Projection Neurons." *Journal of Neurophysiology* 95(2): 1285–90. <https://pubmed.ncbi.nlm.nih.gov/16251264/> (July 1, 2020).
- Brechbühl, Julien et al. 2013. "Mouse Alarm Pheromone Shares Structural Similarity with Predator Scents." *Proceedings of the National Academy of Sciences of the United States of America* 110(12): 4762–67.
- Brill, Julia et al. 2016. "Serotonin Increases Synaptic Activity in Olfactory Bulb Glomeruli." *Journal of Neurophysiology* 115(3): 1208–19. <https://www.physiology.org/doi/10.1152/jn.00847.2015> (June 10, 2020).
- Buck, Linda, and Richard Axel. 1991. "A Novel Multigene Family May Encode Odorant Receptors: A Molecular Basis for Odor Recognition." *Cell* 65(1): 175–87. <http://www.cell.com/article/009286749190418X/fulltext> (November 22, 2021).
- Bywalez, Wolfgang G. et al. 2017. "Dendritic Arborization Patterns of Small Juxtglomerular Cell Subtypes within the Rodent Olfactory Bulb." *Frontiers in Neuroanatomy* 10: 127. <http://journal.frontiersin.org/article/10.3389/fnana.2016.00127/full> (November 22, 2021).
- Cavarretta, Francesco et al. 2018. "Parallel Odor Processing by Mitral and Middle Tufted Cells in the Olfactory Bulb." *Scientific Reports* 8(1): 7625. www.nature.com/scientificreports/ (June 30, 2020).
- Chae, Honggoo et al. 2019. "Mosaic Representations of Odors in the Input and Output Layers of the Mouse Olfactory Bulb." *Nature Neuroscience* 22(8): 1306–17.
- Chand, Annisa N., Elisa Galliano, Robert A. Chesters, and Matthew S. Grubb. 2015. "A Distinct Subtype of Dopaminergic Interneuron Displays Inverted Structural Plasticity at the Axon Initial Segment." *Journal of Neuroscience* 35(4): 1573–90. www.mathworks.com. (November 22, 2021).
- Chaudhury, Dipesh et al. 2010. "Olfactory Bulb Habituation to Odor Stimuli." *Behavioral Neuroscience* 124(4): 490–99. /record/2010-16138-006 (November 22, 2021).
- Chess, Andrew, Itamar Simon, Howard Cedar, and Richard Axel. 1994. "Allelic Inactivation Regulates Olfactory Receptor Gene Expression." *Cell* 78(5): 823–34. <https://pubmed.ncbi.nlm.nih.gov/8087849/> (November 22, 2021).
- Cleland, Thomas A. 2010. "Early Transformations in Odor Representation." *Trends in Neurosciences* 33(3): 130–39. <https://pubmed.ncbi.nlm.nih.gov/20060600/> (November 22, 2021).
- Cleland, Thomas A. et al 2012. "Sequential Mechanisms Underlying

- Concentration Invariance in Biological Olfaction.” *Frontiers in Neuroengineering* 4(JANUARY).
<https://pubmed.ncbi.nlm.nih.gov/22287949/> (May 25, 2021).
- Cleland, Thomas A., Brett A. Johnson, Michael Leon, and Christiane Linster. 2007. “Relational Representation in the Olfactory System.” *Proceedings of the National Academy of Sciences of the United States of America* 104(6): 1953–58. <https://pubmed.ncbi.nlm.nih.gov/17261800/> (November 22, 2021).
- Cleland, Thomas A., and Praveen Sethupathy. 2006. “Non-Topographical Contrast Enhancement in the Olfactory Bulb.” *BMC Neuroscience* 7(1): 1–18. <https://link.springer.com/articles/10.1186/1471-2202-7-7> (November 22, 2021).
- Connelly, Timothy et al. 2015. “G Protein-Coupled Odorant Receptors Underlie Mechanosensitivity in Mammalian Olfactory Sensory Neurons.” *Proceedings of the National Academy of Sciences of the United States of America* 112(2): 590–95.
www.pnas.org/cgi/doi/10.1073/pnas.1418515112 (November 22, 2021).
- Coronas, V. et al. 2002. “In Vitro Induction of Apoptosis or Differentiation by Dopamine in an Immortalized Olfactory Neuronal Cell Line.” *Journal of Neurochemistry* 69(5): 1870–81. <http://doi.wiley.com/10.1046/j.1471-4159.1997.69051870.x> (November 22, 2021).
- Crespo, Carlos et al. 2013. “The Circuits of the Olfactory Bulb. The Exception as a Rule.” *The Anatomical Record* 296(9): 1401–12.
<https://onlinelibrary.wiley.com/doi/10.1002/ar.22732> (November 22, 2021).
- Critchley, Hugo D., and Edmund T. Rolls. 1996. “Hunger and Satiety Modify the Responses of Olfactory and Visual Neurons in the Primate Orbitofrontal Cortex.” *Journal of Neurophysiology* 75(4): 1673–86.
- D’Souza, Rinaldo D., and Sukumar Vijayaraghavan. 2014. “Paying Attention to Smell: Cholinergic Signaling in the Olfactory Bulb.” *Frontiers in Synaptic Neuroscience* 6(SEP): 21.
- Dhawale, Ashesh K. et al. 2010. “Non-Redundant Odor Coding by Sister Mitral Cells Revealed by Light Addressable Glomeruli in the Mouse.” *Nature Neuroscience* 13(11): 1404–12.
<https://www.nature.com/articles/nn.2673> (November 22, 2021).
- Duchamp-Viret, Patricia, Andre Duchamp, and Michel A. Chaput. 2003. “Single Olfactory Sensory Neurons Simultaneously Integrate the Components of an Odour Mixture.” *European Journal of Neuroscience* 18(10): 2690–96. <https://onlinelibrary.wiley.com/doi/10.1111/j.1460-9568.2003.03001.x> (November 22, 2021).
- Egger, Veronica, Karel Svoboda, and Zachary F. Mainen. 2005. “Dendrodendritic Synaptic Signals in Olfactory Bulb Granule Cells: Local Spine Boost and Global Low-Threshold Spike.” *Journal of Neuroscience* 25(14): 3521–30. <https://www.jneurosci.org/content/25/14/3521> (July 14, 2020).
- Ennis, Matthew et al. 2001a. “Dopamine D2 Receptor-Mediated Presynaptic

- Inhibition of Olfactory Nerve Terminals." *Journal of Neurophysiology* 86(6): 2986–97. <https://pubmed.ncbi.nlm.nih.gov/11731555/> (June 29, 2020).
- Ennis, M. et al. 2001b. "Dopamine D2 Receptor–Mediated Presynaptic Inhibition of Olfactory Nerve Terminals." *Journal of Neurophysiology* 86(6): 2986–97. <https://www.physiology.org/doi/10.1152/jn.2001.86.6.2986> (November 22, 2021).
- Fantana, Antoniu L., Edward R. Soucy, and Markus Meister. 2008. "Rat Olfactory Bulb Mitral Cells Receive Sparse Glomerular Inputs." *Neuron* 59(5): 802–14.
- Feinstein, Paul, and Peter Mombaerts. 2004. "A Contextual Model for Axonal Sorting into Glomeruli in the Mouse Olfactory System." *Cell* 117(6): 817–31.
- Firestein, S. 2001. "How the Olfactory System Makes Sense of Scents." *Nature* 413(6852): 211–18. <https://pubmed.ncbi.nlm.nih.gov/11557990/> (November 22, 2021).
- Firestein, S., F. Zufall, and G. M. Shepherd. 1991. "Single Odor-Sensitive Channels in Olfactory Receptor Neurons Are Also Gated by Cyclic Nucleotides." *Journal of Neuroscience* 11(11): 3565–72. <https://www.jneurosci.org/content/11/11/3565> (November 22, 2021).
- Fleischer, Joerg, and Heinz Breer. 2010. "The Grueneberg Ganglion: A Novel Sensory System in the Nose." *Histology and Histopathology* 25(7): 909–15. <http://www.ncbi.nlm.nih.gov/pubmed/20503179> (March 26, 2020).
- Fleischer, Jörg et al. 2006. "Olfactory Receptors and Signalling Elements in the Grueneberg Ganglion." *Journal of Neurochemistry* 98(2): 543–54. <http://www.ncbi.nlm.nih.gov/pubmed/16805845> (March 26, 2020).
- Fletcher, Max L. 2012. "Olfactory Aversive Conditioning Alters Olfactory Bulb Mitral/Tufted Cell Glomerular Odor Responses." *Frontiers in Systems Neuroscience* 6(MARCH): 16–16. <http://journal.frontiersin.org/article/10.3389/fnsys.2012.00016/abstract> (July 2, 2020).
- Fogli Iseppe, Alex, Angela Pignatelli, and Ottorino Belluzzi. 2016. "Calretinin-Periglomerular Interneurons in Mice Olfactory Bulb: Cells of Few Words." *Frontiers in Cellular Neuroscience* 10(OCT2016): 231. <http://journal.frontiersin.org/article/10.3389/fncel.2016.00231/full> (November 17, 2021).
- Friedrich, R. W., and G. Laurent. 2001. "Dynamic Optimization of Odor Representations by Slow Temporal Patterning of Mitral Cell Activity." *Science* 291(5505): 889–94. <https://www.science.org/doi/abs/10.1126/science.291.5505.889> (November 22, 2021).
- Fukunaga, Izumi et al. 2012. "Two Distinct Channels of Olfactory Bulb Output." *Neuron* 75(2): 320–29.
- Fuss, Stefan H., Masayo Omura, and Peter Mombaerts. 2005. "The

- Grueneberg Ganglion of the Mouse Projects Axons to Glomeruli in the Olfactory Bulb." *European Journal of Neuroscience* 22(10): 2649–54. <https://onlinelibrary.wiley.com/doi/10.1111/j.1460-9568.2005.04468.x> (November 22, 2021).
- Gerhold, Kristin A., and Diana M. Bautista. 2009. "Molecular and Cellular Mechanisms of Trigeminal Chemosensation." In *Annals of the New York Academy of Sciences*, Blackwell Publishing Inc., 184–89.
- Gire, David H. et al. 2012. "Mitral Cells in the Olfactory Bulb Are Mainly Excited through a Multistep Signaling Path." *Journal of Neuroscience* 32(9): 2964–75. <https://www.jneurosci.org/content/32/9/2964> (November 22, 2021).
- Gire, David H. et al. 2019. "Balancing Extrasynaptic Excitation and Synaptic Inhibition within Olfactory Bulb Glomeruli." *eNeuro* 6(4). <http://www.ncbi.nlm.nih.gov/pubmed/31345999> (April 2, 2020).
- Gire, David H., and Nathan E. Schoppa. 2009. "Control of on/off Glomerular Signaling by a Local GABAergic Microcircuit in the Olfactory Bulb." *The Journal of neuroscience : the official journal of the Society for Neuroscience* 29(43): 13454–64. <http://www.jneurosci.org/cgi/doi/10.1523/JNEUROSCI.2368-09.2009%5Cnhttp://www.pubmedcentral.nih.gov/articlerender.fcgi?artid=2786286&tool=pmcentrez&rendertype=abstract>.
- Grelat, Anne et al. 2018. "Adult-Born Neurons Boost Odor–Reward Association." *Proceedings of the National Academy of Sciences of the United States of America* 115(10): 2514–19. www.pnas.org/cgi/doi/10.1073/pnas.1716400115 (November 22, 2021).
- Grosmaître, Xavier et al. 2007. "Dual Functions of Mammalian Olfactory Sensory Neurons as Odor Detectors and Mechanical Sensors." *Nature Neuroscience* 10(3): 348–54. <https://pubmed.ncbi.nlm.nih.gov/17310245/> (November 22, 2021).
- Grubb, Matthew S., Antoine Nissant, Kerren Murray, and Pierre Marie Lledo. 2008. "Functional Maturation of the First Synapse in Olfaction: Development and Adult Neurogenesis." *Journal of Neuroscience* 28(11): 2919–32. <https://www.jneurosci.org/content/28/11/2919> (November 22, 2021).
- Hayar, Abdallah, Sergei Karnup, Michael T. Shipley, and Matthew Ennis. 2004. "Olfactory Bulb Glomeruli: External Tufted Cells Intrinsically Burst at Theta Frequency and Are Entrained by Patterned Olfactory Input." *Journal of Neuroscience* 24(5): 1190–99. <https://www.jneurosci.org/content/24/5/1190> (November 22, 2021).
- Homma, R. et al. 2013. "In Vivo Functional Properties of Juxtglomerular Neurons in the Mouse Olfactory Bulb." *Frontiers in Neural Circuits* 7(FEBRUARY 2013): 23. <http://www.ncbi.nlm.nih.gov/pubmed/23459031> (April 2, 2020).
- Hsia, Albert Y., Jean-Didier Vincent, and Pierre-Marie Lledo. 1999. "Dopamine Depresses Synaptic Inputs Into the Olfactory Bulb." *Journal of Neurophysiology* 82(2): 1082–85. <https://www.physiology.org/doi/10.1152/jn.1999.82.2.1082> (November

22, 2021).

- Igarashi, Kei M. et al. 2012. "Parallel Mitral and Tufted Cell Pathways Route Distinct Odor Information to Different Targets in the Olfactory Cortex." *Journal of Neuroscience* 32(23): 7970–85.
- Imai, Takeshi. 2014. "Construction of Functional Neuronal Circuitry in the Olfactory Bulb." *Seminars in Cell and Developmental Biology* 35: 180–88.
- In'T Zandt, Estelle E., Hillary L. Cansler, Heather B. Denson, and Daniel W. Wesson. 2019. "Centrifugal Innervation of the Olfactory Bulb: A Reappraisal." *eNeuro* 6(1).
- Isaacson, Jeffrey S., and Ben W. Strowbridge. 1998. "Olfactory Reciprocal Synapses: Dendritic Signaling in the CNS." *Neuron* 20(4): 749–61.
- Iwata, Ryo, and Hiroshi Kiyonari. 2017. "Mechanosensory-Based Phase Coding of Odor Identity in the Olfactory Bulb." *Neuron* 96: 1139-1152.e7. <https://doi.org/10.1016/j.neuron.2017.11.008>.
- De Jan, Didier Saint, Daniela Hirnet, Gary L. Westbrook, and Serge Charpak. 2009. "External Tufted Cells Drive the Output of Olfactory Bulb Glomeruli." *Journal of Neuroscience* 29(7): 2043–52. <https://www.jneurosci.org/content/29/7/2043> (November 22, 2021).
- Jordan, Rebecca, Izumi Fukunaga, Mihaly Kollo, and Andreas T. Schaefer. 2018. "Active Sampling State Dynamically Enhances Olfactory Bulb Odor Representation." *Neuron* 98(6): 1214-1228.e5.
- Julliard, A. Karyn, Dolly Al Koborssy, Debra A. Fadool, and Brigitte Palouzier-Paulignan. 2017a. "Nutrient Sensing: Another Chemosensitivity of the Olfactory System." *Frontiers in Physiology* 8(JUL).
- Julliard, A. Karyn, Dolly Al Koborssy, Debra A. Fadool, and Brigitte Palouzier-Paulignan. 2017b. "Nutrient Sensing: Another Chemosensitivity of the Olfactory System." *Frontiers in Physiology* 8(JUL). <https://pubmed.ncbi.nlm.nih.gov/28747887/> (November 22, 2021).
- Kaniganti, Tarun et al. 2019. "Sensitivity of Olfactory Sensory Neurons to Food Cues Is Tuned to Nutritional States by Neuropeptide Y Signalling." *bioRxiv*: 19–20. <https://www.biorxiv.org/content/10.1101/573170v2> (June 28, 2020).
- Kass, Marley D. et al. 2013. "Odor-Specific, Olfactory Marker Protein-Mediated Sparsening of Primary Olfactory Input to the Brain after Odor Exposure." *Journal of Neuroscience* 33(15): 6594–6602. <https://www.jneurosci.org/content/33/15/6594> (November 22, 2021).
- Kass, Marley D., Lindsey A. Czarnecki, Andrew H. Moberly, and John P. McGann. 2017. "Differences in Peripheral Sensory Input to the Olfactory Bulb between Male and Female Mice." *Scientific Reports* 7: 45851. <http://www.nature.com/articles/srep45851> (April 9, 2018).
- Kato, Hiroyuki K. et al. 2013. "Parvalbumin-Expressing Interneurons Linearly Control Olfactory Bulb Output." *Neuron* 80(5): 1218–31.

/pmc/articles/PMC3884945/?report=abstract (June 28, 2020).

- Keller, Asaf et al. 1998. "Functional Organization of Rat Olfactory Bulb Glomeruli Revealed by Optical Imaging." *Journal of Neuroscience* 18(7): 2602–12. <https://www.jneurosci.org/content/18/7/2602> (November 22, 2021).
- Kikuta, Shu et al. 2013. "Odorant Response Properties of Individual Neurons in an Olfactory Glomerular Module." *Neuron* 77(6): 1122–35.
- Kiyokage, Emi et al. 2010. "Molecular Identity of Periglomerular and Short Axon Cells." *Journal of Neuroscience* 30(3): 1185–96. <https://www.jneurosci.org/content/30/3/1185> (October 27, 2021).
- Klueh, Ulrike et al. 2006. "Continuous Glucose Monitoring in Normal Mice and Mice with Prediabetes and Diabetes." *Diabetes Technology and Therapeutics* 8(3): 402–12. <https://pubmed.ncbi.nlm.nih.gov/16800762/> (November 22, 2021).
- Kobayakawa, Ko et al. 2007. "Innate versus Learned Odour Processing in the Mouse Olfactory Bulb." *Nature* 450(7169): 503–8. <https://www.nature.com/articles/nature06281> (July 2, 2020).
- Al Koborssy, Dolly et al. 2014. "Cellular and Molecular Cues of Glucose Sensing in the Rat Olfactory Bulb." *Frontiers in Neuroscience* 8(OCT). </pmc/articles/PMC4212682/> (November 22, 2021).
- Kohwi, Minoree et al. 2007. "A Subpopulation of Olfactory Bulb GABAergic Interneurons Is Derived from Emx1- and Dlx5/6-Expressing Progenitors." *Journal of Neuroscience* 27(26): 6878–91. <https://www.jneurosci.org/content/27/26/6878> (November 22, 2021).
- Koldaeva, Anzhelika, Andreas T. Schaefer, and Izumi Fukunaga. 2019. "Rapid Task-Dependent Tuning of the Mouse Olfactory Bulb." *eLife* 8.
- Kondoh, Kunio et al. 2016. "A Specific Area of Olfactory Cortex Involved in Stress Hormone Responses to Predator Odours." *Nature* 532(7597): 103–6. <https://www.nature.com/articles/nature17156> (November 22, 2021).
- Kosaka, Katsuko, and Toshio Kosaka. 2005. "Synaptic Organization of the Glomerulus in the Main Olfactory Bulb: Compartments of the Glomerulus and Heterogeneity of the Periglomerular Cells." *Anatomical Science International* 80(2): 80–90. <https://link.springer.com/article/10.1111/j.1447-073x.2005.00092.x> (November 22, 2021).
- Kosaka, Katsuko, and Toshio Kosaka. 2007. "Chemical Properties of Type 1 and Type 2 Periglomerular Cells in the Mouse Olfactory Bulb Are Different from Those in the Rat Olfactory Bulb." *Brain Research* 1167(1): 42–55.
- Kosaka, Katsuko, Kazunori Toida, Yusuke Aika, and Toshio Kosaka. 1998. "How Simple Is the Organization of the Olfactory Glomerulus?: The Heterogeneity of so-Called Periglomerular Cells." *Neuroscience Research* 30(2): 101–10.
- Kosaka, Toshio, and Katsuko Kosaka. 2011. "'Interneurons' in the Olfactory

- Bulb Revisited." *Neuroscience Research* 69(2): 93–99.
- Kosaka, Katsuko, and Toshio Kosaka. 2016. "Neuronal Organization of the Main Olfactory Bulb Revisited." *Anatomical Science International* 91(2): 115–27. <https://pubmed.ncbi.nlm.nih.gov/26514846/> (November 22, 2021).
- Kosaka, Toshio, Angela Pignatelli, and Katsuko Kosaka. 2019. "Heterogeneity of Tyrosine Hydroxylase Expressing Neurons in the Main Olfactory Bulb of the Mouse." *Neuroscience Research*.
- Koster, N.L. et al. 1999. "Olfactory Receptor Neurons Express D2 Dopamine Receptors." *The Journal of Comparative Neurology* 411(4): 666–73. [https://onlinelibrary.wiley.com/doi/10.1002/\(SICI\)1096-9861\(19990906\)411:4%3C666::AID-CNE10%3E3.0.CO;2-S](https://onlinelibrary.wiley.com/doi/10.1002/(SICI)1096-9861(19990906)411:4%3C666::AID-CNE10%3E3.0.CO;2-S) (November 22, 2021).
- Kouros-Mehr, H. 2001. "Identification of Non-Functional Human VNO Receptor Genes Provides Evidence for Vestigiality of the Human VNO." *Chemical Senses* 26(9): 1167–74. <https://academic.oup.com/chemse/article-lookup/doi/10.1093/chemse/26.9.1167> (November 22, 2021).
- Kovach, Christopher P. et al. 2016. "Mitochondrial Ultrastructure and Glucose Signaling Pathways Attributed to the Kv1.3 Ion Channel." *Frontiers in Physiology* 7(MAY).
- Kovalchuk, Yury et al. 2015. "In Vivo Odourant Response Properties of Migrating Adult-Born Neurons in the Mouse Olfactory Bulb." *Nature Communications* 6(1): 1–12. www.nature.com/naturecommunications (April 28, 2022).
- Kurahashi, Takashi, Graeme Lowe, and Geoffrey H. Gold. 1994. "Suppression of Odorant Responses by Odorants in Olfactory Receptor Cells." *Science* 265(5168): 118–20. <https://www.science.org/doi/abs/10.1126/science.8016645> (November 22, 2021).
- Linster, Christiane, Qiang Nai, and Matthew Ennis. 2011. "Nonlinear Effects of Noradrenergic Modulation of Olfactory Bulb Function in Adult Rodents." *Journal of Neurophysiology* 105(4): 1432–43. <https://www.physiology.org/doi/10.1152/jn.00960.2010> (November 22, 2021).
- Liu, Cambrian Y., Scott E. Fraser, and David S. Koos. 2009. "Grueneberg Ganglion Olfactory Subsystem Employs a cGMP Signaling Pathway." *Journal of Comparative Neurology* 516(1): 36–48.
- Liu, Shaolin et al. 2013. "Olfactory Bulb Short Axon Cell Release of GABA and Dopamine Produces a Temporally Biphasic Inhibition-Excitation Response in External Tufted Cells." *Journal of Neuroscience* 33(7): 2916–26. <http://www.ncbi.nlm.nih.gov/pubmed/23407950> (May 8, 2020).
- Liu, Shaolin, Jason L. Aungst, Adam C. Puche, and Michael T. Shipley. 2012. "Serotonin Modulates the Population Activity Profile of Olfactory Bulb External Tufted Cells." *Journal of Neurophysiology* 107(1): 473–83. <https://www.physiology.org/doi/10.1152/jn.00741.2011> (June 15, 2020).

- Liu, Shaolin, Adam C. Puche, and Michael T. Shipley. 2016. "The Interglomerular Circuit Potently Inhibits Olfactory Bulb Output Neurons by Both Direct and Indirect Pathways." *Journal of Neuroscience* 36(37): 9604–17.
- Liu, Shaolin, and Michael T. Shipley. 2008. "Multiple Conductances Cooperatively Regulate Spontaneous Bursting in Mouse Olfactory Bulb External Tufted Cells." *Journal of Neuroscience* 28(7): 1625–39. <https://www.jneurosci.org/content/28/7/1625> (November 22, 2021).
- Ma, Minghong et al. 2003. "Olfactory Signal Transduction in the Mouse Septal Organ." *Journal of Neuroscience* 23(1): 317–24.
- Macrides, Foteos, and Stephen P. Schneider. 1982. "Laminar Organization of Mitral and Tufted Cells in the Main Olfactory Bulb of the Adult Hamster." *The Journal of Comparative Neurology* 208(4): 419–30. <https://onlinelibrary.wiley.com/doi/10.1002/cne.902080410> (November 22, 2021).
- Maher, Brady J., and Gary L. Westbrook. 2008. "Co-Transmission of Dopamine and GABA in Periglomerular Cells." *Journal of Neurophysiology* 99(3): 1559–64.
- Malnic, Bettina, Junzo Hirono, Takaaki Sato, and Linda B. Buck. 1999. "Combinatorial Receptor Codes for Odors." *Cell* 96(5): 713–23. <https://pubmed.ncbi.nlm.nih.gov/10089886/> (November 22, 2021).
- Margeta-Mitrovic, Marta et al. 1999. "Immunohistochemical Localization of GABA(B) Receptors in the Rat Central Nervous System." *Journal of Comparative Neurology* 405(3): 299–321. <https://pubmed.ncbi.nlm.nih.gov/10076927/> (November 22, 2021).
- Markopoulos, Foivos, Dan Rokni, David H. Gire, and Venkatesh N. Murthy. 2012. "Functional Properties of Cortical Feedback Projections to the Olfactory Bulb." *Neuron* 76(6): 1175–88.
- Masurkar, A. V., and W. R. Chen. 2011. "Calcium Currents of Olfactory Bulb Juxtglomerular Cells: Profile and Multiple Conductance Plateau Potential Simulation." *Neuroscience* 192: 231–46.
- Matsutani, Shinji, and Noboru Yamamoto. 2008. "Centrifugal Innervation of the Mammalian Olfactory Bulb." *Anatomical Science International* 83(4): 218–27.
- McGann, John P. 2013. "Presynaptic Inhibition of Olfactory Sensory Neurons: New Mechanisms and Potential Functions." *Chem. Senses* 38: 459–74. <https://academic.oup.com/chemse/article-abstract/38/6/459/299179>.
- Meister, Markus, and Tobias Bonhoeffer. 2001. "Tuning and Topography in an Odor Map on the Rat Olfactory Bulb." *Journal of Neuroscience* 21(4): 1351–60. <https://www.jneurosci.org/content/21/4/1351> (November 22, 2021).
- Miyamichi, Kazunari et al. 2013. "Dissecting Local Circuits: Parvalbumin Interneurons Underlie Broad Feedback Control of Olfactory Bulb Output." *Neuron* 80(5): 1232–45. <http://dx.doi.org/10.1016/j.neuron.2013.08.027>.

- Moine, Fabian et al. 2018. "Alarm Pheromone and Kairomone Detection via Bitter Taste Receptors in the Mouse Grueneberg Ganglion." *BMC Biology* 16(1).
- Mombaerts, Peter et al. 1996. "Visualizing an Olfactory Sensory Map." *Cell* 87(4): 675–86. <https://pubmed.ncbi.nlm.nih.gov/8929536/> (November 22, 2021).
- Mombaerts, Peter. 2006. "Axonal Wiring in the Mouse Olfactory System." *Annual Review of Cell and Developmental Biology* 22(1): 713–37. <http://www.annualreviews.org/doi/10.1146/annurev.cellbio.21.012804.093915> (March 26, 2020).
- Mori, Kensaku, and Gordon M. Shepherd. 1994. "Emerging Principles of Molecular Signal Processing by Mitral/Tufted Cells in the Olfactory Bulb." *Seminars in Cell and Developmental Biology* 5(1): 65–74.
- Mori, Kensaku, Yuji K. Takahashi, Kei M. Igarashi, and Masahiro Yamaguchi. 2006. "Maps of Odorant Molecular Features in the Mammalian Olfactory Bulb." *Physiological Reviews* 86(2): 409–33. <http://leonlab.bio.uci.edu/index.html> (November 22, 2021).
- Murphy, Gabe J., Daniel P. Darcy, and Jeffry S. Isaacson. 2005. "Intraglomerular Inhibition: Signaling Mechanisms of an Olfactory Microcircuit." *Nature Neuroscience* 8(3): 354–64.
- Murphy, Gabe J., Lindsey L. Glickfeld, Zev Balsen, and Jeffry S. Isaacson. 2004. "Sensory Neuron Signaling to the Brain: Properties of Transmitter Release from Olfactory Nerve Terminals." *Journal of Neuroscience* 24(12): 3023–30.
- Nagayama, Shin, Ryota Homma, and Fumiaki Imamura. 2014. "Neuronal Organization of Olfactory Bulb Circuits." *Frontiers in Neural Circuits* 8(SEP): 98.
- Najac, Marion et al. 2015. "Intraglomerular Lateral Inhibition Promotes Spike Timing Variability in Principal Neurons of the Olfactory Bulb." *Journal of Neuroscience* 35(10): 4319–31. <https://pubmed.ncbi.nlm.nih.gov/25762678/> (November 19, 2021).
- Nakazato, Masamitsu et al. 2001. "A Role for Ghrelin in the Central Regulation of Feeding." *Nature* 409(6817): 194–98. <https://www.nature.com/articles/35051587> (July 6, 2020).
- Negrone, Julia et al. 2012. "Neuropeptide Y Enhances Olfactory Mucosa Responses to Odorant in Hungry Rats" ed. Hiroaki Matsunami. *PLoS ONE* 7(9): e45266. <https://dx.plos.org/10.1371/journal.pone.0045266> (June 28, 2020).
- O'Doherty, J. et al. 2000. "Sensory-Specific Satiety-Related Olfactory Activation of the Human Orbitofrontal Cortex." *NeuroReport* 11(2): 399–403. <https://pubmed.ncbi.nlm.nih.gov/10674494/> (November 22, 2021).
- Oka, Yuki, Masayo Omura, Hiroshi Kataoka, and Kazushige Touhara. 2004. "Olfactory Receptor Antagonism between Odorants." *The EMBO Journal* 23(1): 120–26. <http://emboj.embopress.org/cgi/doi/10.1038/sj.emboj.7600032> (June 28, 2020).

- Oka, Yuki, Yoshiki Takai, and Kazushige Touhara. 2009. "Nasal Airflow Rate Affects the Sensitivity and Pattern of Glomerular Odorant Responses in the Mouse Olfactory Bulb." *Journal of Neuroscience* 29(39): 12070–78.
- Olender, Tsviya, Doron Lancet, and Daniel W. Nebert. 2008. "Update on the Olfactory Receptor (OR) Gene Superfamily." *Human genomics* 3(1): 87–97. <http://humgenomics.biomedcentral.com/articles/10.1186/1479-7364-3-1-87> (June 28, 2020).
- Otazu, Gonzalo H., Honggoo Chae, Martin B. Davis, and Dinu F. Albeanu. 2015. "Cortical Feedback Decorrelates Olfactory Bulb Output in Awake Mice." *Neuron* 86(6): 1461–77.
- Panzanelli, P. et al. 2007. "GABAergic Phenotype of Periglomerular Cells in the Rodent Olfactory Bulb." *The Journal of Comparative Neurology* 502(6): 990–1002. <http://doi.wiley.com/10.1002/cne.21356> (April 2, 2020).
- Parrish-Aungst, S. et al. 2007. "Quantitative Analysis of Neuronal Diversity in the Mouse Olfactory Bulb." *The Journal of Comparative Neurology* 501(6): 825–36. <https://onlinelibrary.wiley.com/doi/10.1002/cne.21205> (November 22, 2021).
- Parsa, Pirooz Victor, Rinaldo David D'Souza, and Sukumar Vijayaraghavan. 2015. "Signaling between Periglomerular Cells Reveals a Bimodal Role for GABA in Modulating Glomerular Microcircuitry in the Olfactory Bulb." *Proceedings of the National Academy of Sciences of the United States of America* 112(30): 9478–83. <https://pubmed.ncbi.nlm.nih.gov/26170298/> (June 30, 2020).
- Petzold, Gabor C., Akari Hagiwara, and Venkatesh N. Murthy. 2009. "Serotonergic Modulation of Odor Input to the Mammalian Olfactory Bulb." *Nature Neuroscience* 12(6): 784–91. <https://www.nature.com/articles/nn.2335> (March 21, 2022).
- Pfister, Patrick et al. 2020. "Odorant Receptor Inhibition Is Fundamental to Odor Encoding." *Current Biology* 30: 1–14. <https://doi.org/10.1016/j.cub.2020.04.086>.
- Pignatelli, Angela, and Ottorino Belluzzi. 2017. "Dopaminergic Neurones in the Main Olfactory Bulb: An Overview from an Electrophysiological Perspective." *Frontiers in Neuroanatomy* 11: 7.
- Pignatelli, Angela, Kazuto Kobayashi, Hideyuki Okano, and Ottorino Belluzzi. 2005. "Functional Properties of Dopaminergic Neurones in the Mouse Olfactory Bulb." *The Journal of Physiology* 564(2): 501–14. <https://onlinelibrary.wiley.com/doi/10.1113/jphysiol.2005.084632> (November 22, 2021).
- Pinching, A. J., and T. P. Powell. 1971. "The Neuropil of the Glomeruli of the Olfactory Bulb." *Journal of Cell Science* 9(2): 347–77.
- Pérez, Nicolás, and Matt Wachowiak. 2008. "In Vivo Modulation of Sensory Input to the Olfactory Bulb by Tonic and Activity-Dependent Presynaptic Inhibition of Receptor Neurons." *Journal of Neuroscience* 28(25): 6360–71. <https://www.jneurosci.org/content/28/25/6360> (November 22, 2021).
- Prud'homme, M. J. et al. 2009. "Nutritional Status Modulates Behavioural

- and Olfactory Bulb Fos Responses to Isoamyl Acetate or Food Odour in Rats: Roles of Orexins and Leptin." *Neuroscience* 162(4): 1287–98. <https://pubmed.ncbi.nlm.nih.gov/19477242/> (July 5, 2020).
- Reisert, Johannes. 2010. "Origin of Basal Activity in Mammalian Olfactory Receptor Neurons." *Journal of General Physiology* 136(5): 529–40. <https://pubmed.ncbi.nlm.nih.gov/20611177/> /pmc/articles/PMC2964517/?report=abstract (June 28, 2020).
- Ressler, Kerry J., Susan L. Sullivan, and Linda B. Buck. 1994. "Information Coding in the Olfactory System: Evidence for a Stereotyped and Highly Organized Epitope Map in the Olfactory Bulb." *Cell* 79(7): 1245–55. [http://www.cell.com/article/0092867494900159/fulltext](https://www.cell.com/article/0092867494900159/fulltext) (November 22, 2021).
- Restrepo, Diego, John H. Teeter, and Detlev Schild. 1996. "Second Messenger Signaling in Olfactory Transduction." *Journal of Neurobiology* 30(1): 37–48. [https://onlinelibrary.wiley.com/doi/10.1002/\(SICI\)1097-4695\(199605\)30:1%3C37::AID-NEU4%3E3.0.CO;2-H](https://onlinelibrary.wiley.com/doi/10.1002/(SICI)1097-4695(199605)30:1%3C37::AID-NEU4%3E3.0.CO;2-H) (November 22, 2021).
- Rodriguez, Ivan, Paul Feinstein, and Peter Mombaerts. 1999. "Variable Patterns of Axonal Projections of Sensory Neurons in the Mouse Vomeronasal System." *Cell* 97(2): 199–208. <https://pubmed.ncbi.nlm.nih.gov/10219241/> (November 22, 2021).
- Rothermel, Markus, and Matt Wachowiak. 2014. "Functional Imaging of Cortical Feedback Projections to the Olfactory Bulb." *Frontiers in Neural Circuits* 8(JULY): 73.
- De Saint Jan, Didier, and Gary L. Westbrook. 2007. "Disynaptic Amplification of Metabotropic Glutamate Receptor 1 Responses in the Olfactory Bulb." *Journal of Neuroscience* 27(1): 132–40. <https://www.jneurosci.org/content/27/1/132> (November 22, 2021).
- Saito, Harumi et al. 2017. "Immobility Responses Are Induced by Photoactivation of Single Glomerular Species Responsive to Fox Odour TMT." *Nature Communications* 8(1): 1–10. www.nature.com/naturecommunications (July 2, 2020).
- Sanhueza, Magdalena, Oliver Schmachtenberg, and Juan Bacigalupo. 2000. "Excitation, Inhibition, and Suppression by Odors in Isolated Toad and Rat Olfactory Receptor Neurons." *American Journal of Physiology-Cell Physiology* 279(1): C31–39. <https://www.physiology.org/doi/10.1152/ajpcell.2000.279.1.C31> (November 22, 2021).
- Sawada, Masato et al. 2011. "Sensory Input Regulates Spatial and Subtype-Specific Patterns of Neuronal Turnover in the Adult Olfactory Bulb." *Journal of Neuroscience* 31(32): 11587–96. <https://www.jneurosci.org/content/31/32/11587> (November 22, 2021).
- Schoppa, Nathan E. 1998. "Dendrodendritic Inhibition in the Olfactory Bulb Is Driven by NMDA Receptors." *Journal of Neuroscience* 18(17): 6790–6802. <https://www.jneurosci.org/content/18/17/6790> (November 22, 2021).

- Schoppa, Nathan E. 2006. "Synchronization of Olfactory Bulb Mitral Cells by Precisely Timed Inhibitory Inputs." *Neuron* 49(2): 271–83.
- Schoppa, Nathan E., and Gary L. Westbrook. 2001. "Glomerulus-Specific Synchronization of Mitral Cells in the Olfactory Bulb." *Neuron* 31(4): 639–51.
- Schwartz, Theodore H. 2003. "Optical Imaging of Epileptiform Events in Visual Cortex in Response to Patterned Photic Stimulation." *Cerebral Cortex* 13(12): 1287–98.
- Shakhawat, Amin et al. 2014. "Visualizing the Engram: Learning Stabilizes Odor Representations in the Olfactory Network." *Journal of Neuroscience* 34(46): 15394–401.
<https://www.jneurosci.org/content/34/46/15394> (November 22, 2021).
- Shao, Z. et al. 2009. "Two GABAergic Intraglomerular Circuits Differentially Regulate Tonic and Phasic Presynaptic Inhibition of Olfactory Nerve Terminals." *Journal of Neurophysiology* 101(4): 1988–2001.
<https://www.physiology.org/doi/10.1152/jn.91116.2008> (November 22, 2021).
- Shao, Zuoyi et al. 2019. "Reciprocal Inhibitory Glomerular Circuits Contribute to Excitation–Inhibition Balance in the Mouse Olfactory Bulb." *eNeuro* 6(3). <https://doi.org/10.1523/ENEURO.0048-19.2019> (November 19, 2021).
- Shepherd, G. M. 1972. "Synaptic Organization of the Mammalian Olfactory Bulb." *Physiological reviews* 52(4): 864–917.
<https://journals.physiology.org/doi/abs/10.1152/physrev.1972.52.4.864> (November 22, 2021).
- Smith, T. Caitlin, and Craig E. Jahr. 2002. "Self-Inhibition of Olfactory Bulb Neurons." *Nature Neuroscience* 5(8): 760–66.
<http://neurosci.nature.com> (November 22, 2021).
- Soria-Gómez, Edgar et al. 2014a. "The Endocannabinoid System Controls Food Intake via Olfactory Processes." *Nature Neuroscience* 17(3): 407–15.
- Soria-Gómez, Edgar et al. 2014b. "The Endocannabinoid System Controls Food Intake via Olfactory Processes." *Nature Neuroscience* 17(3): 407–15.
- Soucy, Edward R. et al. 2009. "Precision and Diversity in an Odor Map on the Olfactory Bulb." *Nature Neuroscience* 12(2): 210–20.
<https://www.nature.com/articles/nn.2262> (July 4, 2021).
- Spors, Hartwig, and Amiram Grinvald. 2002. "Spatio-Temporal Dynamics of Odor Representations in the Mammalian Olfactory Bulb." *Neuron* 34(2): 301–15.
- Storan, Melonie Joanne, and Brian Key. 2006. "Septal Organ of Grüneberg Is Part of the Olfactory System." *The Journal of Comparative Neurology* 494(5): 834–44. <http://doi.wiley.com/10.1002/cne.20858> (March 27, 2020).
- Strotmann, J. et al. 1994. "Olfactory Neurones Expressing Distinct Odorant

- Receptor Subtypes Are Spatially Segregated in the Nasal Neuroepithelium." *Cell & Tissue Research* 276(3): 429–38. <https://link.springer.com/article/10.1007/BF00343941> (November 22, 2021).
- Su, Chih Ying, Karen Menuz, and John R. Carlson. 2009. "Olfactory Perception: Receptors, Cells, and Circuits." *Cell* 139(1): 45–59.
- Takeuchi, Hiroko, Hirohiko Ishida, Satoshi Hikichi, and Takashi Kurahashi. 2009. "Mechanism of Olfactory Masking in the Sensory Cilia." *Journal of General Physiology* 133(6): 583–601. www.jgp.org/cgi/doi/10.1085/jgp.200810085 (November 22, 2021).
- Tamamaki, Nobuaki et al. 2003. "Green Fluorescent Protein Expression and Colocalization with Calretinin, Parvalbumin, and Somatostatin in the GAD67-GFP Knock-In Mouse." *Journal of Comparative Neurology* 467(1): 60–79. <https://pubmed.ncbi.nlm.nih.gov/14574680/> (March 22, 2022).
- Tan, Jie, Agnès Savigner, Minghong Ma, and Minmin Luo. 2010. "Odor Information Processing by the Olfactory Bulb Analyzed in Gene-Targeted Mice." *Neuron* 65(6): 912–26.
- Tanaka, Kana et al. 2009. "Highly Selective Tuning of a Silkworm Olfactory Receptor to a Key Mulberry Leaf Volatile." *Current Biology* 19(11): 881–90.
- Tatti, Roberta et al. 2014. "A Population of Glomerular Glutamatergic Neurons Controls Sensory Information Transfer in the Mouse Olfactory Bulb." *Nature Communications* 5(1): 1–16.
- Tavakoli, Andrej et al. 2018. "Quantitative Association of Anatomical and Functional Classes of Olfactory Bulb Neurons." *Journal of Neuroscience* 38(33): 7204–20.
- Teichert, Manuel, and Jürgen Bolz. 2017. "Simultaneous Intrinsic Signal Imaging of Auditory and Visual Cortex Reveals Profound Effects of Acute Hearing Loss on Visual Processing." *NeuroImage* 159: 459–72.
- Tian, Huikai, and Minghong Ma. 2004. "Molecular Organization of the Olfactory Septal Organ." *Journal of Neuroscience* 24(38): 8383–90.
- Tucker, Kristal et al. 2013a. "Glucose Sensitivity of Mouse Olfactory Bulb Neurons Is Conveyed by a Voltage-Gated Potassium Channel." *Journal of Physiology* 591(10): 2541–61.
- Uchida, Naoshige, Neir Eshel, and Mitsuko Watabe-Uchida. 2013. "Division of Labor for Division: Inhibitory Interneurons with Different Spatial Landscapes in the Olfactory System." *Neuron* 80(5): 1106–9. <http://dx.doi.org/10.1016/j.neuron.2013.11.013>.
- Vassar, Robert et al. 1994. "Topographic Organization of Sensory Projections to the Olfactory Bulb." *Cell* 79(6): 981–91. <https://pubmed.ncbi.nlm.nih.gov/8001145/> (November 22, 2021).
- Vincis, Roberto et al. 2015. "Sensory-Evoked Intrinsic Imaging Signals in the Olfactory Bulb Are Independent of Neurovascular Coupling." *Cell Reports* 12(2): 313–25.

- Wachowiak, Matt. 2011. "All in a Sniff: Olfaction as a Model for Active Sensing." *Neuron* 71(6): 962–73.
<http://www.cell.com/article/S0896627311007859/fulltext> (June 29, 2020).
- Wachowiak, Matt, Winfried Denk, and Rainer W. Friedrich. 2004. "Functional Organization of Sensory Input to the Olfactory Bulb Glomerulus Analyzed by Two-Photon Calcium Imaging." *Proceedings of the National Academy of Sciences of the United States of America* 101(24): 9097–9102. www.pnas.org/doi/10.1073/pnas.0400438101 (November 22, 2021).
- Wachowiak, Matt, and Michael T. Shipley. 2006. "Coding and Synaptic Processing of Sensory Information in the Glomerular Layer of the Olfactory Bulb." *Seminars in Cell and Developmental Biology* 17(4): 411–23.
- Wang, Ze Jun et al. 2019. "Cannabinoid Receptor-Mediated Modulation of Inhibitory Inputs to Mitral Cells in the Main Olfactory Bulb." *Journal of Neurophysiology* 122(2): 749–59.
<https://pubmed.ncbi.nlm.nih.gov/31215302/> (July 9, 2020).
- Wang, Ze Jun, Liqin Sun, and Thomas Heinbockel. 2012. "Cannabinoid Receptor-Mediated Regulation of Neuronal Activity and Signaling in Glomeruli of the Main Olfactory Bulb." *Journal of Neuroscience* 32(25): 8475–79. <https://www.jneurosci.org/content/32/25/8475> (November 22, 2021).
- Whitesell, Jennifer D. et al. 2013. "Interglomerular Lateral Inhibition Targeted on External Tufted Cells in the Olfactory Bulb." *Journal of Neuroscience* 33(4): 1552–63. <https://www.jneurosci.org/content/33/4/1552> (November 22, 2021).
- Whitman, Mary C., and Charles A. Greer. 2007. "Synaptic Integration of Adult-Generated Olfactory Bulb Granule Cells: Basal Axodendritic Centrifugal Input Precedes Apical Dendrodendritic Local Circuits." *Journal of Neuroscience* 27(37): 9951–61.
<https://www.jneurosci.org/content/27/37/9951> (November 22, 2021).
- Wilson, Rachel I., and Zachary F. Mainen. 2006. "EARLY EVENTS IN OLFACTORY PROCESSING." *Annual Review of Neuroscience* 29(1): 163–201.
<https://www.annualreviews.org/doi/10.1146/annurev.neuro.29.051605.112950> (November 22, 2021).
- Windeløv, Johanne A., Jens Pedersen, and Jens J. Holst. 2016. "Use of Anesthesia Dramatically Alters the Oral Glucose Tolerance and Insulin Secretion in C57Bl/6 Mice." *Physiological Reports* 4(11).
[/pmc/articles/PMC4908499/](https://pubmed.ncbi.nlm.nih.gov/27114499/) (November 22, 2021).
- Wu, Jing et al. 2020. "Excitability of Neural Activity Is Enhanced, but Neural Discrimination of Odors Is Slightly Decreased, in the Olfactory Bulb of Fasted Mice." *Genes* 11(4): 433. <https://www.mdpi.com/2073-4425/11/4/433> (April 28, 2020).
- Yeomans, Martin R. 2006. "Olfactory Influences on Appetite and Satiety in Humans." *Physiology and Behavior* 87(4): 800–804.

- Yokoi, Mineto, Kensaku Mori, and Shigetada Nakanishi. 1995. "Refinement of Odor Molecule Tuning by Dendrodendritic Synaptic Inhibition in the Olfactory Bulb." *Proceedings of the National Academy of Sciences of the United States of America* 92(8): 3371–75. <https://www.pnas.org/content/92/8/3371> (November 22, 2021).
- Zak, Joseph D., Jennifer D. Whitesell, and Nathan E. Schoppa. 2015. "Metabotropic Glutamate Receptors Promote Disinhibition of Olfactory Bulb Glomeruli That Scales with Input Strength." *Journal of Neurophysiology* 113(6): 1907–20. <https://pubmed.ncbi.nlm.nih.gov/25552635/> (November 19, 2021).
- Zapiec, Bolek, and Peter Mombaerts. 2020. "The Zonal Organization of Odorant Receptor Gene Choice in the Main Olfactory Epithelium of the Mouse." *Cell Reports* 30(12): 4220-4234.e5.
- Zelles, Tibor, Jamie D. Boyd, Alexandre B. Hardy, and Kerry R. Delaney. 2006. "Branch-Specific Ca²⁺ Influx from Na⁺-Dependent Dendritic Spikes in Olfactory Granule Cells." *Journal of Neuroscience* 26(1): 30–40. <https://www.jneurosci.org/content/26/1/30> (November 22, 2021).
- Zou, Dong Jing, Alexander Chesler, and Stuart Firestein. 2009. "How the Olfactory Bulb Got Its Glomeruli: A Just so Story?" *Nature Reviews Neuroscience* 10(8): 611–18. www.nature.com/reviews/neuro (November 22, 2021).
- Zuurbier, Coert J. et al. 2014. "Optimizing Anesthetic Regimen for Surgery in Mice through Minimization of Hemodynamic, Metabolic, and Inflammatory Perturbations." *Experimental Biology and Medicine* 239(6): 737–46.

Appendix A python scripts

I coded in python functions to control the olfactometer (206A, Aurora Scientific) and run experiment protocols. All codes were run under the python interpreter software Spyder. The olfactometer controller and sequencer API:

olfacto.py

```
from datetime import datetime
import numpy as np
import random
import json
import u3 #LabJack
import fnmatch
import numpy as np
import os
import os.path as path
from os import listdir
from os.path import isfile, join
from IPython.display import display, clear_output
from IPython.html import widgets
from IPython.display import HTML, display
import math
import time
import cv2
import serial
import builtins
import sys
from subprocess import call

#TODO: add foolproof TOO LOW values for MFCs

def callSudoTerminal(cmd='ls',pwd='Synapse1'):

    call('echo {} | sudo -S {}'.format(pwd, cmd), shell=True)

def loadDictionnary(path=None):
    if path == None:
        print("select a dictionnary using the dialog window")
        # path= easygui.fileopenbox()
    with open(path) as json_file:
        data = json.load(json_file)
    #load config file
    print("path")
    print("load dictionnary variables:")
    for key,val in data.items():
        exec(key + '=val')
        print("instanciate "+key)

def startOlfacto(ser,MFC3_init=950/1000.0,dilution_init=0.01):
    """ set the mass flow controller in default state"""
    # MFC3_init=950/1000.0 #mfc3 set at 950 SCCM, value need be 0-1
    setMFC(ser,3,MFC3_init) #mfc3=950
    setDilution(ser,dilution_init) #mfc1=950 mfc2=0

def cutFreshAir(ser):
    print("cutFreshAir")
    setMFC(ser,3,0)

def setFreshAir(ser,MFC3_init=950/1000.0):
    print("setFreshAir")
    setMFC(ser,3,MFC3_init) #mfc3=950

def initLabjackAndOlfacto(syncPort=6,baudrate=9600,
locations=['/dev/ttyACM0','/dev/ttyACM1','/dev/ttyACM2','/dev/ttyACM3','/dev/ttyACM4',
'/dev/ttyACM5','COM12','COM13','COM14']):
```

```
#for PC:
locations=['COM1','COM2','COM3','COM4','COM5','COM6','COM7','COM8','COM9','COM10',
'COM11','COM12','COM13','COM14']
#for
LINUX:locations=['/dev/ttyACM0','/dev/ttyACM1','/dev/ttyACM2','/dev/ttyACM3','/dev
/ttyACM4','/dev/ttyACM5','COM12','COM13','COM14']

#for LINUX, not windows
#ser: olfactometer
#device: labjack

expected='Aurora Scientific 206A'
timeout_=0.01 #controls the behavior of read()
write_timeout_=None #write() is blocking by default, unless write_timeout is
set
inter_byte_timeout_=None #Inter-character timeout

print("\n connected devices (LINUX ONLY)")
callSudoTerminal("ls -l /dev/ttyACM*")

"""init labjack"""

device = u3.U3()

"""init serial"""
for device_ in locations:
    try:
        print("Trying identify "+device_)
        print("\n enabling access permission (ONLY ON LINUX, REMOVE THIS IF ON
WINDOWS)")
        callSudoTerminal("ls -l "+device_)
        callSudoTerminal("chmod 666 "+device_)
        time.sleep(0.5)

        ser = serial.Serial(device , baudrate ,timeout=timeout_
,write_timeout =write_timeout_
,inter_byte_timeout=inter_byte_timeout_)

        ser.write('identify\r'.encode('utf-8'))

        msg = ser.read(999)

        print("msg", msg)
        if msg.decode('utf-8').split('\r\n')[1] == expected:
            print("connected to: "+msg.decode('utf-8').split('\r\n')[1])
            break
    except:
        print("Failed to connect on "+device_)
        del device
        return 0
setLabjack(device, syncPort, 0)
return ser, device #ser for olfacto, device for labjack sync port

def handshakeArduino_linux(expected='Aurora Scientific 206A',
baudrate=9600, locations=['/dev/ttyACM0','/dev/ttyACM1','/dev/ttyACM2','/dev/ttyACM
3','/dev/ttyACM4','/dev/ttyACM5']):
    #for PC:
    locations=['COM1','COM2','COM3','COM4','COM5','COM6','COM7','COM8','COM9','COM10',
'COM11','COM12','COM13','COM14']
    #for
    LINUX:locations=['/dev/ttyACM0','/dev/ttyACM1','/dev/ttyACM2','/dev/ttyACM3','/dev
/ttyACM4','/dev/ttyACM5','COM12','COM13','COM14']

    #for LINUX, not windows
    #ser: olfactometer

    attempts=20

    timeout_=0.1#0.01 #controls the behavior of read()
    write_timeout_=None #write() is blocking by default, unless write_timeout is
set
    inter_byte_timeout_=None #Inter-character timeout

    print("\n connected devices (LINUX ONLY)")
    callSudoTerminal("ls -l /dev/ttyACM*")

    """init serial"""
```

```
for device_ in locations:
    try:
        print("Trying identify "+device_+" with "+expected)
        print("\n enabling access permission (ONLY ON LINUX, REMOVE THIS IF ON
WINDOWS)")
        callSudoTerminal("ls -l "+device_)
        callSudoTerminal("chmod 666 "+device_)
        time.sleep(0.5)

        ser = serial.Serial(device_, baudrate, timeout=timeout_,
                            write_timeout=write_timeout_,
                            inter_byte_timeout=inter_byte_timeout_)

        if expected=='Aurora Scientific 206A':
            #for aurora olfactometer 206A
            ser.write('identify\r'.encode('utf-8'))

            msg = ser.read(999)

            print("\n >>> msg", msg)
            if msg.decode('utf-8').split('\r\n')[1] == expected:
                print("\n\n C O N G R A T U L A T I O N S")
                print("connected to: "+msg.decode('utf-8').split('\r\n')[1])
                break
            else:
                #for simple arduinos
                time.sleep(1)
                for i in range(attempts):

                    msg = ser.readline()

                    try:
                        if expected in expected in
str(msg).split(",")[0].split("b'") : #str(msg).split("\r\n")[1].split(",")[0] ==
expected:
                            print("\n\n C O N G R A T U L A T I O N S")
                            print("connected to: "+expected+"\n")
                            return ser
                            # break
                    except Exception as e :
                        # print(e)
                        pass

                except Exception as e:
                    print(e)
                    print("\nFailed to connect on "+device_)
                    try:
                        del ser
                    except:
                        pass
                    # del device_
                    # return msg
    return ser #ser for olfacto

def initLabjack(syncPort=6):
    """ Connect labjack and set the port "syncPort" LOW """
    #device: labjack handle
    device = u3.U3()
    setLabjack(device, syncPort, 0)
    return device

def getVialsList(path):
    f=open(path, "r", encoding="Latin-1")
    r=f.read()
    tot=len(r.split("\x00\x00\x00\x0bMineral Oil")) - 1
    res=[]
    for i in range(tot):
        res.append((r.split("\x00\x00\x00\x0bMineral Oil")[i].split("\x00")[-
1][1:], r.split("%")[i].split("\x00")[-1][1:]))
        #print(r.split("\x00\x00\x00\x0bMineral Oil")[i].split("\x00")[-1][1:])
        #print(r.split("%")[i].split("\x00")[-1][1:])
    return res

def getSequenceVials(path): #OLD
    f=open(path, "r", encoding="utf8")
```

```
r=f.read()
res=[]
for i in range(len(r.split("Trig\tEdge"))-2):
    #print(">>>" +str(i+1))
    #print(r.split("Trig\tEdge")[i].split("\n")[-1][0])
    res.append(r.split("Trig\tEdge")[i].split("\n")[-1][0])
return res

def setLabjack(device,fio,state):
    #fio 1 2 3 4 5 6 ...
    #state = 0 or 1
    device.setFIOState(fio, state)
    print("FIO"+str(fio)+" set to "+str(state))

def setFinalValve (ser, state,i2cAddress=1):
    #state = "on" or "off"
    #Turn on valve x (if vial: inlet valve)
    #final valve is 8

    print("final valve "+state)
    msg = 'valve '+str(i2cAddress)+" 8 "+state+'\r'
    ser.write(msg.encode('utf-8'))

def setMixingValve (ser, state,i2cAddress=1):
    #state = "on" or "off"
    #Turn on valve x (if vial: inlet valve)
    #mixing valve is 8

    print("mixing valve "+state)
    msg = 'valve '+str(i2cAddress)+" 7 "+state+'\r'
    ser.write(msg.encode('utf-8'))

def setOdourValve (ser,vial, state,i2cAddress=1):
    #state = "on" or "off"
    #Turn on the inlet and outlet valves to vial x on the first vial module
    # print("setOdourValve")
    if isinstance(vial, int):
        print("odour vial "+str(vial)+" "+state)
        if vial > 0:
            msg = 'vial '+str(i2cAddress)+" "+str(vial+4)+" "+state+'\r' #
            ser.write(msg.encode('utf-8'))
        elif vial== -1:
            print("same air, same flowrate")
    if isinstance(vial, tuple):
        for s in vial:
            print("odour vial "+str(s)+" "+state)
            if s > 0:
                msg = 'vial '+str(i2cAddress)+" "+str(s+4)+" "+state+'\r' ###
                ser.write(msg.encode('utf-8'))

def addText (img,msg,yPos=0, font=cv2.FONT_HERSHEY_SIMPLEX, fontScale=1,
fontColor=(0,0,0), lineType=2):
    #add text repeats
    text_width, text_height = cv2.getTextSize(msg, font, fontScale,
lineType)[0]
    if yPos==0:
        bottomLeftCornerOfText=(0,text_height)
    else:
        bottomLeftCornerOfText=(0,yPos)

    cv2.putText (img,msg,
bottomLeftCornerOfText,
font,
fontScale,
fontColor,
lineType)

    return img

def purge (ser,time_,m3=950):
    # vials inlets/outlets closed
    # final valve closed
    # mixing valve opened

    #close every valves
    for i in range(8):
        setOdourValve (ser,i+1,"off")
```

```
setFinalValve(ser,'off')

setMixingValve(ser,'on')
setDilution(ser,0.01)# maximize mfc2 flow
print("purging for "+str(time_/60.0)+" min")
time.sleep(time_)
setMixingValve(ser,'off')

# When the olfact
# ometer is being purged all of the vial
# inlet and outlet valves close and the Mixing valve opens.

def setMFC(ser,n,setpoint,i2cAddress=1):
#   between 0 and 1, and is scaled to the flow rate of the MFC. The MFC's are
#   numbered as follows:
#   MFC 1 = Hi flow (1000 SCCM) for Odor Dilution Air
#   MFC 2 = Lo flow (100 SCCM) for Odor Flow
#   MFC 3 = Hi flow (1000 SCCM) for Clean Air to Exhaust

#   command:
#   MFC <I2C ADDR> <MFC ID> <SETPOINT>
if n==1:
    if setpoint>950/1000:
        print("setpoint too high, set at 1 (950)")
        setpoint=950/1000
    print("set MFC "+str(n)+" "+str(setpoint*1000)+" SCCM")
elif n==2:
    if setpoint>95/100:
        print("setpoint too high, set at 1 (95)")
        setpoint=95/100
    print("set MFC "+str(n)+" "+str(setpoint*100)+" SCCM")
elif n==3:
    if setpoint>950/1000:
        print("setpoint too high, set at 1 (950)")
        setpoint=950/1000
    print("set MFC "+str(n)+" "+str(setpoint*1000)+" SCCM")

msg = 'MFC '+str(i2cAddress)+" "+str(n)+" "+str(setpoint)+'\r'
ser.write(msg.encode('utf-8'))

def setDilution(ser,d,rounding=3,m3=950): ###new 181018
#m3 : total airflow
# see aurora olfactometer manual 206A
#d : dilution
# d=(m2/(m1+m2))*100=100*(m2/m3)
# m3=m1+m2
m1Max=1000
m2Max=100
m2=(d*m3)/100.0
m1=m3-m2
print("set dilution "+str(d))
print("MFC1 "+str(m1)+" MFC2 "+str(m2))
m1=m1/m1Max
m2=m2/m2Max
m1=round(m1,rounding)
m2=round(m2,rounding)
print("MFC1 "+str(m1)+" MFC2 "+str(m2))
setMFC(ser,1,m1)
setMFC(ser,2,m2)

def initGUI(winName="olfactoSequencer (q:quit, s:pause or resume)":
#   global c,cc
WINDOW_NORMAL = 0
cv2.namedWindow(winName,WINDOW_NORMAL)
#   c=0 #counter for repeats of a chosen dilution
#   cc=0 #counter for trials inside a repeat

return winName

def GUI_updateRepeats(winName,c,cc,state,nOfRepeats,nOfTrials):
#   global c,cc
#GUI#####
barDim=500
progressBar=np.ones((2,barDim,3),dtype="uint8")*255
#re-init bar
progressBar[:, :, :]=255 #gwhite
#update progress bar
```

```
c=c*nOfRepeats
cx=int(((c+1)/nOfRepeats)*float(barDim))+1
progressBar[0,:cx,0]=0 #green
progressBar[0,:cx,1]=255 #green
progressBar[0,:cx,2]=0 #green
#cc=cc*nOfTrials
ccx=int(((cc+1)/nOfTrials)*float(barDim) )+1
progressBar[1,:ccx,0]=0 #green
progressBar[1,:ccx,1]=255 #green
progressBar[1,:ccx,2]=0 #green
overSampleBar=30
img=progressBar.repeat(overSampleBar,axis=0)#.repeat(overSampleBar,axis=1)

#add texts
msg='repeat '+str(c+1)+"/"+str(nOfRepeats)+" "+state
img=addText(img,msg,0)
msg='trial '+str(cc+1)+"/"+str(nOfTrials)
img=addText(img,msg,img.shape[0])

#show
cv2.imshow(winName,img)
return c

def GUI_updateTrials(winName,c,cc,state,nOfRepeats,nOfTrials):
#   global c,cc
#   #GUI#####
barDim=500
progressBar=np.ones((2,barDim,3),dtype="uint8")*255
#re-init bar
progressBar[:, :, :]=255 #gwhite
#update progress bar
#c=c*nOfRepeats
cx=int(((c+1)/nOfRepeats)*float(barDim))+1
progressBar[0,:cx,0]=0 #green
progressBar[0,:cx,1]=255 #green
progressBar[0,:cx,2]=0 #green
cc=cc*nOfTrials
ccx=int(((cc+1)/nOfTrials)*float(barDim) )+1
progressBar[1,:ccx,0]=0 #green
progressBar[1,:ccx,1]=255 #green
progressBar[1,:ccx,2]=0 #green
overSampleBar=30
img=progressBar.repeat(overSampleBar,axis=0)#.repeat(overSampleBar,axis=1)

#add texts
msg='repeat '+str(c+1)+"/"+str(nOfRepeats)+" "+state
img=addText(img,msg,0)
msg='trial '+str(cc+1)+"/"+str(nOfTrials)
img=addText(img,msg,img.shape[0])

#show
cv2.imshow(winName,img)
return cc

def saveDictionary(dict_,name="dictionary",path=None):
if path is not None:
    p=path+name+'.json'
else:
    p=name+'.json'

print("saving dictionary in "+p+" :\n")
print(dict_)

with open(p, 'w', encoding='utf-8') as f:
    json.dump(dict_, f, ensure_ascii=False, indent=4)

print("\n")
# Function to return the next
# random number
def getNum(v) :
# Size of the vector
n = len(v)
# Generate a random number within
# the index range
index = random.randint(0, n - 1)
# Get random number from the vector
num = v[index]
# Remove the number from the vector
```

```
v[index], v[n - 1] = v[n - 1], v[index]
v.pop()
# Return the removed number
return num

# Function to generate n non-repeating
# random numbers
def generateRandom(n) :
    v = [0] * n
    l=[]
    # Fill the vector with the values
    # 1, 2, 3, ..., n
    for i in range(n) :
        v[i] = i + 1
    # While vector has elements get a
    # random number from the vector
    # and print it
    while (len(v)) :
        c=int(getNum(v))
#         print(c, end = " ")
        l.append(c)
    return l

def verifNoIteration(l):
    for i in range(1,len(l)):
        if l[i-1]==l[i]:
            return False
    return True

def getRandomListOfValves(numOfVials,nOfRepeat,whichVials=None,noIter=True):
    if whichVials is None:
        whichVials=range(numOfVials)
    valvesList=[]
    for i in range(nOfRepeat):
        valvesList+=generateRandom(numOfVials)
    for i in range(len(valvesList)):
        valvesList[i]=whichVials[valvesList[i]-1]
    if verifNoIteration(valvesList):
        return valvesList
    else:
        return getRandomListOfValves(numOfVials,nOfRepeat,whichVials,noIter)

def saveListOfValves(valvesList,name=" ",path=None):
    d = datetime.now().strftime("%m-%d-%Y %Hh%M")
    valvesList=np.asarray(valvesList,dtype="int8")
    if path is not None:
        np.savetxt(path+"valveSequence "+name+d+".txt",valvesList,fmt="%d")
        print(path+"valveSequence "+name+d+".txt")
    else:
        np.savetxt("valveSequence "+name+d+".txt",valvesList,fmt="%d")
        print("valveSequence "+name+d+".txt")

def dialogFile(root="None",title="select folder(s)"):
    #TODO: set initial directory and title
    class getExistingDirectories(QFileDialog):
        def __init__(self, *args):
            super(getExistingDirectories, self).__init__(*args)
            self.setOption(self.DontUseNativeDialog, True)
            self.setWindowTitle(title)
            if root != "None":
                self.setDirectory(root)
            self.setFileMode(self.Directory)
            self.setOption(self.ShowDirsOnly, False)

self.findChildren(QListView)[0].setSelectionMode(QAbstractItemView.ExtendedSelecti
on)

self.findChildren(QTreeView)[0].setSelectionMode(QAbstractItemView.ExtendedSelecti
on)

qapp = QApplication(sys.argv)
dlg = getExistingDirectories()
if dlg.exec_() == QDialog.Accepted:
    print(dlg.selectedFiles())
return dlg.selectedFiles()

def isSeqVial(seqElement):
    if isinstance(seqElement, int):
```

```
        return seqElement>=-1 or seqElement == -2
    if isinstance(seqElement, tuple):
        return True
    return False

def
generateSeq(valveList,stimulationTime=3,delayBetweenStim=5,delaySyncValve=[0,0],syncMode="None",delayBefore1stStim=0):

    seq=[] #vials (time, vial), if vial = 0: close previous vial and final valve,
open next vial; -3: set sync HI, -4: set sync LO
    t=0
    t+=delayBefore1stStim #actually delay before first delay
    seq.append((t,0))
    for i in range(len(valveList)):
        t+=delayBetweenStim
        if syncMode == "valves":
            seq.append((t-delaySyncValve[0],-3)) #to start sync/final flow earlier
than stim onset
            seq.append((t,valveList[i])) # #seq.append((t,int(valveList[i]))) #stim
            t+=stimulationTime
            seq.append((t,0)) #wait and set next vial
            if syncMode == "valves":
                seq.append((t+delaySyncValve[1],-4)) #to start sync/final flow later
than stim offset
            t=t+delayBetweenStim
            seq.append((t,0))
            print(str(t)+" seconds in seq")
        return seq

def
generateSeqwithDilution(valveList,concentrationList,stimulationTime=3,delayBetween
Stim=5,delaySyncValve=[0,0],syncMode="None",delayBefore1stStim=0):

    seq=[] #vials (time, vial), if vial = 0: close previous vial and final valve,
open next vial; -3: set sync HI, -4: set sync LO
    t=0
    t+=delayBefore1stStim #actually delay before first delay
    seq.append((t,0))
    for i in range(len(valveList)):
        t+=delayBetweenStim
        if syncMode == "valves":
            seq.append((t-delaySyncValve[0],-3)) #to start sync/final flow earlier
than stim onset
            seq.append((t,valveList[i],concentrationList[i])) #
#seq.append((t,int(valveList[i]))) #stim
            t+=stimulationTime
            seq.append((t,0)) #wait and set next vial
            if syncMode == "valves":
                seq.append((t+delaySyncValve[1],-4)) #to start sync/final flow later
than stim offset
            t=t+delayBetweenStim
            seq.append((t,0))
            print(str(t)+" seconds in seq")
        return seq
```

The script to input and start an olfactometer stimuli protocol and generate a sync signal through a labjack, with a display notifying the progress, used in the two-photon imaging, OMMI, and behavioural box experiments.:

olfactoSeq0.4.py

```
# -*- coding: utf-8 -*-
"""
OLFACTOMETER SEQUENCER 0.3b

Created on Mon Oct 21 19:59:05 2019

@author: cstefens

NOTES:
```

careful with stopping the flow between movies in "valves" mode, as the starting of flow makes a strong puff that may blind recording of calcium odour-evoked events

in 0.3c, control over totalAirFlow : default 950 = MFC3 flow rate = MFC1+MFC2 when using vial=-2, total airflow is (dilution-1)*totalAirFlow . (dilution comes from concentrationList)

in 0.3b, there is no repetition, so multiply your vialList if needed, also, concentrationList must contains air dilution for each vials. therefore length of concentrationList and vialList must be the same.

in 0.3,
for puffing: useLabjack=False, syncMode = "valves", delaySyncValue=[0,0] and cutFlowBetween=True

WARNING: (manual aurora 206, p14)

The range of Codor is determined by both the odor flow rate and the total flow rate. Since the maximum odor flow rate is limited to 100 sccm (due to the mass flow controller chosen) and typical total flow rates are between 200 and 950 sccm the typical maximum odor concentration released to the animal is between 50% (100/200) and 10.5% (100/950) of the head space concentration.

The minimum odor concentration released to the animal will be determined by the minimum flow rate of the odor mass flow controller

which we recommend as 5 sccm

(note: the mass flow controller manufacturer specifies flow rates as low as 1 sccm from theodor MFC but we don't recommend running the odor MFC this low). Therefore the minimum concentrations will also be dependent on the total flow rate and will range from 2.5% (5/200) down to 0.53% (5/950) of the head space concentration. This calculation is simplified for the researcher in our control program as the researcher only needs to enter the desired concentration percentage and then the program automatically sets the odor flow rate required to achieve this desired concentration based on the current total flow

rate.

ABORT: after you interrupted kernel, copy this code and launch it in console:

```
#exit labjack
if syncMode:
    setLabjack(device,syncPort, 0) #set sync signal LOW

#exit opencv window
cv2.destroyAllWindows()

#close every valves
for i in range(8):
    setOdourValve(ser,i+1,"off")
setFinalValve(ser,'off')
cutFreshAir(ser)
"""

from olfacto import *

""" PARAMETERS """

#use -1 for air from MF3, -2 for air from MFC1/2 (final valve ON) (set
concentration =0 !)
# ALTERNATIVE: use MFC1/2 for air puffs (vial not used) : vial,dilution=(-2,0)

##### example protocol
valveList=[8]*3*5
concentrationList=[0.1,1,10]*5
delayBetweenStim= 30#120#5#10 #60 #60 #seconds.

#foolproof
if len(valveList)==len(concentrationList):
    print("all fine")
else:
    print("WARNING, valves mismatch concentrations")

#delays
```

```
delayBefore1stStim=0#120# 0 #seconds, actually delay before first delay mentioned
below
stimulationTime= 3#120#3#5 #10 #3 #12 #seconds
delayBetweenStim= 3#60*2#30#120#5#10 #60 #60 #seconds.

# SYNC labjack and valve mode
AlwaysInterrupt=True #not used in 0.3c. keep True. if False: between
concentration/repeat, there is a delay then sync goes back High and do next
concentration
useLabjack=True # False : not using the labjack for sync signal output
syncPort=6 #labjack FIO port to set acquisition of I2C data by the arduino

syncMode = "concentration" #"valves"# # generate high sync signal every
"concentration" or every "valves"
#"valves": sync high at each valves opening+-delays sppecified below, and airflow
should be cut between sync, to be verified
#"concentration" : sync high at each concentrations specified above
delaySyncValve=[0,0]#[20,10]#[12,12] #if syncMode = "valves" :delay in seconds
before and after valve opening [before,after]
cutFlowBetween=False #cut final air flow when sync is Low. WARNING: create a
powerful puff when airflow is back on
# for puffing: useLabjack=False, syncMode = "valves", delaySyncValve=[0,0] and
cutFlowBetween=True

# other
purgeTime=5 #UNTESTED. CHECK IF WORKS #purge duration at the start of each
repeat/concentration, none if set as 0
totalAirFlow=950 #default 950 : this value set the MFC3 flow, and the sum of MFC1
and MFC2

"""generate sequence of (time, vial, air dilution) """
#starting to run protocol set in "seq":
# seq contains (time in seconds, stimulation,dilution)
# stimulation ==-2: just air, no vial open, final valve open -> flowrate may
differ: total air flow= (1-dilution)*totalAirFlow
# stimulation ==-1: just air, no vial open, final valve stay closed
# stimulation =0 : final valve closed at time t
# stimulation =n : valve n will stimulate at time t
# ==-3 : to start sync/final flow earlier than stim onset
# ==-4: to end sync/final flow later than stim offset

#you can provide your own or generate one
#the first element must be: (0,0) and the last one: (endTime in second,0)

seq=generateSeqwithDilution(valveList,concentrationList,stimulationTime,delayBetwe
enStim,delaySyncValve,syncMode,delayBefore1stStim)

""" INIT """
#init

interrupt=False #interruption trigger finishes the current epoch and stop, TOFIX
stimulating=False #stimulating trigger
loopCheckPeriod=1000 #every loopCheckPeriod, check for interruption and other
trigger, off if 0
waitKeyTime=1 #Delay in milliseconds
interRepeatWait=3 #seconds waited between concentration/repeats
quit=False
state="start"
nOfRepeats=1#len(concentrationList)
nOfTrials=len(valveList)#np.where(np.asarray(seq)[: ,1]>0)[0].shape[0] #default

""" init labjack and olfacto, GUI """

if useLabjack:
    device = initLabjack(syncPort=6)
    ser = handshakeArduino_linux(expected='Aurora Scientific 206A')

# ser,device =
initLabjackAndOlfacto(syncPort,locations=['/dev/ttyACM0','/dev/ttyACM1','/dev/ttyA
CM2','/dev/ttyACM3','/dev/ttyACM4','/dev/ttyACM5'])
winName = initGUI()

""" LOOP ON SEQUENCE """
#wait for usere input
if input("input anything to start")== 'y':
    pass
print("starting")
```

```
#start state
startOfIactofacto(ser) #set the mass flow controller in default state
if syncMode == "valves" and cutFlowBetween:
    cutFreshAir(ser)

if syncMode == "concentration" and useLabjack:
    setLabjack(device,syncPort, 1) #set sync high, tells arduino to start I2C with
    scanImage

#set values for the window, global c,cc
c=0 #counter for repeats of a chosen dilution
cc=0 #counter for trials inside a repeat
txt=" diluted vials"

for i in range(nOfRepeats): #to update, from old
    # print("\n>> dilution "+str(concentrationList[i])+" "+txt)
    c=GUI_updateRepeats(winName,c,cc,state,nOfRepeats,nOfTrials)

    if quit:
        print("\nquit")
        cv2.destroyAllWindows()
        break

    #purge
    if purgeTime>0:
        purge(ser,purgeTime)

    #set dilution #TODO: move further and read dilu from seq[j][2]
    # dilu=concentrationList[i]
    # setDilution(ser,dilu)

    N=0#element in the sequence
    t=time.time()
    interruptDisplayed=False
    counter=0 #loopCheckPeriod

    #looping trials , minimize what happens here to not delay time trigger
    cc=0
    while (N<len(seq)):

        if (time.time()-t) >= seq[N][0]: #- timeError: #wait for next element of
the sequence
            print("\nDEBUG if: N "+str(N)+" S[N] "+str(seq[N]))
            #waiting
            if seq[N][1] == 0: #if vial is 0
                print("DEBUG waiting:")
                print(time.time()-t)
                if state!="interrupting":
                    state="waiting"
            if stimulating:
                stimulating=False
                setFinalValve(ser,'off')
                cc+=1# counter trials

            if N>0: #close previous vial valve, try to close vials in 3
previous seq elements
                if isSeqVial(seq[N-1][1]):
                    setOdourValve(ser,seq[N-1][1],"off")
                elif isSeqVial(seq[N-2][1]):
                    setOdourValve(ser,seq[N-2][1],"off")
                elif isSeqVial(seq[N-3][1]):
                    setOdourValve(ser,seq[N-3][1],"off")

            if N+1<len(seq): #open vial for next stimulation
                try:
                    if syncMode == "valves": #quickfix 200131
                        if isSeqVial(seq[N+2][1]) :
                            setOdourValve(ser,seq[N+2][1],"on")
                            setDilution(ser,seq[N+2][2],m3=totalAirFlow)
                            # print("debug2")
                        elif isSeqVial(seq[N+3][1]) :
                            setOdourValve(ser,seq[N+3][1],"on")
                            setDilution(ser,seq[N+3][2],m3=totalAirFlow)
                            # print("debug2")
                        elif isSeqVial(seq[N+1][1]) :
                            setOdourValve(ser,seq[N+1][1],"on")
                            setDilution(ser,seq[N+1][2],m3=totalAirFlow)
```

```
        # print("debug1")
        elif True:
            try:
                if isSeqVial(seq[N+3][1]) :
                    setOdourValve (ser,seq[N+3][1],"on")
                    setDilution (ser,seq[N+3][2],m3=totalAirFlow)
                    # print("debug3")
            except:
                print("seq[N+3][1] doesnt exist. it is normal if
it is the end")

                #close every valves
                for i in range(8):
                    setOdourValve (ser,i+1,"off")
                    setFinalValve (ser,'off')

            except:
                print("something wrong here")

        if N == len(seq)-1:
            print("last element of seq. close everything.")
            #close every valves
            for i in range(8):
                setOdourValve (ser,i+1,"off")
            setFinalValve (ser,'off')
            if useLabjack:
                setLabjack(device,syncPort,0) #cPort,0)

        cc=GUI_updateTrials(winName,c,cc,state,nOfRepeats,nOfTrials)

        #stimulation
        elif isSeqVial(seq[N][1]):
            print("DEBUG stimulation:")
            print(time.time()-t)
            if seq[N][1]==-1:
                print("no stim, baseline air")
            else:
                print("stim, final valve, seq[N][1] ", seq[N][1])
                setFinalValve(ser,'on')
            stimulating=True
            if state!="interrupting":
                state="stimulating"
            cc=GUI_updateTrials(winName,c,cc,state,nOfRepeats,nOfTrials)
            #check for interruption, prepare to stop when this repeat set is
done

        #special cases for "valves" mode at +-delaySync: cut and put back
fresh air; sync and unsync
        elif seq[N][1] == -3:
            if cutFlowBetween:
                setFreshAir(ser,float(totalAirFlow)/1000.0)
            if useLabjack:
                setLabjack(device,syncPort,1)
        elif seq[N][1] == -4:
            if cutFlowBetween:
                cutFreshAir(ser)
            if useLabjack:
                setLabjack(device,syncPort,0)
            print("ok")
        N+=1

        counter+=1 #increment counter for loopCheck
        if counter%loopCheckPeriod==0: #####HERE WAIT KEY

        # TO FIX, ABORT

        k = cv2.waitKey(waitKeyTime) & 0xFF

        if k == ord('q'):
            quit=True
            break

        if k == ord('s'):
            interrupt=True

        if interrupt and not interruptDisplayed: #turn bar to red, finish
current step and wait to continue
            print("\ninterruption "+txt+" vials ")
            print("dilution: "+str(concentrationList[i]))
            print("current stimulation is")
```

```
print("repeat: "+str(c+1)+"/"+str(nOfRepeats))
print("trial: "+str(cc+1)+"/"+str(nOfTrials))
print("wait for the round to finish..\n")

state="interrupting"
cc=GUI_updateTrials(winName,c,cc,state,nOfRepeats,nOfTrials)

interruptDisplayed=True

#out of while

c+=1 #counter for repeats
if syncMode == "concentration" and cutFlowBetween:
    cutFreshAir(ser)
if useLabjack:
    setLabjack(device, syncPort, 0)

#####
if AlwaysInterrupt:
    interrupt=True
if interrupt:
    print("\n >>> >>> interruption succeed <<< <<< ")
    print("press s to resume (in the window) \n ")

state="interrupted"
cc=GUI_updateTrials(winName,c,cc,state,nOfRepeats,nOfTrials)

#stuck in that loop untill press s or q
while True: #check for continue
    #cv2.imshow(winName, img)
    k = cv2.waitKey(1) & 0xFF
    if k == ord('s'):
        interrupt=False
        #cv2.destroyAllWindows()
        break
    if k == ord('q'):
        quit=True
        #cv2.destroyAllWindows()
        break

#####

print("\n >>> >>> waiting for "+str(interRepeatWait) +"seconds <<< <<< \n")
print("press s to pause/resume (in the window)")

t0=time.time()
while (time.time()-t0 < interRepeatWait): #check for continue
    #cv2.imshow(winName, img)
    k = cv2.waitKey(1) & 0xFF
    if k == ord('s'):
        print("pause")
        pause=True
        while pause:
            k = cv2.waitKey(1) & 0xFF
            if k == ord('s'):
                print("resume")
                pause=False
        print( str( interRepeatWait - (time.time()-t0))+ " seconds left..")

    if k == ord('q'):
        quit=True
        #cv2.destroyAllWindows()
        break
#    print("new scan image file")
if syncMode == "concentration":
    if cutFlowBetween:
        setFreshAir(ser, float(totalAirFlow)/1000.0)
    if useLabjack:
        setLabjack(device, syncPort, 1)
    print("sync ON")
#####

""" quitting """
print("\n >>> >>> quitting <<< <<< \n")
#set exit state
if useLabjack:
    setLabjack(device, syncPort, 0) #set sync signal LOW
cv2.destroyAllWindows()
```

```
#close every valves
for i in range(8):
    setOdourValve (ser,i+1,"off")
setFinalValve (ser,'off')
cutFreshAir (ser)

if input("wanna purge 30min? (y/n)")=='y':
    purge(ser,30*60) #purge 30minutes

print("close COM port")
ser.close()#close COM port
```

Python scripts for application of any shape (e.g. ramps, sinus ...) stimuli by modulating odour dilution or flow rate in time, made by adjusting the 3 mass flow controllers of the olfactometer.

apply odour dilution modulation.py

```
from olfacto import *

""" settings """
repeat=5
delayBetween=20 #seconds
triggering=False

#parameters
# initialDil=#0.1
vial=7
max_=10
min_=0.5 #minimum is 0.5
duration=10#seconds #ramp
baselineOdourDuration=3 #seconds #plateau baseline before ramp
rate=20#Hertz #only int
f=2 #frequency sinus ( as in sin(2. * np.pi * f * timestamps))

###time series
ts=True
seq=[5,6,7]*3
repeat=len(seq)

MFC3_init=0.95# 950/1000.0
dilution_init=0.1 #0.01 working so far

""" connecting labjack and olfactometer """
#start labjack-trigger
if triggering:
    device = initLabjack(syncPort=6)
    setLabjack(device,6, 1)

#initialize olfactometer
ser = handshakeArduino_linux(expected='Aurora Scientific 206A')
time.sleep(1)
startOlfacto(ser,MFC3_init ,dilution_init )
time.sleep(1)

""" set pattern """
#rising ramp
# pattern=np.linspace(min_,max_,duration*rate)
# t=np.linspace(0,duration,duration*rate)

#rising ramp with baseline plateau
patternBaseline=np.linspace (min_,min_,baselineOdourDuration*rate)
pattern=np.linspace(min_,max_,duration*rate)
pattern=np.concatenate ((patternBaseline,pattern))
t=np.linspace(0,duration+baselineOdourDuration,(baselineOdourDuration+duration)*rate)

#falling ramp
```

```
# pattern=np.linspace(max_,min_,duration*rate)
# t=np.linspace(0,duration,duration*rate)

#sinus
# w = 2. * np.pi * f
# t=np.linspace(0,duration,duration*rate)
# pattern=((np.sin(w*t)+1)/2 ) * (max_-min_) +min_

for i in range(repeat):
    if ts:
        vial=seq[i]
        print(i+1,"/",repeat)
        # do it, modulation odour dilution
        #open vial
        setOdourValve(ser,vial,"on")
        time.sleep(10) #quick fix
        #set initial dilution
        setDilution(ser,pattern[0])# initialDil )

        #open final valve (flow from MFC1+MFC2)
        setFinalValve(ser,'on')

        #loop over pattern points at the rate mentioned in parametres
        initTime=time.time()
        counter=0
        while (counter<pattern.shape[0]):
            if (time.time() - initTime > t[counter] ):
                print("\n DEBUG time:",t[counter]," value", pattern[counter])
                setDilution(ser, pattern[counter] )
                counter+=1

        #close vial
        setOdourValve(ser,vial,"off")
        #close final valve (flow from MFC1+MFC2)
        setFinalValve(ser,'off')
        #TODO: control MFC1/2 ending behaviour??? useless if final valve closed
        time.sleep(delayBetween)

        #quickfix rebound glitch
        startOlfacto(ser,MFC3_init ,dilution_init )
        time.sleep(1)

#stop trigger
if triggering:
    setLabjack(device,6, 0)
```

apply odour airflow modulation.py

```
from olfacto import *

repeat=3
delayBetween=10 #seconds
triggering=False
#start labjack-trigger
if triggering:
    device = initLabjack(syncPort=6)
    setLabjack(device,6, 1)
#initialize olfactometer
ser = handshakeArduino_linux(expected='Aurora Scientific 206A')
time.sleep(1)
startOlfacto(ser,MFC3_init=950/1000.0,dilution_init=0.01)
time.sleep(1)
"""parameters"""
dilution=10 # in percent
vial=8
max_=950/1000.0 #airflow
min_=0.1#0.01 #airflow
duration=5# 10#seconds
rate=20#20#Hertz
f=0.2 #frequency sinus ( as in sin(2. * np.pi * f * timestamps))
init_MFC2=0

""" set pattern """
#rising ramp
# pattern=np.linspace(min_,max_,duration*rate)
# t=np.linspace(0,duration,duration*rate)
```

```
#falling ramp
# pattern=np.linspace(max_,min_,duration*rate)
# t=np.linspace(0,duration,duration*rate)

#sinus airflux MFC3
w = 2. * np.pi * f
t=np.linspace(0,duration,duration*rate)
pattern=((np.sin(w*t)+1)/2 ) * (max_-min_) +min_

for i in range(repeat):
    print(i+1,"/",repeat)

    #init
    #open vial
    setOdourValve(ser,vial,"on")
    time.sleep(10) #quick fix

    #set initial dilution
    setDilution(ser, dilution )
    #open vial
    setOdourValve(ser,vial,"on")
    #open final valve (flow from MFC1+MFC2)
    setFinalValve(ser,'on')

    #loop over pattern points
    initTime=time.time()
    counter=0
    while (counter<pattern.shape[0]):
        if (time.time() - initTime > t[counter] ):
            print("\n DEBUG time:",t[counter]," value", pattern[counter])
            setDilution(ser, dilution, m3=pattern[counter]*1000.0 )
            counter+=1

    #close final valve (flow from MFC1+MFC2)
    setFinalValve(ser,'off')
    #close vial
    setOdourValve(ser,vial,"off")

    time.sleep(delayBetween)

#stop trigger
if triggering:
    setLabjack(device,6, 0)
```

apply airflow mfc3 patterns.py

```
from olfacto import *
#parameters
triggering=False
pattern="sinus"
customPattern=None #todo
max_=950/1000.0
min_=0.01 #for MFC3 <=0.001 causes rebound, 0.01 is working
duration=10*60 #5*60 #seconds
rate=50 #20#Hertz
f=10 # 0.2 #frequency sinus ( as in sin(2. * np.pi * f * timestamps))

#init and end parameters
MFC3_init=0.95# default is 0.95 #only last 0.1sec...
dilution_init=0.01 #does not matter here, but keep for multipurpose later
MFC3_end=0.95

#start labjack-trigger
if triggering:
    device = initLabjack(syncPort=6)
    setLabjack(device,6, 1)

#initialize olfactometer
ser = handshakeArduino_linux(expected='Aurora Scientific 206A')
time.sleep(0.1)
startOlfacto(ser,MFC3_init,dilution_init)
time.sleep(0.1)
# setFreshAir(ser, 0.01 )triggering=False
```

```
#set pattern to apply
t=np.linspace(0,duration,duration*rate)
if pattern=="risingRamp":
    #rising ramp airflow MFC3
    pattern=np.linspace(min_,max_,duration*rate)
elif pattern=="fallingRamp":
    #falling ramp airflow MFC3
    pattern=np.linspace(max_,min_,duration*rate)
elif pattern=="sinus":
    #sinus airflow MFC3
    w = 2. * np.pi * f
    pattern=((np.sin(w*t)+1)/2 ) * (max_-min_) +min_
elif pattern=="customPattern":
    pattern=customPattern #WARNING: must be same shape as t

# do it, modulation airflow mfc3
initTime=time.time()
counter=0
while (counter<pattern.shape[0]):
    if (time.time() - initTime > t[counter] ):
        print("DEBUG time:",t[counter]," value", pattern[counter])
        setFreshAir(ser, pattern[counter] )
        counter+=1
setFreshAir(ser, MFC3_end )

#stop trigger
if triggering:
    setLabjack(device,6, 0)
```

The following scripts were used to record simultaneously the nose poke investigation with the final valve of the olfactometer, and a camera, during behaviour experiments:

behaviourBoxAcquisition.py

```
# -*- coding: utf-8 -*-
"""
Created on Sun Aug 16 22:01:56 2020

@author: cstefens
"""

"""NOTES:
    to stop kill kernel , ctr+.

    you can interrupt the kernel and the file will be saved anyway
    (truncated because using "w+" open file option allows it )

"""

from olfacto import *
import time
import os

#parameters
saveFilename="121120_pilot_test_pleaseWork_Again.txt" #overwriting ! #in
home/johnstonlab/Python codes/behaviour olfacto box
freq=1000 #in Hz
duration=60*50#30*60 #seconds, you can end it earlier by interrupting the kernel
timeStartAt0=False #set it to False for absolute time
id='beam'

#setting delay from frequency
delay=1/freq #seconds

# connect to the arduino
ser=handshakeArduino_linux(id, baudrate=19200)

# writing to text file
f=open(saveFilename,"w+") #overwriting !
t=time.time()
```

```
if timeStartAt0:
    t_=t
else :
    t_=0

print("writing to text file")
while((time.time()-t)<duration):
    try:
        time.sleep(delay)
        msg=str(ser.readline())
        # print(msg)
        # break
        try:
            #vals are 0 or 1
            vall,val2=msg.split(",")[1][0], msg.split(",")[2][0]
            print(vall)

#msg.split("\r\n")[1].split(",")[1],msg.split("\r\n")[1].split(",")[2]
            f.write( (str(time.time()-t_)+"\t"+vall+"\t"+val2+"\n" ) )
        except Exception as e:
            print("ignored ",str(time.time()-t_)," ",e)
        except KeyboardInterrupt:
            f.close()
            print("finished by KeyboardInterrupt, file is safe")
f.close()
print("finished")
```

cameraBehaviour.py

```
import cv2
import numpy as np
import random
import time

cameraCOM=2 #try -1 to 3... TODO: make automated
fps=30
# saveFilename="test"
saveFilename="PLEASE NAME ME" #overwriting !

#####
saveFilenameVideo=saveFilename+"_video.avi"
saveFilenameStamps=saveFilename+"_videoTimeStamps.txt"

# Create a VideoCapture object
cap = cv2.VideoCapture(cameraCOM)

# Check if camera opened successfully
if (cap.isOpened() == False):
    print("Unable to read camera feed")

# Default resolutions of the frame are obtained.The default resolutions are system
dependent.
# We convert the resolutions from float to integer.
frame_width = int(cap.get(3))
frame_height = int(cap.get(4))

# Define the codec and create VideoWriter object.The output is stored in
'outpy.avi' file.
# fourcc = cv2.cv.CV_FOURCC(*'XVID')
# out = cv2.VideoWriter(saveFilenameVideo,fourcc, fps, (frame_width,frame_height))
out = cv2.VideoWriter(saveFilenameVideo,cv2.VideoWriter_fourcc('M','J','P','G'),
fps, (frame_width,frame_height))

f=open(saveFilenameStamps,"w+") #overwriting !

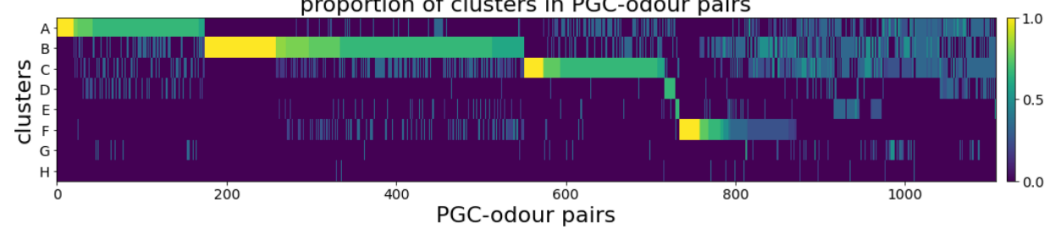
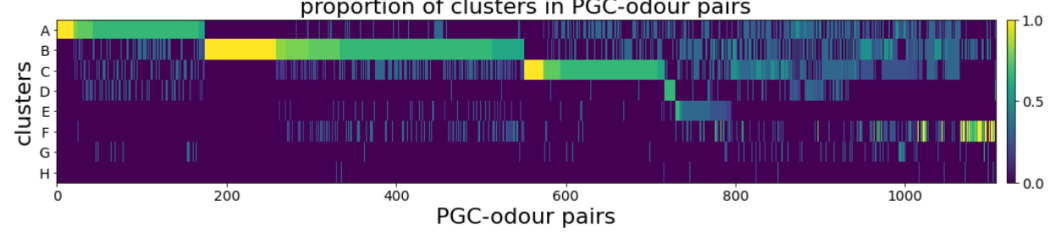
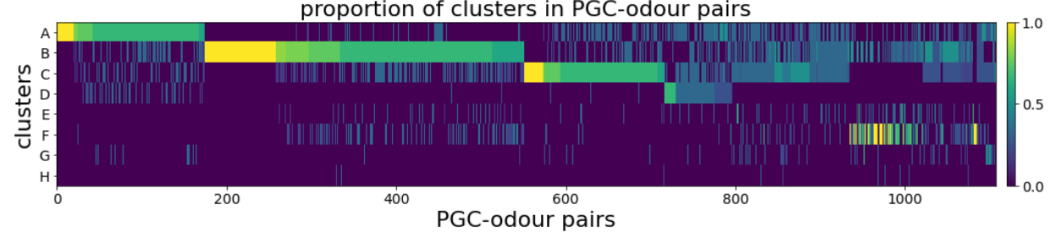
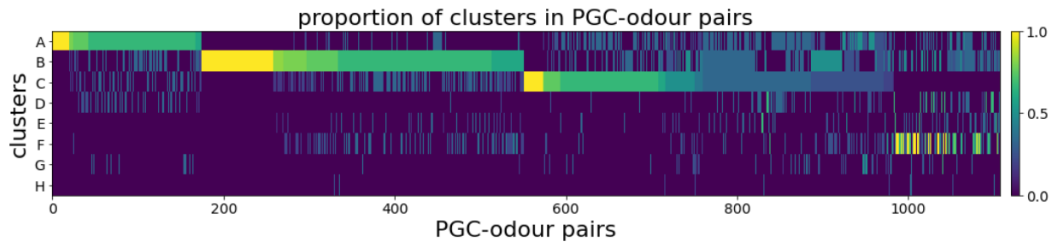
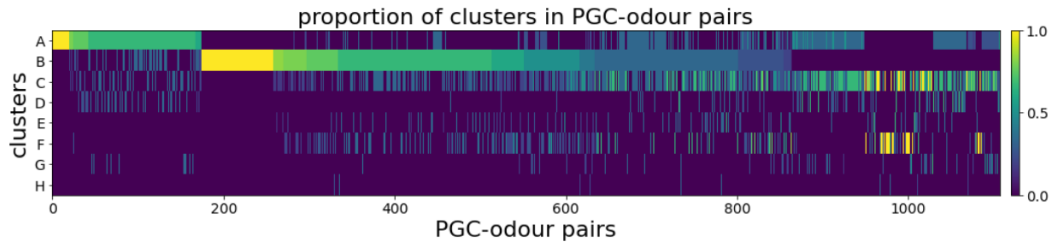
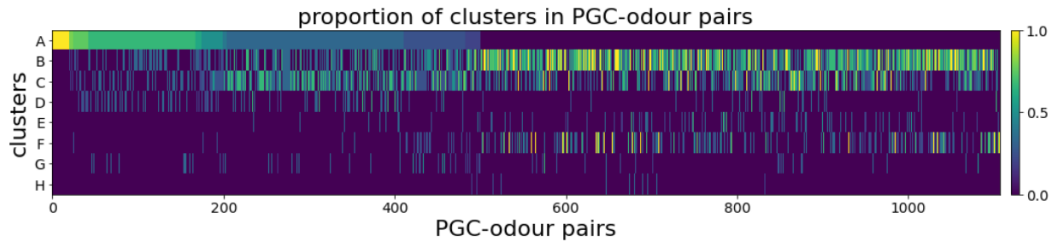
while(True):
    ret, frame = cap.read()
    f.write( str(time.time())+"\n" )
    if ret == True:
        # Write the frame into the file 'output.avi'
        out.write(frame)
        # Display the resulting frame
        cv2.imshow('frame',frame)
        # Press Q on keyboard to stop recording
        if cv2.waitKey(1) & 0xFF == ord('q'):
            f.close()
```

```
        break
    # Break the loop
    else:
        break

# When everything done, release the video capture and video write objects
cap.release()
out.release()

# Closes all the frames
cv2.destroyAllWindows()
try:
    f.close()
except:
    pass
```

Appendix B PGC characteristics details



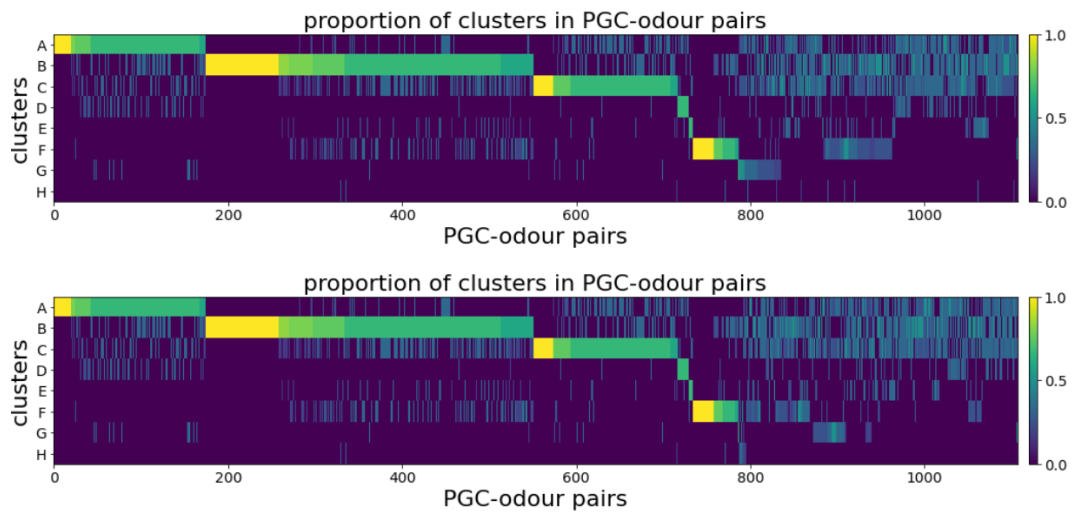


Figure B.1 Sorting of response sequences of PGC-odour per proportion of elicited shapes. This array in each row (PGC-odour) the distribution of each shape (A-H) appearing in the PGC-odour response sequence. It was sorted, in decreasing order, iteratively row by row. The sorting within a row stopped when the value reached 0.5, then the next row is sorted starting from the last sorted column of the previous row. Here is displayed the array after each iteration.

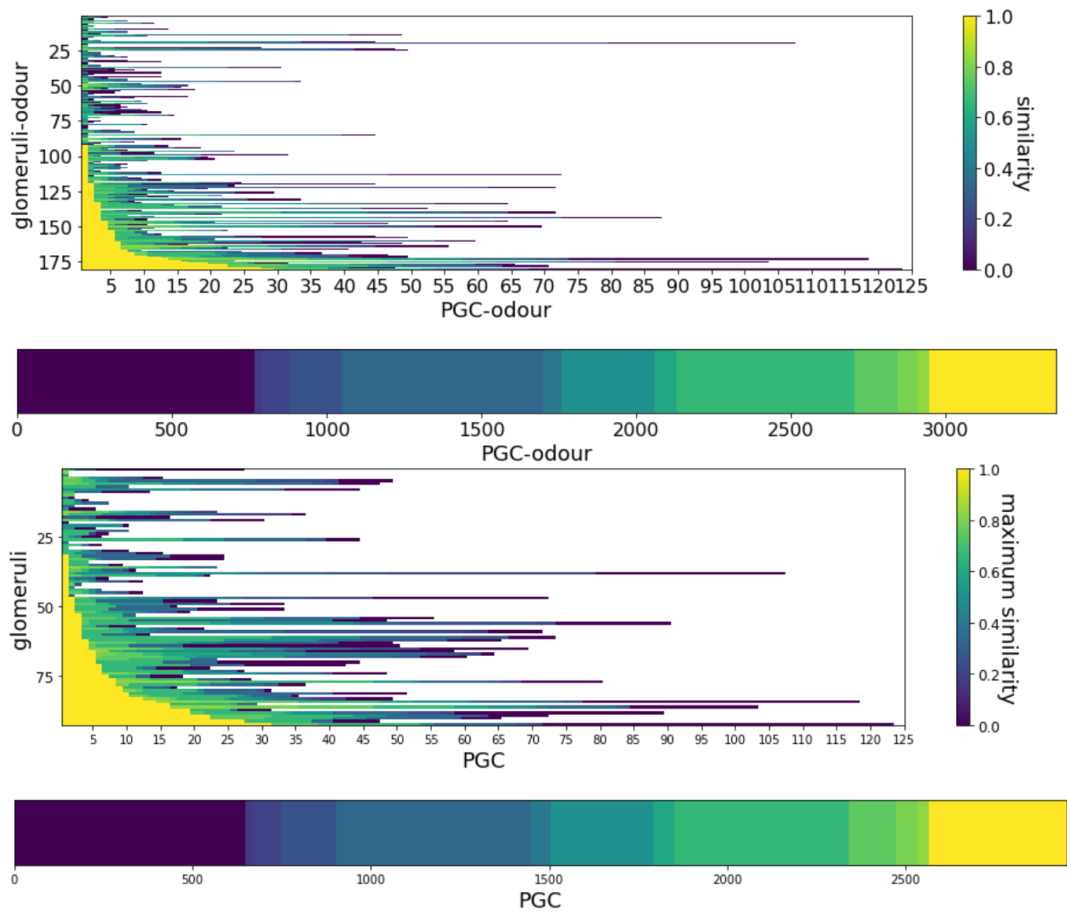


Figure B.2 Distribution of odour-evoked response shape similarities between PGCs and glomeruli. Similarity score between PGC-odour pairs and glomerulus-odour pairs. 1 if all responses correspond to the same clusters, else 0 (top). Maximum similarity of a common odour, used as a connection weight between PGCs and glomeruli (bottom). Connections were counted if maximum similarity >0.12 animals.

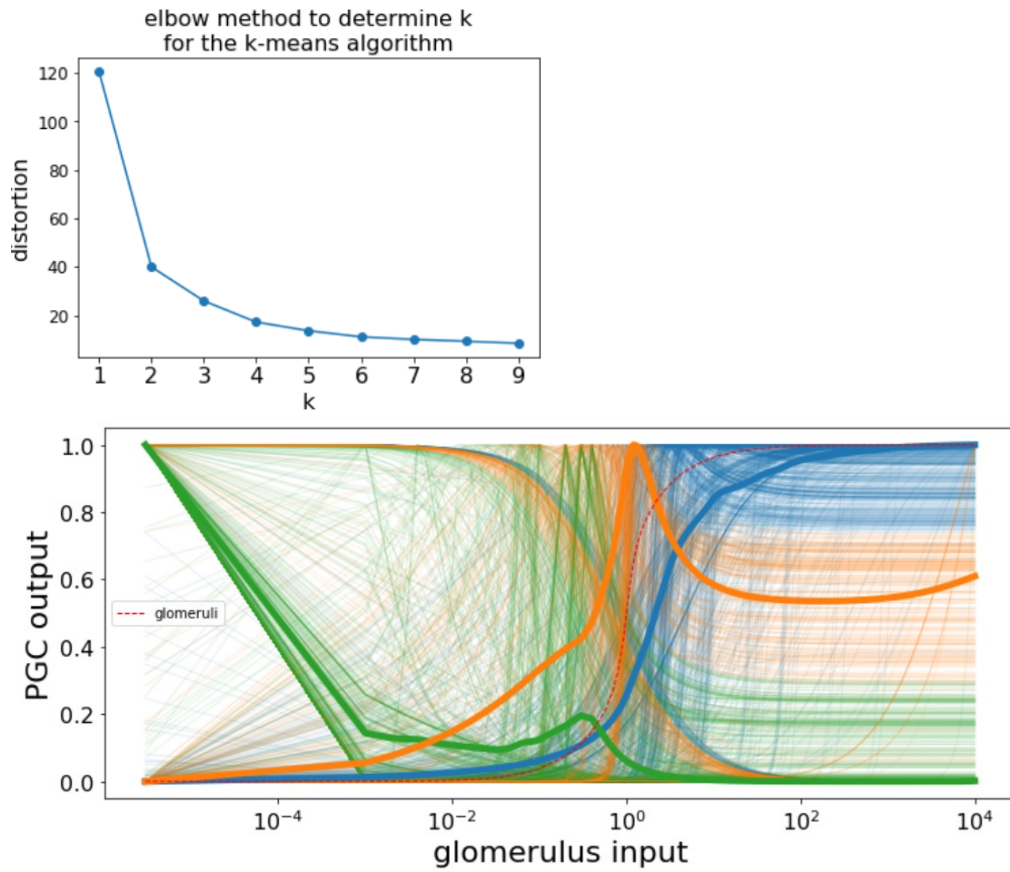


Figure B.3 Determination of the parameter k for clustering transfer functions.

The elbow method helps to determine a value of k that will minimise the distortion of the samples within clusters, k=3 was chosen as it substantially reduced the distortion (left). All the transfer functions are displayed for the 3 clusters (blue, orange, green) and their mean in thick lines (right)

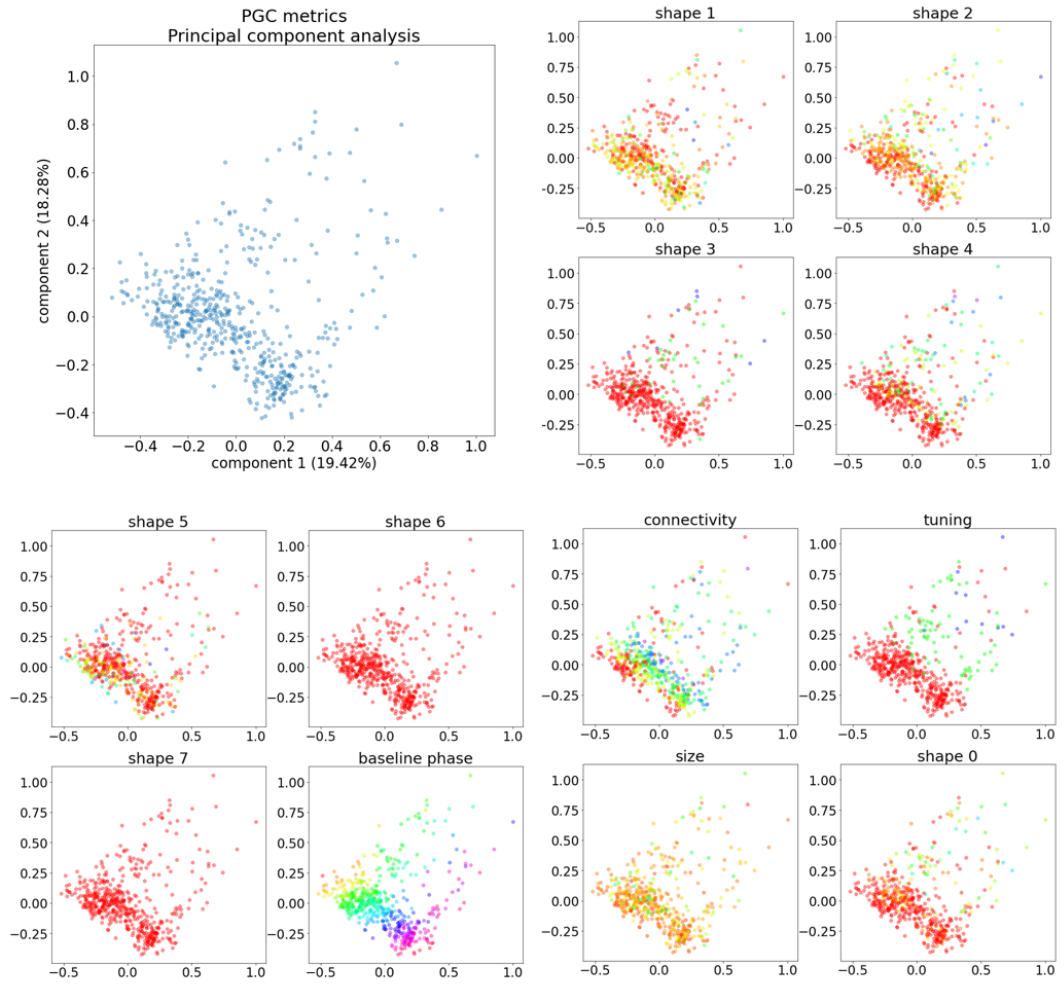


Figure B.4 Colour-coded graduation of PGC metrics in 2D PCA space.

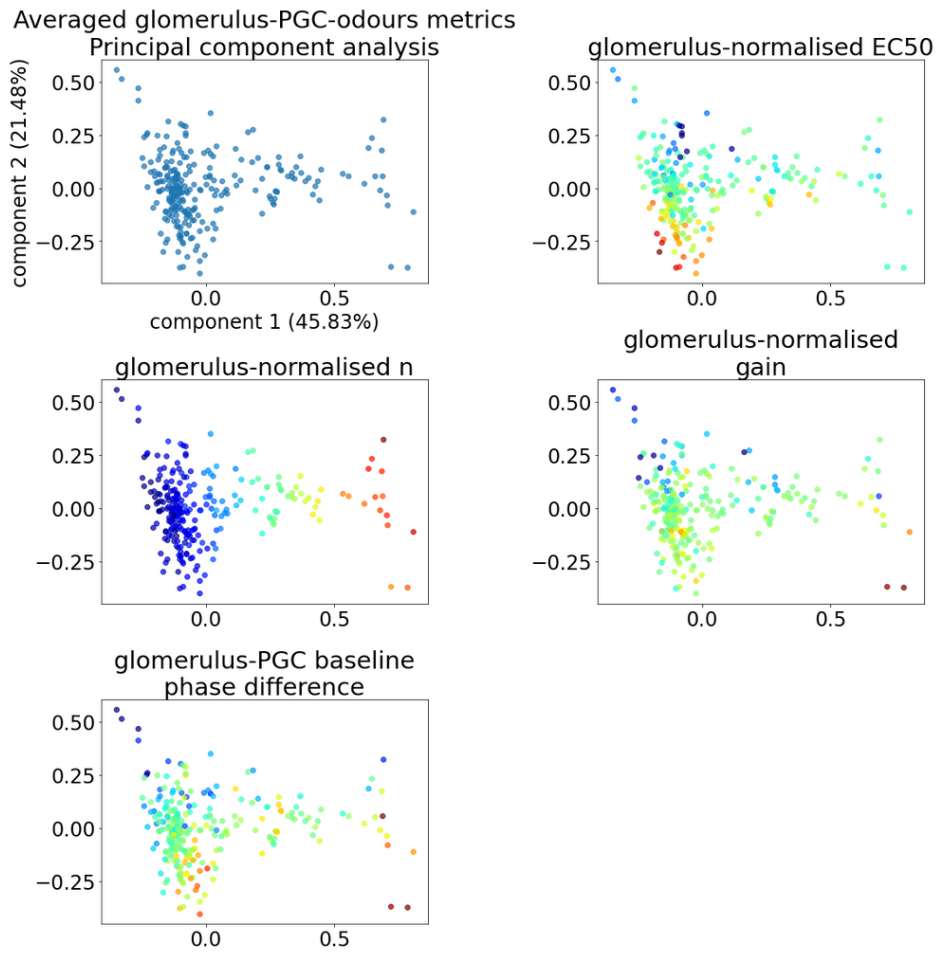


Figure B.4 Colour-coded graduation of PGC-odour metrics in 2D PCA space.

Appendix C sinus and Hill functions fitting

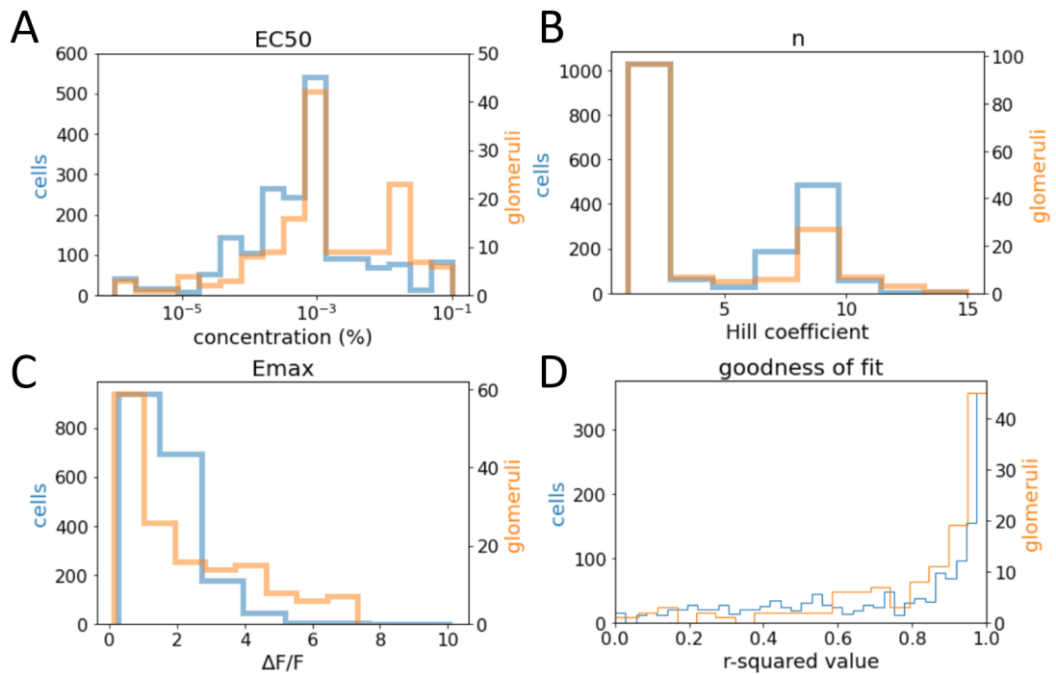


Figure C.1 Fitting of the Hill function. Hill functions were fitted on 3 to 6 activity-concentration points from 1860 PGC-odour and 153 glomerulus-odour pairs from 12 animals, using the `curve_fit` function from the python library `scipy`, with as initial parameters $EC_{50} = 10^{-3}$ and $n = 1$, and as parameters bounds $EC_{50} = [10^{-6}, 10^{-1}]$ and $n = [1, 15]$. **A,B,C.** histograms for the sensitivity (EC_{50}), dynamic range (n), and maximum response (EC_{max}) for PGCs and glomeruli. **D.** R-squared values distribution for all the fittings confirm the error is low with these initial parameters and bounds.

Sinus fitting to ITA oscillations: baseline

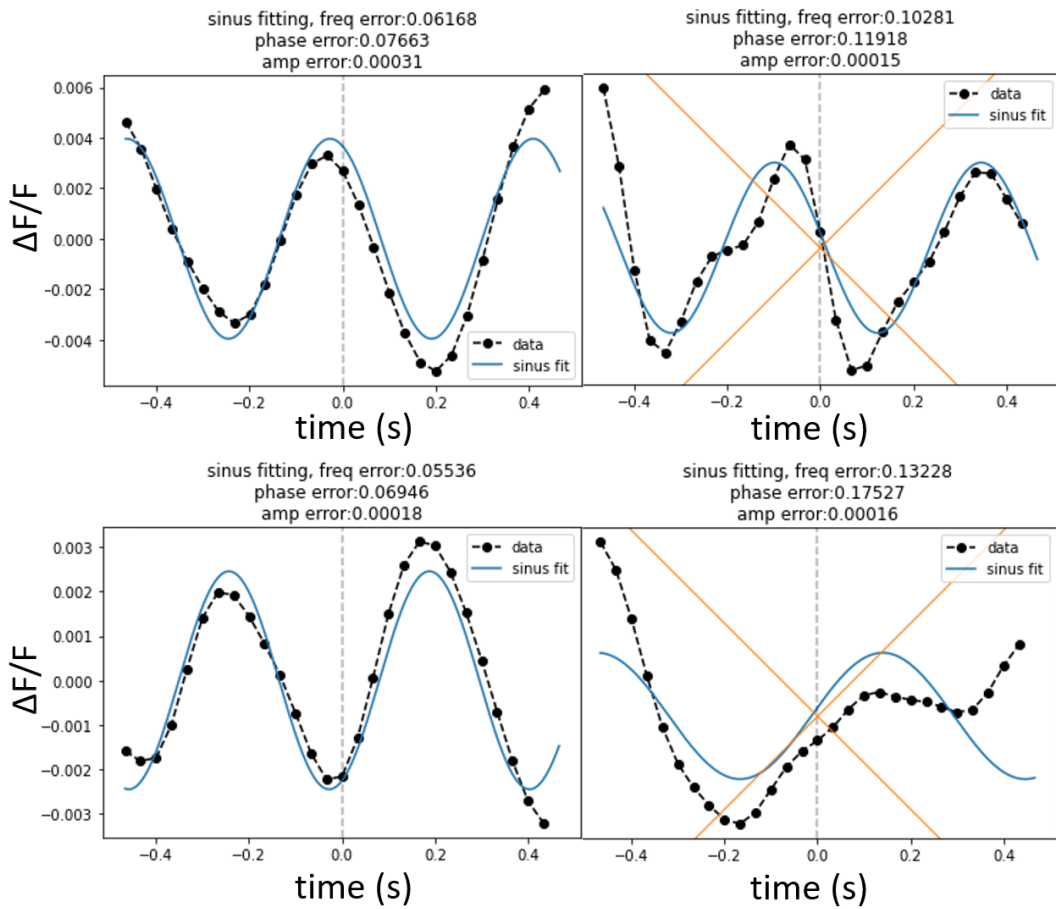


Figure C.2 Fitting of sinusoidal functions on baseline oscillations. Cosines were fitted on interval-triggered average oscillations from the baseline bouts of calcium traces from glomeruli and PGCs. With the `curve_fit` function from the `scipy` python library, the function $r \cos(2\pi ft + \varphi)$ was fitted, where r is the amplitude, f the frequency, and φ the phase. The parameter f was bounded to be between 0.75 and 1.25 the frequency of respiration. The fittings were rejected if the standard deviation error on f was above 0.1. Here are shown, with the standard deviation errors for f , φ , and r , 2 successful fittings on the left, and 2 rejected on the right.

Sinus fitting to ITA oscillations: odours

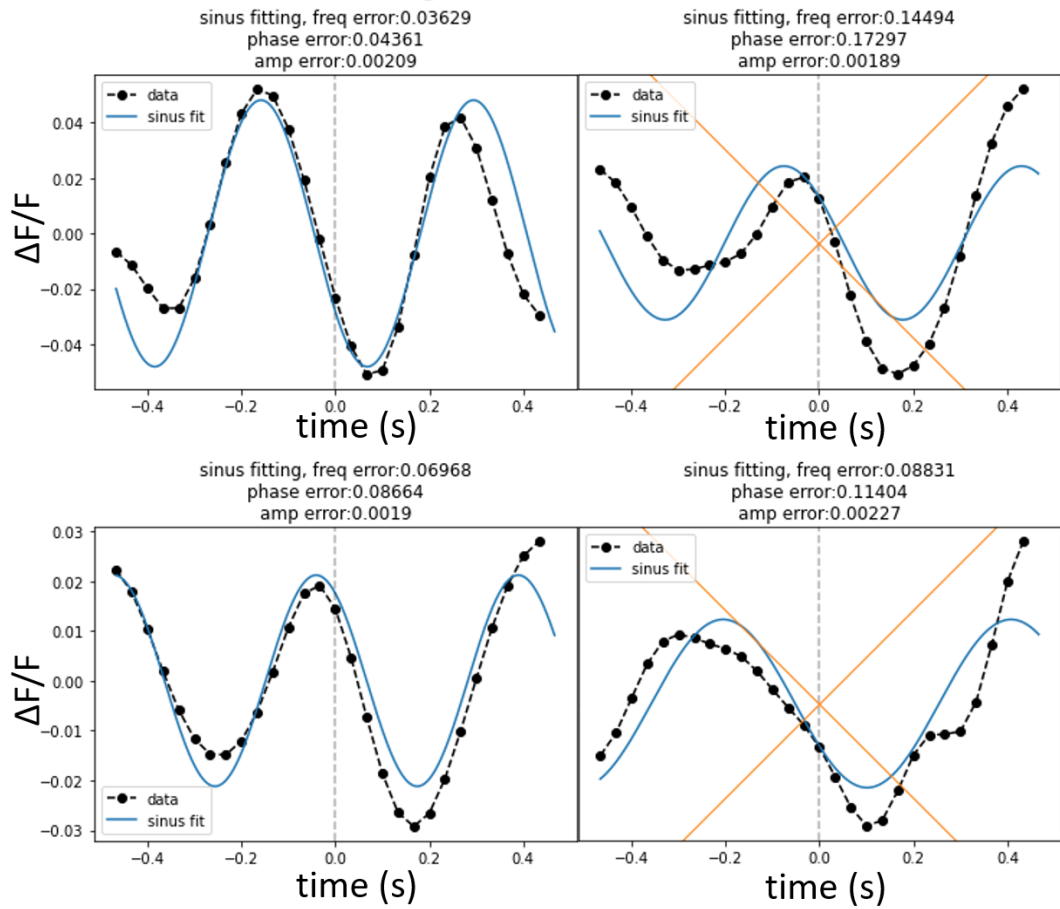


Figure C.3 Fitting of sinusoidal functions on odour-evoked oscillations. Same as the figure C.2 except the amplitudes were higher during odour stimulation than in baseline.

Appendix D PGC activation thresholds for isoamyl acetate

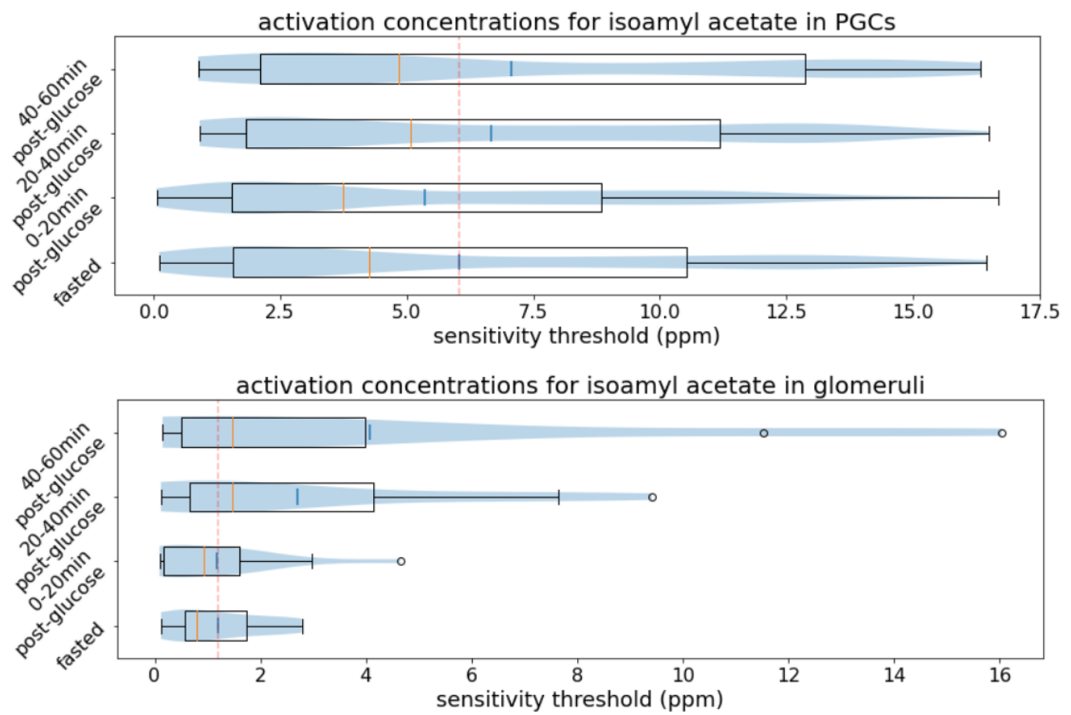


Figure D.1 activation thresholds for isoamyl acetate detected on ramps responses of PGCs and glomeruli. Minimum values of sensitivity threshold (ppm) detected amongst the low, middle, high ramps responses for each PGC and glomerulus. Orange bars are medians. Blue bars are means. The box delimits the lower and upper quartiles. The whiskers show the range of the data, with outliers as circles.